Temp # 76-03500

UNITED TECHNOLOGIES RESEARCH CENTER

UNITED TECHNOLOGIES™

East Hartford, Connecticut 06108

Report R76-912205

Laboratory-Scale Uranium RF Plasma Confinement Experiments

Contract NAS1-13291
Modification No. 2

REPRODUCIBLE COPY
(FACILITY CASEFILE COPY)

REPORTED BY Ward C Roman
Ward C. Roman

APPROVED BY Robert E. Olson
Robert E. Olson
Manager, Fluid Dynamics Laboratory

DATE September 1976

NO. OF PAGES 187

COPY NO. ____

FOREWORD

An analytical and experimental research program on plasma core reactor technology was conducted by United Technologies Research Center (UTRC) under Contract NAS1-13291 with the National Aeronautics and Space Administration (NASA) Langley Research Center. The Technical Monitor of the Contract for NASA during the Contract period was Dr. F. Hohl. The Technical Program Manager for UTRC during the Contract period was Mr. T. S. Latham. The following three reports comprise the required Final Technical Report under the Contract:

1. Rodgers, R. J., T. S. Latham, and N. L. Krascella: Investigation of Applications for High-Power, Self-Critical Fissioning Uranium Plasma Reactors. United Technologies Research Center Report R76-912204, September 1976. Also issued as NASA CR-145048.

2. Roman, W. C.: Laboratory-Scale Uranium RF Plasma Confinement Experiments. United Technologies Research Center Report R76-912205, September 1976 (Present Report). Also issued as NASA CR-145049.

3. Krascella, N. L.: The Spectral Properties of Uranium Hexafluoride and Its Thermal Decomposition Products. United Technologies Research Center Report R76-912208, September 1976. Also issued as NASA CR-145047.

Report R76-912205

Laboratory-Scale Uranium RF Plasma Confinement Experiments

TABLE OF CONTENTS

Page

Report R76-912205

Laboratory-Scale Uranium RF Plasma Confinement Experiments

SUMMARY

An experimental investigation was conducted using the United Technologies Research Center (UTRC) 80 kW and 1.2 MW rf induction heater facilities to aid in developing the technology necessary for designing a self-critical fissioning uranium plasma core reactor (PCR). Pure uranium hexafluoride (UF_6) was injected into argon-confined, steady-state, rf-heated plasmas in different uranium plasma confinement tests to investigate the characteristics of plasma core nuclear reactors. The objectives were: (1) to confine as high a density of uranium vapor as possible within the plasma while simultaneously minimizing the uranium compound wall deposition; (2) to develop and test materials and handling techniques suitable for use with high-temperature, high-pressure gaseous UF_6; and (3) to develop complementary diagnostic instrumentation and measurement techniques to characterize the uranium plasma and residue deposited on the test chamber components. One of the diagnostic techniques which was developed was an optical scanning method for uranium plasma emission and absorption (cw single-frequency tunable dye laser system) measurements yielding radial profiles of temperature and uranium atom number density and x-ray absorption methods for measuring the total amount of confined uranium.

In all tests, the plasma was a fluid-mechanically-confined vortex-type contained within a fused-silica cylindrical test chamber. The test chamber peripheral wall was 5.7-cm-ID by 10-cm-long. Exploratory tests were conducted using the 80 kW rf induction heater (f = 13.56 MHz) with the test chamber at approximately atmospheric pressure and discharge power levels on the order of 10 kW. Four different test chamber flow configurations were tested to permit selection of the configuration demonstrating the best uranium vapor confinement characteristics and minimum wall coating for subsequent tests at higher power and pressure in the 1.2 MW rf induction heater (f = 5.4 MHz) facility.

The test configuration selected for use in the more extensive rf plasma tests using the 1.2 MW rf induction heater employed a radial-inflow vortex, driven by injectors located on only one of the water-cooled endwalls. In addition to exhaust thru-flow ducts located at the center of each endwall, an axial bypass annulus was located near the periphery of the endwall opposite the vortex injectors. A concentric set of water-cooled, fused-silica tubes formed the peripheral wall. The cylindrical test chamber was 5.7-cm-ID by 10-cm-long. This test chamber flow configuration was designed to operate at pressures up to approximately 20 atm and rf

discharge power levels up to about 100 kW. In the majority of tests, a single UF_6 injector protruded 2.0 cm into the test chamber; the injector was located on the centerline axis within the thru-flow duct of one endwall. UF_6 was supplied to the injector from a heated canister system capable of supplying the gaseous UF_6 at temperatures up to 450 K and pressures up to 20 atm. The rf plasma tests in the 1.2 MW rf induction heater were conducted over a range of test chamber pressures from 1 to 12 atm and rf discharge power levels from about 10 to 85 kW. The UF_6 mass flow rate ranged from 0.01 to 0.21 g/s.

Diagnostic measurements included: plasma physical and electrical characteristics; calorimetric power losses; total radiation intensity and radiation intensity in different wavelength bands; on-axis spectral emission scans between 300-700 nm; side-on absorption measurements using both an argon-ion laser system ($\lambda = 514.51$ nm) and a cw single-frequency tunable dye laser system ($\lambda = 591.54$ nm); side-on chordal emission and absorption measurements ($\lambda = 591.54$ nm) using an optical scanning system; diagonal end-on 8 Kev x-ray absorption measurements; and, analysis and identification of the residue deposited on the test chamber components from selected tests using six different complementary analysis techniques; electron diffraction, x-ray diffraction, scanning electron microprobe, IR spectrophotometer, surface profilometer, and secondary ion mass spectrometer instrumentation.

Uranium compound reference standards were developed at UTRC to permit post-test characterization and identification of the residue coatings deposited on the various components of the test chamber. Modifications made to the test chamber configuration and flow control schemes and evaluation by these analysis techniques resulted in further reduction in the residue material deposited on the components of the test chamber. The whitish "mist-like" residue found on the inside diameter of the fused-silica tubes during post-test analysis was identified to be principally uranyl fluoride (UO_2F_2).

At UF_6 mass flow rates of 2.2×10^{-2} g/s, test times up to 41.5 minutes were achieved with less than approximately 20 mg of uranium compound residue wall coating ($< 0.04\%$ of total UF_6 mass flow). If required, longer test times would be possible subject to additional radiation shielding and cooling modifications to the 1.2-MW rf induction heater test tank and resonator section. The introduction of the UF_6 into the rf plasma resulted in a significant increase in the emitted radiation, particularly in the visible and near-UV wavelength bands. At comparable and greater UF_6 mass flow rates (up to 3.2×10^{-2} g/s), optical chordal scans of the absorption by and the emission from the uranium rf plasma discharge were successfully conducted. These measurements provided input to a computer program (optically thick case) which calculated the spectral emission and absorption coefficients and the corresponding radial temperature profile using Kirchhoff's law. Uranium plasma centerline temperatures of approximately 9800 K with a distinct off-axis peak (≈ 8700 K occurring at $r/R = 0.6$) were determined. Edge of plasma temperatures were approximately 6000 K. From these data and additional experimental measurements of the uranium neutral atom

(UI) absorption line width ($\approx$3.5 GHz at λ = 591.54 nm), the radial variation of total uranium atom (UI + UII + UIII) number density within the rf plasma was determined. (Approximately 10^{16} U atoms/cm^3 at the axial midplane centerline of the rf plasma discharge.) To complement these measurements, x-ray absorption measurements were conducted to determine the total amount of uranium confined within the test chamber. Depending on the optical path length chosen, total uranium number density levels up to approximately 4 x 10^{17} atoms/cm^3 were determined. The uranium atom density required to sustain criticality in a typical plasma core reactor is 2 x 10^{19} atoms/cm^3 at an operating pressure of approximately 500 atm. Since the rf plasma tests were run at approximately 2 atm, scaling by pressure alone would indicate that a uranium number density of 8 x 10^{16} atoms/cm^3 in the rf plasma tests would correspond to a uranium vapor partial pressure ratio of the approximate magnitude required for criticality.

In separate tests to maximize the UF_6 mass injection flow rate, up to an order of magnitude increase in the mass flow rate of UF_6 was achieved (2.1 x 10^{-1} g/s) while still maintaining the plasma in a confined mode of operation; the corresponding test time was 1.2 minutes.

The overall test results demonstrated applicable flow schemes and associated diagnostic techniques have been developed for the fluid-mechanical confinement and characterization of uranium vapor within an rf plasma discharge when pure UF_6 is injected under steady-state conditions for long test times into an argon-confined, high-temperature, high-pressure, rf-heated plasma.

RESULTS AND CONCLUSIONS

RF plasma exploratory tests employing the UTRC 80 kW rf induction heater system with pure UF_6 injection yielded the following results:

1. Based on approximately forty tests using four different types of test chamber configurations and flow schemes, an optimum test chamber configuration and flow scheme was identified for use in extended uranium plasma confinement tests employing the UTRC 1.2 MW rf induction heater facility. The test chamber configuration selected was 10-cm-long; the peripheral wall was an externally gas-cooled 5.7-cm-ID x 6.1-cm-OD fused-silica tube. The configuration incorporated endwall-driven vortex injection and a combination of on-axis thru-flow exhaust (both endwalls) and a single annular axial bypass exhaust located in the endwall assembly opposite the vortex injectors.

The above tests were conducted at chamber pressures of 1 atm, rf discharge power levels of approximately 10 kW, argon vortex mass flow rates up to 2 g/s, estimated UF_6 mass flow rates (based on weighing) of hundreths of grams per second, and discharge diameters at the axial midplane of about 5 cm. The discharge power and pressure levels were limited by the safety aspects of the 2-mm-thick gas-cooled fused-silica peripheral wall.

2. With the above configuration and flow scheme, light uranium-compound-coatings on the fused-silica peripheral wall and endwall assemblies accompanied the moderate UF_6 injection flow rate. The rf plasma discharge was relatively well-confined and stable throughout the majority of test conditions. Occasional discharge oscillations were noted ($f \approx 1\text{-}5$ Hz); the discharge was also susceptible to extinguishment by rapid changes in the flow conditions (particularly injection of UF_6).

3. A UF_6 handling and feeder system previously designed to provide a controlled and steady flow of heated UF_6 at temperatures up to 450 K was modified and adapted for these tests. The system was designed to provide UF_6 mass flow rates up to about 5 g/s and subsequent possible injection of UF_6 into test chambers operating at pressures up to 20 atm. The system was tested (no rf plasma present) at UF_6 flow rates up to 5.8 g/s.

4. A multiple-concentric-tube UF_6 injector assembly was developed which could be located concentrically (at different axial positions) within the test chamber endwall assembly and subsequently provide a steady-state flow of gaseous UF_6 into the rf plasma test chamber. High pressure water (20 atm) heated to approximately 350 K via a steam heat exchanger and flowing at 0.14 ℓ/s between the concentric tubes of the UF_6 injector was required to alleviate possible condensation/solidification in the UF_6 transfer line.

RF plasma tests employing the 1.2 MW rf induction heater system with pure UF_6 injection yielded the following results:

1. Based on the prior 80 kW rf plasma exploratory tests, a new test chamber configuration was fabricated. As in the prior tests, the test chamber was 10-cm-long; the peripheral wall, however, was formed by a concentric set of water-cooled fused-silica tubes. The inner tube was 5.7-cm-ID x 6.1-cm-OD and the outer tube was 6.5-cm-ID x 7.3-cm-OD. This test chamber was designed for steady-state operation at rf plasma power levels up to about 100 kW and chamber pressure levels up to approximately 20 atm. The test chamber incorporated a single endwall driven vortex injection scheme and a combination of on-axis exhaust thru-flow and axial-bypass exhaust on the opposing endwall only. This test chamber was operated over a wide range of test conditions including: chamber pressures 1-12 atm, rf plasma discharge power levels 10-85 kW, argon vortex mass flow rates 1-10 g/s, discharge diameters at the axial midplane from 1.5-3.5 cm, and UF_6 injection mass flow rates from 0.01 to 0.21 g/s.

2. An rf plasma test series was conducted with pure UF_6 injection incorporating additional modifications to the test chamber and flow control scheme which further enhanced, within the operating range tested, the uranium vapor confined within the plasma while simultaneously minimizing the deposition of uranium and/or uranium compounds on the walls of the test chamber. Included were changes to the argon vortex injectors, location and size of the UF_6 injector, rf work coil and operating frequency, and cooling in peripheral wall annulus and endwall assemblies.

3. Supporting diagnostic equipment, instrumentation, and analysis techniques were developed applicable to characterizing the uranium rf plasma experiments. These included:

(a) A calorimetric technique for determining the total power deposited into the uranium rf plasma;

(b) A radiometric technique for determining the total radiation emitted from the uranium rf plasma and its distribution within selected wavelength bands;

(c) A spectral emission measurement technique for comparing the spectral emission characteristics of argon-only and uranium/argon rf plasma discharges over a wavelength range from 300-700 nm;

(d) Optical scanning equipment and techniques for obtaining side-on chordal scan measurements of the emission from and absorption by uranium rf plasmas. This technique, combined with additional uranium neutral atom absorption line (λ = 591.54 nm) width measurements using a cw single-frequency tunable dye laser system, permitted estimates of the radial distribution of the uranium atom (UI + UII + UIII) number density within the rf plasma (approximately 10^{16} uranium atoms/cm^3 at the axial midplane centerline of the rf plasma discharge);

(e) A modified Abel inversion method for rotationally symmetric, local thermodynamic equilibrium, optically thick ($0.2 \leq I/I_o \leq 0.8$) plasmas was adapted to the chordal scan measurements to permit determination of the radial profile of the volume emission and absorption coefficients from the chordal emission and absorption measurements. From these and application of Kirchhoff's law, the radial temperature profile within the uranium rf plasma was determined. The uranium plasma centerline temperatures were approximately 9800 K with a distinct off-axis peak of approximately 8700 K occurring at $r/R = 0.6$. The edge of plasma temperatures were approximately 6000 K. The uranium rf plasma temperature conditions determined (6000-10,000 K range) were representative of those expected in future self-critical fissioning uranium plasma core reactor experiments.

(f) An x-ray absorption technique for determining the total uranium mass contained in the rf plasma test chamber was established. This measurement technique supplemented the optical scanning emission and absorption scheme and is applicable within the 3×10^{16} to 3×10^{18} uranium atoms/cm^3 range. Depending on the optical path chosen, total uranium number density levels up to 4×10^{17} atoms/cm^3 were determined from the measurements.

4. Various complementary diagnostic techniques for identifying and characterizing small (milligram) quantities of residue were integrated into a detailed post-test examination of the individual components comprising the test chamber (i.e., fused-silica tube peripheral wall, endwalls, UF_6 injector, on-axis thru-flow exhaust duct, axial bypass exhaust duct). The diagnostic techniques included use of x-ray diffractometer, electron microscope, scanning electron microprobe, IR spectrophotometer, profilometer, and ion scattering spectrometer/secondary ion mass spectrometer instrumentation. A complete catalog of all uranium and/or other compounds possible as residue on the various components was established. These techniques and catalog of compounds aided in minimizing the uranium compound wall deposition, e.g., indicated that silicone grease is unacceptable as a sealant material on the O-rings of the test chamber and the oxygen content of the argon buffer gas supply is high enough to require filtering of the gas supply to reduce one of the sources of oxygen leading to the formation of undesirable uranium oxides on the peripheral wall.

5. A test series was conducted to demonstrate minimum coating of uranium compounds on the peripheral wall of the test chamber after a long sustained operating period. An approximately 50 kW rf plasma with pure UF_6 injected, at a mass flow rate of 0.022 g/s, into the test chamber at 2 atm was operated steady-state for 41.5 minutes. After this extended test time (limited only by radiation loading and water cooling to several existing rf induction heater electrical components), 30.4 mg of

residue (primary UO_2F_2 with a trace of SiO_2) was deposited on the fused-silica peripheral wall. This included approximately 10 mg of silicone grease initially deposited on the ends of the fused-silica tube for sealing the O-rings. The residue was located primarily toward the vortex injector end of the fused-silica tube. The residue represented less than 0.04% of the total UF_6 mass flow.

6. A test series was conducted to determine the maximum mass flow rate of UF_6 that could be injected into the rf plasma (regardless of wall coating) while still maintaining the discharge in a confined, steady-state mode of operation. An approximately 70 kW rf plasma was operated for 1.2 minutes at a chamber pressure of 2 atm; the UF_6 mass flow rate was 0.21 g/s (greater than an order of magnitude increase over that of previous tests). Approximately 135 mg of residue (primarily UO_2F_2 with a trace of UO_3 and SiO_2) was deposited on the fused-silica peripheral wall primarily near the vortex injector end of the tube. Additional changes to the argon vortex injection system, UF_6 injector scheme and O-ring shielding should permit still further increases in the UF_6 mass flow rates attainable.

A principal technology required to establish the feasibility of fissioning uranium plasma core reactors is the fluid mechanical confinement of the hot fissioning uranium plasma with sufficient containment to both sustain nuclear criticality and minimize deposition of uranium or uranium compounds on the confinement chamber peripheral walls. The laboratory-scale rf uranium plasma experiments conducted to date have aided in developing some of the long lead time technologies required to proceed with the PCR experiments. Included has been the development of a test chamber and flow control scheme together with the associated diagnostic instrumentation required to determine the density of uranium vapor within the plasma. In a typical PCR, the uranium atom density required to sustain criticality is 2×10^{19} atoms/cm^3 at an operating pressure of approximately 500 atm; since the rf plasma tests were run at about 2 atm, scaling by pressure alone would indicate that a uranium number density of 8×10^{16} atoms/cm^3 in the rf uranium plasma tests would correspond to a uranium vapor partial pressure ratio of the approximate magnitude required for criticality.

Throughout the entire test series, valuable experimental data were also accumulated on the corrosion aspects of hot, pressurized UF_6. These data will be applicable to future tests, particularly in the initial transfer, handling, filtering, feeding, flow control, flow monitoring, and safety aspects of UF_6.

In addition to continued rf uranium plasma confinement tests, future experiments will include the development of techniques for reconstituting the gaseous compounds in the plasma exhaust mixture and separating the UF_6 from the buffer gas such that it is in a form suitable for reinjection into the plasma.

INTRODUCTION

Fissioning uranium plasma core reactors (PCR's) based on the utilization of fissile nuclear fuel in the gaseous state could be used as a prime energy source for many space and terrestrial applications. In addition to aerospace propulsion applications, several new space power and/or terrestrial options are being considered; these include:

(1) Direct pumping of lasers by fission fragment energy deposition in UF_6 and lasing gas mixtures.

(2) Optical pumping of lasers by thermal and/or nonequilibrium electromagnetic radiation from fissioning UF_6 and/or fissioning uranium plasmas.

(3) Photochemical or thermochemical processes such as dissociation of hydrogenous materials to produce hydrogen.

(4) MHD power conversion systems for generating electricity.

(5) Advanced closed-cycle gas turbine driven electrical generators.

Power extraction from the fission process with nuclear fuel in the gaseous state allows operation at much higher temperatures than those of conventional solid core nuclear reactors. Higher operating temperatures result in more efficient thermodynamic cycles and, in the case of fissioning uranium PCR's, result in applications using direct coupling of energy in the form of electromagnetic radiation. The continuous reprocessing of gaseous nuclear fuel also leads to a low steady-state fission product inventory in the reactor and limits the buildup of long half-life transuranium elements.

Reference 1 discusses the overall status of plasma core reactor technology, the various energy conversion concepts, conceptual designs of various configurations, and a summary of all current research directed toward demonstrating the feasibility of fissioning uranium PCR's.

A principal technology required to establish the feasibility of fissioning uranium plasma core reactors is the fluid mechanical confinement of the hot fissioning uranium plasma with sufficient containment to both sustain nuclear criticality and minimize deposition of uranium or uranium compounds on the confinement chamber peripheral walls. Figure 1 is a sketch of one unit cell configuration of a PCR. The reactor would consist of one or more such cells imbedded in beryllium oxide and/or heavy-water moderator and surrounded by a pressure vessel. In the central plasma fuel zone, gaseous uranium (injected in the form of UF_6 or other uranium compound) is confined by argon buffer gas injected tangentially at the periphery of the cell. In applications in which it is desired to couple thermal radiation from the fissioning uranium plasma to a separate working fluid, the thermal radiation is transmitted through the argon buffer gas layer and subsequently through internally-cooled transparent walls to a working fluid channel such as shown in Fig. 1. The channels would contain particles, graphite fins, or opaque gases to absorb the radiation. The mixture of nuclear fuel and argon buffer gas is withdrawn from one or both endwalls at the axial centerline. For other applications in which it is desired to extract power in the form of nonequilibrium, fission-fragment-induced short wavelength radiation emissions, the transparent wall would be removed and a medium such as lasing gas mixtures would be mixed with either the fissioning uranium fuel or the buffer gas. The reason for this distinction is that most transparent wall materials have intrinsic radiation absorption characteristics at the short wavelengths expected to be emitted from the plasma in the form of fission-fragment-induced nonequilibrium electromagnetic radiation. Typically, for plasma conditions with an edge-of-fuel-region temperature of approximately 5000 K, operating pressures in the fissioning uranium plasma are on the order of 500 atm. This is dependent upon the combined partial pressures of nuclear fuel required for criticality, dissociation products, electrons from ionized species, and some argon buffer gas present in the fuel region.

A long-range program plan for establishing the feasibility of fissioning gaseous UF_6 and uranium plasma reactors has been formulated by NASA. Reference 2 summarizes the plan which comprises the performance of a series of experiments with reflector-moderator cavity reactors. A review of the past work is contained in Ref. 3. Los Alamos Scientific Laboratory (LASL) is currently performing these cavity reactor experiments.

Briefly, the initial reactor experiments currently being assembled at LASL consist of low-power, self-critical cavity reactor configurations employing undissociated, nonionized UF_6 fuel at near minimum temperatures required to maintain the fuel in gaseous form. Power level, operating temperature, and pressure will be systematically increased in subsequent experiments to approximately 100 kW, 1800 K, and 20 atm, respectively. The final approximately 5 MW reactor experiment will operate with a fissioning uranium plasma at conditions for which the injected UF_6 will be dissociated and ionized in the active core.

Performance of static UF_6 critical experiments is currently in progress (Ref. 4). Key objectives of the initial static UF_6 and subsequent flowing UF_6 reactor experiments are to facilitate (1) research on gaseous cavity reactor physics and on nonequilibrium optical radiation from fissioning UF_6, (2) demonstrations of physical applications of nonequilibrium optical radiation such as lasers, and (3) demonstrations of methods for heat extraction for power generation and propulsion applications. A key objective of the final approximately 5 MW fissioning uranium PCR experiment is to provide a facility for demonstrating feasibility of high-reactor-power applications using very intense photon fluxes such as described above.

PCR technology studies at UTRC currently consist of several experiments and theoretical investigations directed toward evaluating the feasibility of the PCR concept. Extensive non-nuclear vortex flow and plasma fluid mechanical research has been conducted over the past fifteen years at UTRC. Past fluid mechanics (non-plasma) experiments (Ref. 5) have indicated that a radial inflow vortex is well-suited for applications which require the preferential containment of a heavy gas within a light gas created by the radial inflow vortex. A radial-inflow vortex flow pattern is characterized by an essentially laminar radial stagnation surface across which there is no net inward radial buffer gas flow.

Other previously reported experiments (Ref. 6) have been conducted on the confinement of argon rf plasmas. These tests were directed primarily toward development of a high-intensity, high-power-density plasma energy source (equivalent black-body radiating temperatures >6000 K). Some of these initial exploratory tests included direct injection of very dilute mixtures of UF_6 (typically, 1% UF_6 in an argon carrier gas) into the argon rf plasma. Coating of the fused-silica peripheral wall occurred but short-time sustained plasma operation was demonstrated. Particle feeder systems were also developed which permitted steady-state injection of carbon (C), tungsten (W), uranium dioxide (UO_2), and uranium oxide (U_3O_8) into test chambers operating at pressures up to 40 atm. In general, these exploratory test results confirmed that simulated fuels could be confined fluid-mechanically with steep concentration gradients at the edge-of-fuel location.

Reference 7 (see also APPENDIX D) summarizes the results of initial exploratory experiments in which pure UF_6 was injected for short times into an argon-confined, steady-state, rf-heated plasma to investigate the characteristics of PCR's.

This research report presents some recent results of the uranium plasma confinement tests together with the associated diagnostics and measurement techniques applicable to PCR's. These tests were conducted using pure UF_6 injected for long time periods into steady-state, argon-confined, rf-heated plasmas. The UTRC 1.2-MW rf-induction heater facility was employed in these latter tests.

DESCRIPTION OF PRINCIPAL EQUIPMENT

UTRC 1.2 MW RF Induction Heater Facility

Primary Heater Components and Test Tank

The experiments reported herein were conducted using the 1.2 MW rf induction heater system. Figure 2 is a block diagram of the 1.2 MW rf induction heater. The operating frequency was selected by means of an L-C type variable frequency oscillator whose 0.5 W output is amplified to approximately 2 kW using a neotron amplifier. The rf operating frequency normally used was approximately 5.4 MHz. The 2 kW output was used to provide rf excitation for the basic rf induction heater stages which receive dc power from the common saturable-reactor-controlled power supply. The 2 kW excitation drives a 40 kW output amplifier which in turn drives an 80 kW buffer amplifier. This buffer amplifier was the actual driving stage for the final power amplifiers. All these stages contain controls for tuning the matching circuit at the final power amplifier input. This allows individual adjustments to be made to the various amplifier systems, thus aiding in increasing the overall system efficiency. The rf output power was supplied by two power amplifier tubes which drive a resonant tank circuit (resonator section) of unique design. The output of the two power amplifiers was resonated by a push-pull resonator. All stages were operated class "C" to provide maximum efficiency. The saturable-reactor-controlled power supply for the 40 kW, 80 kW, and final power amplifier stages was continuously variable in dc voltage from 2 kV to approximately 24 kV. This provided flexibility in selecting power levels compatible with the various experimental test requirements.

A photograph of an assembled test configuration installed concentrically within the set of 9-cm-dia water-cooled rf work coils within the resonator section of the induction heater is shown in Fig. 3. The entire resonator section consisted of two arrays of ten vacuum capacitors, located (as shown in Fig. 3) within a 1.7-m-dia cylindrical aluminum test tank. Each vacuum capacitor array is connected with a single turn work coil. Each work coil consisted of five water-cooled copper tubes which were silver-soldered together to form a single structure. The coils were silver-plated to reduce resistance heating due to the high coil current. The ends of the capacitors were water-cooled and rf chokes were installed in the water cooling lines. All tests reported herein were conducted with atmospheric air in the test tank.

The front of the test tank was a removable dome (shown removed in Fig. 3) containing five (10-cm-dia) view windows for observation of the test section from different angles and/or diagnostic equipment access. An overhead trolley and winch system permitted removal of the dome and allowed rapid access to the test section for inspection of uranium compound residue deposition on different components of the chamber after completion of a test. A mycalex support system (see Fig. 3) was attached to the base of the aluminum test tank and forward section resonator to hold the endwall assembly of the test configuration concentric within the rf work coils.

All components of the rf induction heater were water-cooled with a total water flow rate of about 3.8 ℓ/s. Measurements were made of all the cooling water and gas flow rates, associated temperature rises, and all electrical quantities necessary for performing a component and overall system power balance on the rf equipment. Meters to monitor the voltage, current, and power in various stages of the rf induction heater were used during the tests. Strip-chart recorders were also used to continuously monitor the plate voltage, plate current, and resonator voltage. The rf voltage supplied to the resonator sections was measured with a capacitor-type voltage probe (see Fig. 3). An automatic twenty-four channel stepping-type temperature recorder was used to monitor all the critical thermocouples located throughout the rf induction heater system, the components of the rf test chamber, and the various cooling water and gas inlet reference temperatures.

The rf input power for the plasma discharge was determined by the rf voltage supplied to the resonator section of the heater and the impedance of the plasma and resonator which, in turn, determined the current level. The impedance of the plasma was determined by its size and electrical conductivity.

Gas and Cooling Water Flow System

Figure 4 is a schematic of the argon gas and high-pressure cooling water flow systems. Commercial grade argon gas was supplied to the test chamber (i.e., to the vortex injectors located on the periphery of the endwall) from a 72.5 scm bottle supply. Flow meters were used to measure the argon mass flow rate during the tests. The exhaust gases (argon plus other volatile uranium compounds) were removed from the endwall through exhaust ducts and routed through an appropriate exhaust system (UF_6 condenser system, see Fig. 5). Downstream of the condenser system were flow control valves used to adjust the pressure in the test chamber. The exhaust gases were then ducted to the final neutralizing trap ($NaOH + H_2O$) located on the roof of the laboratory.

To provide the necessary water cooling, two closed-loop, high-pressure cooling systems, each having a total storage capacity of approximately 320 ℓ, were used. Each system employed a positive displacement pump which supplied up to 1.3 ℓ/s of cooling water at approximately 40 atm. A surge suppressor was used in each coolant loop to damp out the pressure pulsations, inherent in these type pumps, to less than 1 percent. Figure 4 shows additional details, including locations of the heat exchangers and flow metering equipment.

Plasma Starting System

A vacuum start technique was used in all the tests, since the UF_6 injector located within the endwall thru-flow duct (see following section entitled TEST CHAMBER CONFIGURATIONS for additional description) precluded the use of auxiliary starter rods. With this technique, the rf plasma was ignited at approximately 10 mm Hg using breakdown of the argon gas which occurred at a resonator voltage of about 4 kV. This technique had the advantage of eliminating the introduction of foreign materials into the test chamber which would be present with dc arc retractable rod starting techniques and also, in conjunction with the argon feed and the exhaust trap system, permitted a partial purge between tests.

UF_6 Transfer System

In support of the rf plasma experiments, a UF_6 handling and feeder system to provide a controlled and steady flow of heated UF_6 at temperatures up to 450 K was developed. Since successful completion of the rf plasma tests, particularly at high power and pressure levels, requires a reproducible, continuous, and safe UF_6 handling and flow monitoring system, considerable effort was devoted toward establishing this capability.

Based on the results of exploratory UF_6 handling and flow metering tests, the need for elimination of as much contamination as possible from the UF_6 supply and flow handling system became apparent. Difficulties experienced in early tests using hot UF_6 included partial clogging of several of the feedlines, total clogging of some small hypotubes, and, on several occasions, complete clogging of 5-mm-ID main transfer lines and valves. The partial and total clogging occurred in some of the tests even when relatively high electrical resistance heater temperatures were employed (≤ 475 K). Analysis of some of the material collected from the clogged lines revealed it to be a combination of UF_4, UO_2, and occasionally a third unidentified compound. Both electron diffraction and IR spectrophotometer diagnostic techniques were used to identify the compounds. To verify the possible causes of residue in the transfer lines, a separate test was conducted wherein two identical parallel feedlines were used, one prepared with normal cleaning (acetone and argon purge) and the other using an acid-flush technique (0.1 N HCl solution, followed by trichlorethylene, and then a heated bakeout followed by outgassing under vacuum conditions for several hours). The results indicated a minimum amount of residue was present in the acid-flush lines as compared to the normally cleaned lines; thus all tests reported herein include this cleaning procedure.

Figure 5 is a schematic diagram of the UF_6 transfer system. The system was designed to provide UF_6 mass flow rates up to about 5 g/s and subsequent possible injection of UF_6 into the test chambers operating at pressures up to approximately 20 atm. Figure 6 shows the vapor pressure curve for UF_6 for the operating ranges of interest. (Refer to APPENDIX C for additional details on the properties and assay of the as-received UF_6.)

The principal components of the UF_6 transfer system (see Fig. 5) were the UF_6 boiler, the boiler heat supply system, and the UF_6 condenser (exhaust) system. The boiler was a 2 ℓ Monel cylinder rated at 200 atm working pressure. Monel was selected because of its resistance to chemical attack by hot, pressurized UF_6. (Refer to APPENDIX C for additional details on the corrosive aspects of UF_6.) A heat exchanger to provide internal heating was located in the bottom of the boiler. The thermocouple wells, heat exchangers, and UF_6 flow lines were all fabricated from 6.4-mm-OD Monel tubing. As shown in Fig. 5, electrical resistance heater tape was wrapped around the majority of components. An insulated 3.5 kW electrical heater surrounded the boiler and was used to reach the desired equilibrium temperature and pressure prior to flowing the UF_6. A variable powerstat (see Fig. 5) controlled the evaporation rate and temperature within the boiler. Figure 7 is a photograph of the UF_6 supply system and associated instrumentation installed adjacent to the test tank.

In the tests reported herein, use of the electrical heater assembly alone was sufficient to provide the required flow rates; in future tests employing higher UF_6 flow rates for longer time periods, electrically-heated gaseous N_2 will be supplied to the UF_6 boiler heat exchanger. In this case, control of the rate of UF_6 evaporation is accomplished using the bypass loop shown in Fig. 5. To serve as a safety (rapid cool-down) device in the event of a UF_6 leak at or near the boiler assembly, a high-pressure (40 atm) cooling water line and valve assembly was connected to the boiler internal heat exchanger coils. Additional safety was provided by a removable plexiglass enclosure which surrounded the boiler and was connected through a 25-cm-dia flexible metal duct to the exhaust gas scrubber system (1800 cfm) located on the laboratory roof.

Chromel-Alumel thermocouples installed in the wells within the UF_6 boiler and connected to a temperature recorder were used for continuous monitoring of the boiler temperature. The gaseous UF_6 exiting the boiler passed through a dual set of welded-bellows-type shutoff valves. A pressurized argon purge line was connected to the UF_6 transfer line Monel tubing at a tee connection. A pressure transducer, burst disc (refer to APPENDIX C for discussion of UF_6 corrosion effects on the stainless steel burst disc), and a thermocouple were also connected into the transfer line adjacent to the purge line. A micro-meter-type welded bellows needle valve was also located in the UF_6 transfer line, followed by another pressure transducer. The Bell & Howell pressure transducers used were Type 4-317; these were variable-resistance-type and employ unbonded strain-gage windings connected in a four-arm bridge. They had an all-welded internal construction and metal-to-metal bonds welded at temperatures approximately three times higher than the operating limit of 625 K. Application of a thin layer of pure nickel onto the 410 stainless steel substrate was required to protect the end face of the transducer from the hot, pressurized UF_6. (Refer to APPENDIX C for additional details on the corrosion aspects of UF_6.) Therefore, a 2.5×10^{-2}-mm-thick pure nickel (99.999%) coating was electroplated onto the 1.5-cm-dia face of the pressure transducer.

A Matheson linear mass flow meter (calibrated for UF_6) was located in the transfer line to provide on-line determination of the UF_6 mass flow rate prior to entering the UF_6 injector within the test chamber. Earlier experience with UF_6 and standard rotameter-type flow meters indicated severe etching and corrosion occurs after relatively short operating times. The linear mass flow meter permitted flow metering of hot UF_6 over a flow rate range from approximately 0.003 to 0.5 g/s. The meter was calibrated at Matheson Corporation at equivalent UF_6 flow rates up to 3.39 g/s. By incorporating a Monel transducer, the meter was capable of handling heated UF_6. The meter basically consisted of an electrically-heated tube and an arrangement of thermocouples to measure the differential cooling caused by the UF_6 gas passing through the tube. The thermoelectric elements generate a dc voltage proportional to the rate of mass flow through the tube. Thus, the meter is relatively insensitive to pressure and temperature changes. After sustained usage of the linear mass flow meter system throughout the test program, a deterioration in the output signal (volts) as a function of the UF_6 mass flow rate was noted. Disassembly and examination of the sensor head and transducer revealed a light grey-green coating; an acetone flush removed part of the coating but a recalibration with argon revealed a change in the meter characteristics. The indicated flow rate remained a linear function of the meter output signal but the slope of the curve was reduced. To rectify this situation, periodic calibrations against a standard calibrated argon flow meter were employed in the remaining test series.

The exhaust from the test chamber, comprised of argon, UF_6, and other volatile uranium compounds, was collected in the UF_6 condenser system located downstream of the test chamber. The condenser system consisted of two 0.5 ℓ stainless-steel vessels (connected in parallel) immersed in liquid N_2. All valves throughout the condenser system were welded-bellows-type. A neutralizing trap (NaOH + H_2O) was located downstream of the condenser system to remove any residual uranium or uranium compounds which passed through the flow trap, shown in Fig. 5.

Test Chamber Configurations

Figure 8 is a sketch showing a cross section of the basic test chamber configuration employed in the 1.2 MW rf induction heater tests with pure UF_6 injection. For simplicity, only half the symmetric chamber is shown. This test chamber configuration was selected based on the results of the exploratory rf plasma test series summarized in APPENDIX D. This test chamber configuration incorporates several features, including the ability to change the axial location of the on-axis UF_6 injector, the injection area of the argon vortex injectors, the ability to vary the distribution of exhaust gas flow (axial bypass), and cooling water to the peripheral wall annulus. (Refer to APPENDIX D, Fig. 92 for a sketch illustrating the endwall exhaust gas scheme used on the left endwall assembly (not shown in Fig. 8).) This endwall had provision for removing the exhaust gas through an axial bypass annulus located on the periphery of the endwall. The axial distance between endwalls was 10 cm. Figure 9 contains photographs showing details of this test chamber configuration and a view through the center viewport of the test tank with an argon rf plasma present. The peripheral wall was comprised of a concentric set of water-cooled fused-silica tubes. (Refer to APPENDIX C for additional details on the properties of the as-used fused-silica tubes.) The inner tube was 5.7-cm-ID x 6.1-cm-OD; the outer tube was 6.5-cm-ID x 7.3-cm-OD. The argon vortex was driven from the right endwall by a set of eight equally-spaced stainless-steel vortex injectors located tangent to the periphery of the endwall. In addition to the axial bypass provision in the left endwall, both endwalls had the option for removing varying amounts of the exhaust gas through the on-axis thru-flow ducts (using independent valve controls). Heat exchangers were located downstream of the endwall assemblies to aid in cooling down the exhaust gases. As shown in Fig. 8, the UF_6 injector, located on-axis and concentrically within the right endwall, was fabricated from a 50-cm-long three concentric copper tube assembly and in the majority of tests was located with the injector tip extending into the test chamber. High pressure water (20 atm) heated to approximately 350 K via a steam heat exchanger (see Figs. 4 and 7) flowed at 0.14 ℓ/s between the concentric tubes of the UF_6 injector. This provided cooling relative to the hot plasma environment while still maintaining a high enough temperature in the injector to permit flowing the pressurized gaseous UF_6 without solidification in the UF_6 transfer line/injector (see Fig. 6).

Diagnostic Equipment

Calorimetric Measurements

The total power deposited into the uranium rf plasma was obtained from an overall test chamber energy balance by summing the power lost by radiation, power deposited into the annular coolant of the peripheral wall, power deposited into the endwall assemblies, power convected out the exhaust ducts, as well as, power deposited into the heat exchanger and UF_6 injector assembly. Measurements were made of all cooling water flow rates using rotameters and/or magnetic-type flow meters. The associated inlet and exit coolant temperatures were monitored with copper-constantan thermocouples located as close to the test region as possible. The power convected out the thru-flow ducts was measured using an exhaust gas heat exchanger installed in each of the exhaust duct lines.

Radiometric Measurements

The power radiated from the uranium rf plasma was measured using a specially constructed radiometer and chopper wheel assembly. A block diagram of the radiometer optical system and associated transmission characteristics are shown in Fig. 10. A Reeder RBL-500 thermopile detector with a quartz window was used as the radiometer sensing element. The output of the thermopile was connected to an operational amplifier and displayed on a strip-chart recorder. Internal rf shielding and rf chokes were required to isolate the radiometer electronic system. Radiation within different wavelength bands was measured using the various transmission cut-on/cut-off filters shown in Fig. 10(b). The response of the thermopile with filters was calibrated using a standard Eppley Laboratory source of spectral irradiance. The total power radiated from the plasma and in each wavelength band was calculated assuming isotropic radiation, including allowance for blockage due to the rf work coils.

Continuous observation of the rf plasma discharge during the tests with pure UF_6 injection was accomplished using an overhead projection screen system. Still pictures (using neutral density filters) taken through the various viewports were used for estimating the discharge diameter and shape (see Fig. 9(b)).

Dye Laser System

Figure 11 is a schematic of the tunable cw single-frequency dye laser used to provide the very narrow uranium line used in the absorption measurements. A Spectra-Physics Model 170 argon-ion laser (10 W) was used for the pump power and was operated at $\lambda = 514.51$ nm. The Spectra-Physics Model 580 dye laser system used is shown in Fig. 12. The unit was used with a methanol and water solution containing Rhodamine 6G dye. Rhodamine 6G absorbs in the wavelength band $\lambda = 480$ to 530 nm and provides laser gain from $\lambda = 540$ to 630 nm. This system permits synchronizing the three possible tuning mechanisms, cavity length, etalon length, and cavity prism. The unit employs a single high-finesse, low-loss piezo-scanned tunable etalon, automatic scanning electronics, a low fm jitter dye circulation system, and a temperature-controlled oven assembly to aid in maintaining stability (single line operation without mode hopping). For high resolution scans, the cavity length was tuned while the etalon was traced in synchronism with the cavity scan. For large bandwidth scans, the etalon was scanned while the cavity length tracked (see Fig. 11). The cavity prism was tracked in synchronism with the etalon to keep the laser power constant. For the majority of the tests reported herein, approximately 1 W of pump power was used. Typical dye laser output powers (narrow line operation at λ = 591.54 nm) were 50 to 100 mW. The λ = 591.54 nm uranium line was selected because it is a relatively strong Uranium I (neutral atom) line and appears well-defined in the spectral emission scans. The lower state for the λ = 591.54 nm line is the Uranium I ground state. The half-width of the laser line at this wavelength was approximately $\Delta\lambda = 10^{-4}$ nm.

Optical Diagnostic System Used for Absorption and Emission Chordal Scans of Uranium Plasma

Figure 13 is a schematic diagram of the optical diagnostic system used for the absorption and emission measurements in the rf plasma tests with pure UF_6 injection. Figure 14 is a photograph of the overall 1.2 MW rf plasma test facility and a portion of the dye laser/optical system located on the pneumatic isolation table. The 1.2 by 1.8 m pneumatic table was required to adequately isolate the dye laser system and majority of associated equipment from all vibrations in the 1.2 MW rf induction heater test facility. In addition, rf shielding and various filter systems were adapted to various electrical components to eliminate rf and undesirable electrical feedbacks and ground loops. The 1.2 MW rf master control console is shown at the left of Fig. 14. To the left of the aluminum test tank is the majority of the flow meters and valving associated with the water cooling systems for the test chamber. Directly to the right of the aluminum front dome is the control equipment for the argon gas system and the UF_6 transfer and feeder system. The instrument rack to the right contains recorders for monitoring the UF_6/rf plasma electrical characteristics, the temperatures of various components of the UF_6 transfer and feeder system, and the pressure transducer outputs from the UF_6 supply system. Each system was installed and checked out separately to verify isolation from possible stray rf interference effects unique to this type of experiment.

As shown in Fig. 13, a Perkin-Elmer Uranium lamp (hollow cathode type) was used as the uranium line reference standard. Earlier tests verified that the uranium lamp did not have sufficient intensity in the wavelength range of interest ($\Delta\lambda$ = 400-600 nm) to be used as the line source in the plasma absorption measurements at a discrete wavelength. A Spectra-Physics confocal Fabry-Perot spectrum analyzer with a free spectral range of 8 GHz ($\approx 10^{-2}$ nm) was used to define and calibrate the tuning wavelength spectrum. A Coherent Radiation power meter was used to permit (together with a beam splitter) continuous monitoring of the dye laser output power at the particular wavelength line selected (normally λ = 591.54 nm). An Ithaco Dynatrac phase-sensitive-detector and lock-in amplifier (Model 391A with automatic frequency tracking) and a dual set of Princeton Applied Research Laboratory (Model 125) chopper-signal-generator assemblies (capable of multiple frequency operation) were used in the system, as shown in Fig. 13. A pair of fixed front surface mirrors

(5-cm-dia and located within a vernier adjustable Oriel mount) were used to direct the approximately 1.5-mm-dia laser beam into the aluminum test tank (parallel to the major axis of the discharge). The second mirror assembly was located on a large I-beam to minimize vibrations. A Jodon beam expander (1.5-cm-dia aperture) and collimator was located inside the test tank, as shown in Fig. 13. Another fixed front surface mirror was located in the test tank approximately 6 cm behind the axial midplane of the fused-silica tube test chamber at an angle of 45 deg to the discharge major axis. This mirror was mounted on a cantilever rod assembly which permitted movement to different axial locations along the major axis of the discharge. The centerline of the expanded and collimated laser beam traversed the concentric set of fused-silica tubes, which form the test chamber, 0.75-cm-off-axis, as shown in Fig. 8. The laser beam exited from the aluminum test tank through an aperture and the central viewport shown in Figs. 13 and 14. A 10-cm-dia aerial lens (f/1.8, focal length = 34.3 cm) was located inside the test tank to aid in focussing the laser beam onto the slit of the monochromator and to correct for the beam divergence through the test chamber.

The final optical tracking system used for making the chordal scans of the plasma emission and absorption, as shown in Fig. 13, evolved after several preliminary designs, ray tracing analyses, and bench test experiments. The optical system design had to account for a certain amount of refraction through the test chamber geometry employed. The effect of the concentric fused-silica tubes was twofold. The refractive effects of concentric, right circular cylinders filled alternately with gas, quartz, water, quartz and air were calculated and are easily predictable. The second effect (surface imperfections), however, was not smoothly varying and cannot be compensated for in the lens and optical system design. This effect had to be calibrated out for each test, i.e., once the rotational orientation of the two concentric fused-silica tubes was selected, they were maintained in that orientation until completion of that particular test. A 1.5-cm-off-axis displacement was employed in the chordal scan measurements. This was dictated by the fixed location of the 10-cm-dia central view window in the large aluminum test tank dome. Fortuitously, the 1.5 cm dimension corresponded to the approximate radius of the rf plasma discharge during normal operation with pure UF_6 injection.

The remainder of the optical diagnostic system included a fixed front surface mirror, a 10-cm-dia, 20-cm-focal length lens, a rotating front surface mirror, and a Jarrel Ash 0.25 m (or 0.5 m with f/8.6 optics) monochromator with f/3.5 optics and an EMI 9558 (or an RCA C-31034 with flat response between 300-900 nm) photomultiplier (S-20 response) tube assembly (see Fig. 13). A specially constructed rf shielded signal generator and controller system was used for operating the General Scanning Inc. mirror motor drive. The mirror drive assembly had an independent frequency, amplitude, and off-set control. The system was set-up to image a source of cross-sectional radius 1.5 cm without vignetting within the monochromator system. Since the source and slit exist in conjugate planes at a magnification ratio of 1.57, the 25 μm square slit arrangement employed in the monochromator represented a scanning aperture 39 μm square at the plane of the discharge centerline (both emission and absorption). For emission measurements, the dye laser beam was blocked and the chopper assembly (85 Hz) located adjacent to the central viewport of the test tank was used (see Fig. 13). For absorption measurements, the chopper assembly adjacent to the dye laser head was used (650 Hz). Calibration checks were included to verify that the dye laser output beam (λ = 591.54 nm) power remained essentially constant for relatively long time periods. The beam splitter and power meter shown in Fig. 13 was used for this on-line determination. The spectrum analyzer was used to verify that the dye laser operated in single mode at the selected wavelength. The uranium lamp was used to select the wavelength of the uranium line used (591.54 nm) and to set the monochromator at the peak of this line. The monochromator, in turn, was used to make the initial setting of the dye laser on this same line. Additional fine tuning was accomplished during the actual UF_6 rf plasma tests by tuning the central frequency control of the dye laser system to maximum absorption.

The optical tracking system was checked out first with only an argon rf plasma present. This permitted a verification of tracking reproducibility and ioslation of the instrumentation from extraneous vibration and/or rf interference effects; reasonably reproducible scans were obtained. The time constant normally used with the phase-sensitive-detector was 125 ms. The signal generator and controller for the scanning mirror was set-up to provide a different scanning rate (approximate factor of 2X) between the plasma discharge centerline to the 1.5-cm-off-axis location and the return scan from the off-axis location back to the discharge centerline. Typically, 10s was required for a scan.

Refer to APPENDIX B for an additional discussion of the calibration methods related to the emission and absorption chordal scans using the optical system shown in Figs. 13 and 14.

Equipment and Systems for Chemically-Analyzing and Characterizing the Residue Deposited on Various Components of the Test Chamber

To permit a detailed analysis of the samples of residue collected from the various components of the test chamber after rf plasma tests with pure UF_6 injection, the following UTRC instrumentation was employed:

1. Taylor-Hobson profilometer (Talysurf-4) -- permitted quantitative determination of the magnitude of surface coating/etching/erosion that may take place on the surface of the fused-silica tube.

2. Perkin-Elmer IR Spectrophotometer (Model 457) -- permitted identification of compounds using IR spectrophotometric absorption measurements (2.5-40 μm wavelength range) of reference material standard compounds and small samples of residue removed from test chamber components.

3. Cameca Scanning Electron Microprobe (Model CAMEBAX) -- permitted determination of the elements present in the residue samples and also scanning electron micrographs. Showed topographical and compositional variations and permitted x-ray mapping of the individual elements present.

4. Norelco X-Ray Diffractometer (Mark II) -- permitted identification of compounds present in the residue samples by subjecting them to copper K_α radiation and comparing the resulting x-ray diffraction patterns with reference standards.

5. Hitachi Electron Microscope using selected area diffraction (SAD) (Model HU-11) -- permitted identification of compounds present in the residue samples by subjecting them to electron bombardment. Also provided indication of relative crystallinity of the material.

6. 3M Ion Scattering Spectrometer (ISS)/Secondary (or sputtered) Ion Mass Spectrometer SIMS (Model 520 B) -- permitted identification of the various elements and compounds present in the residue samples. The unique features of this instrument that distinguish it from the other instruments described above are (a) it was sensitive to just the outer monolayer of the surface, (b) its sensitivity was as high as one part of a monolayer per million, (c) it gave positive identification of the compounds, and (d) it could detect hydrogen and distinguish isotopes of uranium.

DISCUSSION OF TEST RESULTS

Exploratory Tests

Details of the exploratory tests are summarized in APPENDIX D. Basically, the majority of exploratory tests were conducted using the 80 kW rf induction heater with the test chamber at approximately atmospheric pressure and rf discharge power levels on the order of 10 kW. Four different test chamber flow configurations were tested from which the configuration demonstrating the confinement of uranium vapor at the highest pure UF_6 injection rates with minimum wall coating was chosen. The power and pressure levels employed in the exploratory tests were primarily limited by the safety aspects of the thin-walled gas-cooled fused-silica peripheral wall. In these exploratory tests moderate UF_6 injection flow rates were employed, which resulted in light uranium-compound-coatings on the inside surface of the fused-silica tube peripheral wall and endwall assemblies. The rf plasma discharge was reasonably well confined throughout the majority of test conditions. Some discharge oscillations were noted; these oscillations were also quite susceptible to rapid changes in the flow conditions, particularly the introduction of pure UF_6.

General Characteristics of Vortex-Stabilized (Uranium) RF Plasmas

The primary independent variables in the uranium rf plasma tests reported herein were the rf operating frequency, the chamber pressure, the argon mass flow rate, the UF_6 mass flow rate, the dc input power, and the test configuration/flow scheme. The primary dependent variables were the discharge diameter (size and shape), total rf discharge power, power radiated from the plasma discharge, power lost by convection and conduction, and the radial distribution of temperature within the discharge. Several secondary dependent variables would include those that are temperature dependent (i.e., electrical conductivity and thermal conductivity).

The coupling and interactions between the plasma discharge and the high frequency magnetic fields which produced the discharge are most complex. Theories related to rf plasma discharges make numerous simplifying assumptions related to the plasma boundary conditions and conductivity profiles; no one universal theory includes all of the important effects. This is particularly true for convection; the electrical and thermal characteristics of radial-inflow vortex-stabilized rf plasmas strongly depend on this mechanism of heat dissipation. The axial introduction of pure UF_6, as in the tests reported herein, is an additional complication to the flow pattern within the plasma. The shape, size, and stability of the discharge also depends on the effects of convection, in addition to the interaction between the plasma and the fields of the rf work coils.

In the experiments reported herein, argon buffer gas was used to drive the radial-inflow vortex and the UF_6 was injected separately, representative of the gaseous uranium fuel to be contained within the plasma region of the nuclear reactor test chamber. A radial-inflow pattern is generally characterized by an essentially laminar radial stagnation surface across which there is no net inward radial buffer gas flow. The radial position of this surface is normally defined to be the radial location beyond which the density of the uranium fuel is assumed to be essentially zero. This surface can be located as far from the centerline as 90 percent of the total vortex test chamber radius. In actual reactors it is anticipated that the uranium fuel and fission products which diffuse radially outward across the radial stagnation surface will be carried out of the test chamber along with the argon buffer and bypass flow before reaching the peripheral wall. Buffer gas may enter the central uranium fuel region of the vortex by a combination of diffusion across the stagnation surface and from the endwall boundary layer. The gas is removed from the test chamber primarily through the on-axis thru-flow exhaust duct in the endwall; some is also removed through the axial bypass exhaust duct. In an actual full scale reactor, a negative temperature gradient through the buffer gas region toward the peripheral wall insures that a positive density gradient exists through the buffer gas region; this aids in reducing the diffusion of uranium fuel radially outward through the buffer gas. Buoyancy effects must also be considered; however, these effects will be small provided the acceleration due to flow rotation is large relative to the gravitational acceleration. This was accomplished in the uranium rf plasma experiments reported herein by maintaining a moderately high tangential velocity within the plasma region.

To permit a systematic comparison to be made and important trends noted, attempts were made to maintain constant as many of the independent variables as possible during the injection of UF_6; however, changes in the rf power, operating frequency, and associated flow rates were sometimes required to prevent discharge extinguishment and/or plasma oscillations. In general, the introduction of pure UF_6 into the discharge significantly altered the impedance of the plasma which, in turn, determined the plasma size and electrical conductivity. Normally, this was manifested as a significant increase in the radiation emitted from the plasma; correspondingly, a moderate increase in the total power deposited into the plasma due to rf coupling efficiency changes and accompanying parameter changes was also observed. As discussed in APPENDIX D, a significant amount of this radiation increase occurred in the visible and near-UV wavelength bands. In contrast to the earlier exploratory tests conducted at relatively low power and pressure levels, the rf plasma discharge in the 1.2 MW facility tests was considerably more stable and less sensitive to changes in the operating frequency, argon mass flow rate, and the UF_6 mass flow rate. A typical ratio of plasma diameter to peripheral wall diameter was 0.55. Calculations of the plasma diameter decrease expected as a result of the change in operating frequency from the 13.56 MHz (8.5-cm-dia rf work coils) used in the 80 kW exploratory tests compared to the 5.4 MHz (9-cm-dia rf work coils) used in the 1.2 MW tests were in good agreement and confirms the scaling laws that can be applied.

Effect of UF_6 Mass Flow Rate on RF Plasma Absorption Characteristics

Figure 15 is an example of the absorption measurements obtained on-axis at the axial midplane location using part of the optical system shown in Fig. 13. (Refer to Fig. 8 for a sketch of the test chamber configuration.) The 100 percent absorption reference level was obtained by blocking the entrance slit of the monochromator. A 1.25 s damping constant was used in the data recording system and the chopper frequency was 650 Hz for this particular test. Four different UF_6 mass flow rates were employed ranging from 1.3×10^{-2} g/s to 8.2×10^{-2} g/s. Note that axial bypass was employed in these tests to aid in reducing uranium compound coating on the peripheral wall. At the maximum UF_6 mass flow rate used, approximately 98 percent of the incident intensity of the 591.54 nm laser line was absorbed in a single pass through the center of the UF_6/argon rf plasma. After operating for approximately $1\frac{1}{2}$ minutes at this condition, the UF_6 injector metering valve was rapidly shut-off. As noted, the laser line intensity signal did not immediately return to the initial value because of outgassing of residual hot UF_6 from the feed lines and injector assembly. Trace amounts of UF_6 were still observed entering the plasma after approximately 5 minutes. After waiting for the residual UF_6 to outgas, the signal approached the initial value, indicating a relatively small amount of wall coating had occurred. Post-test inspection of the inner fused-silica tube verified this condition.

The type of test shown in Fig. 15 demonstrated that controlled, steady-state injection of increasing amounts of UF_6 could be introduced into the rf plasma while simultaneously conducting rf plasma absorption measurements.

Examples of Radiation, Optical Transmission, and Radial Temperature Profile for a Uranium RF Plasma

TABLE I summarizes the range of operating conditions for the rf plasma tests with optical chordal scan measurements conducted in the 1.2 MW rf induction heater with pure UF_6 injection. Figure 8 is a sketch of the test chamber configuration and Fig. 13 shows the instrumentation used. To illustrate the visual effects of injecting pure UF_6 into the rf plasma, Fig. 16 contains photographs for both argon-only and argon plus UF_6 injection tests as viewed through the center viewport and the two side viewport windows of the aluminum test tank. In this case, no additional neutral density filtering was added for the argon plus UF_6 case. Note that a significant increase in the intensity occurred. Figure 17 is the corresponding example of the total discharge power radiated and distribution of the radiation in different wavelength bands obtained from the rf plasma with pure UF_6 injection. TABLE II summarizes the test conditions for the case presented. The measurements were taken with the radiometer system shown in Fig. 10. The introduction of the pure UF_6 directly into the discharge resulted in a significant increase in the total radiation emitted from the plasma (220 to 1300 nm range) as measured with the radiometer system. This increase may be attributed in part to the cumulative effects of an increase in line and continuum radiation (major effect), an increase in discharge power, an increase in the coupling efficiency, and a change in plasma size and shape. Additional radiometric measurements indicated a significant fraction of this radiation occurs in the visible region of the spectrum (line radiation in the 300 to 720 nm range).

Chordal scan measurements of the emission from and the absorption by the rf plasma with pure UF_6 injection using the system shown in Fig. 13 were made at a single wavelength ($\lambda = 591.54$ nm) and several axial locations: the test chamber axial midplane, adjacent to the right rf work coil, and adjacent to the tip of the UF_6 injector. The output data indicated the measurements in the two central locations were very similar. The measurements made adjacent to the injector tip were nonreproducible; this was attributed to the close proximity to the injector and UF_6 being injected into the rf plasma at this interface, as well as the end effects (nonrotational symmetry existed in this region). Because of the close similarity of the output data between the two central scan locations (axial separation of 1 cm), only the results from the axial midplane location will be included herein. Figure 18 illustrates the shape of the radial profiles for both the emission and absorption coefficients obtained from the test with the highest UF_6 mass flow rate ($\dot{m}_{UF_6} = 3.2 \times 10^{-2}$ g/s). This test case was designated V and the corresponding test conditions are illustrated in TABLE II. Five other separate test cases were conducted at sequentially lower flow rates of UF_6; the lowest corresponding to a UF_6 mass flow rate of 9×10^{-3} g/s (see TABLE I). Note the distinct peaks toward the center of the plasma discharge and rapid decay of both the volume emission and absorption coefficients at approximately $r/R = 0.25$ as a traverse is made toward the edge of the plasma. In this case the plasma diameter, as shown in the right-hand corner of Fig. 18, was 2.8 cm as determined from still photographs.

Figure 19 shows an example of the results of the radial variation in plasma optical transmission (I/I_0) and temperature as determined from the emission and absorption measurements for test case V. The dye laser line used in this and all subsequent tests to be described was the $\lambda = 591.54$ nm line. Recall for this case the emission and absorption chordal scan measurements were taken at the axial midplane of the discharge. The radial temperature profile as shown was determined using Kirchhoff's law (see Figs. 13 and 14 for additional details of the optical scanning system used and APPENDIX B for a summary of Calibration Methods). TABLE II contains additional details on the test conditions for this particular case, which correspond to the maximum mass flow rate of UF_6 used in the chordal scan measurements; the UF_6 mass flow rate was 3.2×10^{-2} g/s. The sketch in the lower portion of Fig. 19 is a simplified cross section of the test chamber configuration employed and indicates the location used for the chordal scan measurements. For comparison, an example of the temperature profile determined from an argon-only plasma test as shown by the dashed curve in the figure illustrates the off-axis type temperature peak obtained from an argon plasma (no UF_6 injection) operating under similar test conditions. The centerline temperature in the argon-only case was approximately 9300 K, with an off-axis peak temperature of about 11,000 K occurring at approximately midradius. The introduction of pure UF_6 into the rf plasma resulted in a suppressed temperature profile at the off-axis position, as shown in Fig. 19, between a radial distance of approximately 0.2-0.8 cm. An off-axis temperature peak was noted at approximately two-thirds of the radial distance out toward the edge of the plasma. The off-axis peaks can be attributed primarily to the mechanism of depositing rf power into an annular region.

Equilibrium Composition Calculations

To aid in the estimation of the total uranium atom number density distribution within the plasma discharge, pure UF_6 and/or UF_6/argon equilibrium composition calculations were made for the current range of test parameters utilizing a computer code based on the procedure described in Ref. 9. The calculations included the partial pressure range from 10^{-4} to 1 atm and temperatures from 300 to 10,000 K. The following species were included: UF_6, UF_5, UF_4, UF_3, F, F^-, F_2, U, U^+, U^{++}, U^{+++}, and E^-. Figures 20 through 22 show examples of the equilibrium composition of UF_6 as a function of temperature. In Figs. 20 and 21 the equilibrium composition of pure UF_6 is shown as a function of temperature for various partial pressures over the ranges of particular interest in these experiments. Note the similarity between the mole fractions of the same species over a relatively wide range of partial pressures as shown in Fig. 21. To illustrate the rapid increase and decrease of the mole fractions of various fluoride compounds of uranium, the abscissa in Fig. 20 was extended to lower temperatures. Very steep slopes are noted particularly in the 2000 K range for a UF_6 partial pressure of 10^{-3} atm. Note that at approximately 7000 K, the concentration of singly-ionized uranium (UII) increases; measurements of the rf plasma characteristics indicate that the rf plasma with argon vortex buffer gas injection has an average temperature in excess of 7000 K for the type of operating conditions reported herein (refer to Fig. 19). For all practical purposes, at pressures of approximately 1 atm, complete thermal decomposition of UF_6 has occurred at temperatures of about 5000 K, as illustrated in Fig. 22.

Figures 23 through 26 show the calculated variations of uranium atom number density with injection partial pressures of UF_6 in a UF_6/argon mixture. Included are the cases for neutral uranium, singly-ionized uranium, doubly-ionized uranium, and total uranium atom number density; that is, all species contributing to the partial pressure at a total pressure of 2 atm; these are representative of the pressure range used in the majority of tests. In these plots the injected partial pressure of UF_6 was the variable parameter. In all the calculations local thermodynamic equilibrium was assumed and lowering of the ionization potential was not included. Inclusion of the ionization potential lowering effect would result in formation of the ion species at a somewhat lower temperature, but the overall effect is not immediately obvious unless the influence of the argon ions interacting with the uranium species is also included. For reference, Fig. 27 illustrates the particle density of an argon plasma showing the argon particle number density as a function of temperature for the various species at a total pressure of 2 atm.

Determination of 591.54 nm Absorption Line Width

To complement the chordal scan absorption and emission measurements and verify the validity of the results, particularly since this is the first time measurements of this type using a dye laser system with uranium rf plasmas has been reported, separate Uranium I ($\lambda = 591.54$ nm) absorption line width measurements were made.

It was anticipated that operating the rf plasma with pure UF_6 injection at the relatively high power and pressure levels may have resulted in significant pressure broadening to the width of the uranium 591.54 nm emission and absorption line. To better estimate the absorption line width, several measurements were made at different pressures and approximately the same test conditions. Calculations of the doppler width for the uranium 591.54 nm line (no pressure broadening) at 1000 K indicated a line width of approximately 0.74 GHz. The doppler effect on the line width varies as the square root of the temperature, therefore at a temperature of approximately 10,000 K the doppler line width would be approximately 2.34 GHz. This compared favorably with the approximately 2.5 GHz measured in the exploratory rf UF_6 plasma absorption measurements reported in APPENDIX D. Figure 28 illustrates the results of the 591.54 nm absorption line width measurements. Again using the $\lambda =$ 591.54 nm laser beam ($\approx 10^{-4}$ nm line width) for determining the absorption line widths as a function of chamber pressure, the absorption line width at 1/2 maximum intensity is shown in Fig. 28 as a function of the chamber pressure. The equation shown at the top of Fig. 28 was used for the calculations. The circle data points shown on the ordinate axis were the calculated line widths with no pressure broadening. The corresponding temperatures are shown adjacent to the data points. The two triangular data points shown, corresponding to the measurements at 1 and 2 atm, agree favorably with the previous measurements. These results were used as inputs for the additional calculations, described in the following section, required to determine the neutral uranium number density based on the emission and absorption calculations.

Determination of Total Uranium Atom Number Density Radial Profile Within Uranium RF Plasma

Figure 29 shows the effect of temperature on the partition functions of Uranium I and Uranium II (Ref. 10); that is, neutral and singly-ionized species. The governing equation is shown at the top of the figure. Z_i is the dimensionless partition function, $g_{i,n}$ is the statistical weight of the particular energy level, $E_{i,n}$ is the energy level, k is the Boltzmann constant, and T is the temperature. The partition functions as a function of temperature show similar increasing trends for the UI and UII over the temperature range from 2000 to approximately 10,000 K.

The variation of the number density of neutral uranium (UI) is shown in Fig. 30 as a function of radial distance from the test chamber centerline; the results are shown for test case V (see TABLE II for summary of test conditions and Fig. 19 for corresponding radial temperature profile). The circle symbols are from the absorption calculations assuming doppler width with no pressure broadening. The triangular symbols are results from the corresponding emission calculations. Having the temperature profile for test case V as a function of radius, as shown in Fig. 19, and the variation of number density of the neutral uranium also as a function of radial distance from the test chamber centerline (Fig. 30), the injected partial pressure of UF_6, dependent on both the temperature and the number density of the Uranium I atom, was determined. Having this information, one can go back to Fig. 23 and determine the injection partial pressure of UF_6 corresponding to the temperature and calculated number density of neutral uranium atoms. Knowing this injection partial pressure of UF_6, one can then make use of the data of Figs. 24 and 25 to calculate the corresponding number density of singly-ionized and doubly-ionized uranium atoms.

To check the validity of these calculations, Fig. 31 shows the mole fraction of UI, UII, and UIII over the temperature range of interest (6000 to 10,000 K) and a four decade partial pressure range (10^{-4} to 10^{-1} atm). Note that this wide range in partial pressure does not significantly alter the mole fraction of the individual constituents. Within this range, the mole fraction contribution of UIII was negligible, as shown in the lower right-hand corner of Fig. 31. This information was important in calculating the results shown in Fig. 32. This figure shows the radial variation of total uranium atom number density; that is, the contribution from the neutral uranium atoms, the singly-ionized, and doubly-ionized species for the UF_6 rf plasma test case V. The total uranium atom number density in atoms/cm^3 is plotted versus the radial distance from the plasma centerline in cm. Refer to TABLE II for additional test conditions. The numbers in parentheses are the corresponding estimated values of the total uranium species partial pressure in atm. For this particular case, the total uranium atom number density reached a maximum of approximately 10^{16} atoms/cm^3 at the centerline of the plasma. At a radial location approximately 1 cm off the centerline axis, another peak occurred corresponding to an atom number density one order of magnitude less than the centerline; that is, 10^{15} atoms/cm^3. This level decayed to approximately 2 x 10^{14} atoms/cm^3 at the edge of the plasma.

An estimate was also made of the total confined uranium mass based on these measurements of the neutral uranium species. The calculated value was 0.03 mg of uranium. Figure 33 is an example showing the radial variation of confined total uranium atoms per unit plasma length at the axial midplane location for the UF_6 rf plasma test case V. Refer to Figs. 19 and 32 for the corresponding radial profiles of transmission, temperature, and total uranium atom number density. Shown above the curve are numbers corresponding to the percent of the total confined uranium atoms. These calculations indicated that a large fraction of the total confined uranium atoms existed at the outer portion of the plasma discharge.

These results can be compared to the uranium total number density obtained from the x-ray absorption measurements as discussed in APPENDIX A. Figure 80 of APPENDIX A compares the uranium number density, in atoms/cm^3, versus the weight flow rate of UF_6 in g/s for several test cases. To compare optical emission and absorption chordal scan measurement results with the x-ray absorption measurement results at similar test conditions, the test case for a 52.5 kW rf plasma at a chamber pressure of 1.7 atm, a UF_6 mass flow rate of 0.028 g/s, an argon flow rate of 2.7 g/s, and a discharge diameter of approximately 3 cm was used. The two curves shown in Fig. 80 correspond to the two different diagonal path lengths assumed in the x-ray measurements. The flow conditions corresponding to test case V used in the optical chordal scan measurements of the emission and absorption are the corresponding test conditions that come closest to matching this case. The discharge power was 58 kW, chamber pressure equal to 1.95 atm, flow rate of UF_6 equal to 0.032 g/s, and discharge diameter equal to 2.8 cm (at the axial midplane). For these conditions, but with the UF_6 mass flow rate corresponding to 0.032 g/s (Fig. 80), the bounds on the x-ray measurements which determine the total confined uranium mass are from 2.8×10^{16} atoms/cm^3 corresponding to the 23 cm path up to 6.4×10^{16} atoms/cm^3 for the 9.5 cm path length case. The results shown in Fig. 33 for the radial variation of confined total uranium atoms at the axial midplane for the UF_6 rf test case V indicate a total of 7.3×10^{15} atoms/cm^3/unit length. The corresponding total volume based on the equivalent of a cylindrical plasma with the total mass distributed uniformly would yield a total uranium number density of 4.4×10^{16} atoms/cm^3. This total includes the species consisting of neutral ionized uranium, singly-ionized and doubly-ionized uranium atoms; excluded were other uranium-fluoride compounds. This agreement is good and most encouraging from the standpoint of one measurement technique made completely independently agreeing well with a second independent measurement scheme.

Uranium RF Plasma Tests Incorporating Modifications to Test Chamber/Flow Scheme

TABLE III summarizes part of the rf plasma tests conducted in the 1.2 MW rf induction heater with pure UF_6 injection into the rf plasma and incorporating different modifications to both the test chamber and flow control scheme. The objective was to determine what modifications to the test chamber/flow control schemes would further improve the confinement characteristics of the uranium plasma while at the same time aid in minimizing the wall coating by uranium compounds. To permit a more direct comparison, all tests were conducted over a time period of five minutes. A summary of eleven (11) representative tests are shown by numbers 1 through 11 in TABLE III. The range of test conditions are also shown and include: the mass flow rate of the argon, axial bypass exhaust, and UF_6; the electrical parameters related to the rf plasma, the total emitted radiation, the chamber pressure, the discharge diameter at the axial midplane, the corresponding I/I_0 absorption level measured at the axial midplane on-axis location using the dye laser system, and the weight of residue deposited on the inside diameter of the fused-silica tube based on post-test examination. A Mettler balance calibrated to 1 μg was used for the weight determination in these and all subsequent tests reported herein. The basic configuration used in all tests is shown in Fig. 8. Figure 34 is a photograph showing typical fused-silica tubes after use in this test series. The degree of coating extended from a relatively heavy to a fairly light coating as can be seen in the photograph. Figure 35 contains close-up photographs showing additional wall coating details of four of the fused-silica tubes during post-test inspection (refer to TABLE III for corresponding test conditions and weight of residue deposited on the fused-silica tubes). The majority of the coating occurred in the central region of the fused-silica tubes. Some residue was also observed at both end regions adjacent to the O-ring seal location. A representative example of the IR spectrophotometric absorption measurements taken of some of the residue collected from the inside surface of the fused-silica tube after the plasma tests with pure UF_6 injection is shown in Fig. 36. Refer to TABLE III for the corresponding test conditions. In all cases a thin wafer KBr matrix was used with the Perkin-Elmer IR spectrophotometer to obtain these IR traces as a function of wavelength. In addition to the weight of the residue wall coating measured and the results of the IR absorbance measurements, visual observations of the uranium plasma behavior and stability were included in analyzing the test results. In general, the overall results indicated that using argon vortex injectors that had small inside diameters (0.17-cm-ID) which provided a relatively high injection velocity and a UF_6 injector assembly with a 0.3-cm-ID and protruding approximately 1 cm from the face of the endwall permitted a relatively high confinement of the UF_6 with minimum wall coating.

In the majority of the tests the IR spectrophotometric measurements indicated a combination of uranyl fluoride (UO_2F_2) and uranium oxide (αUO_3) present on the inside surface of the fused-silica tube. In some tests, traces of SiO_2 and silicone grease were noted in the IR transmission scans. As shown in Fig. 36(c) operating the peripheral wall at an elevated temperature by reducing the flow of annular cooling water by an order of magnitude resulted in a noticeable increase in the SiO_2 content of the residue material collected. A heavier wall coating was also observed. It should be pointed out that caution should be applied when interpreting the results and trends obtained from only a dozen or so tests. Many more tests would be required to give a true statistical sampling representation. In another selected test, an extra heavy coating of silicone grease was applied to the O-rings at each end of the fused-silica tube prior to assembly for the hot flow test with pure UF_6 injection. The post-test IR transmission profile is shown at the bottom of Fig. 36.

To aid in the evaluation of all various wall coatings possible, a cataloging of possible compounds to serve as laboratory standards for these and future tests was included; the results are discussed in APPENDIX C. As an example, the peak corresponding to the wavelength of 7.2 μm was originally labeled as an unidentified compound; after completion of the laboratory standards, this was later identified to be αUO_3 and was also confirmed by other analyses.

Uranium RF Plasma Tests With Sustained Operating Times

TABLE IV is a summary of the long run time uranium rf plasma tests. Attempts were made to keep all operating conditions approximately the same for all tests. TABLE IV summarizes the key test parameters including the test conducted for the maximum sustained operating time of 41.5 minutes. This test was terminated due to cracking of the Mycalex (super 500) radiation/electric insulation shields located on the vacuum capacitors in the upper and lower resonator sections of the 1.2 MW rf induction heater test tank (see Fig. 3). The cause was attributed to excessive sustained radiation loading leading to component fracture. Redesign and the adaptation of cooling to this component should permit considerably longer test times to be obtained, if required. Figure 37 is a plot of the weight of residue material deposited on the inside diameter of the fused-silica tubes as determined from the post-test weighing analysis as a function of test time in minutes. This test series indicated that the addition of silicone grease to the O-rings and use of as-received UF_6 resulted in a significant contribution to the residue coating on the fused-silica tubes (refer to TABLE IX of APPENDIX C for a property assay of the as-received UF_6). Part way into the test program it became obvious that the use of silicon O-rings, silicone grease, unfiltered argon from the laboratory bottle farm, and as-received UF_6 resulted in a fairly linear increase in the residue deposited on the fused-silica tubes as a function of test time (see circle symbol data points in Fig. 37). To aid in reducing this residue, the O-rings were coated with Kel-F oil. This particular lubricant, arrived at after trying other materials such as hydrocarbons, fluorosilicone, and halocarbons, provided the seal necessary between the fused-silica tube and the endwall while eliminating the silica gel present in silicone grease and other compounds for thickening purposes which apparently reacted on the surface and caused additional deposits. The UF_6 was also filtered through a NaF trap to remove possible hydrogen fluoride contamination. The tests conducted with these changes are shown by the triangular symbols in Fig. 37. A reduction in the residue wall coating by approximately a factor of 2 was noted. In the lower left-hand corner of Fig. 37, the range of silicone grease residue initially deposited on the fused-silica tubes is shown on the ordinate axis. This quantity ranged from approximately 5 to 12 mg. This quantity is included as the error bands on the measurements for the different test times since it was impossible to deposit the same weight of silicone grease on all the O-rings prior to a given test series. A change to viton O-rings was also included as indicated by the square symbol in Fig. 37. In this case, since the viton O-ring is somewhat harder and less deformable than the silicone O-ring and the dimensions of the concentric fused-silica tubes are not exact, an improper seal was obtained as observed during the vacuum pump down prior to ignition. Subsequently, it was determined that silicone O-rings were the best choice as used with the Kel-F oil and filtered UF_6. In addition, because of possible moisture present in the argon (up to 500 ppm) a zeolite trap was used to filter the argon prior to introducing it into the test chamber through the vortex injectors. The longest run time test employed all these modifications and is shown by the diamond symbol in Fig. 37. The resultant 30.4 mg of residue corresponded to the 41.5 minutes of continuous operation with a UF_6 flow rate of 2.2 x 10^{-2} g/s. It is anticipated that further improvements to the flow scheme could be made to reduce this minimum wall coating still further. Also included would be the necessary radiation shielding and cooling required over the vacuum capacitors and resonators; this modification would probably permit operation for several hours without shutdown. The additional limiting factor would be the quantity of UF_6 in the boiler assembly.

Figure 38 contains electron photomicrographs and the corresponding x-ray maps at a magnification of 3000X obtained from a sample of residue from the inside surface of the fused-silica tube after the rf plasma test with pure UF_6 injection for a 30 minute duration. The electron microprobe instrumentation described in the Description of Principal Equipment section was used. This particular test employed the viton O-rings, Kel-F oil, and filtered UF_6 (NaF trap). Note in the photograph labeled (b) in Fig. 38 the x-ray map showing silicon as a white area is very obvious against the background. For this particular test, 35.7 mg of residue coating was deposited on the inside surface of the fused-silica tube; this occurred primarily in the central region. Using the IR spectrophotometric analysis, this compound was identified to consist primarily of uranyl fluoride (UO_2F_2), as shown in Fig. 39. In this test series, attempts were made to analyze approximately the same mass of material; the results of the IR transmission measurements shown in Fig. 39 for the UO_2^{2+} peaks at 10.6 μm indicate an increasing absorbance with test time. To illustrate the type of wall coating occurring after sustained long run time tests, Figs. 40 and 41 are photographs of the fused-silica tubes taken during post-test inspection. The corresponding test times are indicated above each case. In all tests, the mass flow rate of UF_6 was maintained constant at 2.2 x 10^{-2} g/s.

Uranium RF Plasma Tests With Maximum Injection of UF_6

TABLE V summarizes the operating conditions for the rf plasma tests conducted in the 1.2 MW rf induction heater with the maximum pure UF_6 injection flow rate obtained in tests to date. The objective of this test was to determine, under the constraints of the existing test configuration and available flow schemes, the maximum steady-state injection flow rate of UF_6 possible while still maintaining the plasma in a confined steady-state mode of operation. The results indicated that a UF_6 injection flow rate approximately one order of magnitude higher than previously used in other tests was possible (see Fig. 37). This is shown in TABLE V to correspond to 2.1 x 10^{-1} g/s. For this case the total discharge power was 67 kW at a chamber pressure of 2 atm. Some difficulty was encountered in exactly determining discharge diameter and radiated power since part of the discharge was displaced away from the central region of the test chamber (toward left endwall assembly). Post-test examination of this test resulted in a residue deposition on the inside diameter of the fused-silica tube of 134.7 mg after an operating test time of 1.2 minutes. Figure 42 shows post-test photographs of the fused-silica tube and the silicone O-rings used in this particular test. Note that the majority of the coating occurred toward the argon vortex injector end of the fused-silica tube. This would indicate that in future tests devoted to injecting increased amounts of UF_6 into the plasma discharge, additional refinements may be required in both the injector scheme for argon as well as the UF_6 injector design. The effect of the relatively high radiation levels accompanying this test are illustrated in the bottom portion of Fig. 42. Silicone O-rings were used with Kel-F oil; it was apparent that erosion occurred on that portion of the O-rings which faced the plasma region, i.e., exposed to the intense visible and near UV radiation. To permit future tests to be conducted at comparable uranium flow rates and long time periods, a different design endwall assembly which would incorporate shielding of the required O-ring surfaces from the intense radiation from the plasma will be necessary. Figure 43 shows photographs of the electron micrographs at two different magnifications taken of the sample residue from the inside surface of the fused-silica tube after the rf plasma test with maximum UF_6 injection.

Figure 44 shows the corresponding photographs of the x-ray maps of the same sample residue. Included are the x-ray maps showing uranium, fluorine, silicon, and oxygen. Again, it can be noted as in prior tests of this type, the dominance of both uranium and silicon. This was also concurred in by the IR spectrophotometric measurements.

Summary of Chemical Analyses of Deposited Residues

To permit a determination of the magnitude of the surface coating/etching/erosion that may have taken place on the surface of the inside diameter of the fused-silica tubes, a Taylor-Hobson (Talysurf 4) profilometer, described in the Principal Equipment section, was employed. Figures 45 and 46 show an example of the results obtained from these measurements. After completing the majority of the rf plasma tests with UF_6 injection discussed in the previous section with the accompanying degree of wall coating, the question arises as to the actual surface characteristics of the deposited residue; that is, is there indeed a combination of surface coating with accompanying etching and erosion that may have taken place on the fused-silica tube? The Taylor-Hobson profilometer is the instrument that was used to aid in providing the answer to this question. This particular instrument is a very sensitive surface measuring instrument which accurately traces the profile of surface irregularities with reference to an optical flat. Figure 45 illustrates the typical surface characteristics on the inner portion of the fused-silica tube after exposure to the test conditions of case 11 shown in TABLE III. In this particular test, a UF_6 mass flow rate of 0.05 g/s was used for a test time of 5 minutes. Figure 45(a) is a photograph of a cross section of the tube and the associated coating. The nominal maximum thickness recorded using the profilometer in a series of these measurements was approximately 1 μm. The profilometer trace shown in Fig. 45(b) is from the local area with maximum residue on the inner surface of the fused-silica tube. For this measurement a diamond stylus was traversed axially across the selected section of the surface of the tube by the motorized drive unit and the up and down movement of the stylus relative to the optical flat was electronically recorded on the strip-chart trace shown in Fig. 45(b). The maximum amplification of this particular instrument is 10^5. It was calibrated relative to an NBS optical flat standard prior to the measurements taken on the fused-silica tube. As can be noted from Fig. 45 and also Fig. 46, which is a trace obtained using an expanded scale, the measurements indicate that a definite surface etching with possible combined etching and erosion had occurred in addition to the local deposition of small quantities of material onto the tube. This analysis technique, therefore, can complement the other techniques used in identifying the nature of the deposited residues.

The secondary ion mass spectrometer technique is another example of a powerful analysis apparatus which was employed in this particular test program. A 3M ion-scattering spectrometer, details of which are discussed in the Description of Principal Equipment section, was used. In this technique a primary beam of ions is directed at the surface being studied at fixed energies (less than 3 kv). Some of these ions are scattered into an electrostatic energy analyzer mounted at a fixed angle relative to the incident ion beam. Experimentally one finds that some of the atoms and compounds sputtered from the surface by the primary beam are ionized (secondary ions) and these ions are then analyzed in the mass spectrometer. The sputtered yield and the degree of ionization both depend on the ion being measured and the properties of the substrate. As a consequence, one needs reference standards to do quantitative work with the secondary ion mass spectrometer (SIMS). Figure 47 is an example of the surface chemical analysis of the uranium compound residue obtained using the SIMS system. Figure 47(a) shows a commercially prepared pure uranyl fluoride (UO_2F_2) reference standard. The atomic mass units (AMU) corresponding to the various elements and compounds are shown on the abscissa (for example, 238-U^+, 254-UO^+, 257-UF, 270-UO_2^+, etc.). Figure 47(b) shows an example of the SIMS output obtained using a residue sample from a fused-silica tube after an rf plasma test with pure UF_6 injection. This particular sample was prepared from the water soluble residue which was treated with nitric acid (HNO_3) to drive off the HF and then reheated to form the oxide. In both Figs. 47(a) and (b) the penetration depth was several hundred angstroms. The results obtained using the SIMS instrumentation agreed with those obtained using the other analysis techniques and provides a complementary system for use in future tests.

Figures 48 and 49 show examples of several pertinent IR transmission scans obtained using the IR Spectrophotometer System. Included are the results obtained from several small samples of residue removed from different sections of the test chamber after selected rf plasma tests with pure UF_6 injection; Figs. 48(a), (b), (c) show the standards for the uranyl fluoride, the silicone grease, and the Kel-F oil as used on the O-ring seals. Figure 49 shows examples of the IR spectrophotometric absorption measurements taken of samples from the surface of the UF_6 injector, endwall, thru-flow exhaust duct, and axial bypass exhaust duct. In all cases, the predominance of the UO_2^{++} (uranyl cation) was observed. The residue removed from the surface of the endwall contained more of an indication of silicone grease than that removed from other sections. This was anticipated due to the closeness of the O-rings to the endwall and the secondary flow effects that exist in this region.

Chemically-pure standard samples of uranium compounds and other reaction compounds possible in the hot flow rf plasma tests with pure UF_6 injection were also analyzed and cataloged using a thin wafer KBr matrix preparation technique. Refer to APPENDIX C for additional discussion. TABLE VI lists the various samples now available within our Laboratory with an indication if the compound displays a distinguishable spectrum. In several of the earlier rf plasma tests with pure UF_6 injection, the whitish residue found on the fused-silica tube was relatively water soluble. This has since been identified as primarily uranyl fluoride (UO_2F_2) and shows up in the IR spectrum as UO_2^{++} (uranyl cation). In some of the tests, an indication of silicone grease was observed to be present on the fused-silica tube and/or endwall surface (see Fig. 49(b)). As discussed previously, changing the O-ring sealant material from silicone grease to Kel-F oil has resulted in reduced contamination due to the silicone products. Because uranyl fluoride (UO_2F_2) was the principal constituent found in the residue on the fused-silica tubes in the majority of the rf plasma tests with pure UF_6 injection, figures 50 and 51 show electron photomicrographs and photographs of the x-ray maps taken of the standard reference material uranyl fluoride (UO_2F_2) as commercially received (separate batches were also prepared at UTRC). Different magnifications were employed ranging from 2400X to 6000X, as shown, and the obvious appearance of the relatively strong concentration of uranium indicated by the white area in Fig. 51 is evident.

To permit positive identification of elemental uranium in the residue deposits found in the exhaust duct (axial bypass portion) by an alternate analysis (compared to the scanning electron microprobe), uranium absorption spectra of the water soluble portion of the residue from the axial bypass exhaust duct is shown in Fig. 52(a). For comparison, Fig. 52(b) shows the standard absorption spectrum of uranium in aqueous solution as reported in Ref. 11. These standard reference data have also been duplicated in recent tests conducted at UTRC. Both the wavelength position and molar extinction coefficient amplitude are important in accurately defining the constituent.

After completion of the above analysis, another sample of the residue was added to water, stirred, and filtered through a 5 μm teflon filter. After being thoroughly mixed and left setting for several hours, no > 5 μm size particles were collected. The original weight of the deposit was 61.8 mg . 61.6 mg was the measured weight of the soluble portion. The weight of U (soluble portion) was 44.2 mg; the weight of F (soluble portion) was 11.4 mg. The corresponding mole ratio is $UF_{3.2}$. From the above data and assuming that U and F are present as UO_2F_2 and UF_4, then the sample consists of 22.1 mg of UO_2F_2 and 36.8 mg of UF_4; the total combined weight would be 58.9 mg. In this calculation, 2.9 mg of H_2O was assumed present to give the correct mass balance. Reference 12 gives the solubility of UF_4 as between 1×10^{-4} ($\approx$31 mg) and 3×10^{-4} ($\approx$93 mg) mole/ℓ at 25 C.

To illustrate the overall correlation of the various diagnostic techniques used to analyze the sample residue which appeared on the various components in the test chamber, Figs. 53 through 67 are examples highlighting some of the results. The overall results obtained in this final series of tests in the 1.2 MW rf induction heater facility concurred with the results from the early exploratory tests discussed in APPENDIX D. The exception to this is shown in Fig. 53, wherein additional x-ray diffraction patterns obtained from the post-test analysis of residue on the inside of the fused-silica tube after rf plasma tests with pure UF_6 injection indicated crystalline γUO_3 to be present. γUO_3 is a monoclinic form of the oxide of uranium not noted to be present in the earlier tests. As shown in Fig. 53, this was observed to be present in both low and high UF_6 flow rate tests. It appears that γUO_3 becomes more highly crystalline at the higher UF_6 flow rate conditions. Also shown in Fig. 53(c) is the x-ray diffraction pattern of a sample taken from the endwall indicating a highly amorphous degenerate pattern but again with the beginnings of γUO_3 appearing. All other results agreed well with the previous analysis reported in APPENDIX D. Figure 54 shows an example of the electron diffraction analysis conducted on dispersed powder from the UO_2F_2 standard reference. This can be compared with the electron photomicrographs shown in Figs. 50 and 51. Figures 55 through 57 are examples of the analysis conducted using the electron microprobe and electron diffraction techniques applied to the sample residue removed from the central portion of the endwall after an rf plasma test with pure UF_6 injection. A back-scattered electron micrograph is shown in Fig. 55(c), which illustrates the typical topographical variations present. This sample case was near the central portion of the right endwall adjacent to the UF_6 injector. Figure 56(a) through (d) shows the accompanying x-ray maps corresponding to uranium, fluorine, copper, and oxygen, respectively. At a magnification of 300X, the predominance of uranium, as shown by the white area, is again evident. In Fig. 57, the corresponding electron diffraction analysis results are shown obtained from the same endwall sample. Figure 57(a) shows two highly magnified photographs of the residue (to illustrate the crystallinity) and Fig. 57(b) are the corresponding electron diffraction patterns obtained from the same sample. In this case the amorphous structure of the material can be noted in the electron micrographs; the presence of UF_4 and UO_2 is apparent. Due to the close similarity in the line spacings for both UO_2 and U_4O_9, as taken from the American Society of Testing Materials x-ray card file, exact identification between the two could not be made.

Figures 58 through 60 are some examples of electron photomicrographs, x-ray maps, and the corresponding electron diffraction patterns obtained from a sample residue removed from the UF_6 injector after an rf plasma test with pure UF_6 injection. The sample residue was taken from the area near the tip of the UF_6 injector. Figure 58 illustrates (at several different magnifications) the topographical variations present. Comparing Fig. 58 with Fig. 55, the obviously different topographical variations become apparent. Figure 59 shows the corresponding photographs of the x-ray maps of this sample from the UF_6 injector. The presence of uranium, as shown in Fig. 59(a), is again apparent and predominates over the fluorine and oxygen.

However, in this case, the x-ray showing copper (Fig. 59(c)) indicates an apparent presence of a significant amount of copper. Care was taken in preparing these samples not to scrape off any metallic copper from the outside surface of the UF_6 injector. Copper tubing is the prime constituent of the UF_6 injector. Figure 60 shows examples of the electron diffraction patterns obtained from the same sample residue and photographs of the corresponding samples at moderate and high magnification. An amorphous material was present in addition to UF_4, UO_2, and αUO_3, and single crystals of an unknown compound. UO_2 and αUO_3 are difficult to identify due to the overlap in the d-spacings of these compounds and those shown in the lower left portion of Fig. 60 (i.e., U_4O_9 and U_3O_8).

To give an indication of the type of residue obtained from the on-axis thru-flow exhaust duct after a hot flow test with UF_6 injection, Figs. 61 and 62 are examples of the electron photomicrographs obtained and the corresponding x-ray maps. Again, note the different topographical variations occurring when compared with the x-ray maps shown in Figs. 55 and 58 corresponding to residue material obtained from the endwall assembly and UF_6 injector, respectively. The results indicate a pattern similar to that obtained from the endwall residue results, as shown in Fig. 56, where the predominance of uranium set in a trace background of fluorine, oxygen, and copper is apparent. It was expected that the residue samples removed from the axial bypass exhaust duct to be somewhat different than those removed from the on-axis exhaust duct; the reason being attributed to the distinct different in temperatures. The temperature of the thru-flow exhaust duct is considerably higher than that in the axial bypass (approximately a factor of 5-10X). To determine the possible effect of the axial downstream location in the duct itself on the residue characteristics, Figs. 63 through 66 are examples of the electron photomicrographs and the corresponding x-ray maps of residue samples removed from the axial bypass exhaust duct for positions both near and far from the endwall assembly. The difference was approximately 20 cm. A comparison can also be made between the results of the residue samples obtained from the on-axis thru-flow exhaust duct and those obtained from the axial bypass exhaust duct at two different axial locations. The hotter exhaust temperature in the on-axis thru-flow exhaust duct combined with the heat exchangers result in a rather rapid quench effect. This is apparent in the more amorphous structure observed in Fig. 61 corresponding to the sample residue from the on-axis thru-flow exhaust duct. There also is a difference in the morphology structure relative to axial position in the exhaust ducts from where the sample was taken. This can be noted when comparing Figs. 63 and 65.

Figure 67 shows examples of the x-ray diffraction patterns obtained from the post-test analysis of the sample residue obtained from the on-axis thru-flow exhaust duct and the axial bypass exhaust duct using x-ray diffraction analysis techniques. In both cases, the amorphous pattern observed was comprised principally of U_3O_8. For comparison, a UO_2F_2 standard reference sample is indicated at the bottom of Fig. 67.

Upon comparing the results of all the various analysis techniques employed to date, it becomes apparent that a direct one-to-one comparison is not easily accomplished. Part of this is attributed to the statistical nature of sampling and comparing the various samples with the different analysis schemes. Reproducibility of the test conditions from test-to-test is reasonably good; however, the portion of the test components where samples are removed may vary slightly from test-to-test.

In general, the following trends were observed. UO_2F_2, UO_2, SiO_2, and a trace of γUO_3 were identified as residue constituents on the fused-silica tube peripheral wall. UF_4, UO_2, and UO_2F_2 were identified as residue constituents on the endwall surfaces. The same constituents were identified as being present on the UF_6 injector; in addition, αUO_3 was also detected. The electron microprobe x-ray maps also showed the distinct presence of Cu in quantities comparable to the U. The exhaust ducts contained traces of UO_2F_2, U_3O_8, and UF_4. The electron photomicrographs of the various samples of residue removed from the different components each possessed a different crystalline structure. The analysis techniques developed and applied during this portion of the research program will be applicable to future experiments which include development of techniques for reconstituting the gaseous compounds in the plasma exhaust mixture, minimizing the wall coating, and conditioning the exhaust gas such that it is in a form suitable for reinjection into the plasma (recycled - closed-loop operation).

REFERENCES

1. Latham, T. S., F. R. Biancardi, and R. J. Rodgers: Applications of Plasma Core Reactors to Terrestrial Energy Systems. AIAA Paper 74-1074, AIAA/SAE 10th Propulsion Conference, San Diego, CA., October 21-23, 1974.

2. Rodgers, R. J., T. S. Latham, and J. F. Jaminet: Preliminary Design and Analyses of Planned Flowing Uranium Hexafluoride Cavity Reactor Experiments. United Technologies Research Center Report R76-912137-1, March 1976.

3. Helmick, H. H., et al.: Preliminary Study of Plasma Nuclear Reactor Feasibility. Los Alamos Scientific Laboratory Report LA-5679, August 1974.

4. Bernard, W., et al.: Research Program on Plasma Core Assembly. Los Alamos Scientific Laboratory Report LA-5971-MS, May 1975.

5. Mensing, A. E. and J. S. Kendall: Experimental Investigation of Containment of a Heavy Gas in a Jet-Driven Light-Gas Vortex. United Aircraft Research Laboratories Report D-910091-4, March 1965. Also issued as NASA CR-68926.

6. Roman, W. C. and J. F. Jaminet: Development of RF Plasma Simulations of In-Reactor Tests of Small Models of the Nuclear Light Bulb Fuel Region. United Aircraft Research Laboratories Report L-910900-12, September 1972.

7. Roman, W. C.: Plasma Core Reactor Simulations Using RF Uranium Seeded Argon Discharges. AIAA Paper 75-861, AIAA 8th Fluid and Plasma Dynamics Conference, Hartford, CT., June 16-18, 1975.

8. Anon.: International Critical Tables, Vol. V. McGraw-Hill Book Co., Inc., New York, New York, 1930.

9. Gordon, S. and B. J. McBride: Computer Program for Calculation of Complex Chemical Equilibrium Compositions, Rocket Performance, Incident and Reflected Shocks and Chapman-Jouquet Detonations. NASA SP-273, 1971.

10. Krascella, N. L.: Theoretical Investigation of the Composition and Line Emission Characteristics of Argon-Tungsten and Argon-Uranium Plasmas. United Aircraft Research Laboratories Report G-910092-10, September 1968.

11. Rodden, C. J.: Analysis of Essential Nuclear Reactor Materials. U. S. Atomic Energy Commission, 64-60035, 1964.

REFERENCES (Concluded)

12. Katz, J. J. and E. Rabinowitch: Chemistry of Uranium. USAEC, Technical Information Service, Oak Ridge, Tenn., 1958.

13. Drellishak, K. S., et al.: Partition Functions and Thermodynamic Properties of Argon Plasma. Physics of Fluids, Vol. 6, No. 9, September 1963.

14. Olsen, N.: Numerical Methods for Reducing Line and Surface Probe Data. Society for Industrial and Applied Mathematics Review, Vol. 2, 1960, pp 200-206.

15. Freeman, M. P. and S. Katz: Determination of a Radiance-Coefficient Profile From the Observed Asymmetric Radiance Distribution of an Optically Thin Radiating Medium. J. Opt. Soc. Amer., Vol. 53, 1963, pp 1172-1179.

16. Freeman, M. P. and S. Katz: Determination of the Radial Distribution of Brightness in a Cylindrical Luminous Medium with Self-Absorption. J. Opt. Soc. Amer., Vol. 50, 1960, pp 826-830.

17. Elder, P. W., et al.: Determination of the Radial Profile of Absorption and Emission Coefficients and Temperature in Cylindrically Symmetric Sources with Self-Absorption. Appl. Opt., Vol. 4, No. 5, May 1965, pp 589-592.

18. Braun, W. G.: Technique for Measuring the Absorption Coefficient of a Plasma. Rev. of Sci. Instr., Vol. 36, No. 6, June 1965.

19. Langlois, G.: Corrosion de Materidux Metalliques par l'Hexafluorure d'Uranium a Haute Temperature. Centre d'Etudes Nuclaires de Saclay Rapport C.E.A. 2385, 1963.

LIST OF SYMBOLS

A	Absorption coefficient, arbitrary units
AMU	Atomic mass unit, dimensionless
c	Speed of light, 3x10^8 m/s
E	Emission coefficient, arbitrary units or x-ray energy, Kev
$E_{i,n}$	Energy of n^{th} level in ionization species i, cm^{-1}
f	Rf operating frequency, MHz
Δf doppler	Doppler line width, nm
$g_{i,n}$	Statistical weight of n^{th} level in ionization species i
I_o	Incident or source intensity, arbitrary units
I/I_o or I/I_A	Transmission, dimensionless
$\log_{10}(I/I_o)$	Absorbance, dimensionless
$I_\lambda/I_{o,\lambda}$	Internal transmittance, dimensionless
k	Boltzmann constant, 1.38x10^{16} erg/deg K
L	Path length, cm
ℓ	Liters
m	Particle mass, g
$\dot{m}_{AR}$	Argon mass flow rate, g/s
$\dot{m}_{UF_6}$	UF_6 mass flow rate, g/s
N	Uranium total number density, atoms-cm^{-3}
N_A	Atom number density, atoms-cm^{-3}
N_i	Number density of species i, atoms-cm^{-3}

LIST OF SYMBOLS (Continued)

N_{UI}	Number density of neutral uranium atoms, atoms-cm^{-3}
N_{UII}	Number density of singly-ionized uranium atoms, atoms-cm^{-3}
N_{UIII}	Number density of doubly-ionized uranium atoms, atoms-cm^{-3}
N_{UT}	Total number density of uranium atoms, atoms-cm^{-3}
N_{UTC}	Total uranium atoms confined per unit plasma length, atoms/cm^3-cm^{-1}
N_x	Particle density of species x, cm^{-3}
P	Pressure, atm, mm Hg, or torr
Pc	Chamber pressure, atm
P_P	Partial pressure, atm
P_{TOTAL}	Total pressure all species, atm
P_{UF_6}	UF_6 injection partial pressure, atm
Q	Power, kW
Q_R	Power radiated, kW
Q_T	Total rf discharge power, kW
R	Radius, cm
r	Radial distance, cm
T	Temperature, deg K
t	Time, min or s
V	Voltage, volts
$\overline{V}_{Ar}$	Argon injection velocity, m/s
$\overline{V}_{UF_6}$	UF_6 injection velocity, m/s

LIST OF SYMBOLS (Concluded)

W	Weight of residue material on fused-silica tubes, mg or power, Watts (W)
Z_i	Partition function for ionization species i, dimensionless
λ	Wavelength, nm or microns
X_i	Mole fraction of species i, dimensionless
X	Uranium mole fraction, dimensionless
$\Delta\lambda$	Wavelength band, nm
$\Delta\lambda\nu$	591.54 nm absorption line width at one-half maximum intensity, GHz
μ	Absorption coefficient, cm^2/atom
ϵ_1	Molar extinction coefficient, ℓ/mole-cm
θ	Angle, deg
ϵ,α,γ	Designation of different crystalline forms of uranium compounds

APPENDIX A

SUPPORTING X-RAY ABSORPTION MEASUREMENTS OF URANIUM CONFINED IN RF-HEATED PLASMAS WITH PURE UF_6 INJECTION*

This APPENDIX summaries the exploratory x-ray absorption tests conducted using argon rf plasma discharges seeded with pure UF_6. These tests complemented the tests reported in APPENDIX D and the main portion of this report. The objectives were: (1) to develop an x-ray absorption method for measuring the amount of uranium confined in high-density, rf-heated uranium plasmas; (2) to fabricate equipment to accomplish those measurements; and (3) to integrate this method with rf plasma tests to demonstrate use of this equipment.

To accomplish this the following was included: a mockup test assembly to simulate the system to be used for measuring uranium density in the rf-heated uranium plasma tests was fabricated and tested; argon, UF_6, and argon-UF_6 mixture x-ray absorption measurements to develop and calibrate the system for measuring uranium density in the plasma tests were conducted; a test chamber for rf plasma tests which accommodates the x-ray measurement system was fabricated; the measurement system was installed and calibrated (with room temperature argon) in the 1.2 MW rf-induction heater facility; initial argon and argon-UF_6 mixture absorption measurements were conducted during rf-heated argon-only and argon-pure UF_6 injection plasma tests.

Estimates to determine the amount of x-ray absorption by uranium for a range of x-ray energies indicated that absorption of 3 to 25 KeV x-rays can be used to determine amounts of uranium at densities of interest (3×10^{16} atoms/cm^3 to 3×10^{18} atoms/cm^3).

Detailed calculations were made to determine the amount of x-ray absorption by uranium for x-ray energies of 4.8, 8, and 17.8 KeV. These energies are characteristic of the emission from titanium, copper, and molybdenum x-ray target materials, respectively. The variation of the fraction of x-rays transmitted with uranium number density is shown in Fig. 68 for 10 and 15 cm path lengths. Path lengths of 10 and 15 cm are typical of those used in tests in the 80 kW and 1.2 MW rf-heater facilities, respectively. The results shown in Fig. 68 indicate that x-rays from a copper target may be used to measure the density of uranium atoms, over the range of densities which are of interest in the plasma core reactor experiments. A mockup test assembly was fabricated to simulate the system to be used for measuring uranium density in the rf-heated uranium plasma experiments (the test assembly is shown in Fig. 69).

---

*Tests were conducted by Richard C. Stoeffler.

Preliminary experiments were conducted using a UTRC (nonportable) x-ray spectrometer. In these tests, UF_6 gas was the source of uranium atoms and was contained in a 2.54-cm-ID by 15-cm-long cylinder with 0.125-mm-thick Mylar windows on each end. The amount of x-ray absorption by the uranium atoms was determined by comparing the x-ray signal transmitted through the chamber containing UF_6 with that transmitted through a physically identical chamber which was evacuated. The intensity of x-rays transmitted through the test chambers were measured using a Norelco scintillation detector employing a thallium activated sodium iodide crystal and a Tennelec Model TC 216 amplifier - pulse height analyzer and counter-timer.

X-ray absorption measurements were made for UF_6 pressures from approximately 1 to 100 mm Hg corresponding to uranium densities of approximately 3.3×10^{16} atoms/cm^3 to 3.3×10^{18} atoms/cm^3, respectively. The measured fraction of x-rays transmitted are compared with the transmission calculated for UF_6 using Beer's law in Fig. 70. The experimentally determined values of transmission are given by the circular symbols and calculated transmission for UF_6 is given by the solid curve (the absorption by the fluorine was calculated to be approximately 2.5 percent of that by the uranium). The UF_6 pressure was measured using a pressure gage except for the data at the highest pressure. For this data point the pressure was not measured directly but was calculated to be between 76 mm Hg and 140 mm Hg from calculations based on residual pressures after removal of known volumes of UF_6 from the test chamber. The data indicate that agreement between calculated and measured transmission was good and tend to confirm that the characteristic x-rays from a copper target x-ray tube can be used to measure uranium densities from 3×10^{16} atoms/cm^3 to 3×10^{18} atoms/cm^3.

System for X-ray Absorption Measurements

The system used to make UF_6 and argon x-ray absorption measurements during calibration and rf-heated uranium plasma tests is shown schematically in Fig. 71. The system consists of the x-ray generator, the test chamber for containing the test gases (argon, UF_6, and argon-UF_6 mixtures), and the x-ray detection components. The x-ray generator consists of a Diano Corporation CA 8-S/copper x-ray diffraction tube with an XRD-6 x-ray power supply and controller supplied by single-phase 220 V/40 A service through a 7.5 kVA isolation transformer. The emitted x-rays from the target pass through a collimator with a vertically oriented 0.125-mm-wide slit and are reflected at the Bragg angle for 8 KeV ($\lambda = 0.154$ nm) x-rays from a magnesium oxide (MgO) crystal monochromator before passing through the test chamber. The test chamber consisted of a 5.7-cm-ID fused-silica tube with metal endwalls. The endwalls contained ports for supplying and exhausting test gases and x-ray viewing ports having windows which appear almost totally transparent to 8 KeV x-rays. The distance between the windows was 22.4 cm. The x-rays were detected using a Norelco scintillation detector (photomultiplier tube with a thallium-activated sodium iodide crystal mounted in a light-tight enclosure at the window end) with a high voltage 0.9 kV regulated dc power supply. A Tennelec TC 216 linear amplifier and single-channel analyzer was used to process the output signal from the scintillation detector and to provide an input signal into a Tennelec TC 545 counter-timer and a TC 590 rate meter. The rate meter output signal was recorded using a strip-chart recorder. In most tests, the x-ray intensity was obtained directly from the rate meter; however, in some tests conducted earlier in the program, the intensity was determined from the output of the counter-timer. The scintillation detector output was also displayed on an oscilloscope. The rate meter and oscilloscope signals were used as visual aids during alignment of the components of the x-ray measurement system.

Description of Chamber-Crystal-Slit System and Procedure Used in Calibration Tests

The details of the test chamber and the chamber-crystal-slit arrangement used during calibration tests are shown in Fig. 72(a) and the photograph in Fig. 73. The test chamber consisted of a 5.7-cm-ID fused-silica tube and two copper endwalls. The x-ray beam from the x-ray collimator (having a 0.025-mm-wide vertically-oriented slit) was reflected at the Bragg angle for 8 KeV x-rays parallel to the chamber axis through 6.35-mm-dia ports located in each endwall. The ports were sealed using 0.125-mm-thick Mylar windows. X-rays transmitted through the far port are detected through two 0.635-mm-wide slits (vertically-oriented) spaced 1.58-mm apart, using the scintillation detector. During these tests, the crystal was located approximately 3.8 cm from both the exit of the x-ray collimator and the near viewing port window and, the 0.634-mm-wide slots were located approximately 2.54 cm and 12.7 cm from the far viewing port window and detector, respectively (as measured along the beam path). A mechanism for adjusting the width of a horizontally-oriented slit located between the crystal and near viewing window is shown in the photograph of Fig. 73. This slit was not used during the calibration and rf plasma tests.

Calibration tests were made, using this test chamber-crystal-slit system, with pure argon, pure UF_6, and argon-UF_6 mixtures at 300 K in the test chamber. During tests with pure argon or pure UF_6, x-ray absorption was determined by comparing the x-ray intensity, I_o, obtained with the chamber evacuated to the x-ray intensity, I, obtained with the chamber at known pressures of argon or UF_6. Absorption measurements were made for argon pressures from 5 mm Hg (1.7×10^{17} atoms/cm^3) to 700 mm Hg (2.4×10^{19} atoms/cm^3) and UF_6 pressures from 5 mm Hg (1.7×10^{17} atoms/cm^3) to 86 mm Hg (2.9×10^{18} atoms/cm^3). The following procedure was used in the calibration tests with UF_6-argon mixtures. I_o was measured with the chamber evacuated. The chamber was filled with UF_6 to a known pressure (UF_6 pressure ranged from 5 mm Hg to 52.5 mm Hg). Argon was added to the chamber at partial pressures in steps up to 700 mm Hg. At each step the intensity, I, was measured. The absorption by UF_6 was determined by comparing I for each UF_6 and argon partial pressure with the intensity I_o multiplied by I/I_o for the partial pressure of argon as calculated from Beer's law. Two techniques were used to make the absorption measurements: (1) the system was aligned with the crystal positioned to maximize I_o as detected through either of the two 0.635-mm-wide far slits, and with the crystal position fixed, the intensity I was measured as the chamber pressure was varied; (2) with the system aligned as in (1) the crystal was traversed perpendicularly to the chamber axis so that the x-ray beam scanned the width of the viewing ports and the maximum I.

Description of Chamber-Crystal-Slit System and Procedure Used in RF-Heated Plasma Tests

The details of the test chamber and chamber-crystal-slit arrangement used during the rf-heated plasma tests are shown in Fig. 72(b) and the photograph in Fig. 74. The rf-heated plasma test configuration differed slightly from that used during the calibration tests. The system was arranged so that the x-ray beam traverses the plasma core region diagonally (path length equal to 23.0 cm), passing through the chamber axis where the maximum uranium density is expected to occur. Accordingly, 6.35-mm-wide by 19-mm-long x-ray viewing ports were located in the endwalls, as shown in Fig. 72(b), to allow passage of the x-ray beam. During these tests 0.105-mm-thick beryllium windows were used to seal the viewing ports. X-rays transmitted through the far port were detected by the scintillation detector through a 0.635-mm-wide vertically-oriented slit mounted on the face of the detector. The crystal was located approximately 12.7 cm and 4.4 cm from the exit of the x-ray collimator (with 0.025-mm-wide vertically-oriented slit) and near viewing port window, respectively. The 0.635-mm-wide slit mounted on the face of the detector was located approximately 4.6 cm from the far viewing port. The crystal position was fixed during rf-heated plasma tests.

This test chamber-crystal-slit system was calibrated using pure argon and the procedure described previously for a fixed crystal position. Argon absorption measurements were made for argon pressures from 50 mm Hg (1.7×10^{18} atoms/cm^3) to 1790 mm Hg (5.8×10^{20} atoms/cm^3).

The following procedure was used to determine uranium density from x-ray absorption measurements in an rf-heated uranium-argon plasma using the 1.2 MW rf-induction heater system. The x-ray intensity, I_o, was measured with the test chamber evacuated. Argon was injected tangentially (through vortex injectors shown in Fig. 72(b) into the test chamber and exhausted to vacuum through an axial thru-flow exhaust and axial bypass exhaust ducts. The chamber pressure was maintained at 10 mm Hg until the rf discharge was initiated and then increased to the pressure used for operation with UF_6 injection, approximately 1.7 atm. The variation of x-ray intensity, I_A, with amount of rf power supplied to the rf-heated argon plasma was measured (rf power was varied from 30 kW to 56 kW). UF_6 was injected axially into the test chamber using the UF_6 transfer system described in the main portion of this report and the variation of x-ray intensity, I, with UF_6 flow rate was measured (UF_6 flow rate was varied from 0.013 g/s to 0.134 g/s). UF_6 density was determined by computing the ratio $I/I_A = (I/I_o)/(I_A/I_o)$ (for comparable rf power levels) and using Beer's law, $I/I_o = e^{-\mu N_i L}$ where μ is the absorption cross section for uranium in cm^2/atoms, ($\mu = 1.12 \times 10^{19}$ cm^2/atom for uranium and 8.0 KeV x-rays), N_i is the number density in atoms/cm^3, and L is the path length in cm. During some tests with a pure argon plasma the variation of I_A with pressure level in the test chamber was measured and the ratio of I_A to I_o was used with Beer's law and the perfect gas law to calculate average argon temperatures.

Results From Calibration Tests With Pure Argon

Calibration data obtained using the calibration system (Figs. 72(a) and 73) and the rf-heated plasma system (Figs. 72(b) and 74) and pure argon at 300 K are presented in Fig. 75. The measured variation of fraction of x-rays transmitted, I/I_o, with variation in argon pressure, P_A, was compared with the theoretical variation calculated using Beer's law and the perfect gas law. Data obtained using the calibration system by traversing the crystal and with the crystal fixed are given by the circular and square symbols, respectively. The intensity ratios obtained for a given argon pressure by traversing the crystal (one for each of the two slits) were in good agreement, generally differing by less than 10 percent. Data obtained using the rf-heated plasma system with the crystal position fixed are given by the triangular symbols. Agreement between experiment and theory is good for intensity ratios up to approximately 10^{-2} (argon pressures up to approximately 900 mm Hg). At pressures greater than 900 mm Hg the argon appears (except for one data point) less dense than that predicted using Beer's law. It is possible that the x-ray beam is not monochromatic and that at large values of absorption, I/I_o less than 10^{-2}, the intensity of high-energy components (possibly harmonics) in the beam becomes important relative to the intensity of the primary component (absorption decreases with increasing x-ray energy) making the measured argon density appear less than that given by theory. It would be possible to operate at argon pressures greater than 900 mm Hg and intensity ratios greater than 10^{-2} by using an x-ray tube having a target such as molybdenum which emits x-rays having energies (17.8 KeV) greater than those emitted from a copper target x-ray tube. However, measurement of uranium densities near 10^{16} atoms/cm^3 would be more difficult (theoretical $I/I_o = 0.992$ for 17.8 KeV x-rays compared with 0.974 for 8 KeV x-rays).

Results From Calibration Tests With Pure UF_6

Calibration data obtained using the calibration system (Figs. 72(a) and 73) and pure UF_6 at 300 K are presented in Fig. 76. The measured variation of fraction of x-rays transmitted, I/I_o, with UF_6 pressure, P_{UF_6}, is compared with the theoretical variation. Data obtained using the calibration system by traversing the crystal and with the crystal fixed are given by the circular and square symbols, respectively.

During these tests the UF_6 canister was depleted and it was necessary to replenish it. Data obtained before the UF_6 was replenished are given by the open symbols in Fig. 76 and are in good agreement with theory. During initial tests conducted after the UF_6 was replenished, the system was contaminated (apparently with HF since the quartz test chamber and pressure gage glass were etched) and apparent uranium and fluorine compounds were deposited in the system (white "mist" deposits on inside of quartz tube are evident in Fig. 73). During subsequent calibration tests, it appeared that the injected UF_6 reacted with the contaminants in the system resulting in a reduction of UF_6 density with time and, therefore, an increase in x-ray intensity with time. The data obtained during these tests are denoted by the solid symbols in Fig. 76 and have been corrected for the time-wise drift in x-ray intensity. These data are also in good agreement with theory; however, the discrepancies between experiment and theory are greater than those which occurred before the system was contaminated. In general, the agreement between data and theory is good. However, for intensity ratios, I/I_o, greater than approximately 10^{-2} (UF_6 pressures greater than approximately 60 mm Hg) the UF_6 (as did argon) appears less dense than that predicted using Beer's law.

Results From Calibration Tests With Mixtures of Argon and UF_6

Calibration data obtained using the calibration system (Figs. 72(a) and 73) and mixtures of argon and UF_6 are presented in Fig. 77. Data obtained with the crystal stationary (unflagged symbols), the crystal traversed (flagged symbols), and before and after apparent contamination of the system (open and solid symbols, respectively) are presented for UF_6 partial pressures from 5 mm Hg up to 52.5 mm Hg and argon partial pressures from 0 to 700 mm Hg. In general, the data indicate fair agreement with theoretical intensity ratios. These data also indicate that the measured density of UF_6 decreases with increasing argon pressure and that this difference increases with increasing UF_6 pressure. This behavior would be expected, based on results obtained for pure argon and pure UF_6 (see Figs. 75 and 76), when the partial pressures of argon and UF_6 are such that the total fraction of x-rays transmitted is less than about 10^{-2}. The dashed curve through the data in Fig. 26 is the approximate locus for the total fraction of x-rays transmitted equal to 10^{-2}. For data located to the right of the curve the total fraction transmitted is less than 10^{-2} and to the left greater than 10^{-2}.

For clarity, only data obtained at one slit location (obtained by traversing the crystal) are presented. At P_{UF_6} = 15 mm Hg the values of I/I_o measured at the second slit location were up to 37 percent greater than those presented in the figure, and at P_{UF_6} = 25 mm Hg the values of I/I_o measured at the second slit location were as much as 43 percent less than those presented. These data were obtained after contamination of the system and were corrected for the time-wise drift in x-ray intensity. However, the possibility of large errors occurring was greater during these tests because long test times were required to ensure complete mixing of the argon-UF_6 gas mixtures.

Results From RF-Heated Plasma Tests With Pure Argon

Data obtained using the rf-heated plasma system (Figs. 72(b) and 74) and pure argon are presented in Fig. 78. The measured variations of intensity ratio, I/I_o, with change in argon pressure are compared with theoretical variations. Comparisons are made for calibration data obtained with no plasma (solid symbols) (argon temperature equal to approximately 300 K) and with the plasma present (open symbols for tests in which rf power was measured, power is noted by the numbers near the symbols). Tests were conducted, with the plasma present, with all of the argon exhausted through the thru-flow exhaust (unflagged symbols) and with argon exhausted through both the thru-flow and axial bypass exhausts (flagged symbols). Data were obtained for argon plasma pressures from approximately 1.2 atm to 2.9 atm and rf-heated plasma power levels from approximately 30 kW to 56 kW. These data indicate, although the amount of scatter is appreciable, that I/I_o increases with increasing rf power (increasing temperature and decreasing density) and decreases with increasing pressure (increasing density). The solid curves shown in Fig. 78 were calculated using Beer's law and the perfect gas law for argon at 300 K, 500 K, and 1000 K, 8 KeV x-rays, and a 23.0-cm-long path length. A comparison of the measured data with these curves indicates that the average temperature is approximately 500 K. The dashed curves shown in Fig. 78 were calculated for argon and 9.5 cm of path length at 2000 K, 5000 K, 10,000 K, and 15,000 K and 13.5 cm of path length at 300 K (hot plasma was assumed to occur between the end of the UF_6 injection probe (see Fig. 72(b)) and the endwall containing the exhaust duct). The remaining path length between the beryllium windows was assumed to contain 300 K argon. Comparison of the measured data with these curves indicates argon plasma temperatures which are not unrealistic; however, sensitivity is poor at high temperatures. Sensitivity could be increased by decreasing the amount of path length containing cold gas (i.e., mounting the beryllium windows nearer to the plasma). Also, the fraction of x-rays transmitted is very sensitive to temperature assumed for the cold argon. For example, at a P_A = 1.7 atm and a plasma temperature of 15,000 K, increasing the temperature of cold argon by 25 percent increases I/I_o by 100 percent.

To average I/I_o for argon at 1.7 atm which is the argon pressure for operation of the test chamber with UF_6 injection, is approximately 0.02. Therefore, UF_6 could be injected at densities up to 2.3×10^{17} atoms/cm^3 (corresponding to about 7 mm Hg at 300 K) without decreasing the total intensity ratio to a value less than 10^{-2} (data presented in Figs. 75 and 76 indicate that at I/I_o less than 10^{-2}, UF_6 and argon appeared to be less dense than that predicted by theory).

Results From Tests With RF-Heated Uranium Plasmas

X-ray absorption measurements were made in a series of tests to determine uranium density in rf-heated uranium plasmas. During these tests, 3.2 g/s of argon were injected tangentially around the UF_6 which was injected axially at flow rates between 0.013 g/s and 0.134 g/s. The chamber pressure was maintained at 1.7 atm and the rf-power in the plasma increased from 38 kW at a UF_6 flow rate of 0.013 g/s to 75 kW at a flow rate of 0.134 g/s. The flow was exhausted through the thru-flow and axial bypass exhausts.

In some tests the rf-power deposited in the plasma with UF_6 injection was greater than that which could be maintained with a pure argon fixed buffer gas injection rate. To determine uranium density by comparing x-ray intensities obtained with and without UF_6 injection, it was necessary to isolate the effects of changes in rf-power level. The variation of intensity ratio, I_A/I_o, for pure argon, with amount of rf-power deposited in the plasma was measured and is shown in Fig. 79 (circular symbols). A straight line approximation is used to represent and extrapolate these data to rf-power levels which occurred during operation with UF_6 injection. The measured variation of intensity ratio, I/I_o, for argon-UF_6 mixtures with rf-power is also shown in Fig. 79 (square symbols with UF_6 flow rates in g/s given next to the symbols).

The fraction of x-rays transmitted through the UF_6, I/I_A, was determined using the measured fraction transmitted through the argon-UF_6 mixture, I/I_o, and the fraction transmitted through argon I_A/I_o obtained from the straight line approximation shown in Fig. 79 at equivalent rf-power levels.

The intensity ratio I/I_o was used with Beer's law for uranium to calculate the uranium number density. The variation of uranium number density with UF_6 flow rate is shown in Fig. 80. The variation is presented for assumed UF_6 path lengths of 23.0 cm and 9.5 cm (circular and square symbols, respectively). Corresponding rf-power levels are noted next to the symbols. These data indicate that the uranium number density increases with increases in UF_6 flow rate and that the rate of increase decreases for UF_6 flow rates greater than approximately 0.08 g/s. Maximum uranium densities of 1.65×10^{17} atoms/cm^3 (path length = 23.0 cm) and 3.85×10^{17} atoms/cm^3 (path length = 9.5 cm) were measured for a UF_6 flow rate equal to 0.093 g/s.

In some tests at UF_6 flow rates greater than approximately 0.093 g/s, the measured x-ray intensity decreased with time (for fixed test conditions) indicating that UF_6 or uranium compounds were being deposited on the beryllium windows. Further evidence that UF_6 or uranium compounds had been deposited on the windows was obtained in subsequent tests with pure argon after the UF_6 injection was stopped. X-ray intensity ratios were significantly less than those attained with pure argon prior to UF_6 injection. The data presented in Fig. 79 were obtained from tests in which the x-ray intensity obtained with UF_6 injection did not decrease with time (unflagged symbols) and from tests in which intensities obtained with pure argon subsequent to tests with UF_6 injection were approximately the same as intensities obtained prior to UF_6 injection (flagged symbols).

The x-ray absorption equipment and measurement techniques developed and tested were used to supplement the optical methods (described in main text) for determining the amount and distribution of uranium vapor confined in the uranium plasma within the operating range tested. For future rf uranium plasma tests in which the atom density of confined uranium may exceed levels greater than approximately 10^{16} atoms/cm^3, the x-ray absorption scheme will be a required measurement technique.

APPENDIX B

EMISSION AND ABSORPTION CALIBRATION METHODS

In the case of cylindrically symmetric, optically thin (i.e., where photons emitted from the inner region of the plasma are not absorbed before reaching the outer boundary) plasmas, the relationship between the radial profile of the volume emission coefficient and the profile of the emitted intensity can be expressed in the form of an integral equation. The inverse of this equation can be obtained from the Abel inversion formula and several numerical techniques based on this formula have been developed (Refs. 14 and 15).

The problem of spatially resolving the volume emission coefficient when the source is not optically thin, using the transmission and emitted intensity profiles as input data, has been considered by a number of authors. If the plasma source is a cylindrical column with circular cross section, and the optical properties of the plasma depend only on r, the distance from the axis, Freeman and Katz (Ref. 16) and Elder (Ref. 17) have developed numerical methods for the solution. They have shown that the spatial distribution of the absorption coefficient is a prerequisite for the determination of the emission coefficient in an optically thick plasma. In this case, the radiative transfer equation is not an Abel equation, since the radial distribution of the absorption coefficient must be taken into account and solution for the emission coefficient is more difficult. The absorption coefficient can be determined from the attenuation of the intensity of the probing beam (dye laser beam in the case of the experiments reported herein) of radiation traversing the plasma source. The radiation emitted by the probed section of the source must be subtracted from the emerging radiation before the attenuation can be found. A key requirement is that the probing laser beam flux is greater than or equal to the emitted radiant flux. The availability of high power cw tunable single-frequency dye lasers which match and/or exceed the spectral radiance of the uranium plasma discharges of the type discussed herein satisfy this requirement.

Reference 18 describes a method utilizing an iterative procedure to find the radial distribution of the emission coefficient once the radial distribution of the absorption coefficient has been determined. At the pressures and temperatures used in the rf uranium plasma experiments reported herein, the assumption of local thermodynamic equilibrium is justified; thus, the temperature profile can be obtained directly from the emission and absorption coefficients by applying Kirchhoff's law. Kirchhoff's law states that the local ratio of the emission to absorption coefficients must be equal to the Plank function at that particular wavelength and at the local temperature.

The radial distributions of the emission and absorption coefficients were determined, as discussed in the main portion of this report, from two sets of side-on observations of the uranium plasma discharge made along different chords at distances r from the axis of symmetry. Reference 18 contains details of the formally convergent iteration technique that was used to obtain the spatial resolution of the volume emission and absorption coefficients for the case of the strongly self-absorbing uranium plasma. The employment of the powerful tunable dye laser system (narrow line monochromatic radiation) simplified the transmission profile measurements of the uranium plasma discharge. Alternative schemes such as the double-path method (Ref. 19) depend on the exact superpositioning of the source and reflected image; this would have been extremely difficult due to the physical constraints within the 1.2 MW rf induction heater test tank. An assumption that must be invoked in the application of this experimental technique is that the absorption coefficient must be approximately constant over the wavelength interval equal to the spectral slit width. Other assumptions are that the optical system is such that the dispersive element of the monochromator subtends approximately the same small solid angle from points along the chord through the plasma discharge and that the entrance slit-width of the monochromator is small compared to the plasma radius. Under these conditions, the system was calibrated absolutely by physically replacing the uranium plasma discharge with a calibrated standard source of spectral radiance (G.E. T/24-7) and comparing the two signals.

One area which required additional bench testing was the possible beam steering of the laser beam as it propagated through the test chamber and plasma source. Separate tests combined with a ray tracing analysis verified the degree of refraction present and the optical system was modified to account for this. The surface imperfections present on the surfaces of the fused-silica tubes were not uniform and therefore could not be compensated for in the lens and optical system. This effect was calibrated out for each particular test; i.e., once the rotational orientation of the two concentric fused-silica tubes was selected, they were maintained in that fixed orientation until completion of that particular test.

The phototube and optical system were calibrated using the G.E. T/24-7 lamp of known spectral radiance in place of the plasma discharge. All other components of the test chamber and monochromator/recording instrumentation remained unchanged. The signal at the photomultiplier (EMI-9558) tube operating at 900 V that correlates with the radiance was measured. The spectral radiance of the G.E. T/24-7, EPI#EPUV-1048 operating at 30 amp and at 591.54 nm was 21.3 $\mu W \cdot mm^{2} \cdot nm^{-1} \cdot St^{-1}$. The power incident on the detector was calculated according to the relationship:
$P(W) = R_{\lambda,\Omega}(w \cdot mm^{-2} \cdot nm^{-1} \cdot St^{-1}) \cdot A(mm^{2}) \cdot \Delta\lambda(nm) \cdot \Omega(St) \cdot \epsilon$; where, P(W) is the power incident on the detector, $R_{\lambda,\Omega}$ is the spectral radiance at right angles, A is the area of the tungsten strip focused through the input slit of the monochromator, $\Delta\lambda$ is the spectral width of the monochromator, Ω is the solid angle of the optics, and ϵ is the efficiency of the system. Note that $\Delta\lambda$ is the full width at half maximum as measured with the monochromator using a low pressure mercury lamp as the light source. The Gaussian slit function of the monochromator was replaced with a

rectangular slit of full height and width equal to that of the spectral width of the monochromator. For the particular emission line used (591.54 nm), the power is concentrated in a much narrower line width (4.082×10^{-3} nm). The magnification of the overall optical system was 1.57. Thus, a 25 μm x 25 μm square on the entrance slit of the monochromator viewed a 39 μm x 39 μm square of surface area at the centerline of the plasma. The calibration factor for the phototube was then determined in terms of the power incident on the photomultiplier tube per unit voltage output. Note that the same optical system (see Fig. 13) was used for both the rf plasma tests and the source calibration tests; the solid angle of the optics and the efficiency were unchanged. This permitted determination of the relationship between the spectral radiance for the rf uranium plasma and the output voltage of the photomultiplier tube.

APPENDIX C

SUPPORTING CHEMICAL ANALYSES--REFERENCE STANDARDS--PROPERTY DATA ON FUSED SILICA AND AS-RECEIVED UF_6

One of the key components in the test chamber used throughout this test program was the fused-silica peripheral wall. The tubes used were purchased from U. S. Fused Quartz Corporation; this company was selected over several other competitors primarily due to price, availability, and quality control of the dimensional tolerances. TABLE VII lists the physical, thermal, electrical, and optical properties of the fused-silica tubes used in the experiments reported herein.

As additional improvements were made to the test chamber configuration and flow scheme, which in turn further reduced the residue material deposited on the various components, the purity level of the components themselves (in particular the fused-silica tube peripheral wall) became increasingly important. To provide an estimate of the purity of the fused-silica tubes used in the rf plasma experiments with pure UF_6 injection, spectrochemical data were obtained from U. S. Fused Quartz Corporation to permit a comparison with the analyses conducted at UTRC. TABLE VIII summarizes the results. Because of the possibility that the batch of fused silica used in the preparation of the as-received 5.7-cm-ID x 6.1-cm-OD fused-silica tubes may have been different than the reference standard fused silica, a separate analysis was also included. This is shown in the last two columns of TABLE VIII. The overall results indicate good agreement; actually the UTRC analytical results are more favorable for the case of the Al_2O_3 impurity constituent than those reported by U. S. Fused Quartz Corporation.

As part of the overall analysis of the fused-silica tubes, several comparisons were made to a reference standard relative to the degree of residual thermal stress observed to be present in the fused-silica tubes after tests using the rf plasma with pure UF_6 injection. Figure 81 illustrates the varying degree of thermal stress present which ranged from negligible to relatively high. In several of the exploratory tests with the rf plasma and pure UF_6 injection which were accompanied by a moderate degree of residue coating on the peripheral walls, post-test cracking of the tubes was noted. In all cases, this was attributed to the relatively high degree of residual thermal stress present in the central portion of the tube as observed using polarized light as shown in Fig. 81(b). The later tests in the series, wherein relatively small amounts of wall coating occurred, little or no evidence of residual thermal stress was noted and no post-test cracks occurred (see Fig. 81(d)).

As in the case of the fused-silica tube impurities, another possible contributing factor to the formation of the different types of compounds found in the post-test analysis of the residue material was the impurity level of the UF_6. Consequently, an analysis was performed and an assay made on the as-received UF_6. TABLE IX summarizes the results. The impurity level of the various elements are indicated per million parts of total uranium. Note that the minimum weight percent of the UF_6 in the material was 99.98. The UF_6 was purchased through Allied Chemical Corporation in 2.2 kg batches.

To provide additional information on the possible influence of moisture, UF_6 contamination, O-ring sealant material, and temperature-time history on the etching/corrosion aspects of the fused-silica, a series of laboratory-scale tests were conducted. 350 cc vessels fabricated from the same batch of fused silica as used in the actual tests were subjected to different types of controlled tests. Part of the results are shown in the photograph of Fig. 82. Refer to TABLE X for the corresponding test conditions. The vessels were evacuated to 10^{-4} mm Hg prior to being filled with the small quantities of UF_6, as shown in Fig. 82. For test case I, shown in Fig. 82, 0.9 g of as-received UF_6 was transferred into the vessel. Immediately upon filling, a white snowflake-like mist appeared on the wall. After several minutes at room temperature, there was a partial transition to a yellowish/light green compound formation in the central region together with apparent etching at the end regions. Uniform application of heat (330 K for 1 hr) resulted in no noticeable change to the compound in the central region; sublimation of the white crystals was observed. Slow cooling followed by a room temperature soak for 72 hours resulted in a redeposition of the white crystals in the central region and a trace formation of a yellowish/green/brown deposit near the end region (adjacent to the stopcock used with the silicone grease). Evacuating the contents of the vessel after the long soak period left the white mist-like etching and the yellowish/green compounds; the white crystals disappeared. Post-test analysis using the IR spectrophotometer indicated the yellowish/green compound to be composed primarily of silicone grease, UO_2F_2, and H_2O. Analysis of the white 'mist-like etching portion revealed the compound to be primarily UO_2F_2, H_2O, and SiO_2; thereby supporting the observation that local etching had indeed occurred. The second test (see Fig. 82 and TABLE X) was similar to test I; however, Kel-F oil was used on the stopcock and the UF_6 was filtered by passing it through NaF anhydrous powder to remove the HF. A similar temperature time history was again employed in this test. The results indicated a very small amount of "whitish mist" (much less than the prior test) and no yellowish/green compound formation or coloration. The third test (see Fig. 82 III and TABLE X) used filtered UF_6, the standard silicone grease on the stopcock but included a vessel bake-out procedure prior to filling with 1.2 g of UF_6. After exposure to the same temperature-time history as the prior two tests, the post-test examination revealed the fused-silica tube to be relatively clear with some slight (pale green) coloration in the vicinity of the silicone grease interface. The final test (IV) used filtered UF_6, Kel-F oil on the stopcock, and included the vessel prebake-out procedure prior to filling with 0.9 g of UF_6. Exposure to the same temperature-time history as the prior three tests indicated the tube to be relatively clear with negligible discoloration in the vicinity of the stopcock. The overall test results indicated that noticeable etching occurred when as-received UF_6 was transferred into the vessels containing silicone grease on the transfer line stopcock and employing no vessel prebake-out procedure. The use of filtered UF_6 and Kel-F oil resulted in much less etching, discoloration, and compound formation. Inclusion of a prebake-out procedure to the vessels prior to filling with filtered UF_6 again helped to reduce the etching/discoloration; however, this procedure was not practical in the rf plasma tests due to physical constraints.

To assist in analyzing the wall deposition samples, Figs. 83 through 86 contain examples of the compound standards used in the IR spectrophotometric absorption measurements. Refer to TABLE III for a complete summary of all the material samples used in the IR spectrophotometric analysis. A detailed cataloging of the possible uranium compounds that may form with the associated diffraction pattern lines and physical characteristics was also conducted and is shown in TABLE XI.

Due to the unavailability of experimental data on the corrosion aspects of hot, pressurized UF_6, information was accumulated throughout this test program which will also be applicable to future tests. Figure 87 shows an example of the rate of corrosion in microns per hour as a function of temperature for different materials exposed to relatively low pressure UF_6. The preferred use of Monel and nickel can be seen when compared to the other materials. An example of the type of corrosion observed during the test program reported herein is shown in Fig. 88. A small 0.005-cm-thick 316 stainless steel burst disc was used in the UF_6 transfer system, as shown in Fig. 5. Photographs (a) and (b) of Fig. 88 show two different magnifications of the pressure side of the as-received disc. The photographs labeled (c) and (d) in Fig. 88 are the corresponding areas after prolonged exposure to hot, pressurized UF_6. The disc ruptured due to intergranular fracture induced by the corrosion effect of the UF_6. Considerably more data will be required over a wide range of operating conditions to fully document the possible corrosive effects that long time exposure to hot, pressurized UF_6 can have on various materials. In the tests reported herein, careful post-test inspection of the different components provided a qualitative indication of the degree of corrosion taking place.

APPENDIX D

EXPLORATORY RF URANIUM HEXAFLUORIDE (UF_6) SEEDED ARGON DISCHARGE EXPERIMENTS*

This APPENDIX summarizes the initial exploratory tests conducted at UTRC using argon rf plasma discharges seeded with pure UF_6 with application to future uranium plasma core reactor simulation experiments. The objectives were: (1) to investigate techniques for fluid-mechanical confinement of uranium plasmas with minimum deposition of uranium or uranium compounds on the peripheral wall of the test chamber; (2) to initiate the development and testing of materials and handling techniques suitable for use with high-temperature, high-pressure gaseous UF_6; and (3) to initiate the development of diagnostic instrumentation and measurement techniques to characterize the uranium plasma and deposited residue material.

Description of Equipment and Test Procedure

The majority of the experiments were conducted using a 80 kW rf induction heater system. Several initial follow-on test series were also conducted using a 1.2 MW rf induction heater system.

For the sake of continuity, the initial experiments conducted using the 1.2 MW rf induction heater will be discussed in this APPENDIX. A description of the facility can be found in the main portion of this report.

Figure 89 is a schematic diagram of the 80 kW rf induction heater system. A photograph of an assembled exploratory test configuration installed under the $2\frac{1}{2}$ turn, 7.5-cm-dia, water-cooled rf work coil (0.7 μH) of the 80 kW facility is shown in Fig. 90. The easily modified work coil is connected to the output of the power amplifier by means of a tunable π-coupling network (Fig. 89). The initial system was modified to operate at 13.56 MHz and low-speed motor drives were installed on the plate and load tuning capacitors to aid in efficiently coupling rf power into plasmas having a relatively wide range of sizes and impedances (primarily due to the introduction of pure UF_6).

Figure 91 contains schematic diagrams of the various test chamber flow configurations employed in the exploratory tests conducted in the 80 kW rf facility. Different configurations were tested to permit selection of the flow geometry with the best confinement characteristics. A gas-cooled 5.7-cm-ID x 6.1-cm-OD fused-silica tube formed the peripheral boundary of the test chamber. A symmetrically-

---

*Part of the results from this exploratory research effort have been reported in Ref. 7.

arranged set of water-cooled endwalls spaced 10 cm apart formed the axial boundary of the test chamber. Argon was injected through a set of vortex injectors equally-spaced around the periphery of one or both endwalls to provide the confining flow. As shown in Fig. 91(d), some tests were conducted with the argon gas injected tangentially through hypo-sized injectors (ultrasonically-drilled) located within the fused-silica peripheral wall itself. The exhaust gases were removed through one or both endwalls using thru-flow ducts on the centerline and/or off-axis annular exhaust ducts.

To permit steady-state injection of pure UF_6 into the plasma, several types of concentric-tube, water-cooled copper injectors were fabricated and located concentrically within the on-axis thru-flow duct. UF_6 was selected as the form of uranium bearing compound for injection into the plasma because it could be supplied in a gaseous form. Earlier tests in previous research programs had indicated that injection of uranium in the form of small particulates was a more difficult technology. However, UF_6 is very reactive chemically and must be heated to be sure that it remains in the gaseous state and does not condense on the injector walls prior to entering the plasma test chamber. Therefore, special cleaning procedures, operating procedures, and heating and feeding techniques had to be employed. These included the use of steam augmentation and electrical heater assemblies throughout the UF_6 injector and feed systems to eliminate the possible condensation and subsequent plugging of the UF_6 feeder lines. As shown in Figs. 91(a) and 91(d), the UF_6 injector could be extended into the test chamber/plasma region to eliminate some of the end effects. The various test chamber flow geometries and combinations thereof, permitted a wide variation in the types of flow conditions obtainable with UF_6 injection. Based on the exploratory test results, the type of test chamber flow configuration shown in cross section in Fig. 92 was selected for transitional tests in the 1.2 MW rf induction heater system. This geometry has several attractive features (e.g., ability to vary the distribution of exhaust gas flow (axial bypass); ease of change in the injection area of the argon vortex injectors; and, ease of change in the location of the on-axis UF_6 injector).

As in the 80 kW rf tests, the axial length between endwalls was 10 cm. Because of the higher power, higher pressure, and associated radiation levels involved, a concentric set of water-cooled fused-silica tubes (in contrast to the single fused-silica tube peripheral wall shown in Fig. 92) were used as the peripheral wall. The inner tube was 5.7-cm-ID x 6.1-cm-OD; the outer tube was 6.5-cm-ID x 7.3-cm-OD. The water-cooled copper endwalls incorporated provisions for driving the vortex from one (or symmetrically from both -- not shown in Fig. 92) endwall. The other endwall had provision for removing the exhaust gas through an axial bypass on the periphery of the endwall, as shown in Fig. 92. Both endwalls have the option for removing varying amounts of the exhaust gas through the on-axis thru-flow ducts. The UF_6 injector, located on-axis and concentrically within one endwall, was fabricated from a 50-cm-long three concentric copper tube assembly. In the majority of tests, the injector tip protruded into the test chamber. High pressure water (20 atm) heated to approximately 350 K via a steam heat exchanger flowed at 0.14 ℓ/s between the concentric tubes of the UF_6 injector. This provided cooling relative to the hot plasma environment while still maintaining a high enough temperature in the injector to permit flow of the pressurized gaseous UF_6 without solidification and subsequent plugging in the UF_6 transfer line.

The total power deposited into the plasma was obtained from an overall test chamber heat balance by summing the power lost by radiation, power deposited into the annular coolant of the peripheral wall, power deposited into the endwall assemblies, power convected out the exhaust ducts, as well as, power deposited into the effluent gas heat exchanger and UF_6 injector assemblies.

The power radiated from the plasma was measured using a radiometer and chopper wheel assembly. Radiation within different wavelength bands was measured using various filters. The response of the thermopile with filters was calibrated using a standard source of spectral irradiance. The total power radiated from the plasma and in each wavelength band was calculated assuming isotropic radiation including allowance for blockage due to the rf work coils. The physical size and shape of the plasma was determined from photographs taken using various neutral density filters.

Figure 93 is a schematic of the diagnostic systems used in the exploratory rf plasma tests. A Jarrel-Ash 0.25-m Ebert monochromator and an EMI 9558 (S-20 response) photomultiplier detector was used to obtain spectral emission data between 300-700 nm. Twenty-five μm-wide entrance and exit slits were employed. These measurements were taken on-axis at the midplane of the test chamber. The scanning rate was 100 nm/min and the data were recorded on a strip-chart recorder; measurements were obtained for both argon only and argon plus UF_6 plasmas.

The optical measurements also included side-on absorption measurements using a cw single-frequency, tunable dye laser system. The feasibility of this technique was investigated in these exploratory tests as a possible means for determining the number density and spatial distribution of uranium vapor contained within the discharge boundary in future UF_6 rf plasma tests containing uranium vapor of heavy concentrations. Refer to the main portion of this report for a detailed description of the dye laser system. This technique is also compared with an x-ray absorption method for measuring the amount of uranium confined in the rf-heated uranium plasmas (results discussed in APPENDIX A).

In these exploratory tests, the laser beam ($\approx$1.5-mm-dia) traversed the test chamber on the major axis at a distance 1 cm away from the tip of the UF_6 injector; the UF_6 injector extended 1 cm into the test chamber. This position was selected since prior rf plasma tests (argon only) included chordal scans at this location from which temperature profiles were determined.

UF_6 rf plasma exploratory tests conducted in the 1.2 MW induction heater facility did not include the dye laser system, but the argon-ion laser system operating at 514.5 nm was used for additional side-on absorption measurements taken on-axis at the axial midplane of the test chamber. The test setup was similar to that shown in Fig. 93.

To permit a preliminary analysis of the quantity and composition of the wall deposition incurred after several selected UF_6 rf plasma tests, samples of the wall residue were collected and analyzed by means of electron diffraction, x-ray diffraction, electron microprobe, and IR spectrophotometric techniques.

In general, the exploratory tests (80 kW and 1.2 MW) were first conducted with only argon injected into the test chamber. After sufficient time to establish equilibrium (also for the thermocouple outputs used in the calorimetric measurements to reach steady-state levels), pure UF_6 was injected for various time periods (typically, several minutes). Normally, a series of UF_6 tests were conducted with the same fused-silica tube prior to shutdown for post-test examination.

Discussion of Results

TABLE XII is a summary of the exploratory tests conducted using the 80 kW rf induction heater, including a brief description of the test chamber configuration and flow control scheme, range of test conditions, number of tests conducted, and pertinent comments applicable to each. A direct one-to-one comparison between each of the various configurations was difficult because of the different operating characteristics associated with each test. Also, due to time and cost constraints, each configuration by no means represents the optimum in design and sizing of the various components.

Based on the overall test results, the test chamber flow configuration shown in Fig. 91(a) was selected as the one best-suited for use in the initial rf plasma tests employing the 1.2 MW rf induction heater system. With this configuration, a relative maximum mass flow rate of pure UF_6 injected directly into the argon plasma was achieved with corresponding light wall coating, thus offering potentially the best confinement characteristics. In addition, this test chamber flow configuration possesses significant flexibility in the control of the flow field and exhaust gas distribution as described previously.

To illustrate the effect of the pure UF_6 injection on the plasma discharge, Fig. 94 shows the operating conditions and results of corresponding radiation measurements for a typical exploratory test. In the majority of tests, attempts were made to maintain constant as many of the independent variables as possible during the injection of UF_6. However, changes in the rf power and/or tuning and associated flow rates were sometimes required to prevent discharge extinguishment or plasma oscillations. In general, the introduction of pure UF_6 into the discharge significantly altered the impedance of the plasma which, in turn, determined the plasma size and electrical conductivity. Figure 95 is a photograph taken in the exploratory test series of a typical rf plasma with pure UF_6 injection. The introduction of the UF_6 was manifested principally as a significant increase in radiation emitted from the plasma; correspondingly, a moderate increase in the total power deposited into the plasma was also observed. The table and bar graph of Fig. 94 illustrates both these effects. Note that a significant amount of the increase in radiation occurred in the visible and near-UV wavelength bands. At the relatively low discharge power and pressure levels of these exploratory tests, the discharge was quite sensitive to changes in both the argon mass flow rate and the UF_6 mass flow rate. Occasionally, when the UF_6 injection mass flow rate exceeded a certain level, corresponding to a given set of test conditions, distortion occurred (plasma unsteadiness) in the central region of the plasma; this was usually followed by extinguishment of the discharge.

Periodically throughout the exploratory rf plasma tests, spectral emission measurements throughout the wavelength band from 300-700 nm were taken on-axis at the axial midplane using a 0.25-m monochromator system. Figure 96 illustrates some results obtained for the wavelength band between 400 to 460 nm. Many of the strong argon, uranium, and fluorine lines present in the wavelength range from 300-700 nm have been identified, cataloged, and compared with those documented in the literature.

To demonstrate the feasibility and practicality of using a cw single-frequency tunable dye laser system for making uranium plasma absorption measurements, several tests were conducted using the dye laser system illustrated in Fig. 93. Significant effort had to be devoted to properly shielding the entire dye laser and associated diagnostic equipment from the rf fields. As shown in Fig. 93, the dye laser beam traversed the test chamber on the major axis at a distance of 1 cm away from the tip of the UF_6 injector. Based on prior spectral emission chordal scans taken under similar test conditions (argon only), the temperature profiles determined (based on both absolute line and continuum radiation) indicated centerline temperatures of approximately 8000 K exist with a slight off-axis peak at a radius ratio of about 0.5.

Figure 97 shows an example of the absorption measurements obtained from the actual strip-chart recorder output in the exploratory rf plasma experiments with pure UF_6 injection. The 591.54 nm uranium line was selected as it is a relatively strong uranium I line and appeared well-defined in the spectral emission scans. The lower state for the 591.54 nm line is the uranium I ground state. The half-width of the laser line at the 591.54 nm wavelength was approximately 10^{-4} nm. To obtain the measurements shown in Fig. 97, the scanning generator of the dye laser system was activated to an automatic continuous scan mode as shown by the output data in the left portion of Fig. 97. Only argon was present in the rf plasma discharge during these initial scans. The 8 GHz range (free spectral range of the confocal Fabry-Perot spectrum analyzer) translates to approximately 10^{-2} nm on the wavelength scale. Many such scans at different operating test conditions were completed with only several (at fixed test conditions) shown in Fig. 97 for simplicity. The test conditions for the argon-only case were similar to those shown in the table in Fig. 94. The zero reference line (zero transmission) is shown at the top of Fig. 97. As noted, no absorption was detected for any of the argon-only test conditions. When pure UF_6 was injected into the discharge, sufficient time was allowed for all conditions to come to equilibrium (≈ 10 s); additional scans were then completed. Results from tests at two different UF_6 mass flow rates are shown at the right of Fig. 97. The first case corresponds to a UF_6 mass flow rate of approximately 0.02 g/s. The measurements indicate an absorption of approximately 25 percent (corresponding to an $I/I_o = 0.75$). Doubling the mass flow rate of UF_6 to approximately 0.04 g/s increased the relative absorption to about 55 percent ($I/I_o = 0.45$) for the second case. Based on an assumed 50-50 occupancy (ground state/excited state), a temperature of 8000 K, an optical path length of 2 cm (relatively small core due to close proximity of the UF_6 injector), and including a factor for ionization reduction, the ground state neutral uranium UI atom number density based on the absorption measurements were estimated to be approximately 8×10^{12} atoms/cm^3 and 2×10^{13} atoms/cm^3, respectively, for the two cases. This compares with approximately 10^{14} atoms/cm^3 based on temperature and pressure calculations. These results are encouraging and demonstrated that a dye laser system combined with optical scanning instrumentation may be employed in future rf plasma uranium confinement tests to permit chordal scans of the spatial absorption distribution; from this and other measurements the total number density and spatial distribution of uranium vapor contained within the discharge boundary may be determined.

Periodically throughout the exploratory test series, portions of the fused-silica peripheral tubes were examined for thermal stress and wall deposition. Figure 98 is a photograph of two of the tubes used in the exploratory tests with pure UF_6 injection. The analysis indicated thermal stress was present in the central region of the fused-silica tube, generally following the outline of the rf work coil. This was as expected due to the limited air jet cooling supplied to the fused-silica tube and the close proximity of the rf plasma to the wall during the majority of tests. The fused-silica tube numbered 8 in Fig. 98 is representative of the type of wall coating obtained after about two minutes of operation in the relatively high UF_6 mass flow rate range.

TABLE XIII is a summary of the exploratory tests conducted in the 1.2 MW rf induction heater using the basic test chamber flow configuration shown in Fig. 92. In these tests, the higher power, higher pressure argon rf plasma discharge employed in the 1.2 MW rf induction heater tests was less susceptible to perturbations due to the injection of pure UF_6. Thus, a greater mass flow rate of UF_6 could be injected while still maintaining a well-confined, stable discharge. Occasionally, under certain extreme combinations of test conditions, indications of plasma unsteadiness were observed to occur.

The maximum mass flow rate of pure UF_6 employed was approximately 0.1 g/s. This corresponded to a chamber pressure of 1.7 atm, argon plasma power level of about 70 kW, and argon buffer gas mass flow rate of 3.2 g/s. The test at maximum UF_6 flow rate extended over a time interval of ten minutes. The residue in the central portion of the fused-silica tube for this particular test was approximately 25 mg.

During the latter part of the exploratory tests using the 1.2 MW rf induction heater, ten tubes were selected for analysis of wall deposits by several techniques, including electron diffraction, x-ray diffraction, electron microprobe, and IR spectrophotometry. TABLE XIV is a summary of the results and shows the types of compounds deposited on the peripheral wall. Figure 99 is a photograph showing four of the ten tubes that were analyzed. Only one complete test was conducted prior to the removal of these tubes from the test section. Note that approximately an order of magnitude reduction in the deposition of uranium compounds was achieved in these tests. It should be pointed out that a relatively uniform deposition of approximately 19 mg is difficult to detect visually. The SiO_2 detected using the IR spectrophotometer, was believed to be from the fused-silica tube itself and partly due to the silicone grease used in the O-rings for sealing the fused-silica tube to the endwall assembly. The agreement between the different analysis techniques is reasonable considering the statistical nature of sampling the residue and partial exposure to the atmosphere in the preparation of the small samples. In addition to the results shown in TABLE XIV for the fused-silica peripheral wall tube, trace amounts of UF_4 were found to be present on the surface of the endwalls, UF_6 injector, and within the exhaust thru-flow duct. Figures 100 through 104 show examples of the results obtained from the various analysis techniques employed in these exploratory tests. Figure 100 illustrates the type of electron diffraction patterns obtained. For the particular sample shown, the primary compound was UO_2 with a trace amount of UF_4. The tabular data to the right of the actual diffraction pattern photograph gives additional details on the compounds characteristics. Photomicrographs of the residue wall coating (800X magnification) corresponding to the three principal color samples analyzed are shown in Fig. 101. The distinctly different crystalline structure of each is clearly evident in the photographs. Figure 102 contains four photographs showing the different x-ray diffraction patterns obtained from post-test analysis of the fused-silica tube residue. In all cases, the samples were subjected to copper K_α radiation in a Debye camera. In addition to the three color powders obtained (black, rust, green), a black chip sample was also included for comparison. The distinctly different x-ray diffraction patterns from each sample is evident from the photographs. Figure 103 contains three photographs showing the distribution of U, F, and O from samples of the black powder residue wall coating from a post-test x-ray analysis. The magnification was approximately 350X. Figure 104 is an example of the recorder output trace obtained from the IR spectrophotometry absorption measurements of a post-test analysis of the residue wall coating. At the bottom of the trace is noted the particular compounds associated with the peaks.

Figure 105 shows an example of some of the absorption measurements obtained in the 1.2 MW rf plasma exploratory experiments with pure UF_6 injection. Refer to Fig. 93 for the basic diagnostic setup. In these tests, an argon-ion laser beam of approximately 300 mW power and operating at a wavelength of 514.5 nm was used. The 514.5 nm line was selected because of its relatively high output power, and because a cataloged singly-ionized uranium line also corresponds to the 514.5 nm wavelength. Figure 105 shows the change in transmission (I/I_o) which occurred with various changes in the UF_6 mass flow rate. A semi-log plot was used to give an indication of the possible exponential dependence of the transmission on the UF_6 mass flow rate. In this case the UF_6 mass flow rate would be related to the concentration. The product of absorption coefficient, concentration, and optical path length forms the exponent in the relationship with transmission. Post-test calibration indicated the transmission returned to approximately the initial value, thus confirming the observation of minimum wall coating. Figure 106 is a photograph showing a typical rf plasma with pure UF_6 injection within the 1.2 MW rf induction heater.

These initial exploratory test results indicate promising techniques have been investigated for fluid-mechanical confinement of uranium in argon-confined high-temperature, high-pressure, rf-heated plasmas with pure UF_6 injection. Included has been the initial development of the associated handling and feeder techniques for steady-state injection of pure UF_6 into the rf plasma discharge. Various diagnostic techniques have also been initiated and applied to determine some of the uranium plasma characteristics and composition of the uranium compound wall deposition.

Based on these exploratory test results, continuing tests to further increase the quantity of uranium confined within the rf-heated argon plasma, while simultaneously minimizing deposition of the uranium compounds on the peripheral walls of the plasma test chamber combined with the associated diagnostics, is recommended; the results of these tests are described in the main portion of this report.

TABLE I

SUMMARY OF RANGE OF OPERATING CONDITIONS FOR RF PLASMA TESTS WITH CHORDAL SCAN MEASUREMENTS CONDUCTED IN 1.2 MW RF INDUCTION HEATER WITH PURE UF_6 INJECTION

See Fig. 8 for Sketch of Test Chamber Configuration
See Fig. 13 for Schematic of Diagnostic System Used for Chordal Scan Measurements
See Figs. 16 Through 19 for Examples of Measurement Results

Argon Injection Mass Flow Rate.	2.45-2.58 g/s
Argon Injection Velocity.	19.4-21.6 m/s
Percent Axial Bypass Flow	35-48
UF_6 Injection Mass Flow Rate.	$9\text{x}10^{-3}$-$3.2\text{x}10^{-2}$ g/s
UF_6 Injection Velocity.	0.2-0.7 m/s
Mass Ratio.	0.004-0.012
Chamber Pressure.	1.7-1.95 atm
RF Discharge Power.	47-58 kW
RF Operating Frequency.	5.4190-5.4270 MHz
Power Radiated (220-1300 nm).	15.1-19.5 kW
Fraction of Total Discharge Power Radiated.	0.29-0.34
Discharge Diameter at Axial Midplane.	2.6-2.8 cm
Test Time	2 min
Residue Deposition.	4.3-8.1 mg

TABLE II

SUMMARY OF OPERATING CONDITIONS FOR CHORDAL SCAN MEASUREMENTS OF TEST V CONDUCTED IN 1.2 MW RF INDUCTION HEATER WITH RF PLASMA AND PURE UF_6 INJECTION

See Fig. 8 for Sketch of Test Chamber Configuration

See Fig. 7 for Schematic of Diagnostic System Used for Chordal Scan Measurements

Argon Injection Mass Flow Rate	2.58 g/s
Argon Injection Velocity	21.6 m/s
Percent Axial Bypass Flow	48
UF_6 Injection Mass Flow Rate	3.2×10^{-2} g/s
UF_6 Injection Velocity	0.7 m/s
Mass Ratio	0.012
Chamber Pressure	1.95 atm
RF Discharge Power	58 kW
RF Operating Frequency	5.4210 MHz
Power Radiated (220-1300 nm)	19.5 kW
Fraction of Total Discharge Power Radiated	0.34
Discharge Diameter at Axial Midplane	2.8 cm
Test Time	2 min
Residue Deposition	8.1 mg

TABLE III

SUMMARY OF RF PLASMA TEST SERIES WITH PURE UF_6 INJECTION CONDUCTED IN 1.2 MW RF INDUCTION HEATER AND INCORPORATING DIFFERENT MODIFICATIONS TO TEST CHAMBER AND FLOW CONTROL SCHEMES

All Tests Conducted for 5 Minutes
Unloaded Resonator Frequency $f_u \approx 5.4180$ MHZ

Test No	Configuration and Flow Control Scheme	RF Operating Frequency, f-MHz	Argon Injection Mass Flow Rate, $\dot{m}_{Ar}$-g/s	Percent Axial Bypass Flow	Argon Injection Velocity, $\bar{V}_{Ar}$-m/s	UF_6 Injection Mass Flow Rate, m_{UF_6}-g/s	UF_6 Injection Velocity, $\bar{V}_{UF_6}$-m/s	Mass Ratio, UF_6/Ar	RF Discharge Power, Q_T-kW	Chamber Pressure, P_c-atm	Power Radiated in (220-1300nm) Band, Q_R-kW	Fraction of Total Discharge Power Radiated, Q_R/Q_T	Discharge Diameter at Axial Midplane, d-cm	Weight of Residue Deposited on Fused-Silica Tube, W-mg	I/I_o Absorption Measurement Using 591.54 nm Line at Axial Midplane on-Axis Location
1	See Fig.8 for general configuration, UF_6 injector tip located 2 cm from endwall - 0.24-cm-ID argon vortex injectors - 0.17-cm-ID UF_6 injector - 10 cm axial distance between endwalls	5.4250	3.22	35.4	27.05	0.02	0.41	0.006	47.1	1.95	14.8	0.31	2.85	18.1	0.67
2		5.4170	3.22	35.4	27.05	0.02	0.41	0.006	44.2	1.95	13.7	0.31	2.80	17.6	0.69
3		5.4317	3.22	35.4	27.05	0.02	0.41	0.006	44.7	1.95	13.6	0.30	2.90	18.4	0.65
4		5.4200	3.41	28.7	27.74	0.03	0.62	0.009	62.1	2.00	20.4	0.33	3.05	12.7	0.54
5		5.4243	3.27	18.3	28.88	0.04	0.83	0.012	54.7	1.85	18.3	0.33	2.95	18.0	0.41
6		5.4317	3.41	43.1	31.75	0.02	0.41	0.006	51.3	1.70	16.2	0.32	2.90	13.3	0.68
7		5.4302	3.60	52.2	33.87	0.03	0.62	0.008	47.7	1.75	15.1	0.32	3.00	17.0	0.56
8	Annular cooling water flow rate reduced 10x from 1 1ℓ/s to 1 11ℓ/s	5.4317	3.41	12.0	30.07	0.02	0.41	0.006	52.6	1.85	16.7	0.32	2.95	38.9	0.70
9	Argon vortex injectors 0.17-cm-ID, UF_6 injector tip located 2-cm from endwall	5.4304	2.45	42.4	58.78	0.02	0.41	0.008	43.9	1.40	13.3	0.30	3.00	22.1	0.67
10	Argon vortex injectors 0.17-cm-ID, UF_6 injector tip located 1-cm from endwall	5.4304	2.68	28.4	59.95	0.03	0.62	0.011	45.8	1.45	14.8	0.32	2.95	14.6	0.52
11	Argon vortex injectors 0.17-cm-ID, UF_6 injector tip located flush with endwall	5.4250	2.68	19.4	52.89	0.05	1.04	0.018	40.5	1.65	12.8	0.32	3.10	15.0	0.36

TABLE IV

SUMMARY OF LONG RUN TIME TESTS CONDUCTED IN 1.2 MW RF INDUCTION HEATER WITH RF PLASMA AND PURE UF_6 INJECTION

(Attempts were made to keep all operating conditions approximately the same for all tests. See Figs. 34 and 35 for photographs of fused-silica tubes after tests.)

Argon Injection Mass Flow Rate	2.63 g/s
Argon Injection Velocity	42.9 m/s
Percent Axial Bypass Flow	19
UF_6 Injection Mass Flow Rate	2.2×10^{-2} g/s
UF_6 Injection Velocity	0.6 m/s
Mass Ratio	0.008
Chamber Pressure	1.75 atm
RF Discharge Power	44 kW
RF Operating Frequency	5.4304 MHz
Power Radiated (220-1300 nm)	13.7 kW
Fraction of Total Discharge Power Radiated	0.31
Discharge Diameter at Axial Midplane	3.1 cm
Range of Test Time	5-41.5 Min*
Range of Residue Deposition	12.7-35.7 mg

---

*41.5 minute test was terminated due to cracking of Mycalex (Super 500) radiation/electric insulation shield located on vacuum capacitors in resonator section. Cause attributed to excessive sustained radiation loading.

TABLE V

SUMMARY OF OPERATING CONDITIONS FOR TEST CONDUCTED IN 1.2 MW RF INDUCTION HEATER WITH RF PLASMA AND MAXIMUM PURE UF_6 INJECTION FLOW RATE

(See Fig. 42 for Photograph of Fused-Silica Tube and O-Rings After Test)

Argon Injection Mass Flow Rate	2.45 g/s
Argon Injection Velocity	40 m/s
Percent Axial Bypass Flow	0.37
UF_6 Injection Mass Flow Rate	0.21 g/s
UF_6 Injection Velocity	2.7 m/s
Mass Ratio	0.09
Chamber Pressure	2 atm
RF Discharge Power	67 kW
RF Operating Frequency	5.4200 MHz
Power Radiated (220-1300 nm)	21.8 kW*
Fraction of Total Discharge Power Radiated	0.325*
Discharge Diameter at Axial Midplane	3.3 cm*
Test Time	1.2 Min
Residue Deposition	134.7 mg

*Exact determination difficult since discharge was displaced away from central location of test chamber.

TABLE VI

SUMMARY OF MATERIAL SAMPLES USED IN IR SPECTROPHOTOMETRIC ANALYSIS

Sample	Available Within UTRC	IR Spectrum Completed	Displays Distinguishable Spectrum
KBr	Yes	Yes	Standard Blank - No Charac.
Silicone Grease	Yes	Yes	Yes
$SiO_2 \cdot xH_2O$	Yes	Yes	Yes
Kel-F oil	Yes	Yes	Yes
Silicon O-ring Decomposition Products	Yes	Yes	Yes
U	Yes	No (Thin Film Technique Could be Used)	-
UO	No	No	-
UO_2	Yes	Yes	No
UO_3-amorphous	Yes	Yes	Yes
αUO_3-hexagonal	Yes	Yes	Yes } Difficulty in Determining Crystalline Structure.
ϵUO_3-monoclinic	Yes	Yes	Yes
γUO_3-monoclinic	Yes	Yes	Yes
UO_4 (Laboratory Prepared)	Yes	Yes	Yes
U_3O_8	Yes	Yes	Yes
U_4O_9	No	No	-
Cu	Yes	No (Thin Film Technique Could be Used)	-
CuF_2	Yes	Yes	Yes
UF_4	Yes	Yes	No
UF_5	No	No	-
U_2F_9	No	No	-
$UO_2Cl(UO_2^+)$	Yes (Trace Quantities Only)	Yes	Yes
$UO_2F_2(UO_2^{++})$	Yes	Yes	Yes

TABLE VI (Concluded)

Sample		Available Within UTRC	IR Spectrum Completed	Displays Distinguishable Spectrum
UCl_3	(UF_3 unavailable but similar in charac.)	Yes	No	- -
UC		Yes	Yes	No
UC_2		Yes	Yes	No
UN		Yes	Yes	No
U_2N_3		Yes	Yes	No
U_3N_4		Yes	Yes	No
USi_2		Yes	Yes	No

TABLE VII

PHYSICAL, THERMAL, ELECTRICAL, AND OPTICAL PROPERTIES OF FUSED-SILICA TUBES USED IN UF_6 RF PLASMA EXPERIMANTS

Density.	2.2 g/cc
Hardness	6 Mohs'
Thermal coefficient of expansion*.	5.5×10^{-7} C^{-1}(20 C-1000 C)
Thermal conductivity	3.2×10^{-3} cal/cm^2/s/C/cm
Specific heat.	0.175 cal/g C
Thermal diffusivity.	8.5×10^{-3} cm^2/s
Tensile strength	4.8×10^2 atm
Compressive strength	10^4 atm
Young's modulus at 20 C.	7.2×10^5 atm
Bulk modulus at 20 C	3.8×10^5 atm
Shear modulus at 20 C.	3.1×10^5 atm
Poisson's ratio.	0.14
Dielectric strength.	410 V/mil at 50 C/MHz
Dielectric loss factor	$< 4 \times 10^{-4}$ at 20 C/MHz
Dielectric constant.	3.8 at 20 C/MHz
Strain point	1070 C appx.
Annealing point.	1140 C appx.
Softening point.	1670 C appx.
Fusing point	1750 C appx.
Index of refraction.	1.45845
Optical transmission	See Fig. 10
Resistance to corrosion.	Not affected by most pure molten metals or by any acid except hydrofluoric at all temperatures and phosphoric above 400 C

*Low coefficient of expansion makes fused-silica tubes highly resistant to most severe thermal shock.

TABLE VIII

SUMMARY OF SPECTROCHEMICAL ANALYSIS OF FUSED SILICA AS USED IN RF PLASMA TESTS WITH PURE UF_6 INJECTION

Analysis Conducted Prior to Hot Flow Tests

	Concentration - ppm		
Impurity Constituent	Mass Spectrometer Data Supplied by U.S. Fused Quartz Corp.	Analytical Results Obtained at UTRC Using Small Sample Provided by U.S. Fused Quartz Corp.	Analytical Results Obtained at UTRC Using Actual 57-mm-ID x 61-mm-OD Tube of Test Chamber
Fe_2O_3	5	< 4	< 3
CaO	12	<50	< 30
Na_2O	4	6	4
B_2O_3	-	8	3
Al_2O_3	< 50	11	9
MgO	2	< 2	< 3
PbO	-	20	6
NiO	-	0.05	0.4
CuO	-	< 0.2	0.3
Li_2O	1	3.6	2.4
TiO_2	2	< 0.5	< 0.5
K_2O	4	< 1.2	< 1.2
As	0.08	< 10	< 10
P	nondetectable	< 100	< 100
Zr_2O_3	3	< 1	< 1
Ca	0.2	-	-
B	0.5	-	-

TABLE IX

PROPERTIES AND ASSAY OF AS - RECEIVED UF_6
(This Analysis Was Performed on Samples Removed in The Liquid and Homogeneous State)

Vapor pressure of vessel at 96 C	4 atm abs.
Minimum weight percent of UF_6 in material	99.98
Maximum mole percent hydrocarbons, chlorocarbons, and partially substituted halohydrocarbons	Nil
Number of parts of elements indicated per million parts of total uranium	
Antimony	< 0.7
Bromine	< 5.0
Chlorine	< 5.0
Niobium	< 0.1
Phosphorus	< 12.0
Ruthenium	< 0.7
Silicon	< 3.0
Tantalum	< 0.7
Titanium	0.6
Total number of parts of elements forming nonvolatile fluorides, Having a vapor pressure of one atm or less at 300 C, per million parts of total uranium	< 83
Number of parts of elements or isotopes indicated per million parts of U-235	
Chromium	< 1200
Molybdenum	< 21
Tungsten	< 104
Vanadium	42
U-233	< 500
U-232	< 0.110
Thermal neutron absorption of total impurity elements as equivalent parts of boron per million parts of total uranium	< 1.7
Total of gamma activity due to fission products and U-237 as percent of gamma activity of aged natural uranium	< 20
Beta activity due to fission products as percent of Beta activity of aged natural uranium	< 10
Alpha activity from all transuranic elements in disintegrations per minute per gram of total uranium	< 1500

TABLE X

SUMMARY OF TEST CONDITIONS FOR SMALL-SCALE FUSED-SILICA VESSELS (350 cc) USED WITH GRAM QUANTITIES OF UF_6 IN LABORATORY TESTS

See Fig. 82 for Post-Test Photographs of Vessels

Test Case	Prefill Evacuation	Gms UF_6 Transferred	UF_6 Pretreatment	Vessel Pre-Bakeout	Stop-Cock Sealant	Heating Temperature for 1 Hour	Post-Heating Room Temp. Soak Time
I	10^{-4} mm Hg	0.9	as-received	No	Silicone grease	330 K	72 hrs.
II	10^{-4} mm Hg	0.9	filtered	No	Kel-F oil	330 K	72 hrs.
III	10^{-4} mm Hg	1.2	filtered	Yes	Silicone grease	330 K	72 hrs.
IV	10^{-4} mm Hg	0.9	filtered	Yes	Kel-F oil	330 K	72 hrs.

TABLE XI

CATALOGED LIST OF (EIGHT) STRONGEST LINES OF POSSIBLE REACTANTS/COMPOUNDS AND ASSOCIATED LINE SPACINGS

Data Taken From American Society of Testing Materials X-ray Card File

Compound	ASTM X-ray Card File No.	d-spacing, Å							
U	11-628	2.93	2.56	2.52	2.48	2.28	1.78	1.53	
UO	17-659	2.83	2.46	1.74	1.48	1.42			
UO_2	5-0550	3.157	2.735	1.934	1.649	1.579			
αUO_3	12-43	4.17	3.44	2.65	1.98	1.78	1.71	1.58	1.32
UO_3	15-201	4.98	3.45	3.26	(Also documented is 18-1429; 4.13, 3.46, 3.29)				
αU_3O_8	8-244	4.10	3.37	2.61	2.21	1.95	1.76	1.69	1.56
U_3O_8	23-1460	4.15	3.53	2.60	(also documented 23-1345; 4.15, 3.53, 2.60)				
U_4O_9	20-1344	3.14	2.721	1.92	1.64	1.248	1.047	0.919	
UF_3	9-339	3.67	3.58	3.21	2.06	2.02	1.80	1.74	1.44
UF_4	12-701	7.52	6.63	4.21	4.18	3.95	3.72	3.55	3.29
UF_5	4-447	5.66	4.68	3.62	3.61	2.44	2.35	2.08	1.96
UF_6	9-166	5.20	4.51	4.34	4.10	3.80	3.22	2.67	2.56
U_2F_9	4-860	4.15	3.42	1.98	1.79	1.65	1.45	1.40	1.37
UO_2F_2	4-833	5.22	3.53	3.29	2.09	1.94	1.80	1.63	1.37
*UO_2F_2	4-230	5.18	3.51	3.21	2.60	2.10	1.95	1.80	1.78
UC	9-214	2.87	2.47	1.75	1.49	1.43	1.13	1.11	1.01
UC_2	6-372	3.04	2.98	2.49	1.91	1.77	1.73	1.53	1.24
U_2C_3	6-709	3.29	2.85	2.55	1.58	1.47	1.09	1.07	1.02
UN	11-315	2.81	2.44	1.72	1.47	1.12	1.09	0.99	0.94
UN_2	10-93	3.02	2.62	1.86	1.59	1.22	1.19	1.02	0.89
U_2N_3	15-426	4.34	3.08	2.66	1.88	1.61	1.53	1.22	1.19
CU	4-0836	2.08	1.87	1.27	1.09	1.04	0.90	0.85	0.81

α - Hexagonal
* - Rhombohedral

TABLE XII

SUMMARY OF EXPLORATORY TESTS CONDUCTED IN 80-KW RF INDUCTION HEATER USING ARGON BUFFER GAS AND PURE UF_6 INJECTION

Test Chamber 5.7-cm-ID x 10-cm-long
on-axis UF_6 injection (flush to 3 cm into chamber)

Test Chamber Configuration and Flow Control Scheme	Range of Test Conditions (all tests conducted at operating frequency of 13.56 MHz)	No. of Tests	Comments
Single endwall driven vortex injection Combination of on-axis thru-flow (both ends) and single axial bypass exhaust * See Fig. 91(a).	Argon mass flow rate 0.15-1.5 g/s UF_6 mass flow rate 0.005-0.04 g/s*** Chamber pressure 1-1.2 atm Axial bypass flow 0-100% On-axis thru-flow 0-100% RF discharge power 2-15 kW Discharge diameter 3.8-5.5 cm	16	Relatively high UF_6 flow rates obtained with light coating on central region of peripheral wall Well confined, stable discharge over wide range of test conditions.
Coaxial flow endwall argon injection, bluff body stabilization. Combination of on-axis thru-flow (both ends) and single axial bypass exhaust. See Fig. 91(b).	Argon mass flow rate 0.010-2.1 g/s UF_6 mass flow rate 0.005-0.03 g/s Chamber pressure 1 atm Axial bypass flow 0-100% On-axis thru-flow 0-100% RF discharge power 2-11 kW Discharge diameter 4.5-5.5 cm	8	Central region and extremities of peripheral wall became heavily coated in all tests. Ellipsoidially-shaped discharge extending close to peripheral wall Discharge sensitive to changes in argon/UF_6 mass flow rate. Difficult to tune rf load during UF_6 injection.
Symmetrical endwall driven vortex injection. No on-axis thru-flow. Symmetrical large radius exhaust annuli. See Fig. 91(c).	Argon mass flow rate 0.10-1.5 g/s UF_6 mass flow rate 0.005-0.035 g/s Chamber pressure 1 atm RF discharge power 2-15 kW Discharge diameter 4-5.5 cm	10	Central region became moderately coated in all tests. Discharge sensitive to changes in argon/UF_6 mass flow rate Retuning load required during UF_6 injection to eliminate extinguishment. Occasional discharge oscillation noted.
Peripheral wall driven vortex injection** (endwall augmentation used in some tests). See Fig. 91(d).	Argon mass flow rate 0.08-0.2 g/s UF_6 mass flow rate 0.005-0.03 g/s Chamber pressure 1 atm Axial bypass flow 0-100% On-axis thru-flow 0-100% RF discharge power 2-8 kW Discharge diameter 4.5-5.5 cm	5	Entire peripheral wall became heavily coated Apparent turbulence noted along discharge boundary. Flow control limited due to fixed vortex injector area. Excessive heating of peripheral wall occurred.

*Test configuration and flow control scheme selected for follow-on tests in 1.2 MW rf induction heater system.
**The peripheral wall injection flow control scheme was used with both the first and third test chamber configurations.
***Estimate based on UF_6 canister weighing before and after test

TABLE XIII

SUMMARY OF RF PLASMA EXPLORATORY TESTS CONDUCTED IN 1.2-MW RF INDUCTION HEATER USING ARGON BUFFER GAS AND PURE UF_6 INJECTION

See Fig. 92 for Sketch of Basic Test Configuration
On-Axis UF_6 Injection From One Endwall Only

Test Chamber Configuration and Flow Control Scheme	Range of Test Conditions		
Dual Endwall Driven Vortex Injection On-Axis Thru-Flow (Both Endwalls) No Axial Bypass	Argon Mass Flow Rate	1.8 - 3.4	g/s
	On-Axis Thru-Flow Through One Endwall	0 - 25	%
	RF Discharge Power	20 - 60	kW
	Range of RF Operating Frequency	5.4700 - 5.5000	MHz
	Discharge Diameter	2.5 - 3.1	cm
	Chamber Pressure	2 - 12	atm
	UF_6 Mass Flow Rate	0.008 - 0.13	g/s
	Test Time	0.17 - 10	min
Single Endwall Driven Vortex Injection On-Axis Thru-Flow (One Endwall Only Opposite Vortex Drive) Single Axial Bypass (Endwall Opposite Vortex Drive)	Argon Mass Flow Rate	2.2 - 3.85	g/s
	Axial Bypass Flow	0 - 52	%
	RF Discharge Power	30 - 85	kW
	Range of RF Operating Frequency	5.4778 - 5.4878	MHz
	Discharge Diameter	2.3 - 3.3	cm
	Chamber Pressure	2 - 5	atm
	UF_6 Mass Flow Rate	0.013 - 0.131	g/s
	Test Time	0.25 - 10	min

TABLE XIV

SUMMARY OF ANALYSIS OF RESIDUE SAMPLES TAKEN FROM INSIDE OF FUSED-SILICA TUBES AFTER RF PLASMA EXPLORATORY TESTS WITH PURE UF_6 INJECTION

Total of 10 Tubes Analyzed

See Fig. 99 for Photograph Showing Examples of Wall Coating

Analysis Technique	Compound or Element Present in Residue Sample		
	Green Color Sample	Rust Color Sample	Black Color Sample
Electron Diffraction	UF_4	UF_4	U_3O_8, UO_2, U_4O_9
X-Ray Diffraction	UF_4	UO_2, U_4O_9	U_3O_8, UO_3(hexagonal)
Electron Microprobe	U, F, Trace amnt. of O	U, O, F	U, O, F
IR Spectrophotometry	UO_2, UO_2F_2, SiO_2	UO_2F_2, SiO_2, UO_2	UO_2, SiO_2

FIG. 1

DETAILS OF PLASMA CORE REACTOR UNIT CELL

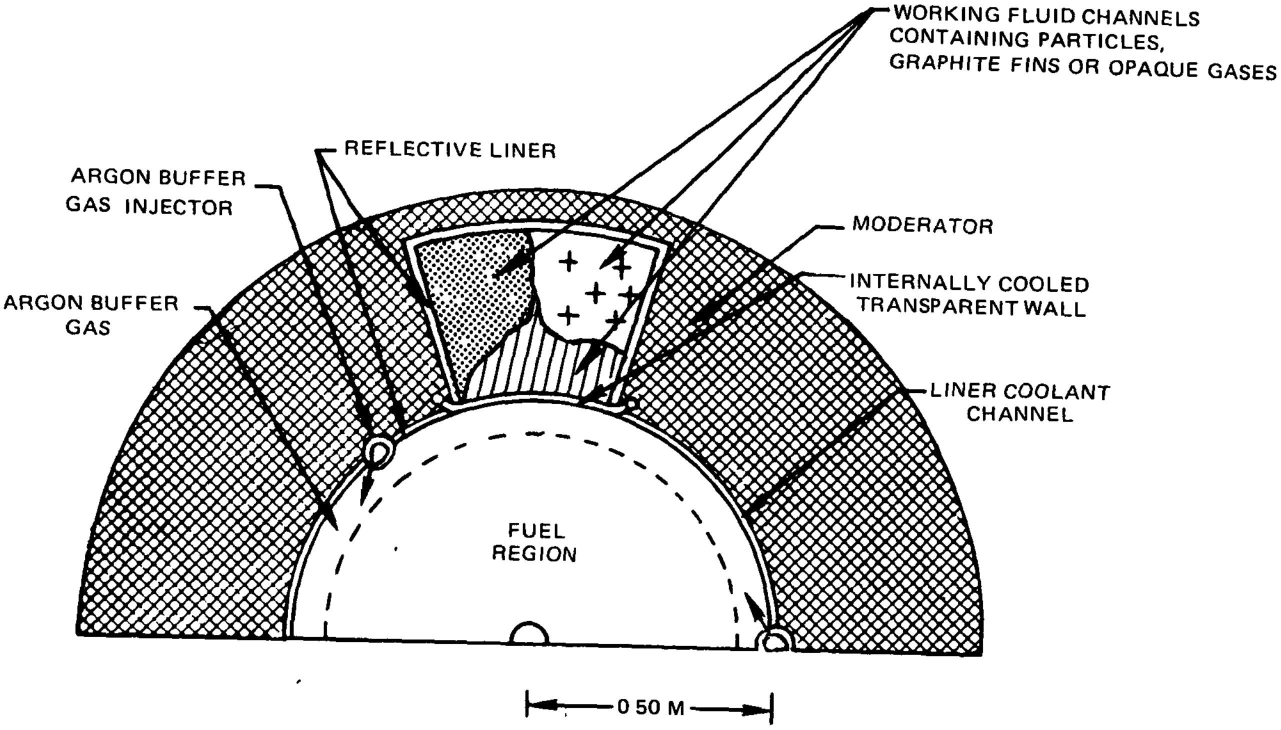

FIG. 2

BLOCK DIAGRAM OF UTRC 1.2 MW RF INDUCTION HEATER

OPERATING FREQUENCY = 5.4 MHz

POWER LEVELS SHOWN ARE MAXIMUM DESIGN VALUES

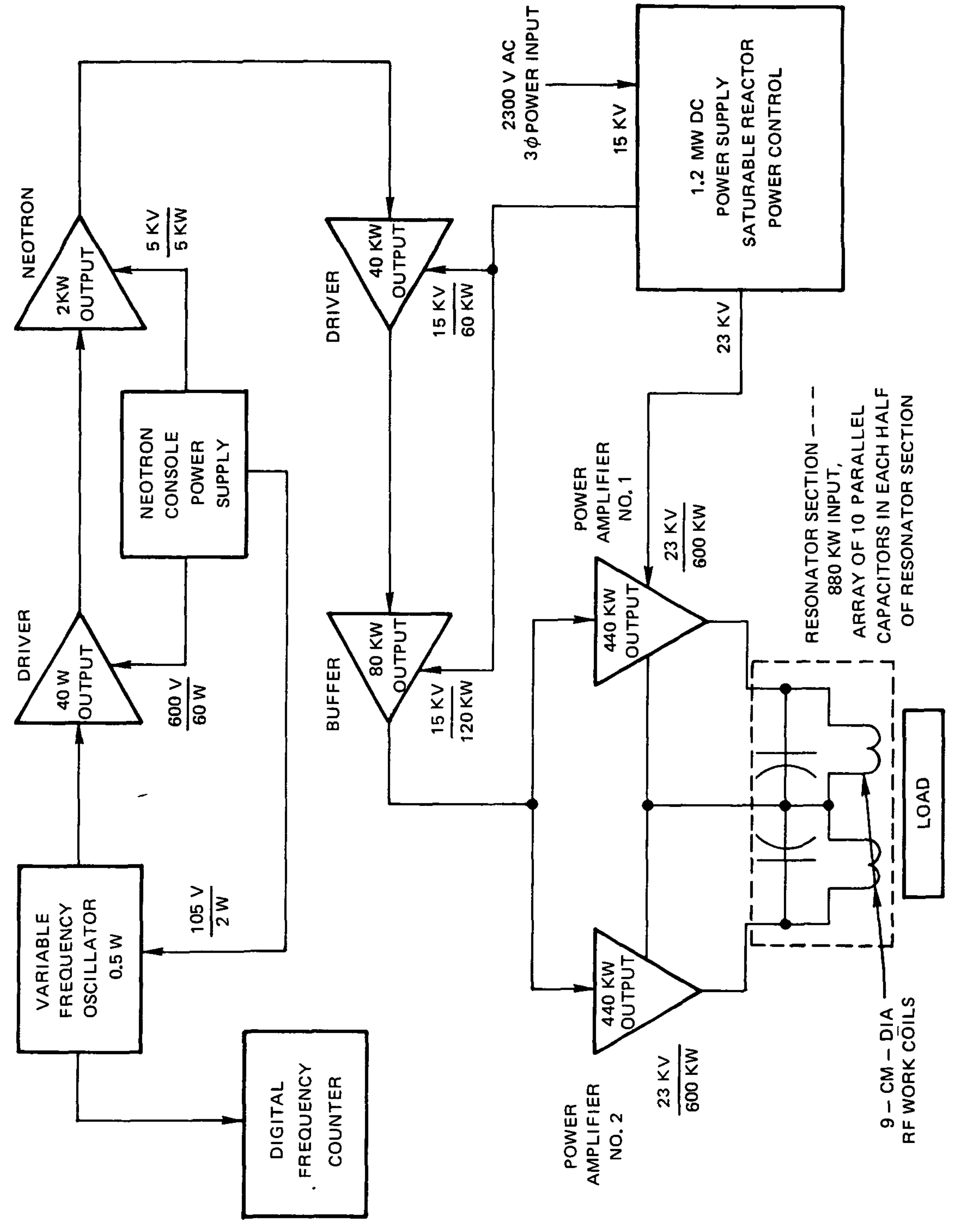

FIG. 3

PHOTOGRAPH OF TEST CHAMBER CONFIGURATION INSTALLED IN 1.2 MW RF INDUCTION HEATER

FRONT ALUMINUM DOME WITH VIEW PORTS REMOVED FOR CLARITY

TEST SECTION AXIAL DISTANCE – 10 CM

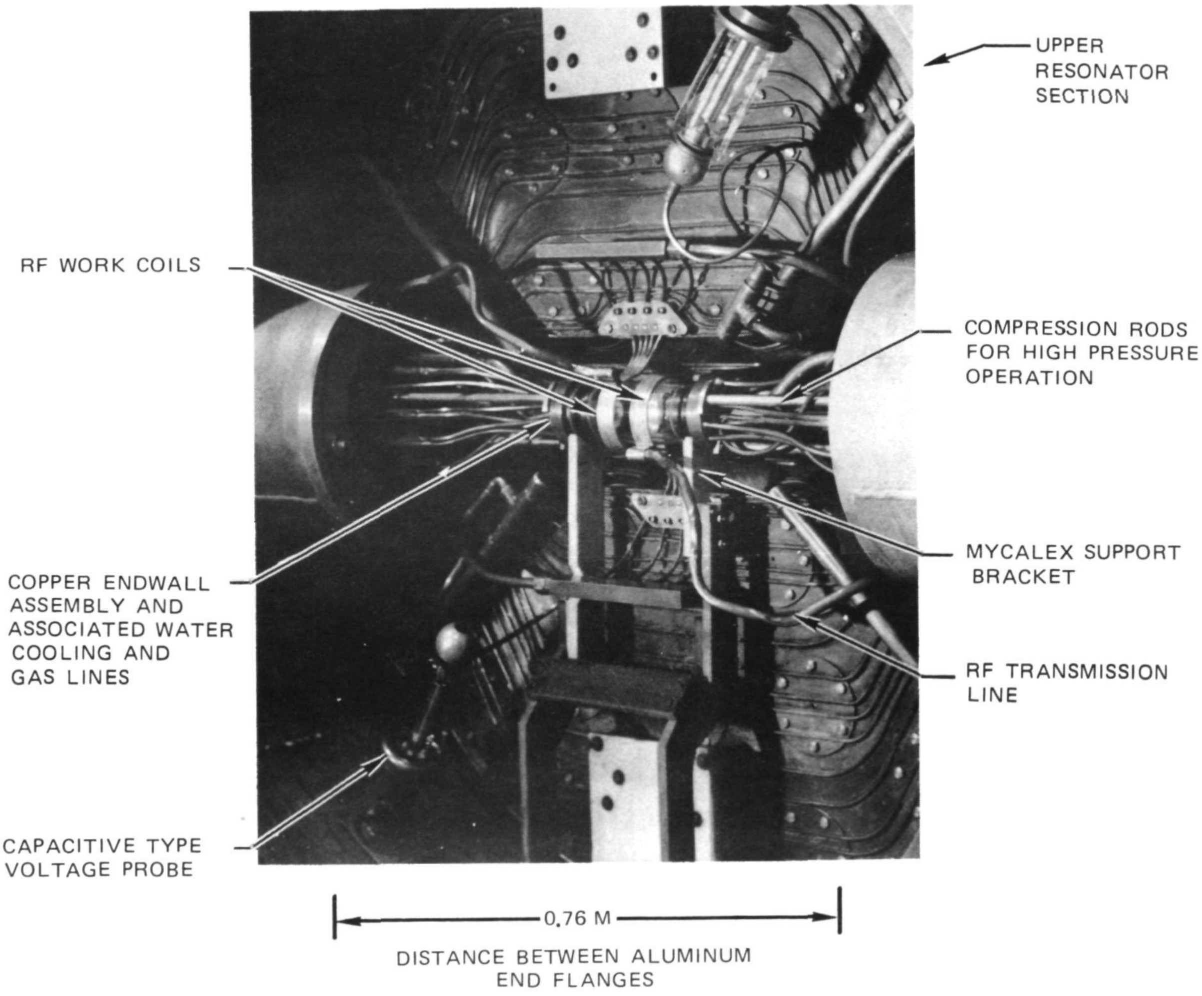

R06–185–6

FIG. 4

SCHEMATIC OF 1.2 MW RF INDUCTION HEATER GAS AND COOLING WATER FLOW SYSTEMS

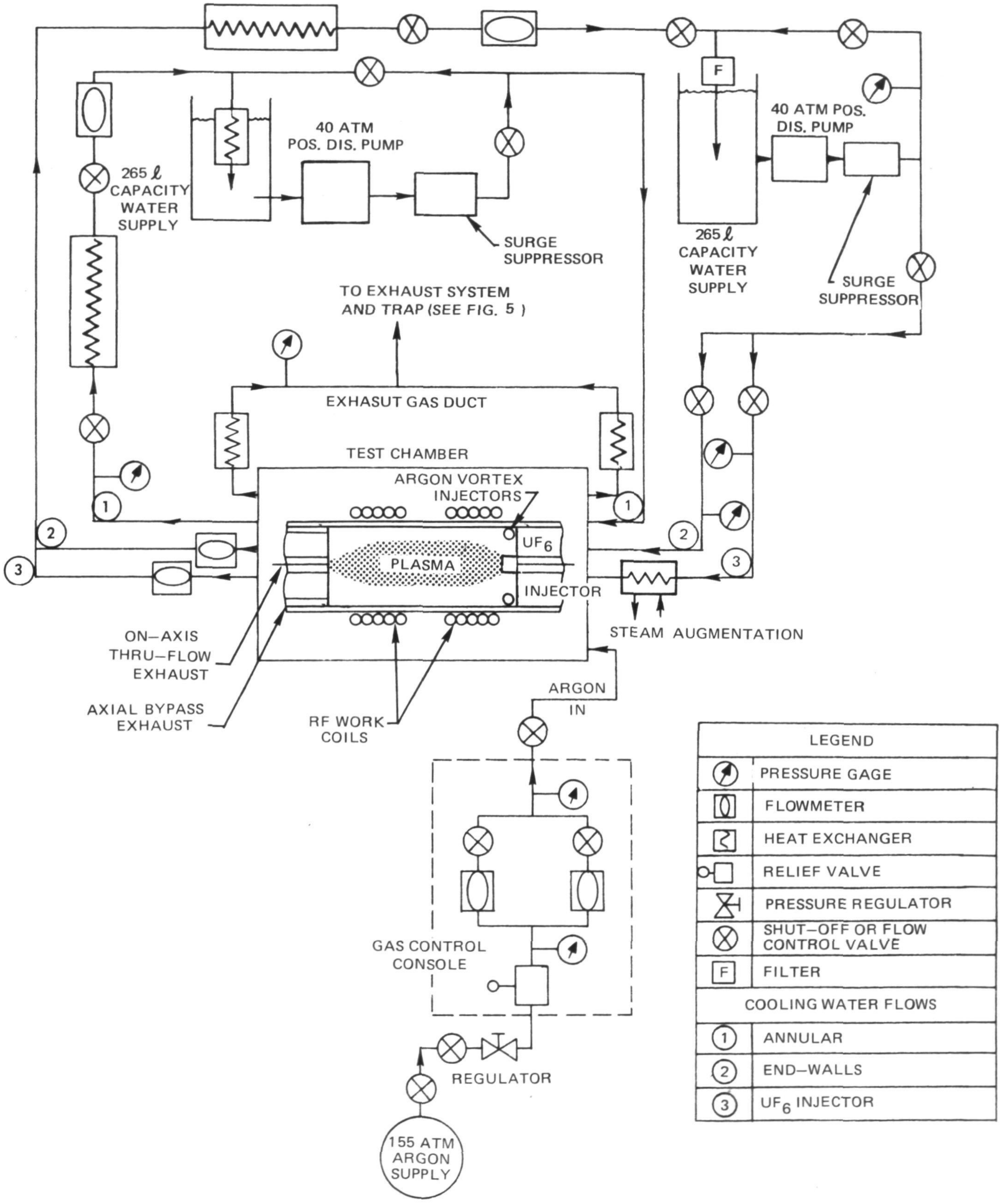

76–04–63–1

FIG. 5

SCHEMATIC DIAGRAM OF UF_6 TRANSFER SYSTEM

DESIGN POINT FLOW RATE = 5 G/S

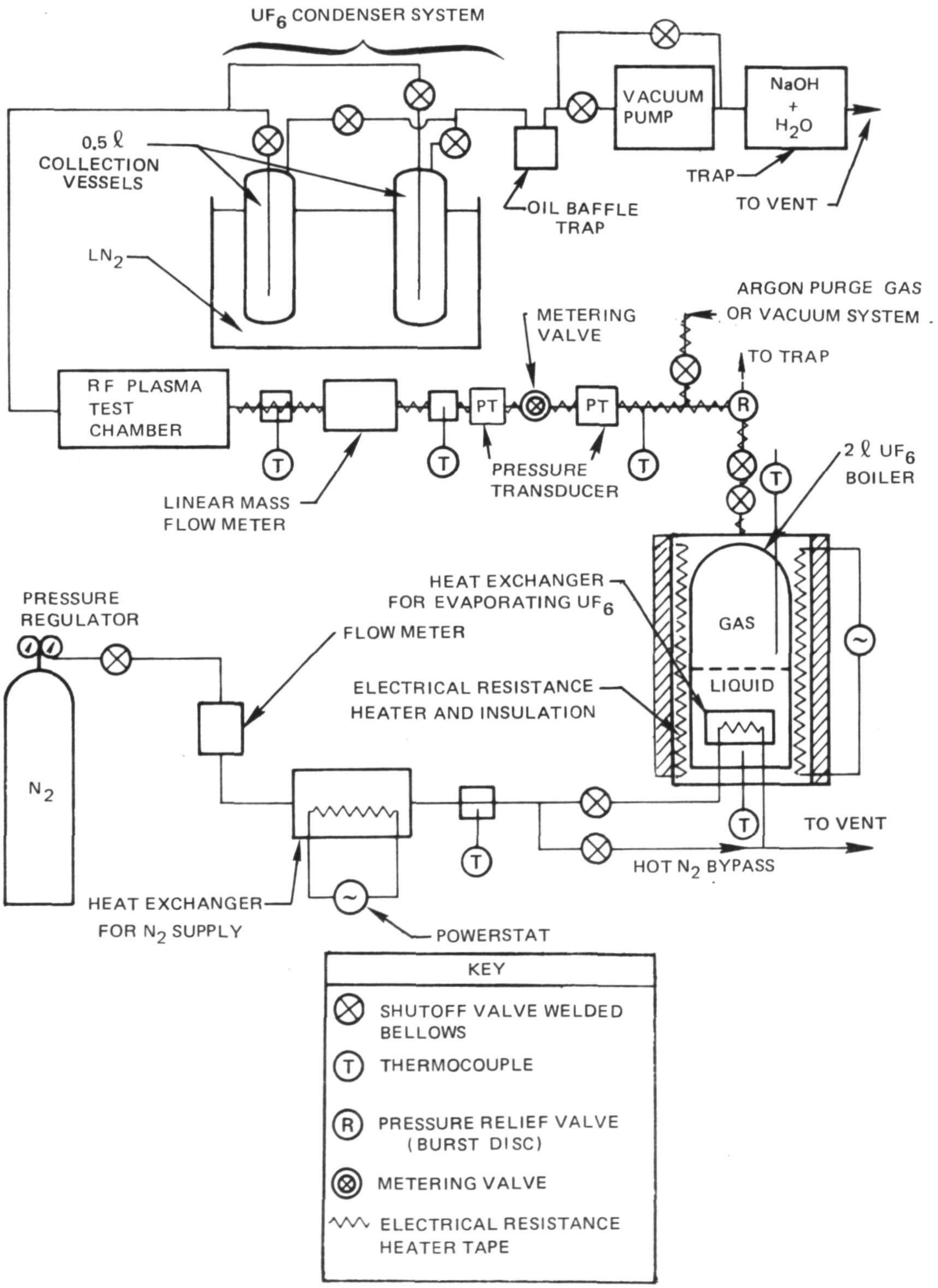

FIG. 6

VAPOR PRESSURE CURVE FOR UF_6

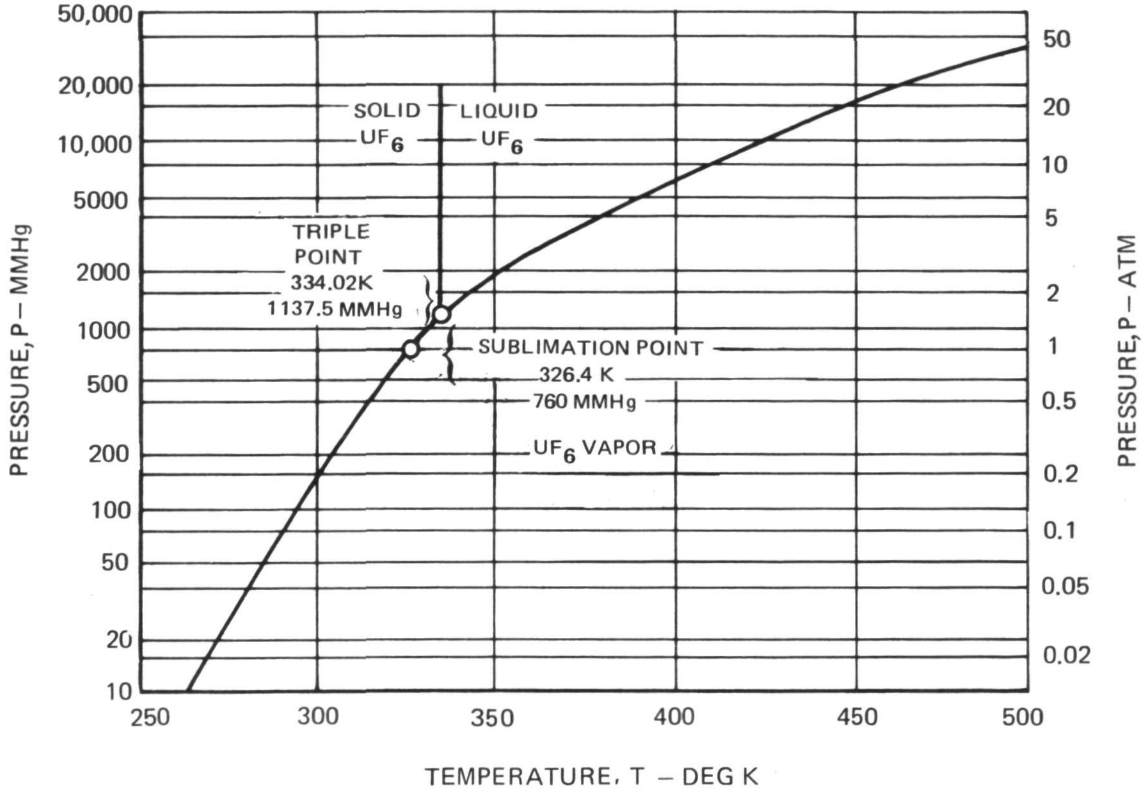

PHOTOGRAPH OF 1.2 MW RF PLASMA TEST TANK, UF_6 TRANSFER SYSTEM AND ASSOCIATED INSTRUMENTATION

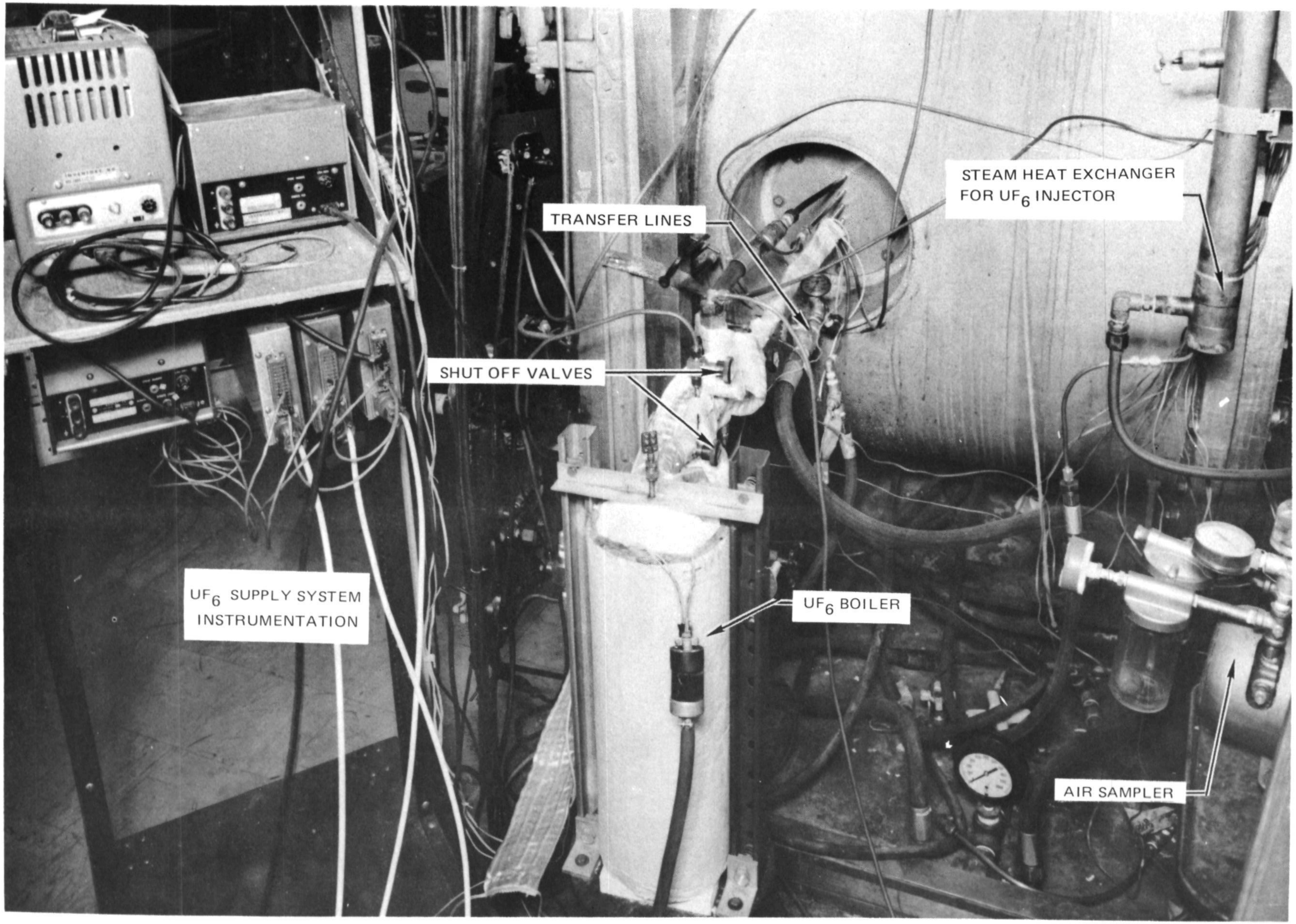

FIG. 7

SKETCH OF TEST CHAMBER CONFIGURATION USED IN TESTS IN 1.2 MW RF INDUCTION HEATER USING PURE UF_6 INJECTION

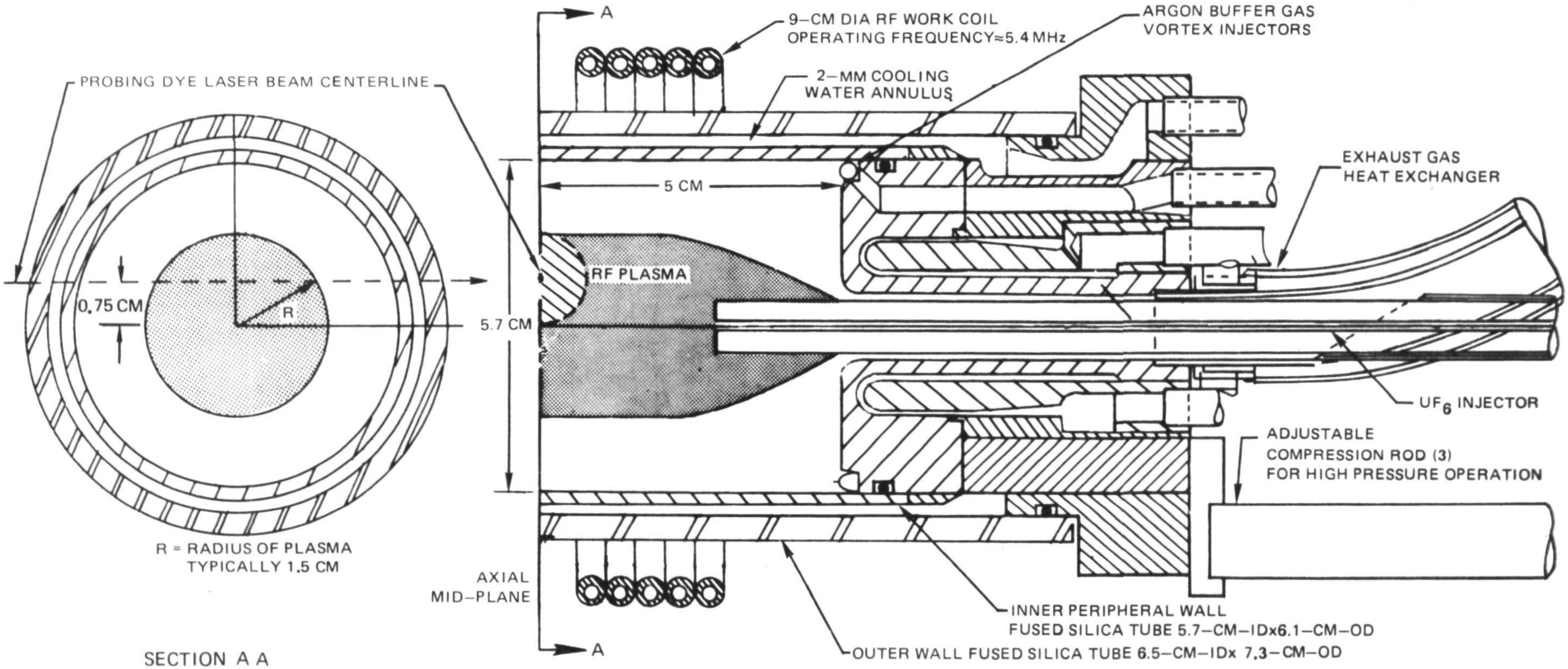

RO3–38–2

FIG. 8

FIG. 9

PHOTOGRAPHS SHOWING DETAILS OF TEST CHAMBER CONFIGURATION FOR UF_6 RF PLASMA TESTS

a) CLOSEUP VIEW OF 10–CM AXIAL LENGTH TEST CHAMBER – ALUMINUM FRONT COVER REMOVED

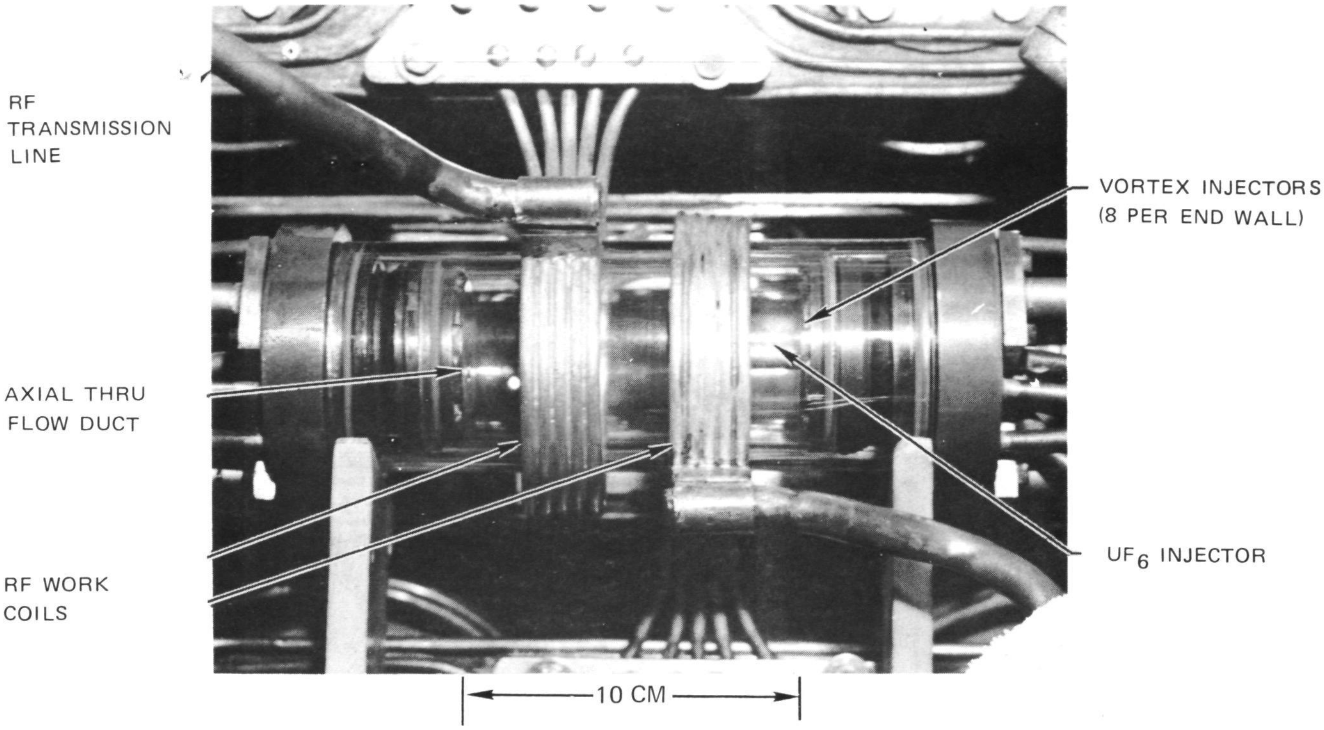

b) VIEW THROUGH CENTER VIEW PORT WITH ARGON RF PLASMA PRESENT (NO UF_6 INJECTION)

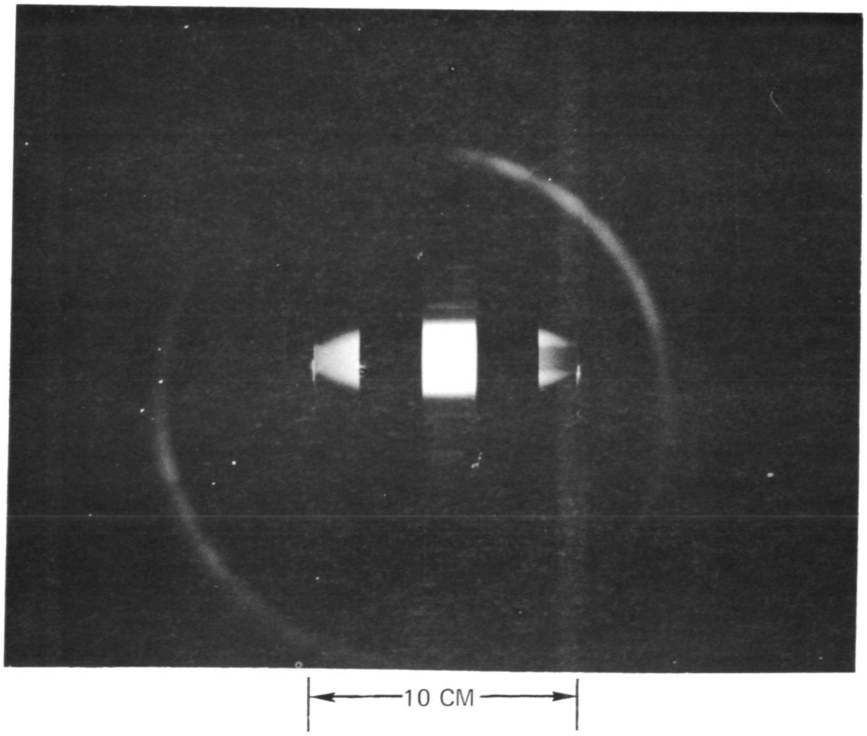

CHAMBER PRESSURE = 1 ATM DISCHARGE POWER = 20 KW

DISCHARGE DIAMETER = 3.1 CM

RADIOMETER OPTICAL SYSTEM

a) BLOCK DIAGRAM

b) TRANSMISSION CHARACTERISTICS

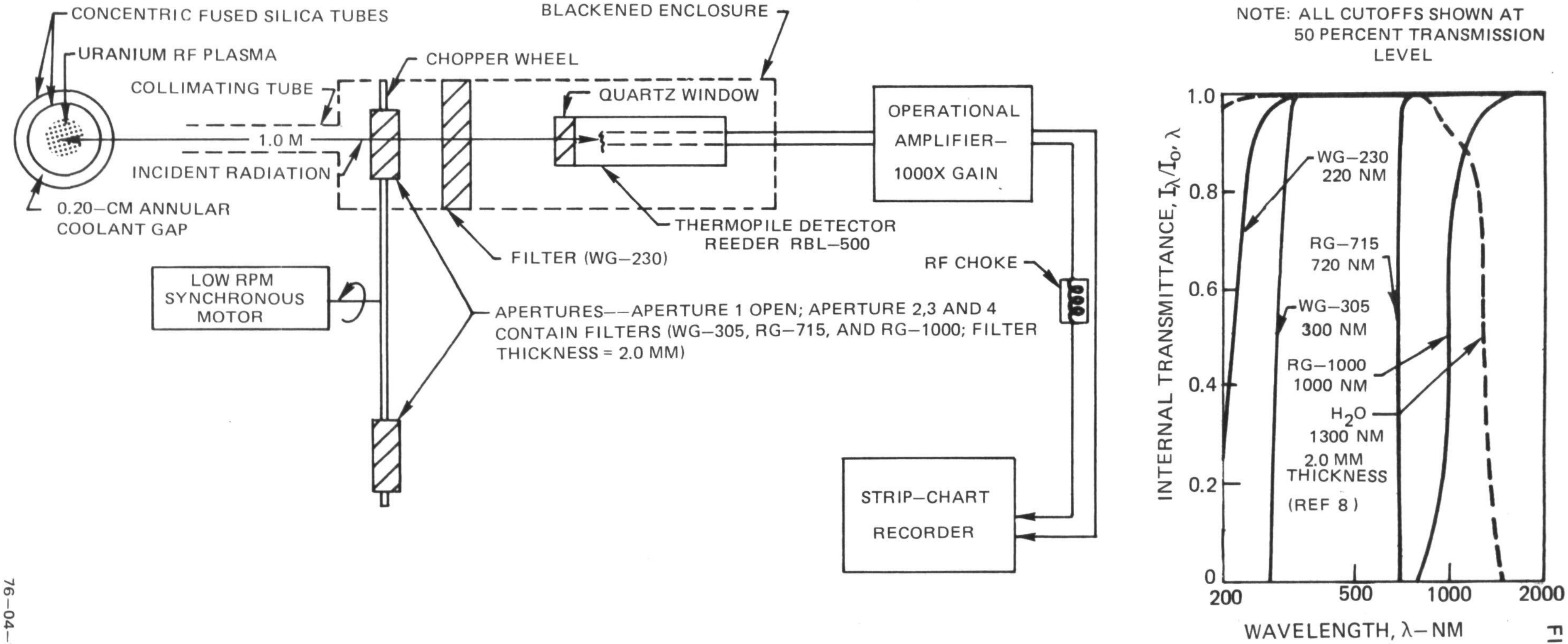

FIG. 10

76–04–99–1

FIG. 11

SCHEMATIC OF TUNABLE CW SINGLE–FREQUENCY DYE LASER

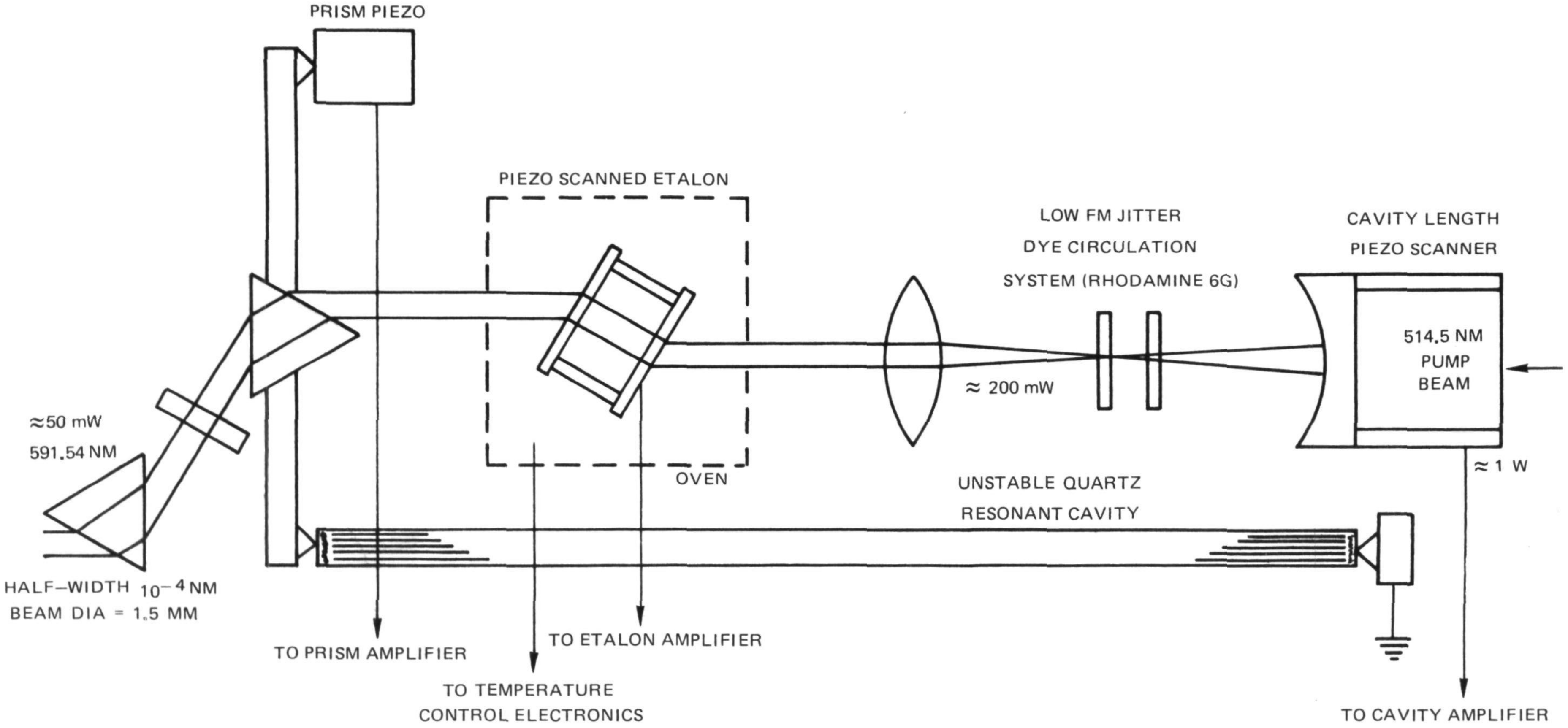

FIG. 12

PHOTOGRAPH OF DYE LASER SHOWING DETAILS OF INTERNAL COMPONENTS

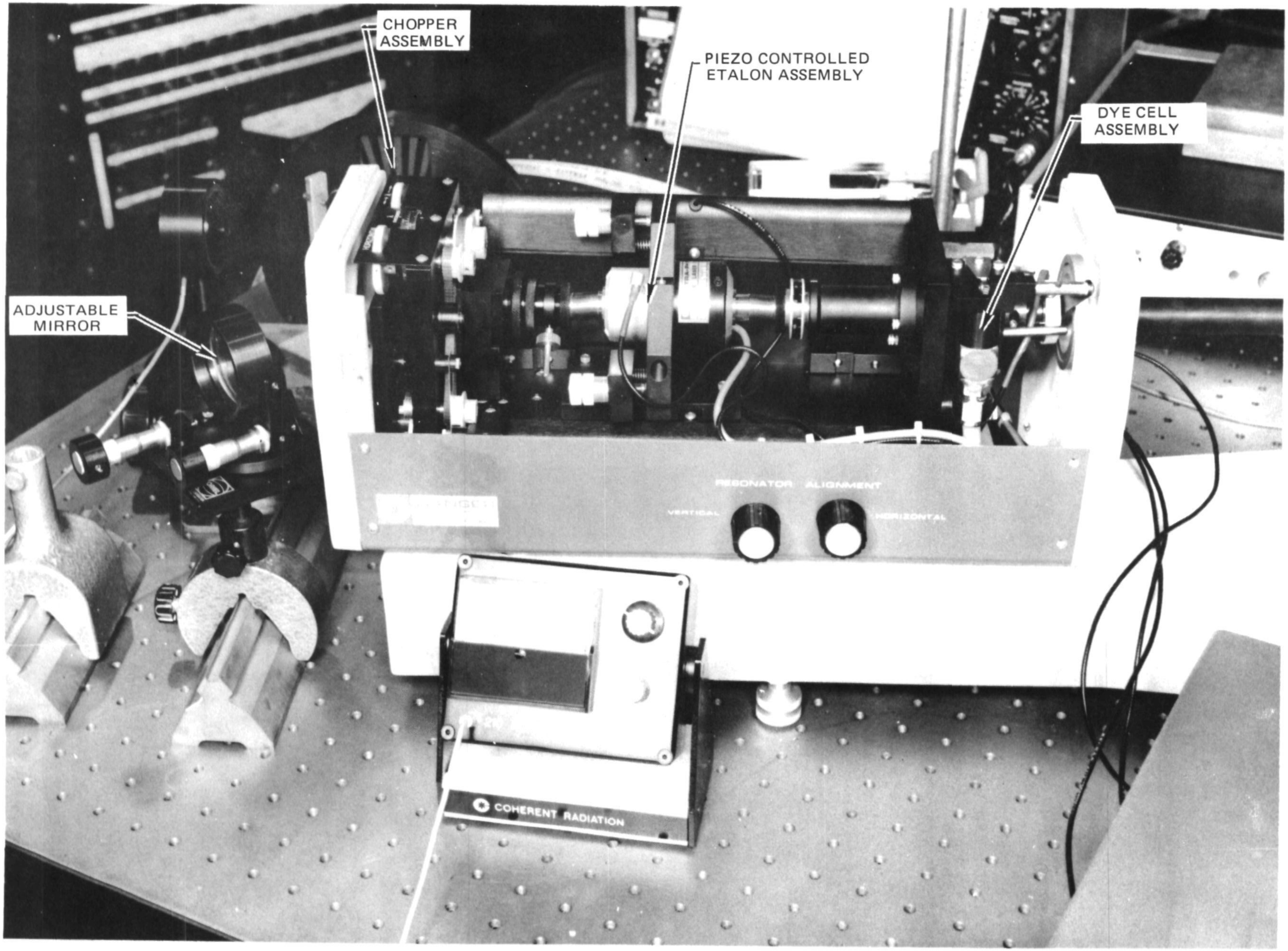

FIG. 13

SCHEMATIC OF OPTICAL DIAGNOSTIC SYSTEM USED FOR ABSORPTION AND EMISSION MEASUREMENTS IN RF PLASMA TESTS WITH PURE UF_6 INJECTION

SEE FIG. 14 FOR PHOTOGRAPH OF SYSTEM

SEE FIG. 8 FOR SKETCH OF TEST CHAMBER AND LASER BEAM LOCATION

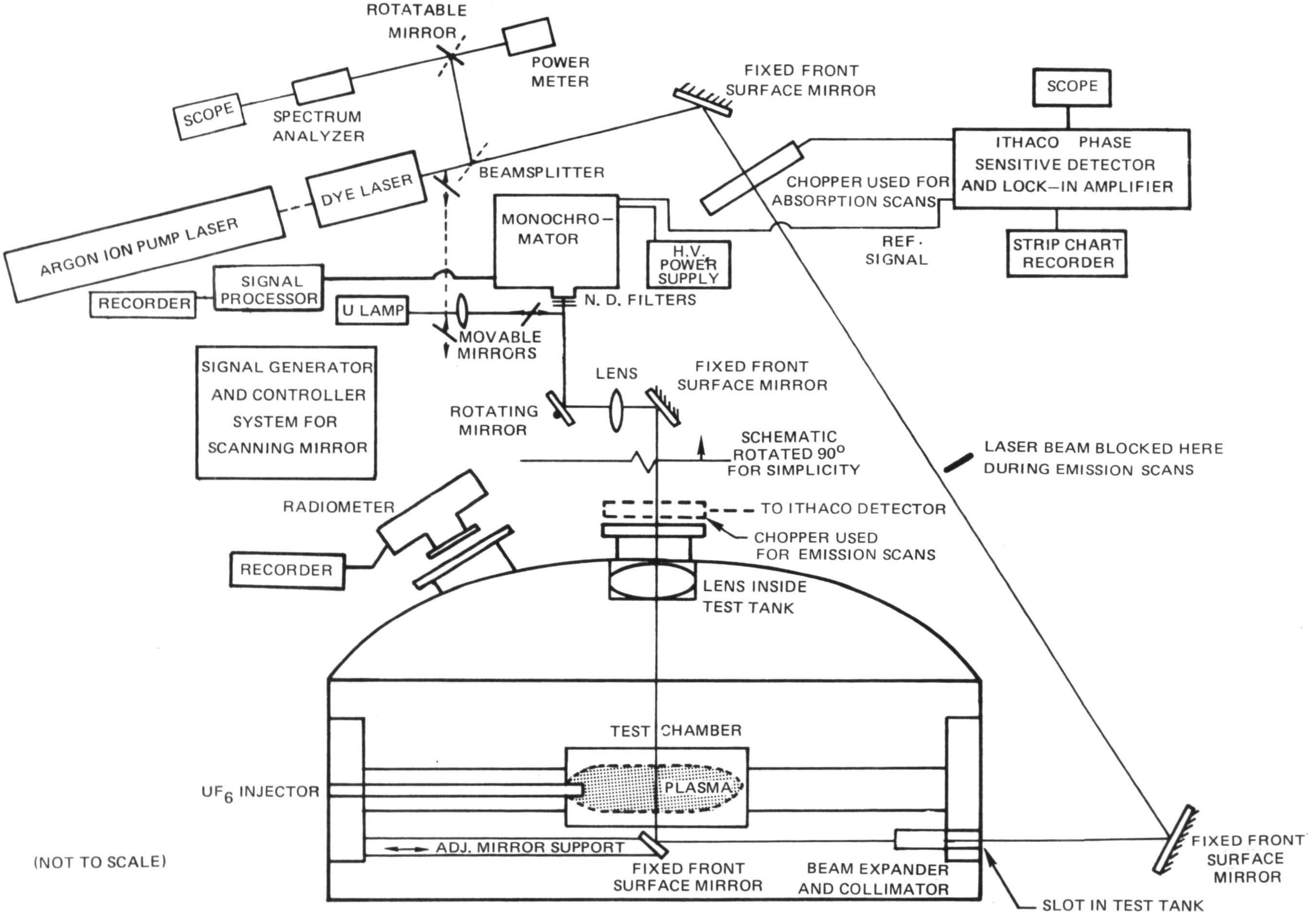

PHOTOGRAPH OF 1.2 MW RF ARGON/UF_6 PLASMA TEST FACILITY AND DYE LASER SYSTEM

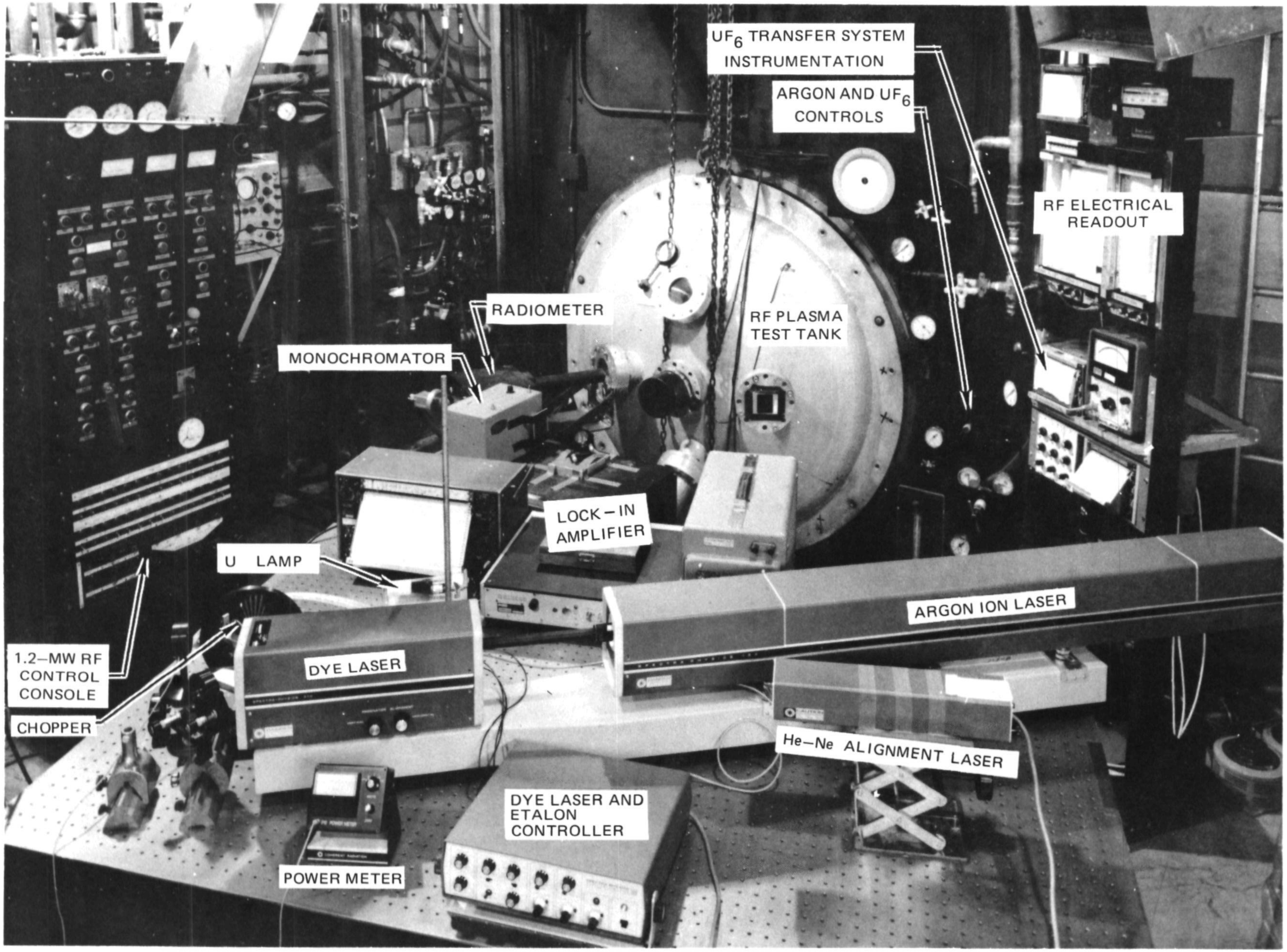

EXAMPLE OF ABSORPTION MEASUREMENTS OBTAINED IN 1.2 MW RF PLASMA–DYE LASER TESTS

P_C = 2 ATM Q_T = 55 KW T≃9500°K

URANIUM I DYE LASER LINE = 591.54 NM LOCATED ON CENTERLINE AT AXIAL MID–PLANE

DYE LASER BEAM DIAMETER – 1.5 MM PLASMA DISCHARGE DIAMETER = 3 CM

SEE FIG. 8 FOR SKETCH OF TEST CHAMBER CONFIGURATION

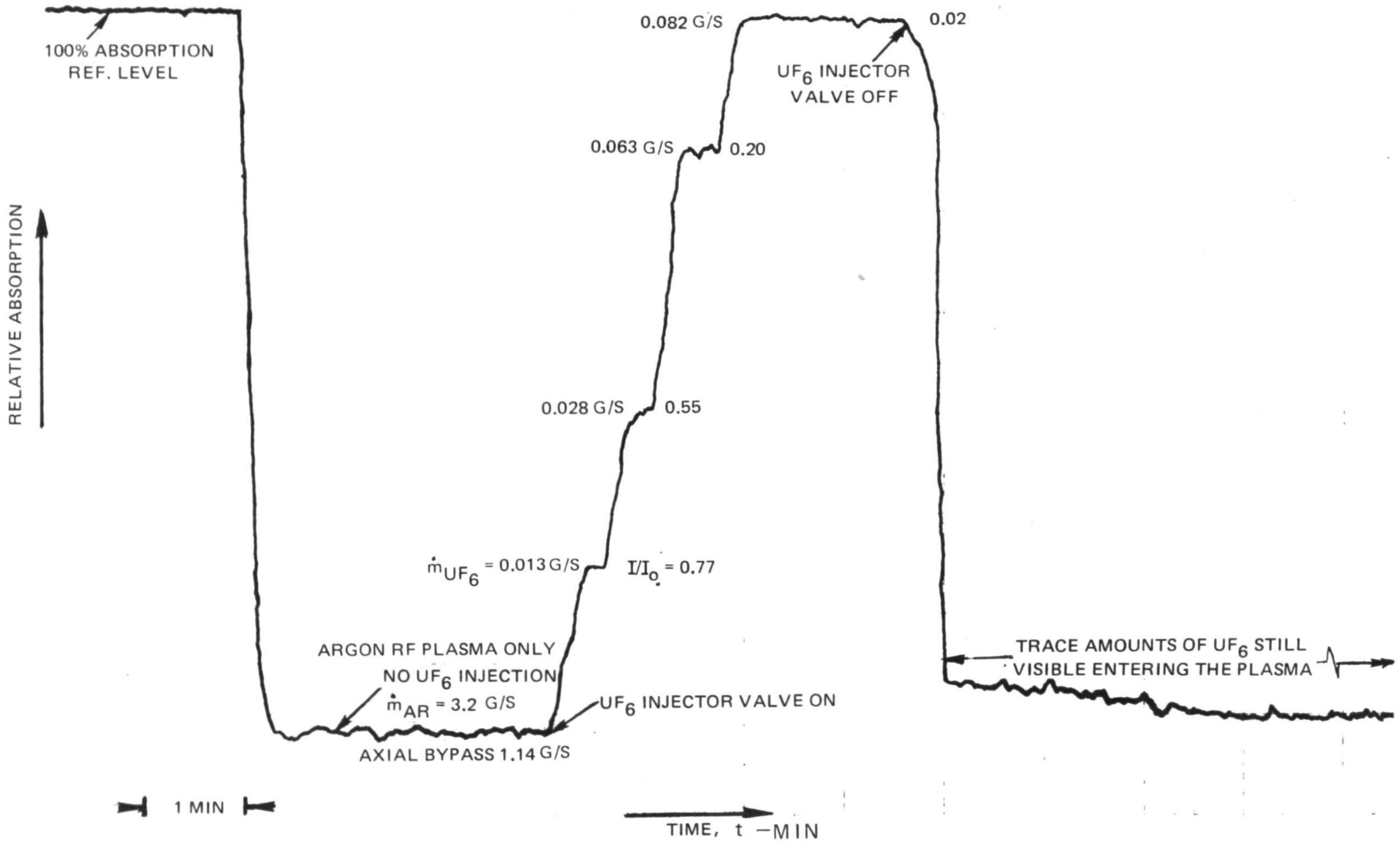

FIG. 16

PHOTOGRAPHS OF RF PLASMA TEST WITH PURE UF_6 INJECTION

TEST CASE V

SEE TABLE II FOR ADDITIONAL TEST CONDITIONS

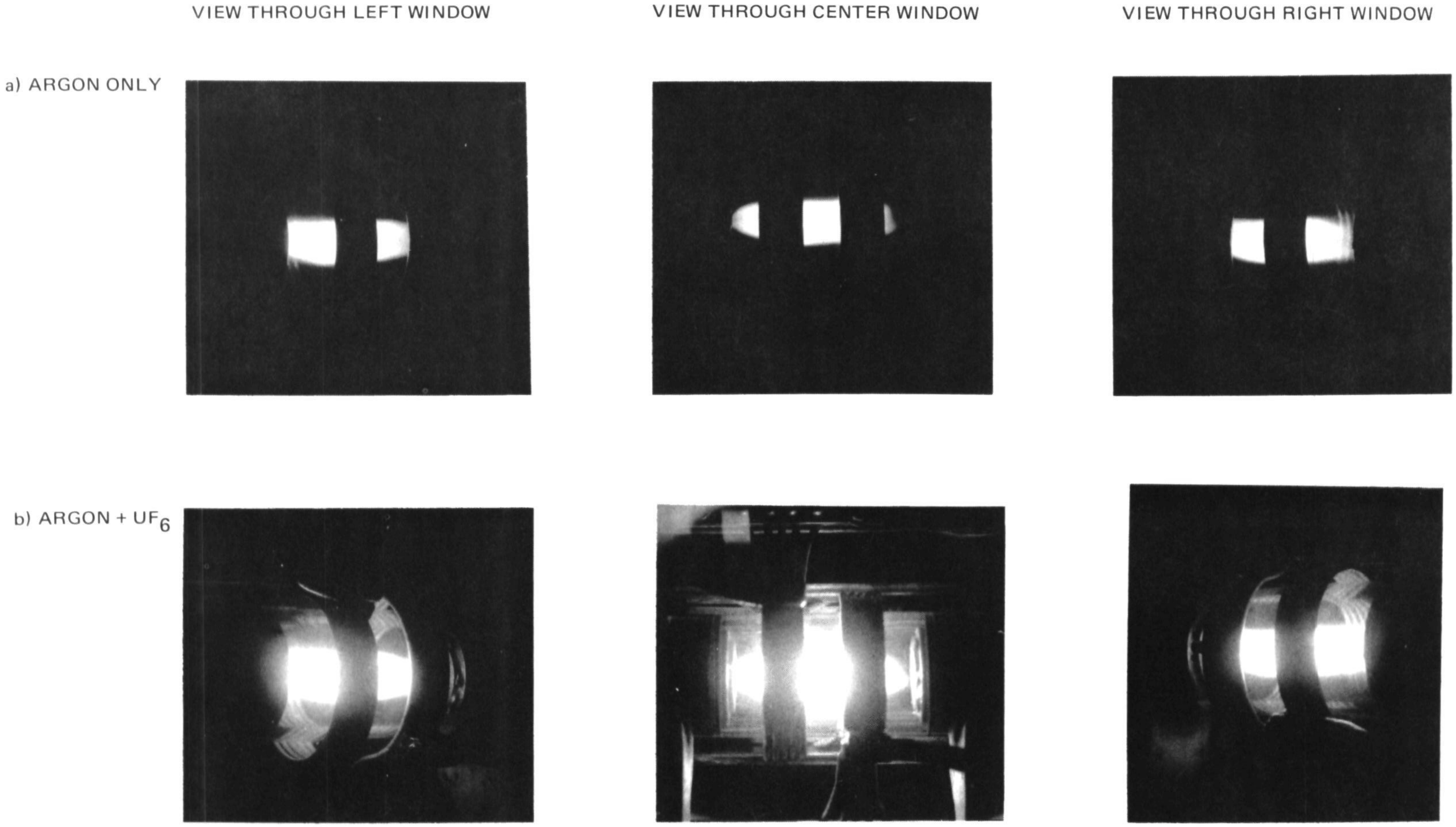

76–03–251–2

FIG. 17

EXAMPLE OF TOTAL DISCHARGE POWER, POWER RADIATED AND ITS DISTRIBUTION IN DIFFERENT WAVELENGTH BANDS FROM RF PLASMA TESTS WITH PURE UF_6 INJECTION CONDUCTED IN 1.2 MW RF INDUCTION HEATER

SEE TABLE II FOR TEST CONDITIONS–TEST CASE V

MEASUREMENTS TAKEN WITH RADIOMETER SYSTEM SHOWN IN FIG. 10

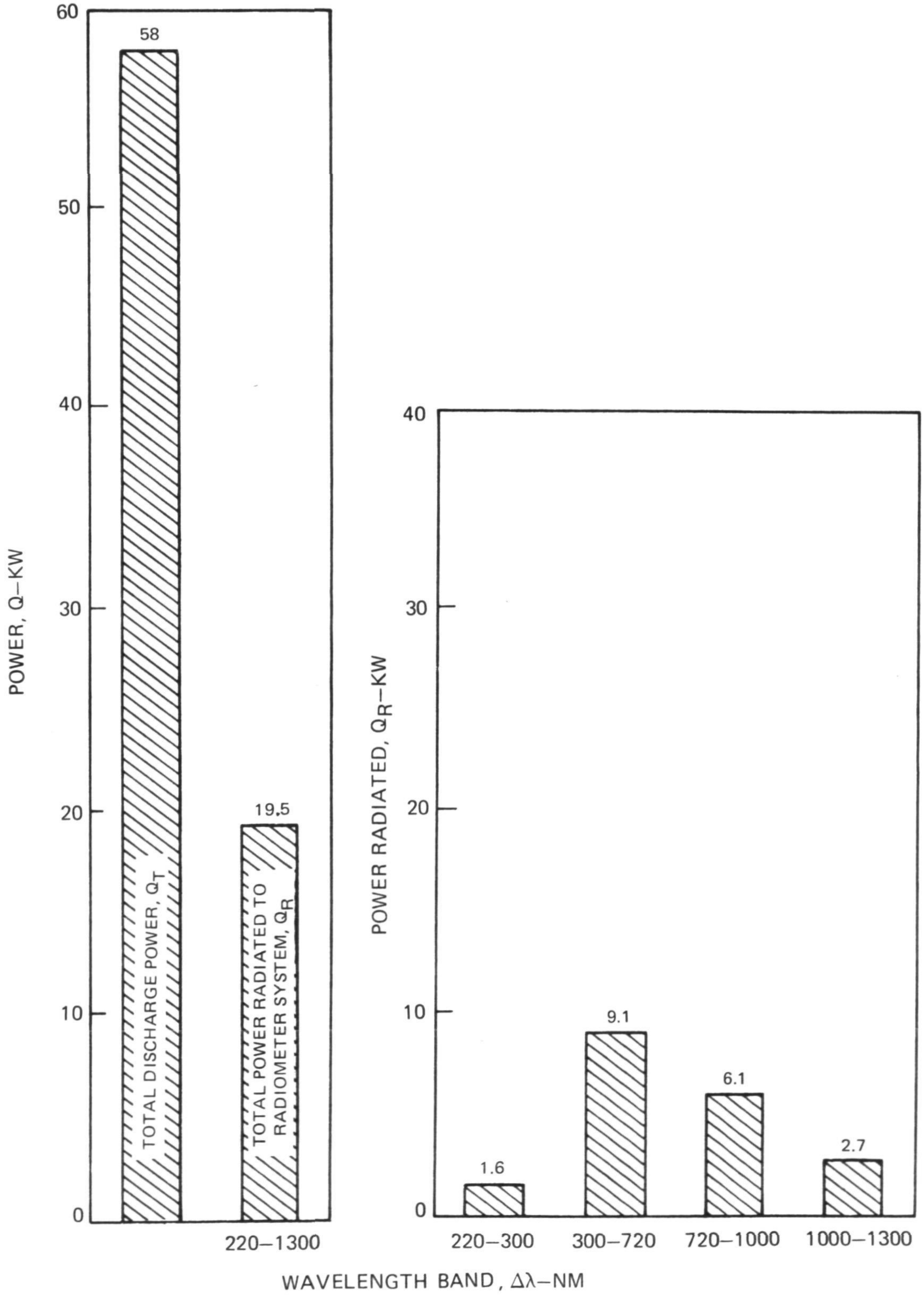

76–04–122–1

EXAMPLE OF RADIAL PROFILES OF EMISSION AND ABSORPTION COEFFICIENT FOR RF PLASMA TEST WITH PURE UF_6 INJECTION

TEST CASE V

SEE TABLE II FOR ADDITIONAL TEST CONDITIONS

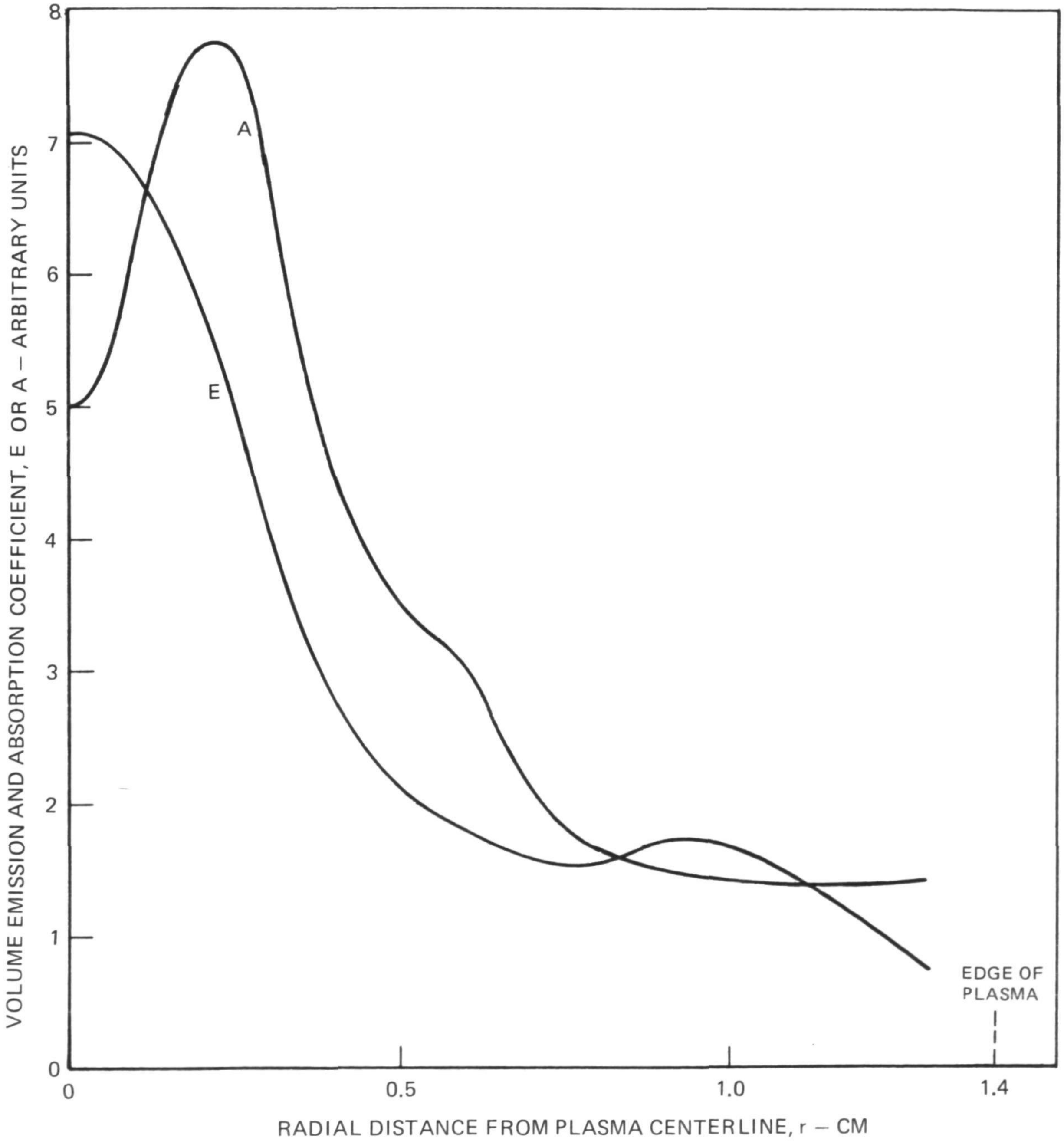

FIG. 19

EXAMPLE OF RESULTS OF RADIAL VARIATION IN TEMPERATURE AND TRANSMISSION OBTAINED WITH PURE UF_6 INJECTION INTO RF ARGON PLASMA

DYE LASER LINE USED: 591.54 NM
EMISSION AND ABSORPTION CHORDAL SCAN MEASUREMENTS TAKEN AT AXIAL MID–PLANE OF DISCHARGE
RADIAL TEMPERATURE PROFILE DETERMINED USING KIRCHOFF'S LAW
SEE FIG.13 FOR SCHEMATIC OF OPTICAL TRACKING SYSTEM USED
SEE TABLE II FOR ADDITIONAL TEST CONDITIONS

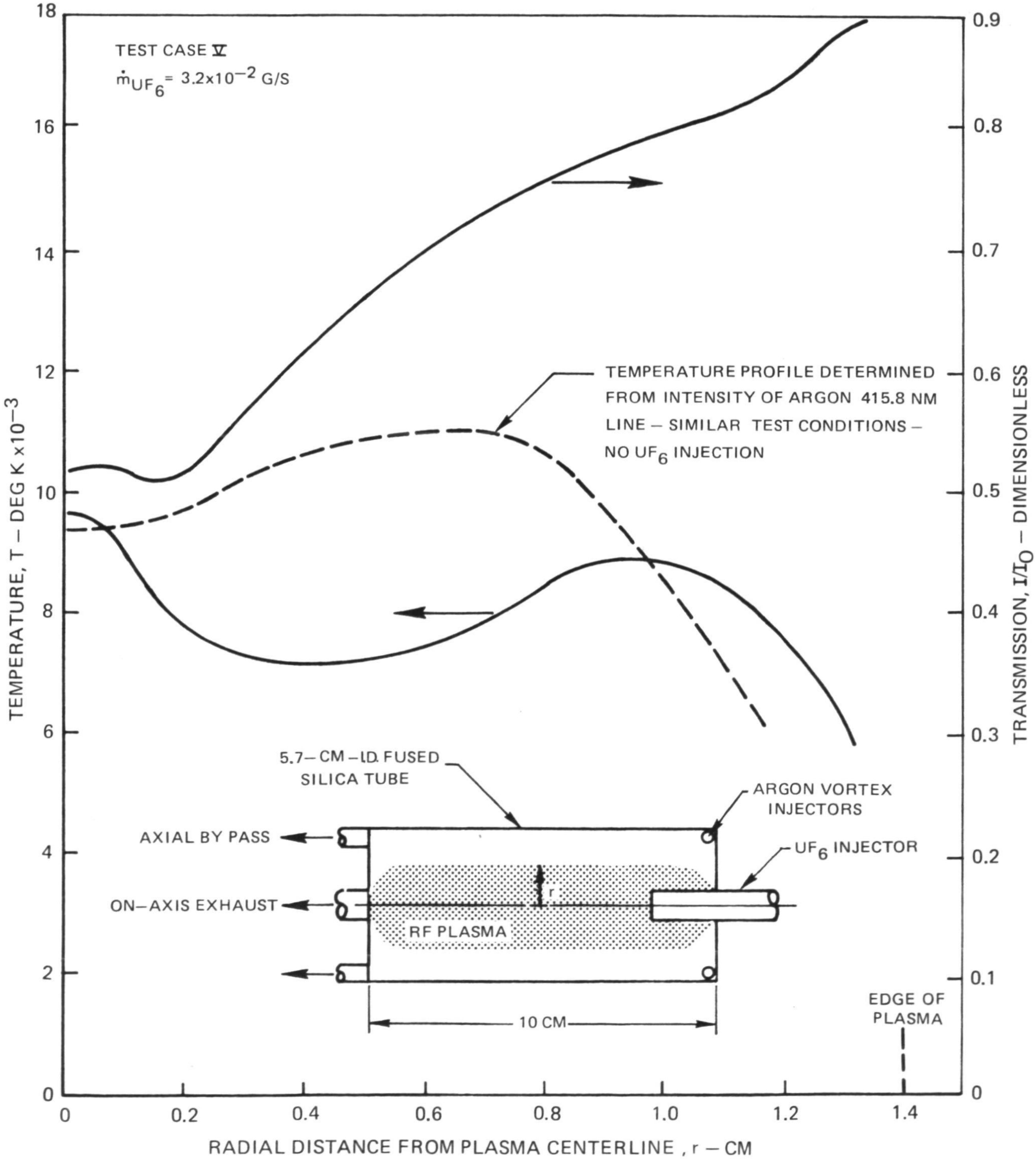

EQUILIBRIUM COMPOSITION OF UF_6 AT A PARTIAL PRESSURE OF 0.001 ATM

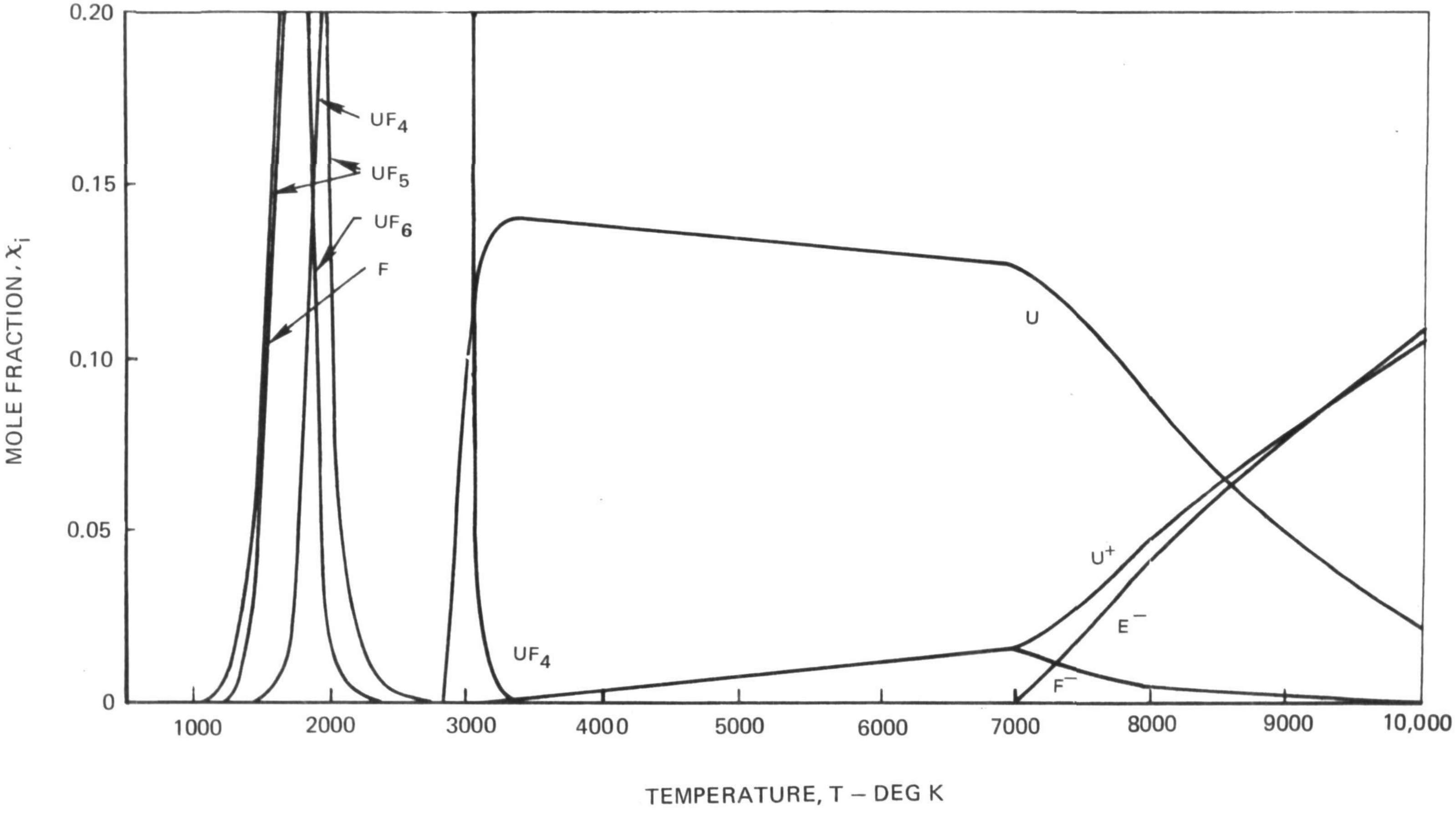

FIG. 21

EQUILIBRIUM COMPOSITION OF UF_6 AT SEVERAL PARTIAL PRESSURES

(a) P_P = 1.0 ATM

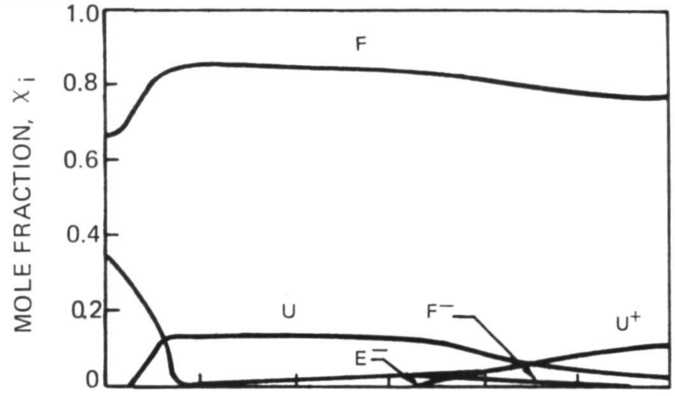

(b) P_P = 0.1 ATM

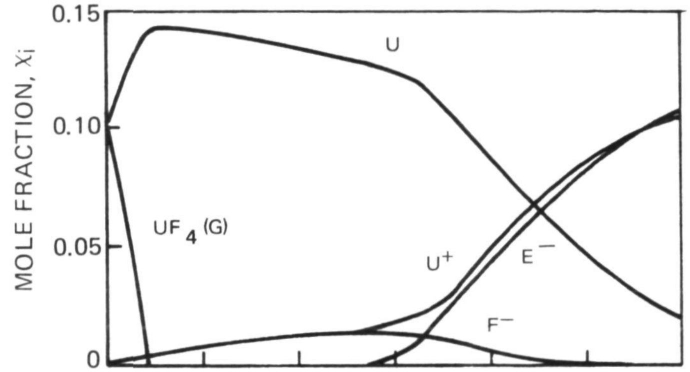

(c) P_P = 0.01 ATM

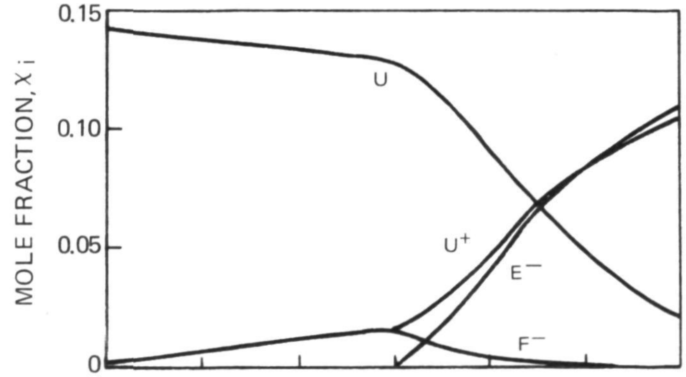

(d) P_P = 0.0001 ATM

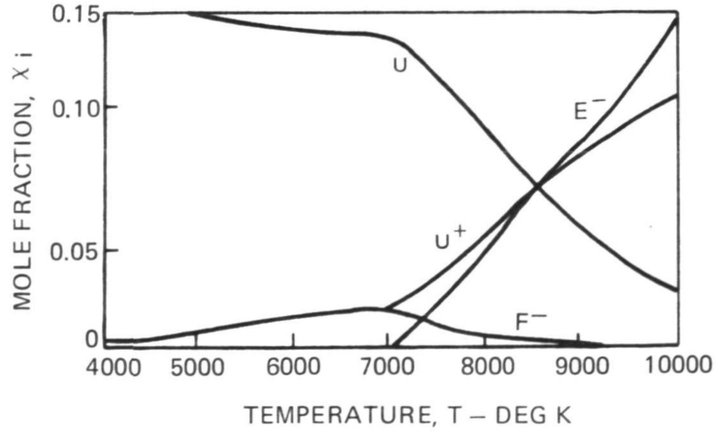

THERMAL DECOMPOSITION OF UF_6 AS A FUNCTION OF TEMPERATURE

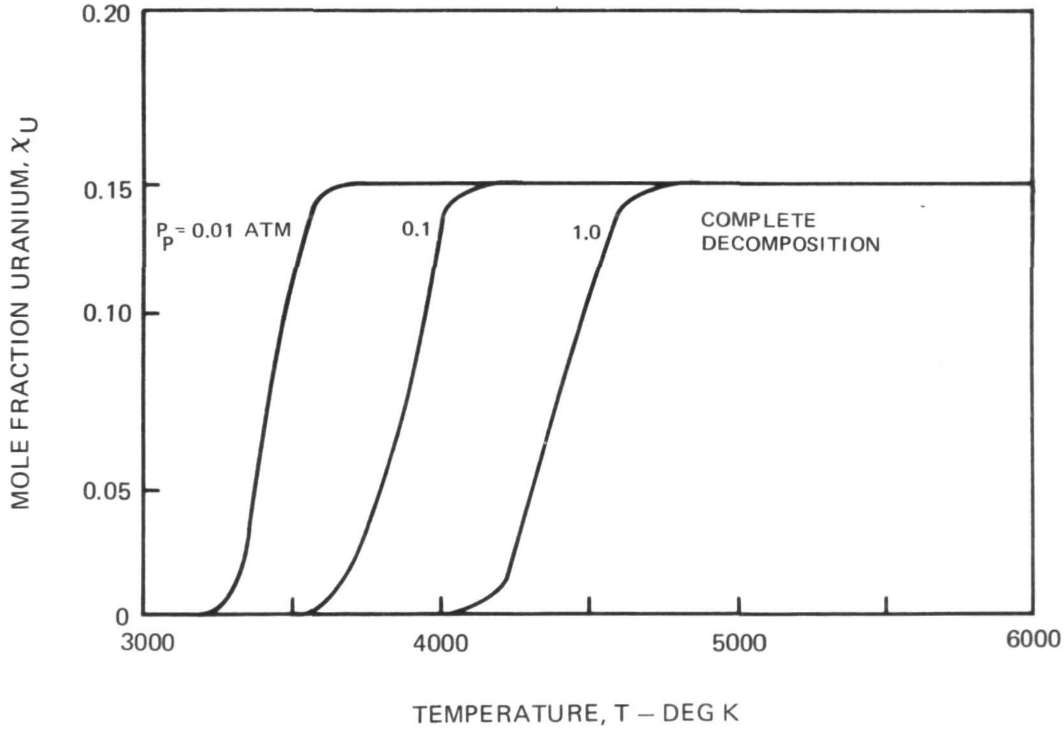

FIG. 23

VARIATION OF NEUTRAL URANIUM ATOM NUMBER DENSITY WITH UF_6 PARTIAL PRESSURE IN A UF_6/Ar MIXTURE

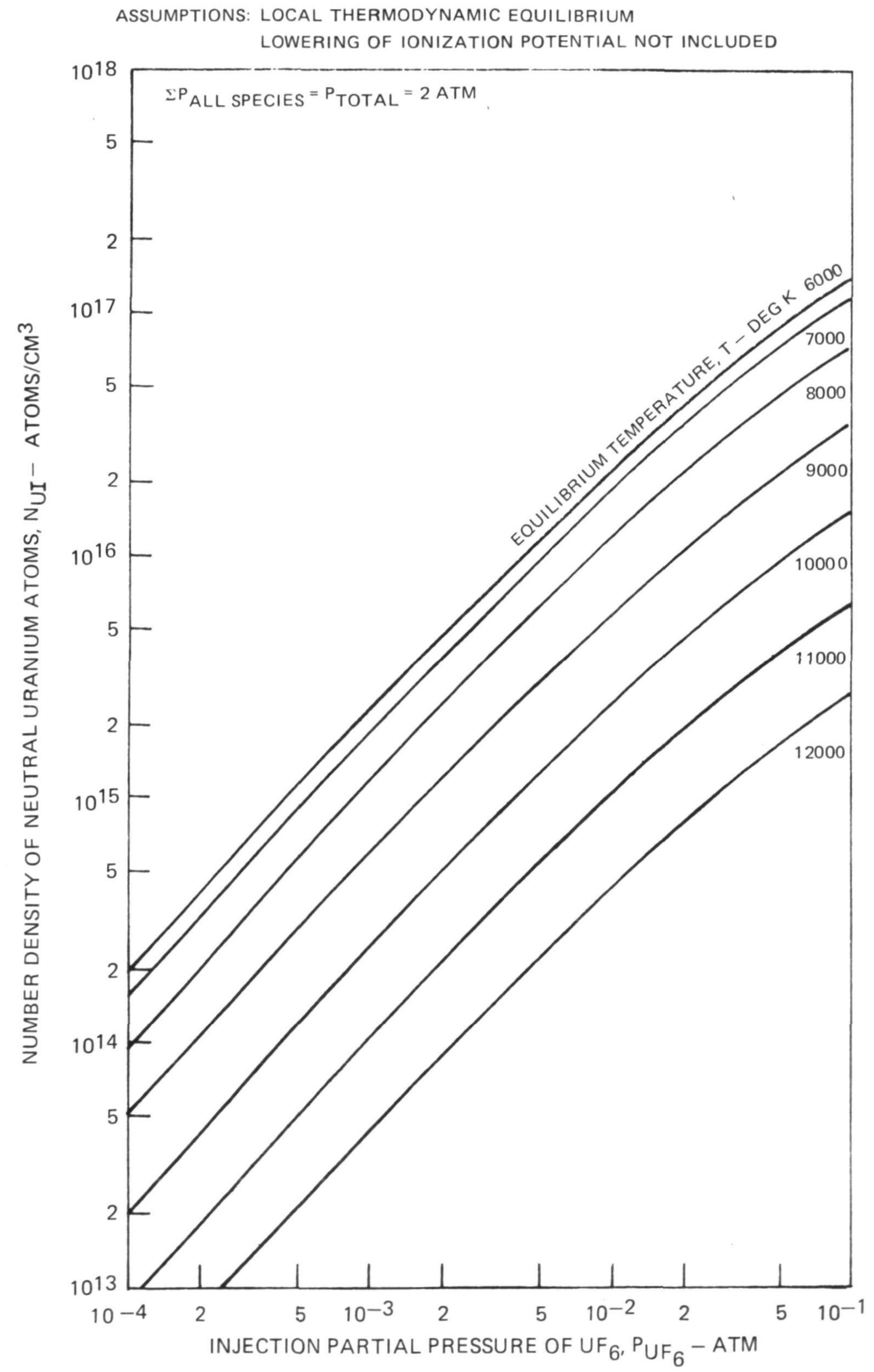

FIG. 24

VARIATION OF SINGLY IONIZED URANIUM ATOM NUMBER DENSITY WITH UF_6 PARTIAL PRESSURE IN A UF_6/Ar MIXTURE

ASSUMPTIONS: LOCAL THERMODYNAMIC EQUILIBRIUM
LOWERING OF IONIZATION POTENTIAL NOT INCLUDED

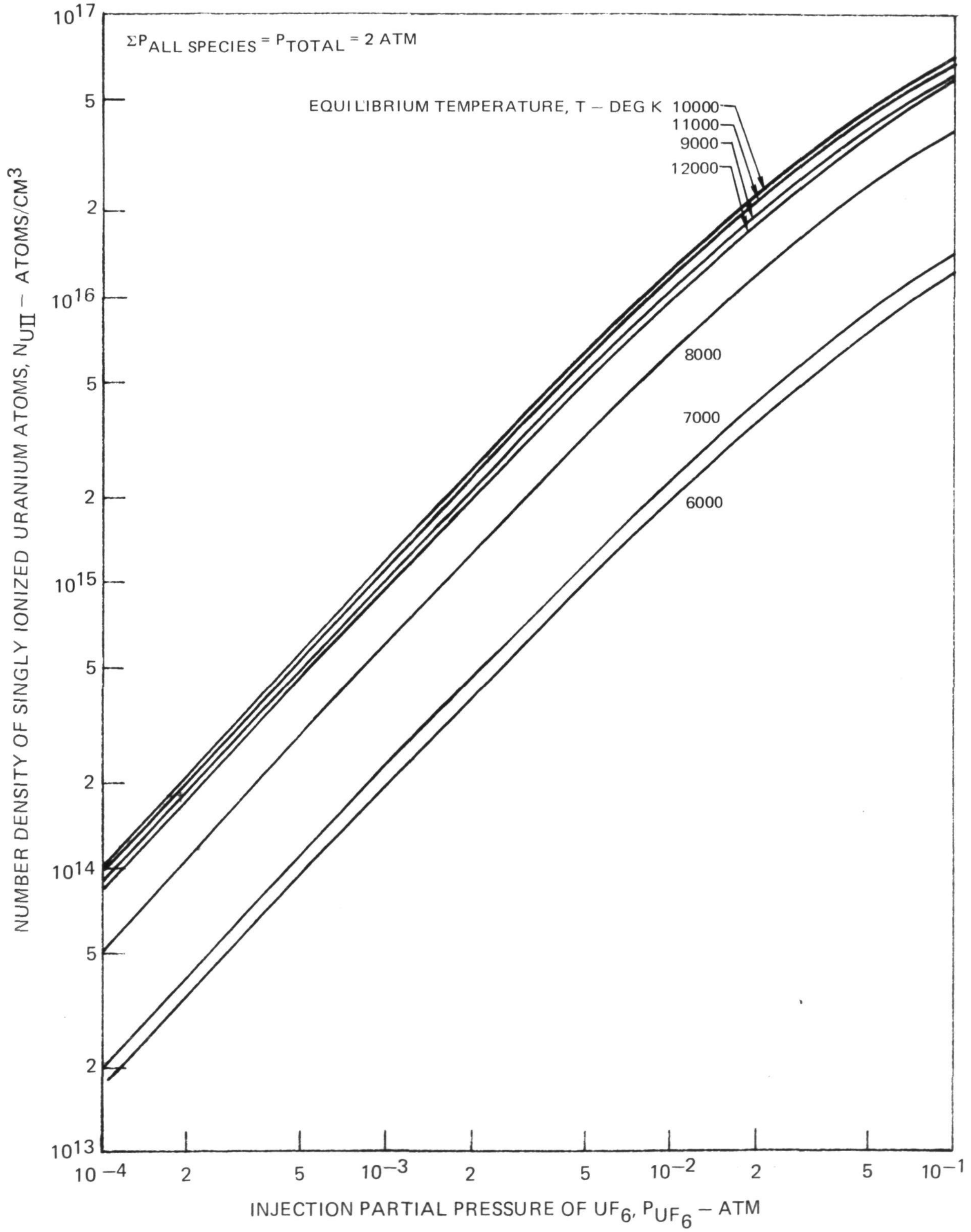

76–04–7–4

FIG. 25

VARIATION OF DOUBLY IONIZED URANIUM ATOM NUMBER DENSITY WITH UF_6 PARTIALLY PRESSURE IN A UF_6/Ar MIXTURE

ASSUMPTIONS: LOCAL THERMODYNAMIC EQUILIBRIUM
LOWERING OF IONIZATION POTENTIAL NOT INCLUDED

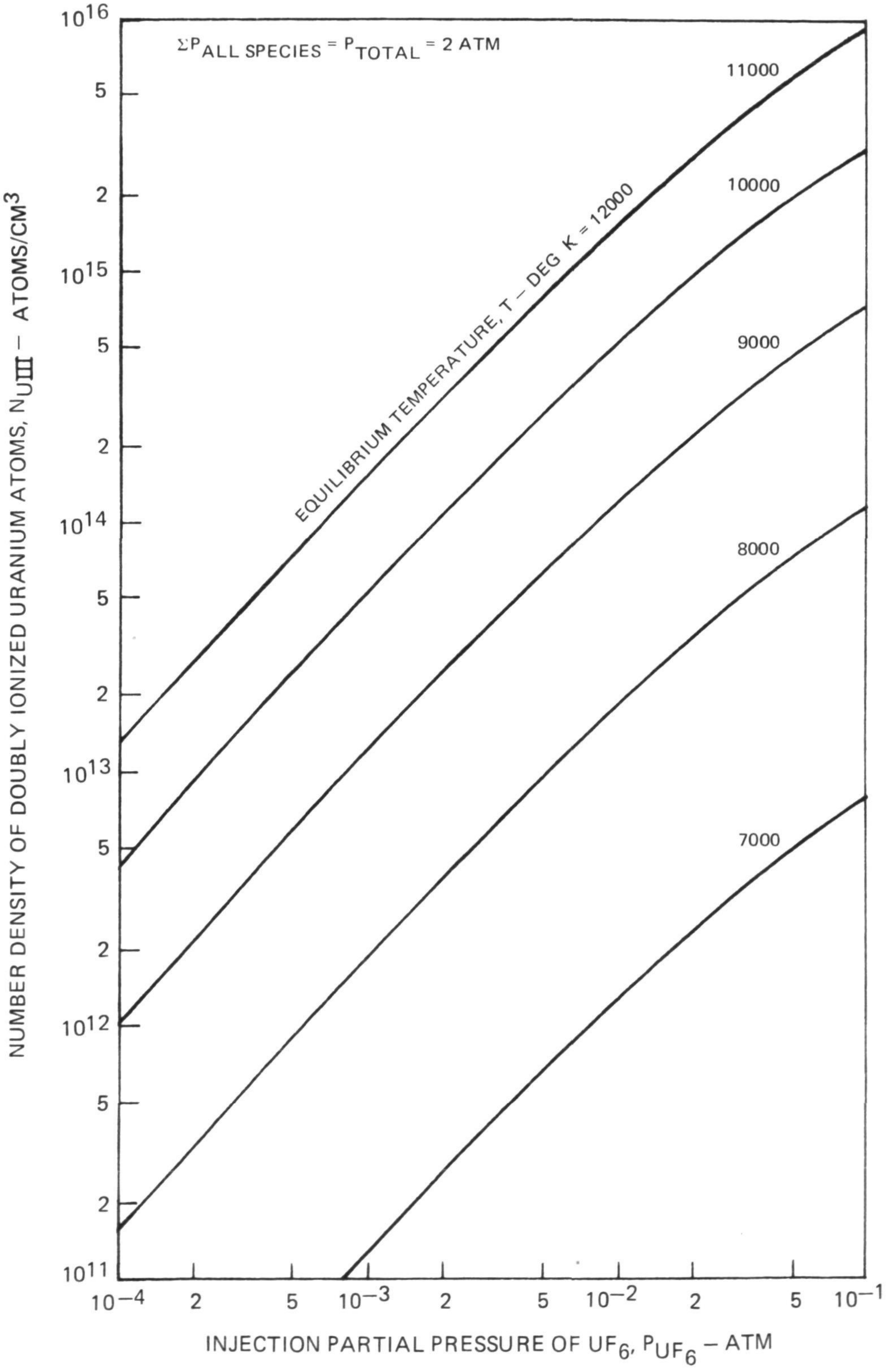

FIG. 26

VARIATION OF TOTAL URANIUM ATOM NUMBER DENSITY WITH UF_6 PARTIAL PRESSURE IN A UF_6/Ar MIXTURE

ASSUMPTIONS: LOCAL THERMODYNAMIC EQUILIBRIUM
LOWERING OF IONIZATION POTENTIAL NOT INCLUDED

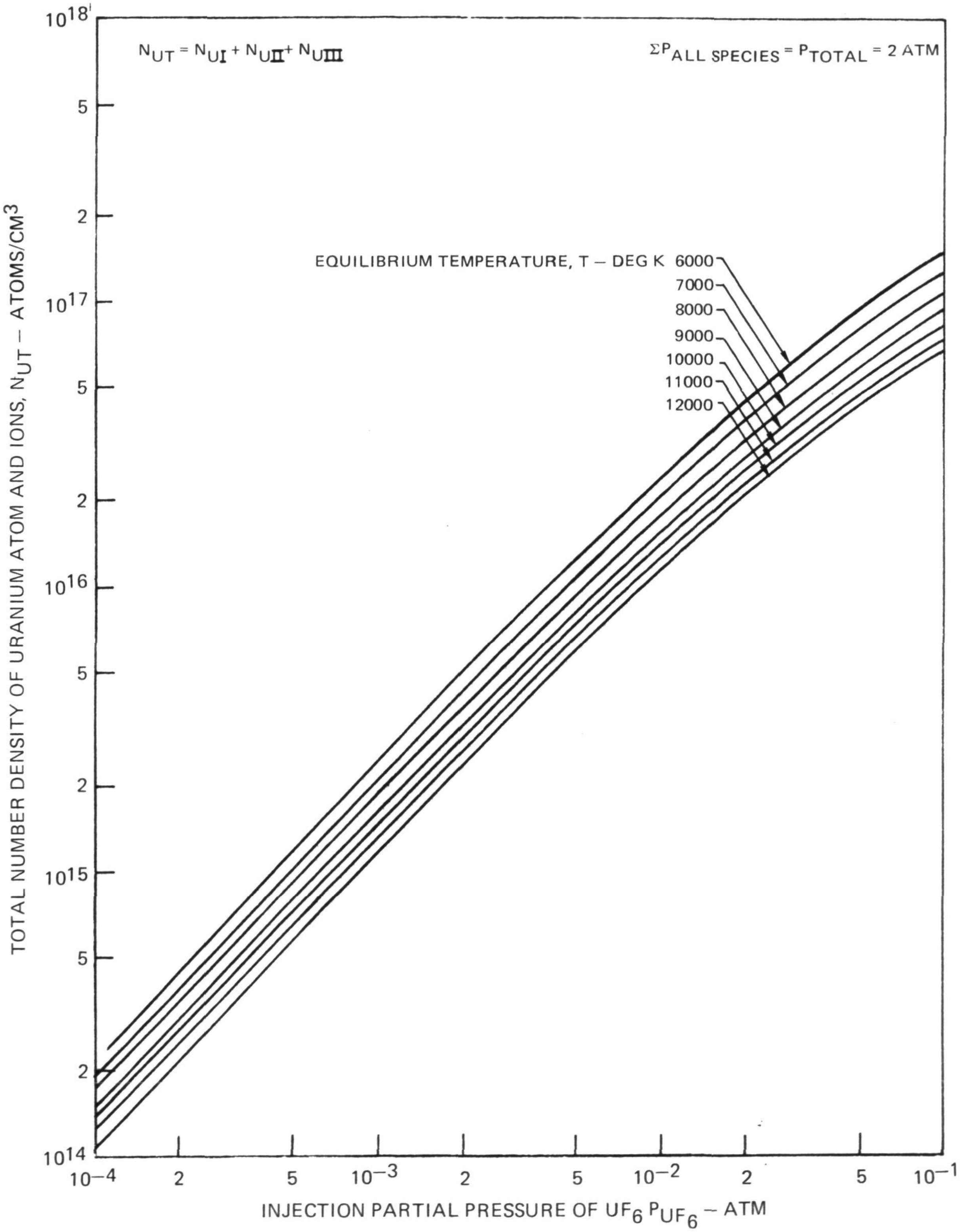

ARGON EQUILIBRIUM COMPOSITION DATA

PRESSURE = 2 ATM
(REF. 13)

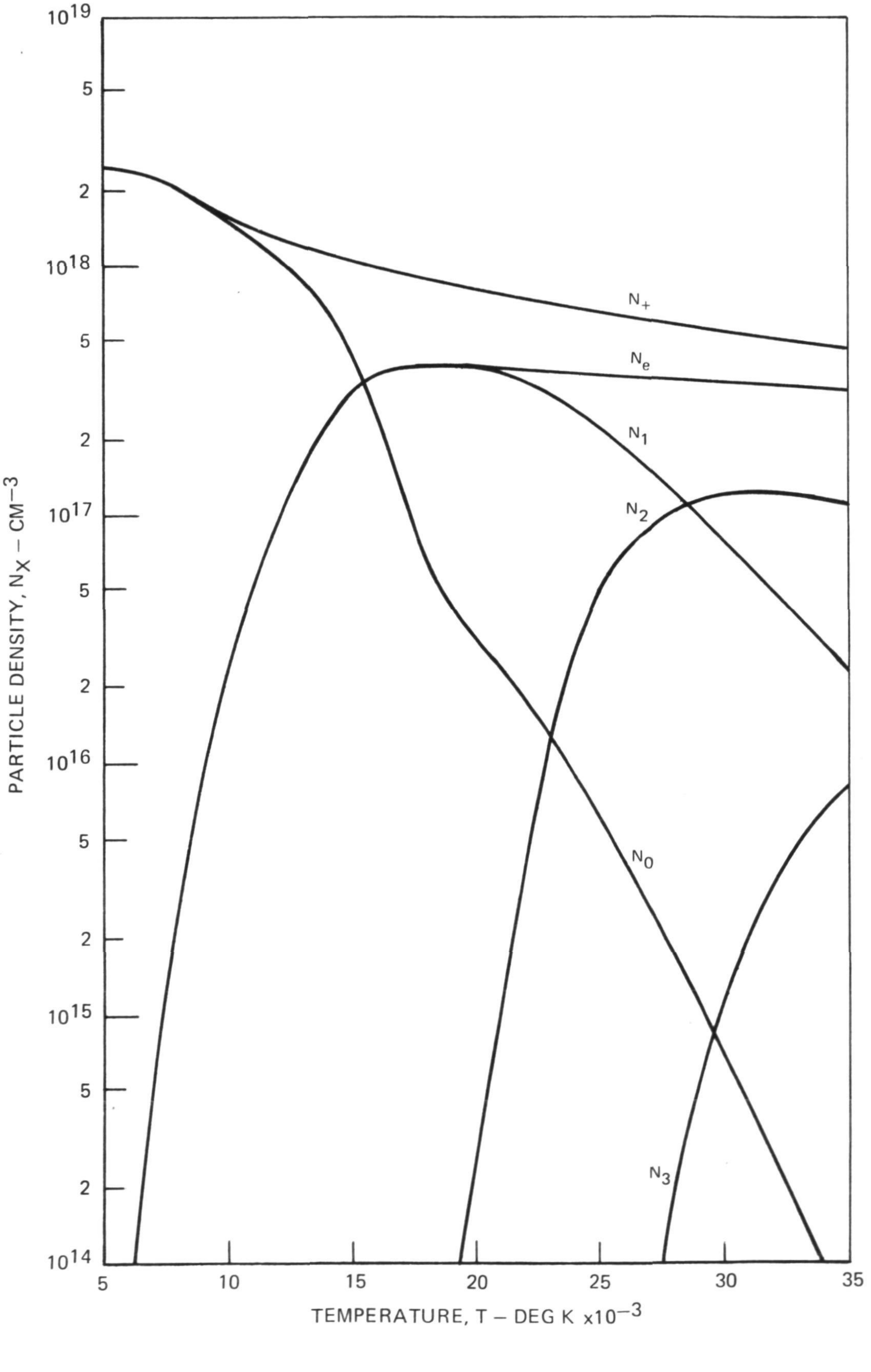

FIG. 28

RESULTS OF MEASUREMENTS OF 591.54 NM LASER BEAM ABSORPTION LINE WIDTHS AS A FUNCTION OF CHAMBER PRESSURE FOR RF PLASMA TEST WITH PURE UF_6 INJECTION

$$\Delta f_{DOPPLER} = \left[\frac{2kT}{mc^2} \log_e 2 \right]^{1/2} f$$

CONVERSION 8 GHz = 10^{-2} NM

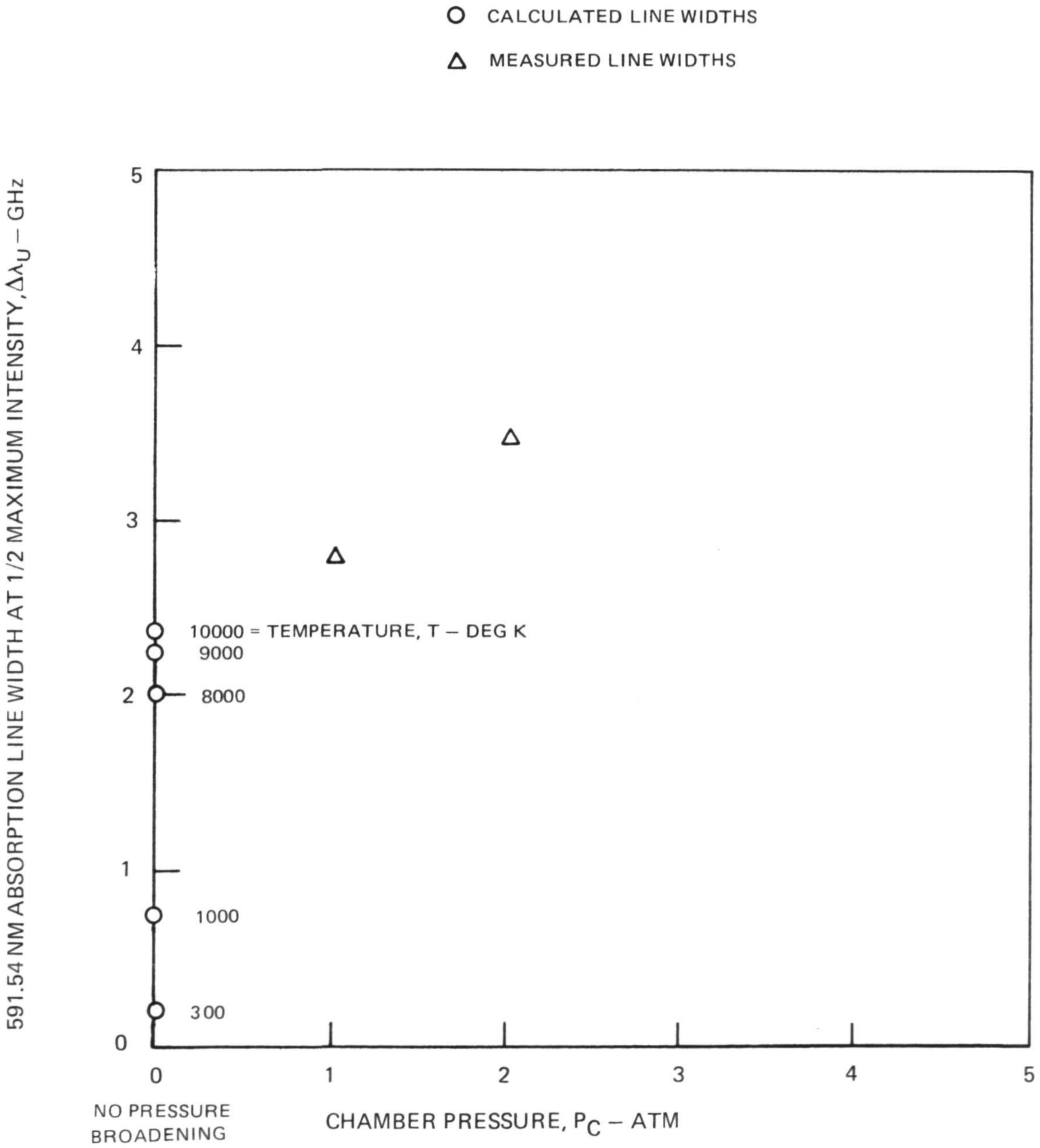

FIG. 29

EFFECT OF TEMPERATURE ON THE PARTITION FUNCTIONS OF URANIUM (U I AND U II)

$$Z_i = \sum_n g_{i,n}\, e^{-E_{i,n}/kT}$$

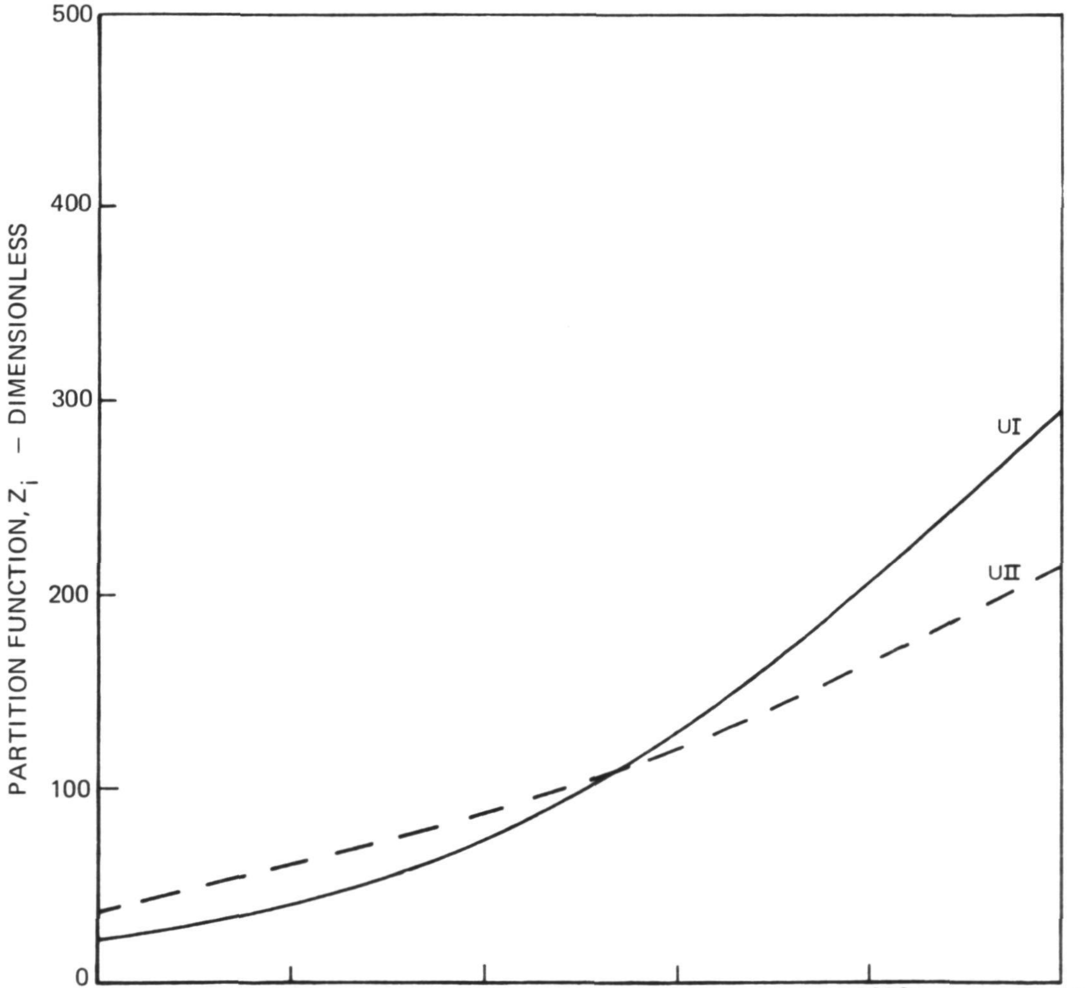

VARIATION OF NUMBER DENSITY OF NEUTRAL URANIUM (UI) AS A FUNCTION OF RADIAL DISTANCE FROM TEST CHAMBER CENTERLINE

TEST CASE V

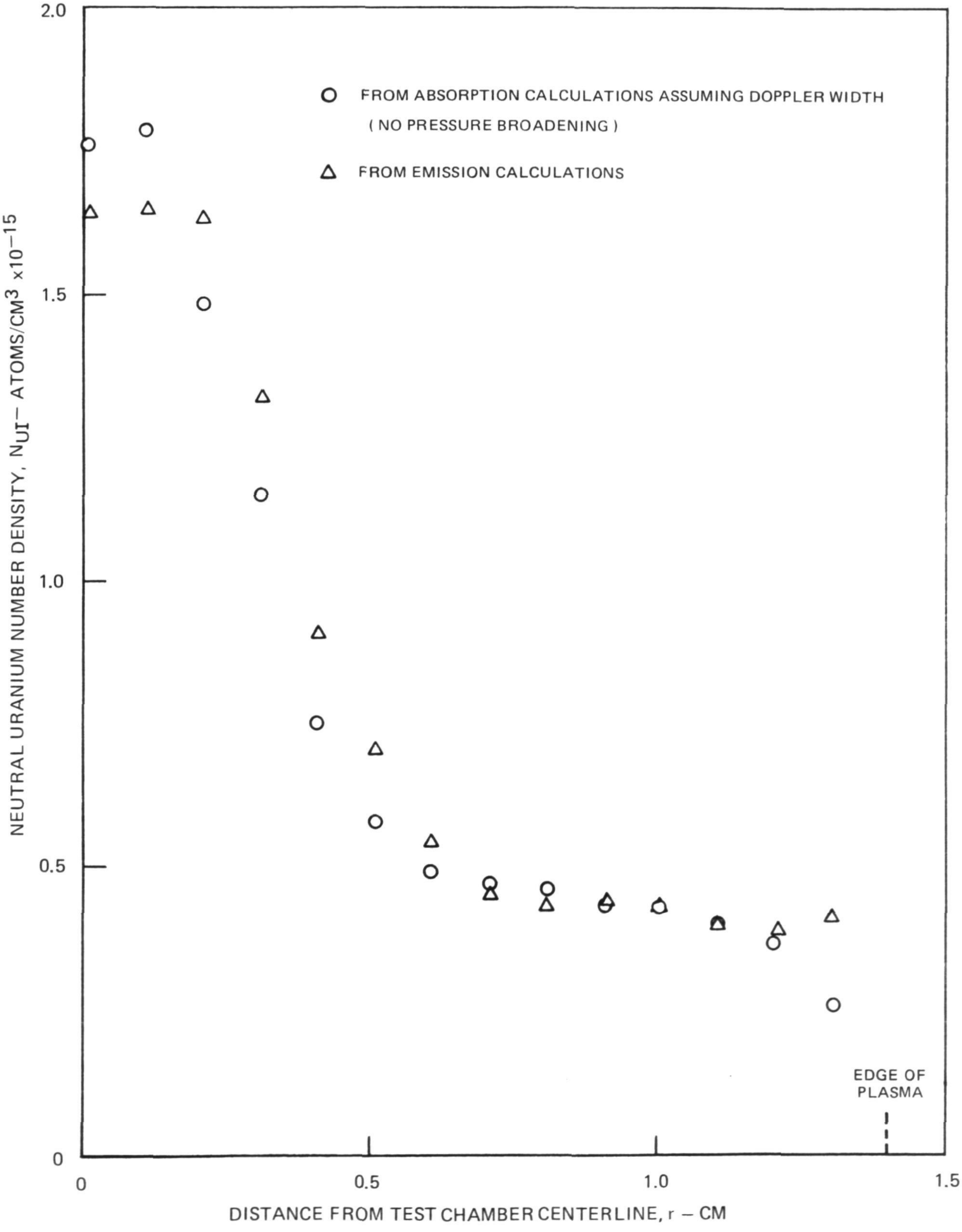

FIG. 31

EQUILIBRIUM COMPOSITION OF UF_6 OVER TEMPERATURE RANGE 6000–10,000K AND PARTIAL PRESSURE RANGE $10^{-4} - 10^{-1}$ ATM

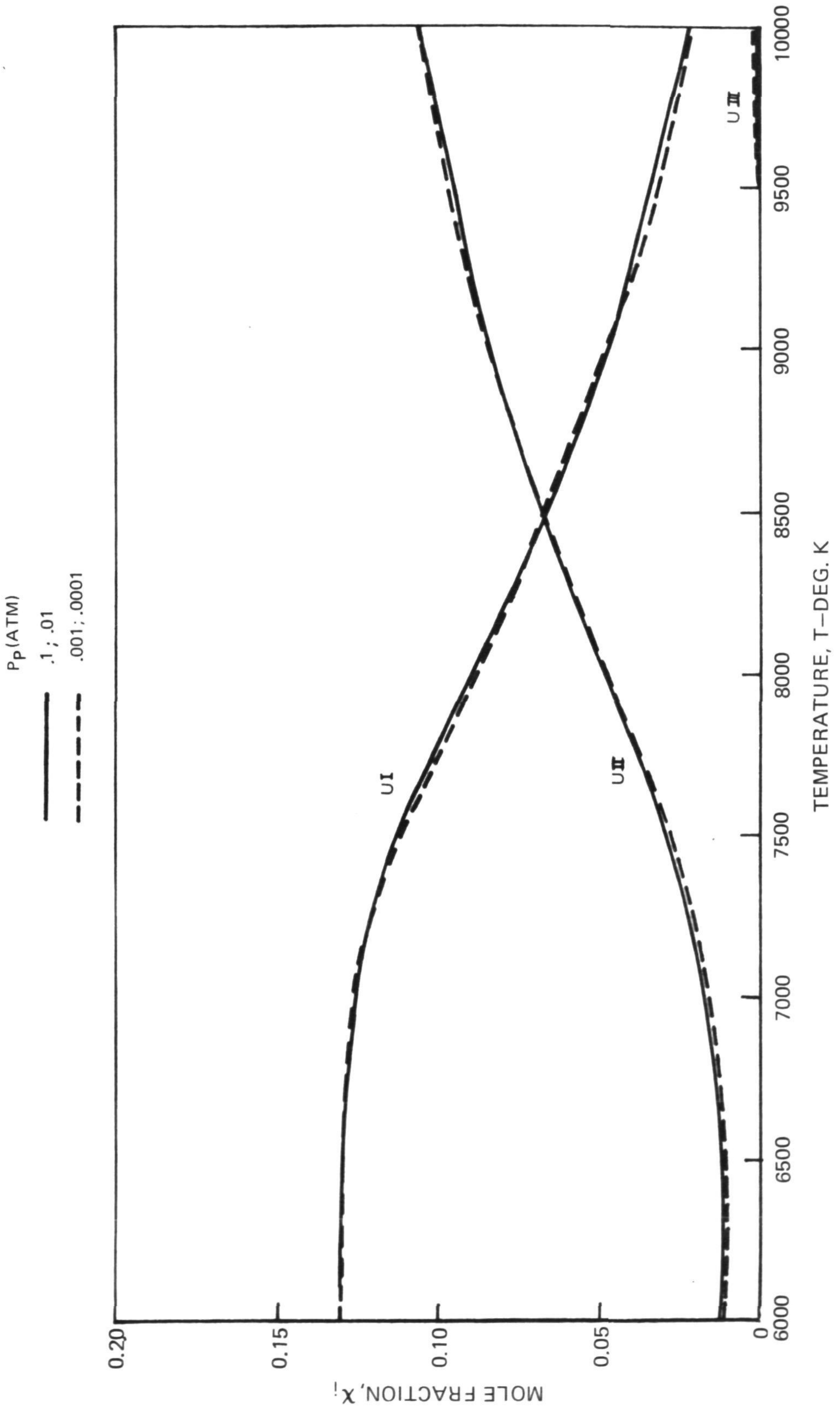

FIG. 32

RADIAL VARIATION OF TOTAL URANIUM ATOM (UI, UII, UIII) NUMBER DENSITY FOR UF_6 RF PLASMA TEST CASE V

SEE TABLE II FOR ADDITIONAL TEST CONDITIONS

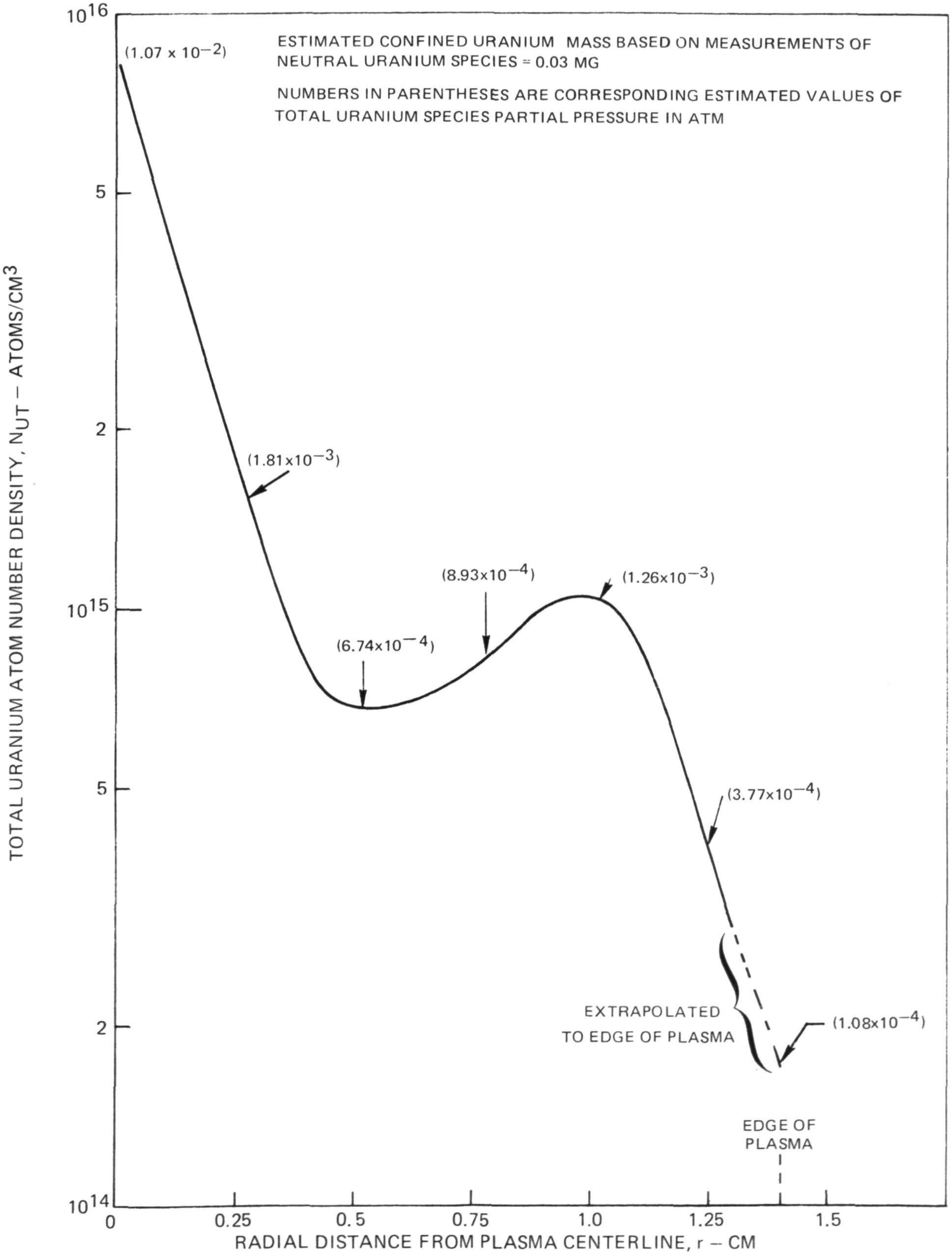

76–04–56–1

EXAMPLE OF RADIAL VARIATION OF CONFINED TOTAL URANIUM ATOMS AT AXIAL MIDPLANE FOR UF_6 RF PLASMA TEST CASE V

SEE TABLE II FOR ADDITIONAL DETAILS

SEE FIGS. 19 AND 32 FOR CORRESPONDING RADIAL PROFILES OF TRANSMISSION, TEMPERATURE AND TOTAL URANIUM ATOM NUMBER DENSITY

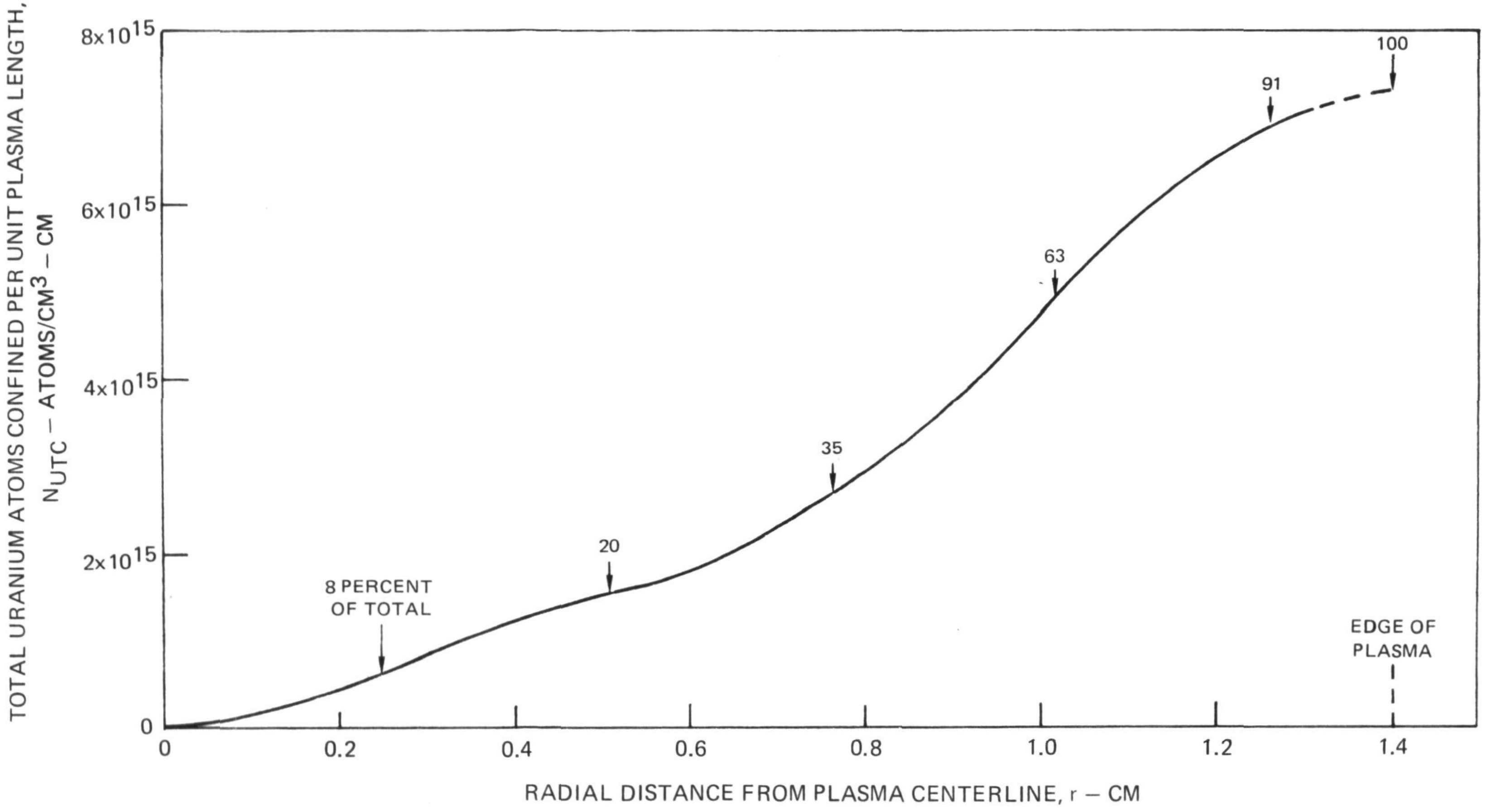

PHOTOGRAPH OF FUSED SILICA TUBES USED IN RF PLASMA TESTS WITH PURE UF_6 INJECTION AND INCORPORATING MODIFICATIONS TO TEST CHAMBER/FLOW SCHEME

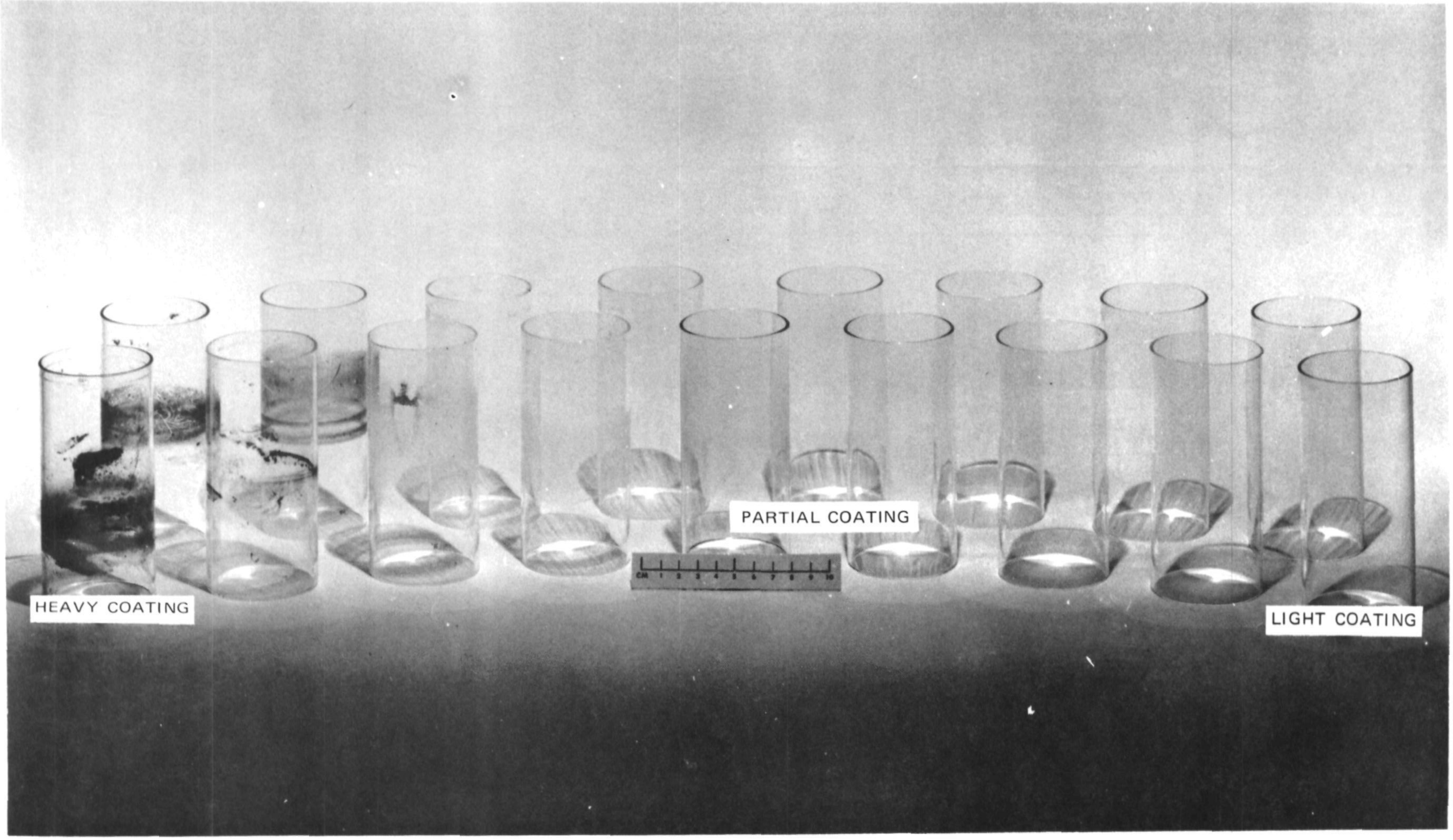

FIG. 34

FIG. 35

PHOTOGRAPHS OF FUSED SILICA TUBES USED IN RF PLASMA TESTS WITH PURE UF_6 INJECTION AND INCORPORATING MODIFICATIONS TO TEST CHAMBER/FLOW SCHEME

SEE TABLE III FOR CORRESPONDING TEST CONDITIONS

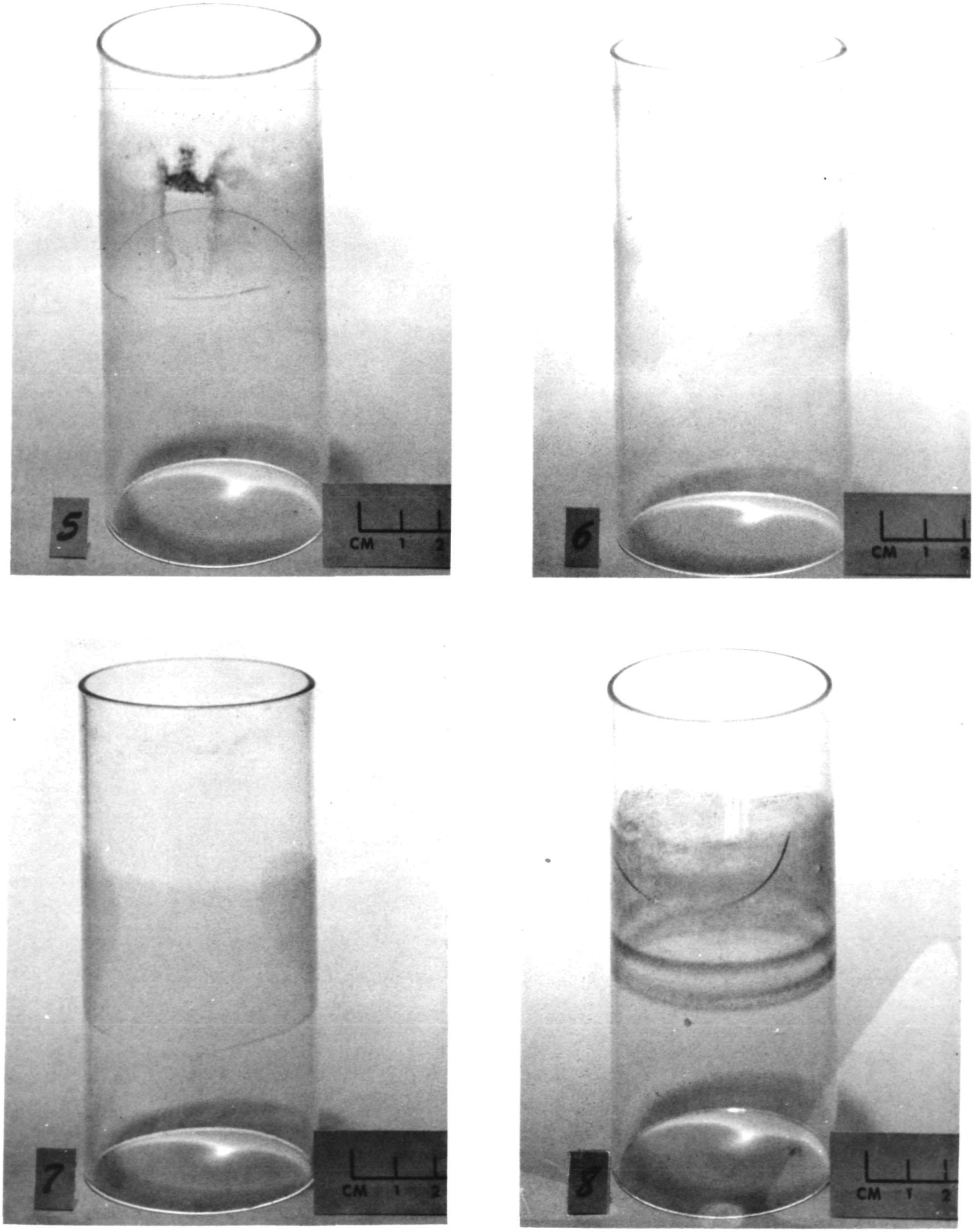

76–04–40–2

FIG. 36

EXAMPLES OF IR SPECTROPHOTOMETRIC ABSORPTION MEASUREMENTS TAKEN OF RESIDUE ON INNER SURFACE OF FUSED TUBE AFTER RF PLASMA TEST WITH PURE UF_6 INJECTION

SEE TABLE III FOR RANGE OF TEST CONDITIONS
THIN WAFER KBr MATRIX USED WITH PERKIN ELEMER MODEL 457

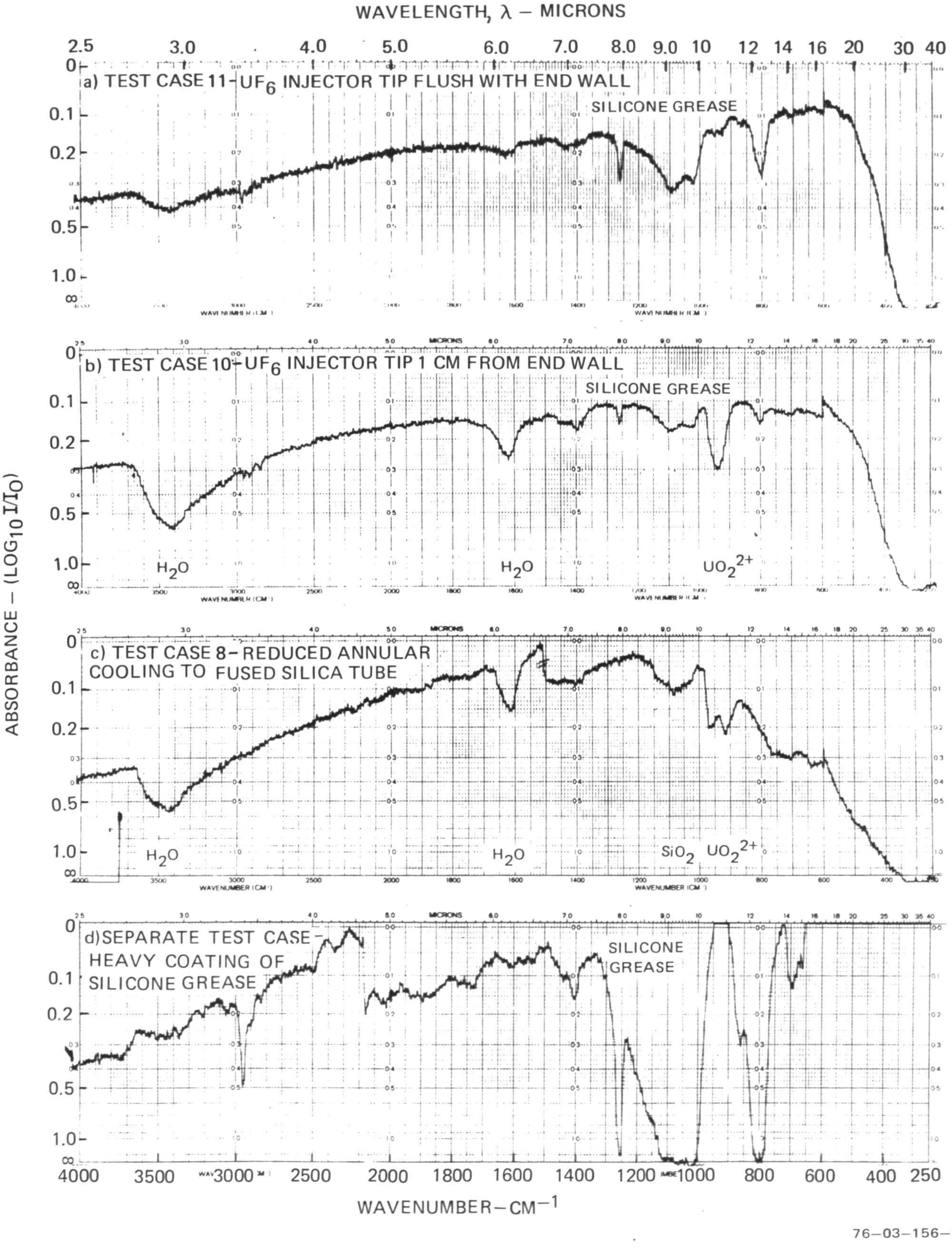

FIG. 37

RESIDUE DEPOSITION ON FUSED SILICA TUBES AFTER LONG RUN TIME TESTS WITH RF PLASMA AND PURE UF_6 INJECTION

SEE TABLE IV FOR ADDITIONAL TEST CONDITIONS

SEE FIGS. 40 AND 41 FOR PHOTOGRAPHS OF FUSED SILICA TUBES FROM SELECTED TESTS

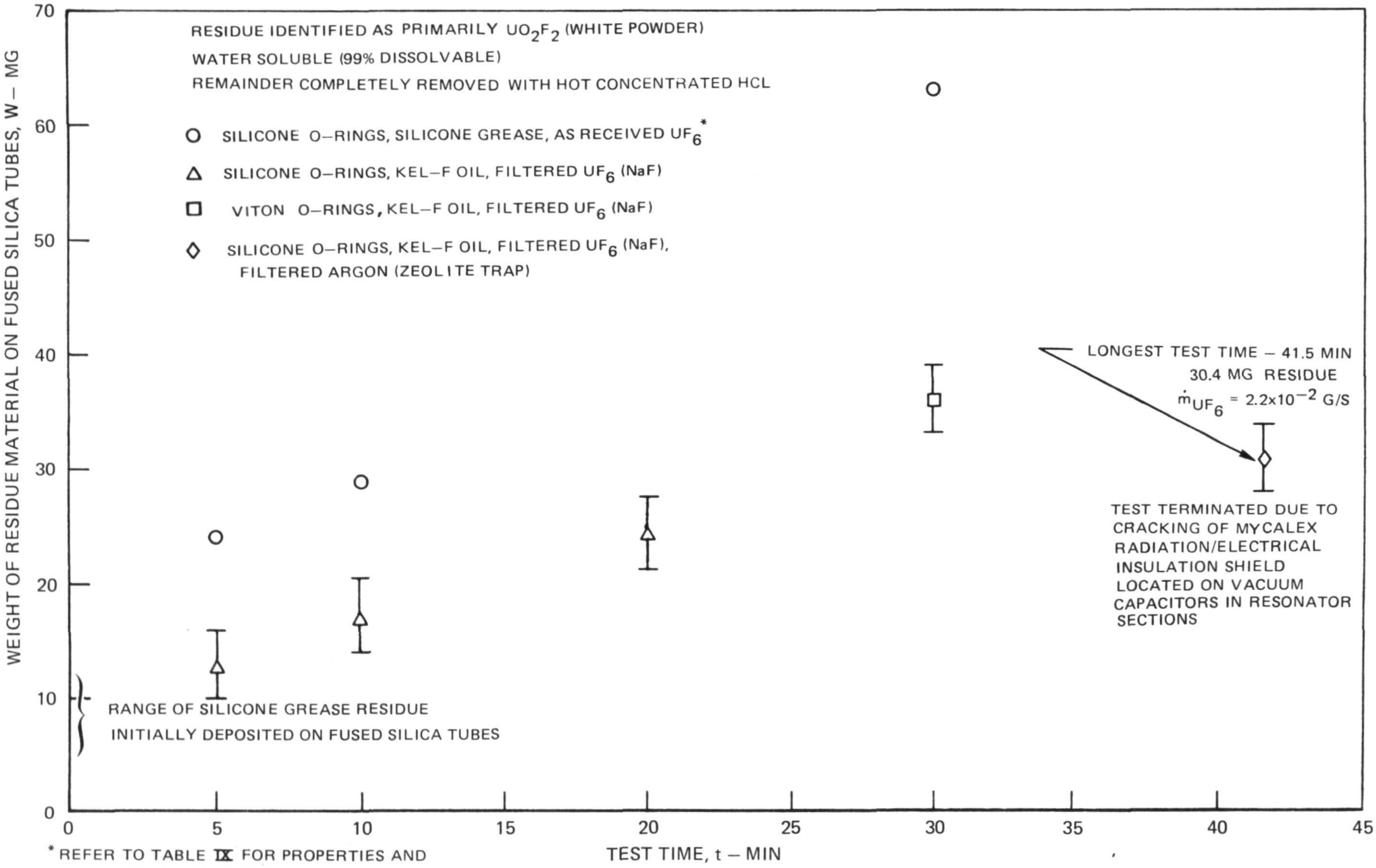

* REFER TO TABLE IX FOR PROPERTIES AND ASSAY OF AS–RECEIVED UF_6

FIG. 38

ELECTRON PHOTOMICROGRAPHS AND X–RAY MAPS OF A SAMPLE RESIDUE FROM INSIDE SURFACE OF FUSED SILICA TUBE AFTER RF PLASMA TEST WITH PURE UF_6 INJECTION FOR 30 MINUTE DURATION

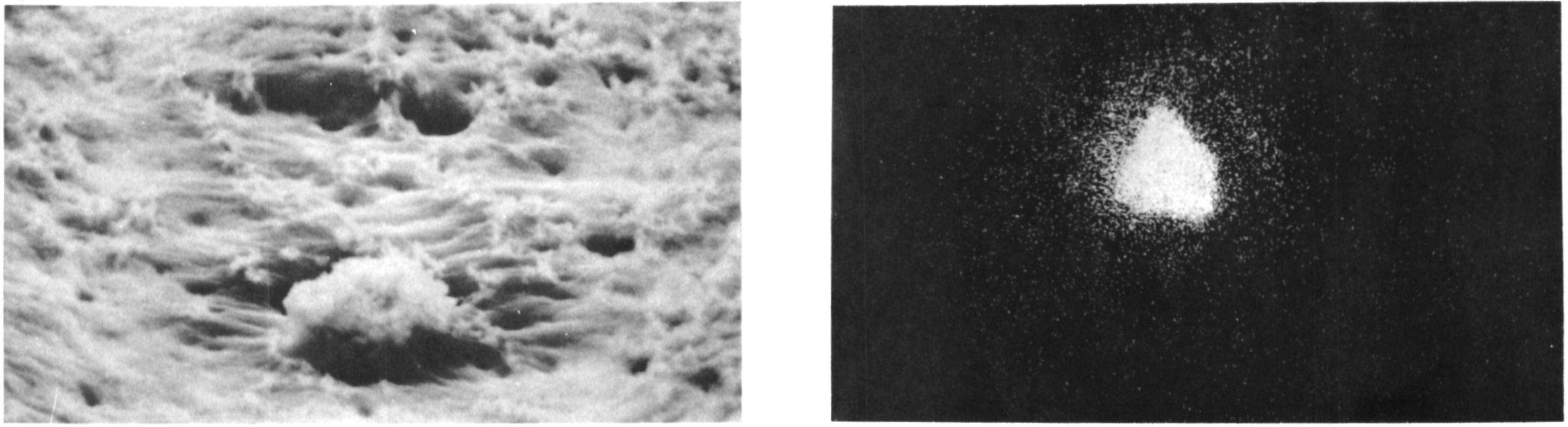

a) ELECTRON PHOTOMICROGRAPH

MAG: 3000x

b) X–RAY SHOWING SILICON (WHITE AREA)

MAG: 3000x

c) X–RAY SHOWING URANIUM

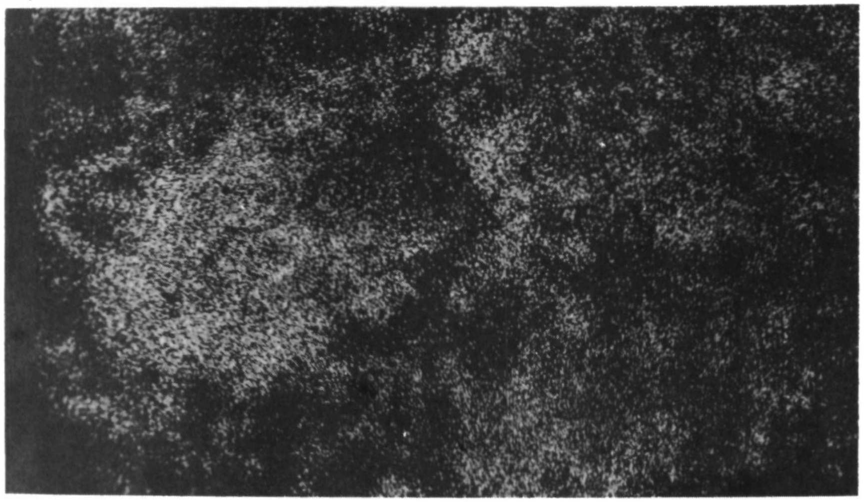

MAG: 3000x

FIG. 39

EXAMPLES OF IR SPECTROPHOTOMETRIC ABSORPTION MEASUREMENTS OBTAINED WITH LONG RUN TIME RF PLASMA TESTS WITH PURE UF_6 INJECTION

RESIDUE REMOVED FROM FUSED SILICA TUBE

THIN WAFER KBr MATRIX USED WITH PERKIN ELMER MODEL 457

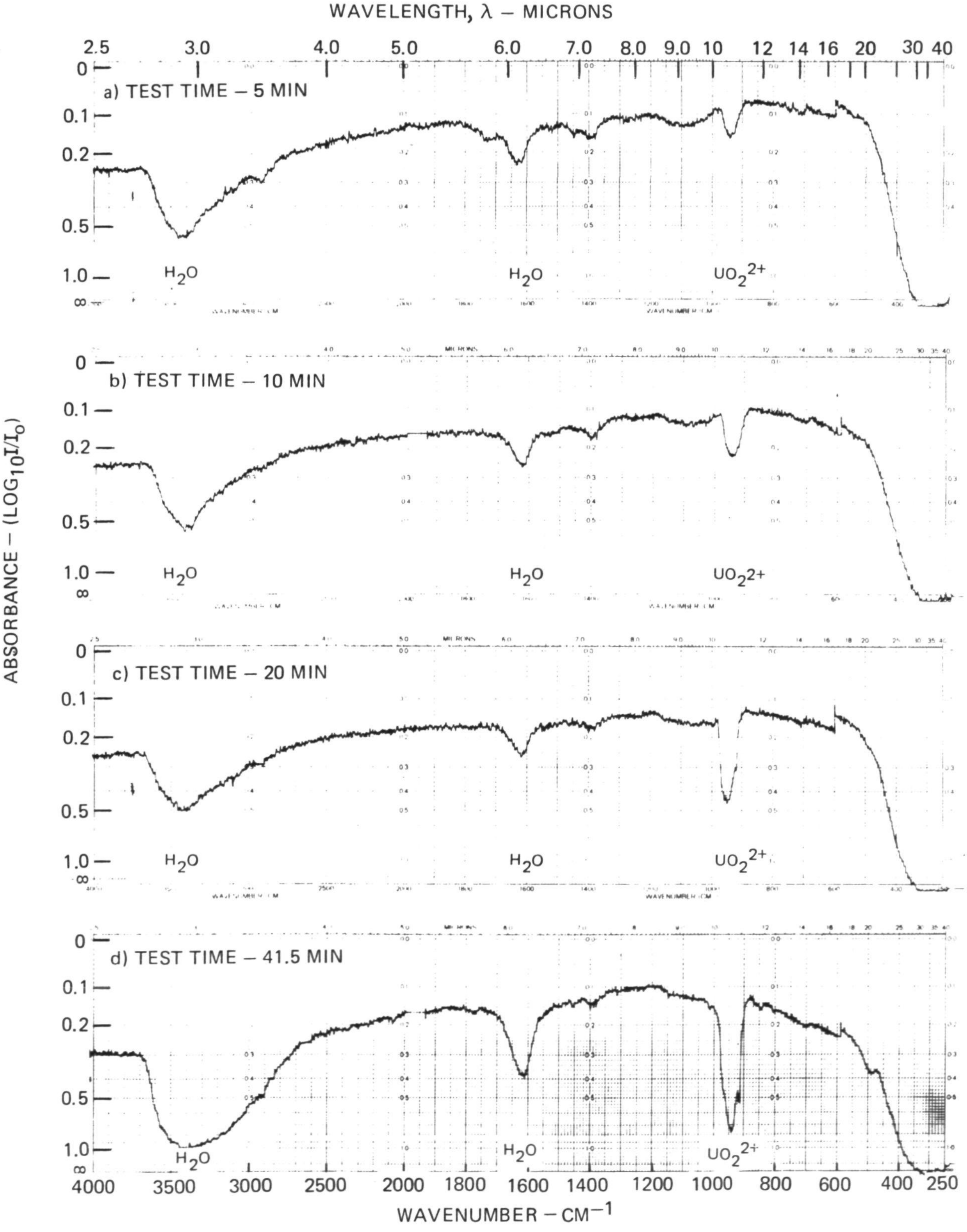

FIG. 40

PHOTOGRAPHS OF FUSED SILICA TUBES AFTER LONG RUN TIME
RF PLASMA TESTS WITH PURE UF_6 INJECTION

SEE TABLE IV FOR ADDITIONAL DETAILS

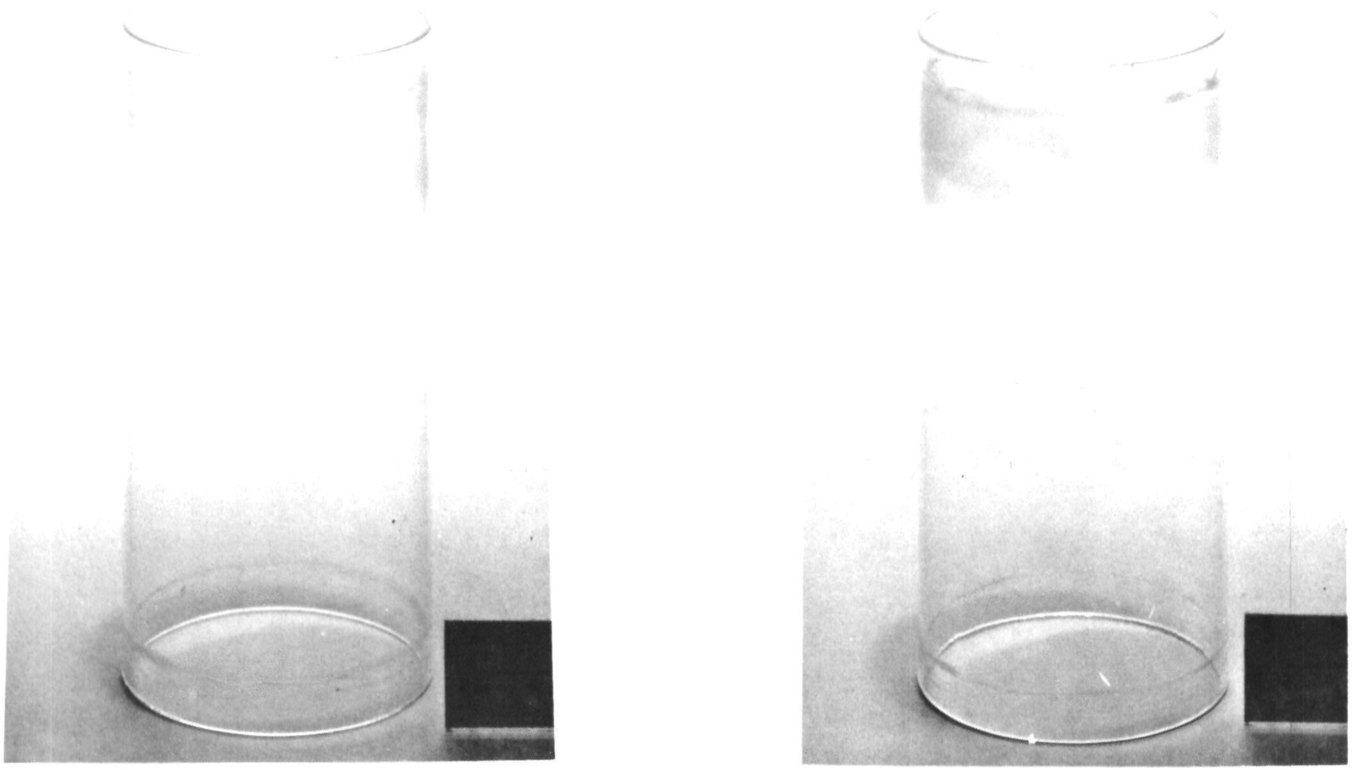

a) TEST TIME–5 MIN
$\dot{m}_{UF_6} = 2.2 \times 10^{-2}$ G/S

12.7 MG RESIDUE

b) TEST TIME–10 MIN
$\dot{m}_{UF_6} = 2.2 \times 10^{-2}$ G/S

17.2 MG RESIDUE

76–03–252–1

FIG. 41

PHOTOGRAPHS OF FUSED SILICA TUBES AFTER LONG RUN TIME RF PLASMA TESTS WITH PURE UF_6 INJECTION

SEE TABLE IV FOR ADDITIONAL DETAILS

ARGON VORTEX INJECTOR END AT TOP

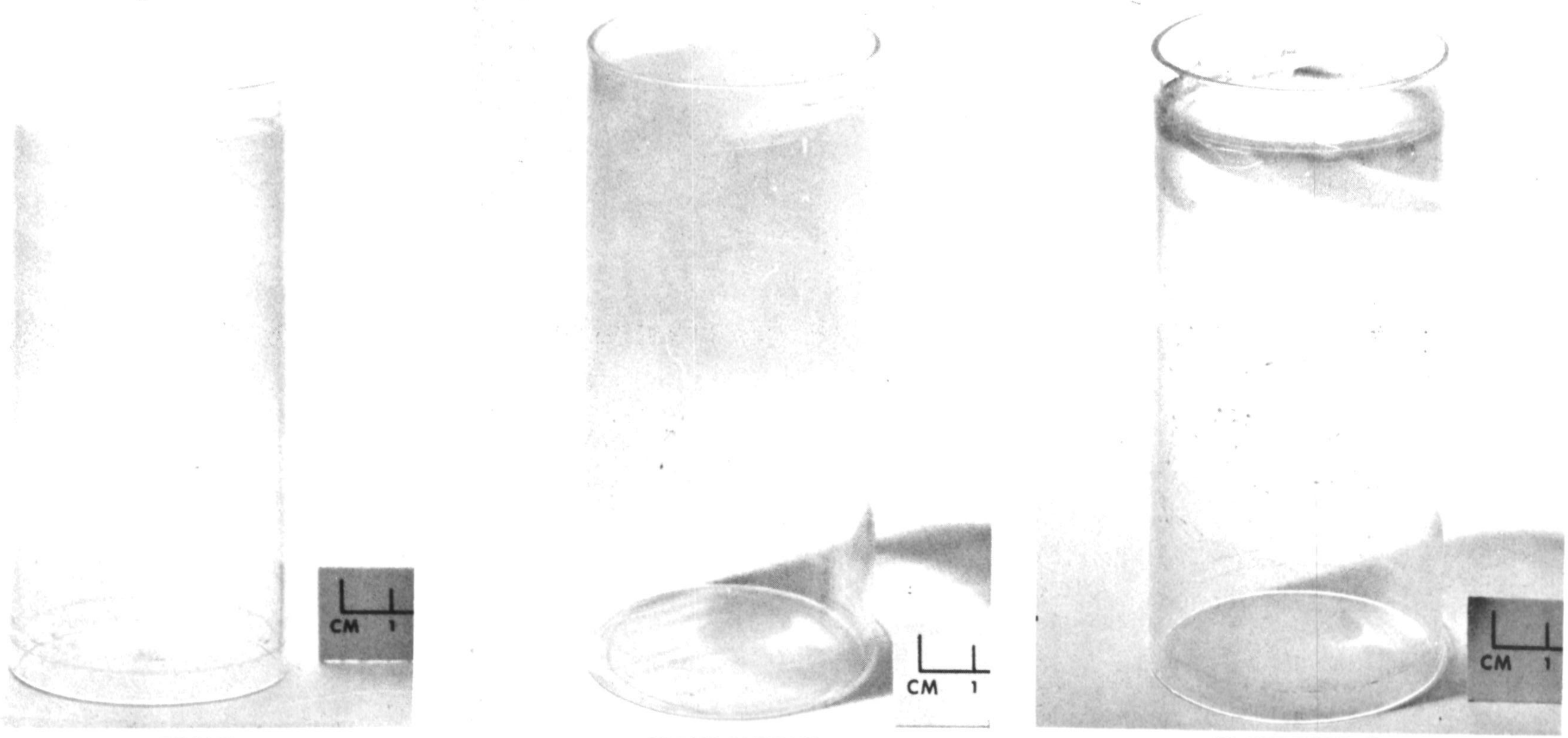

a) TEST TIME – 20 MIN
$\dot{m}_{UF_6} = 2.2 \times 10^{-2}$ G/S

23.9 MG RESIDUE

b) TEST TIME – 30 MIN
$\dot{m}_{UF_6} = 2.2 \times 10^{-2}$ G/S

35.7 MG RESIDUE

c) TEST TIME – 41.5 MIN
$\dot{m}_{UF_6} = 2.2 \times 10^{-2}$ G/S

30.4 MG RESIDUE
(INCLUDING APPROXIMATELY 10 MG OF SILICONE GREASE INITIALLY DEPOSITED ON TUBES FOR PROVIDING O–RING SEAL)

FIG. 42

PHOTOGRAPHS OF FUSED SILICA TUBE AND SILICONE O–RINGS AFTER RF PLASMA TEST WITH MAXIMUM INJECTION OF PURE UF_6

SEE TABLE V FOR ADDITIONAL DETAILS

a) TEST TIME – 1.2 MIN $\dot{m}_{UF_6} = 0.21$ G/S

134.7 MG RESIDUE

ARGON VORTEX INJECTOR END AT TOP

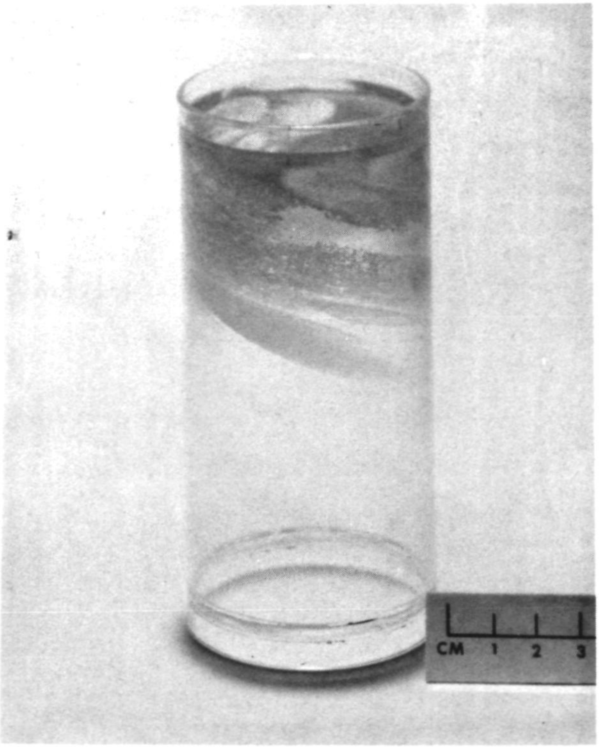

b) SILICONE O–RINGS AS USED WITH KEL–F OIL

NOTE EROSION ON PORTION THAT FACED PLASMA REGION

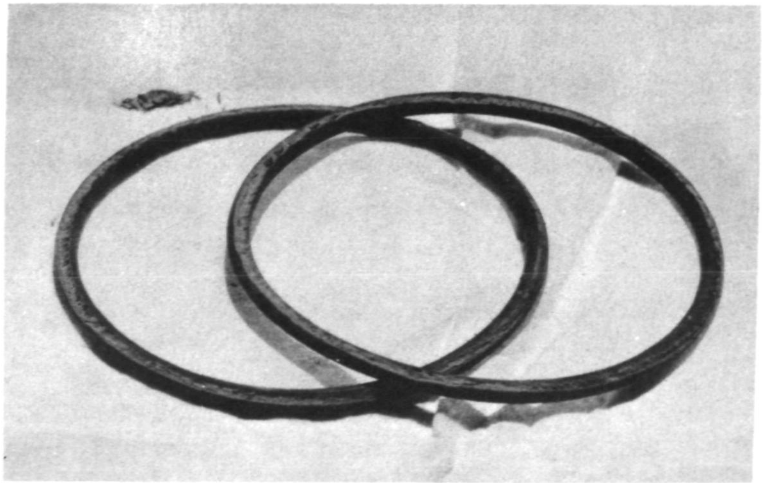

FIG. 43

ELECTRON PHOTOMICROGRAPHS OF A SAMPLE RESIDUE FROM INSIDE SURFACE OF FUSED SILICA TUBE AFTER RF PLASMA TEST WITH MAXIMUM PURE UF_6 INJECTION

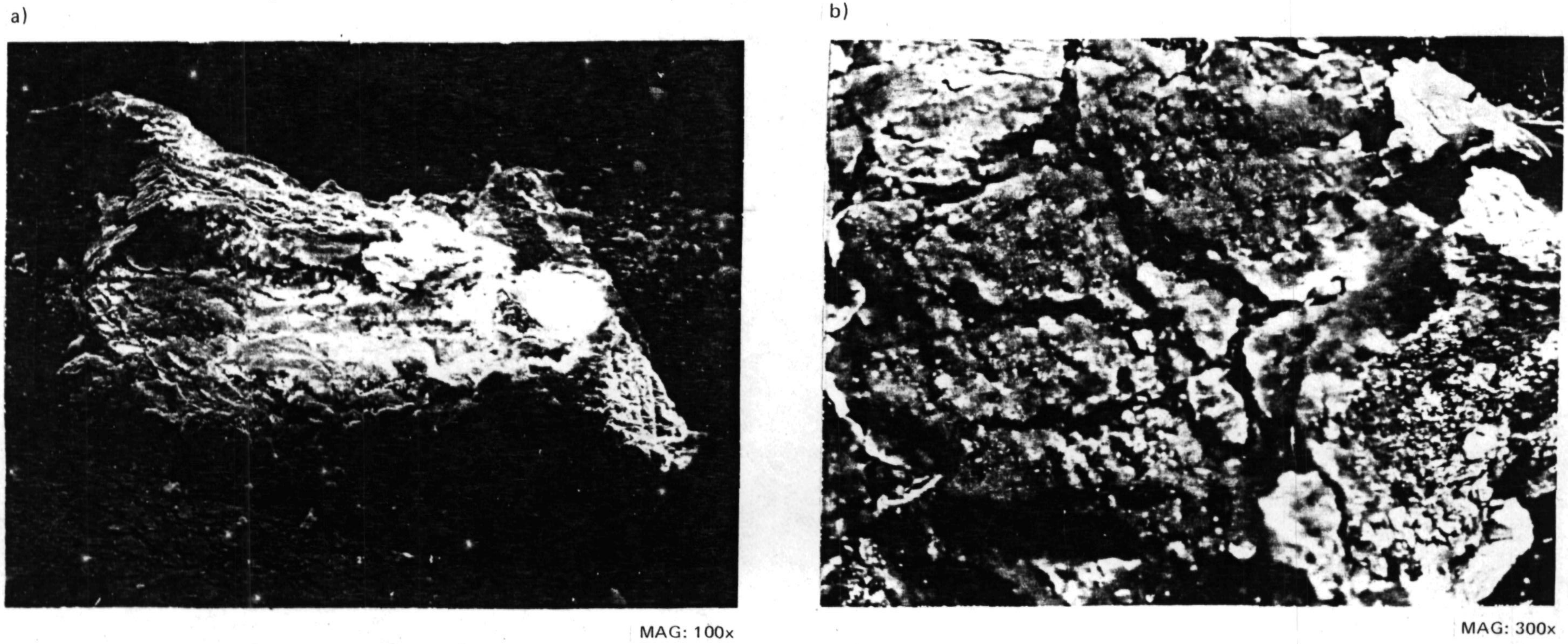

FIG. 44

PHOTOGRAPHS OF X–RAY MAPS OF A SAMPLE RESIDUE FROM INSIDE SURFACE OF FUSED SILICA TUBE AFTER RF PLASMA TEST WITH MAXIMUM PURE UF_6 INJECTION

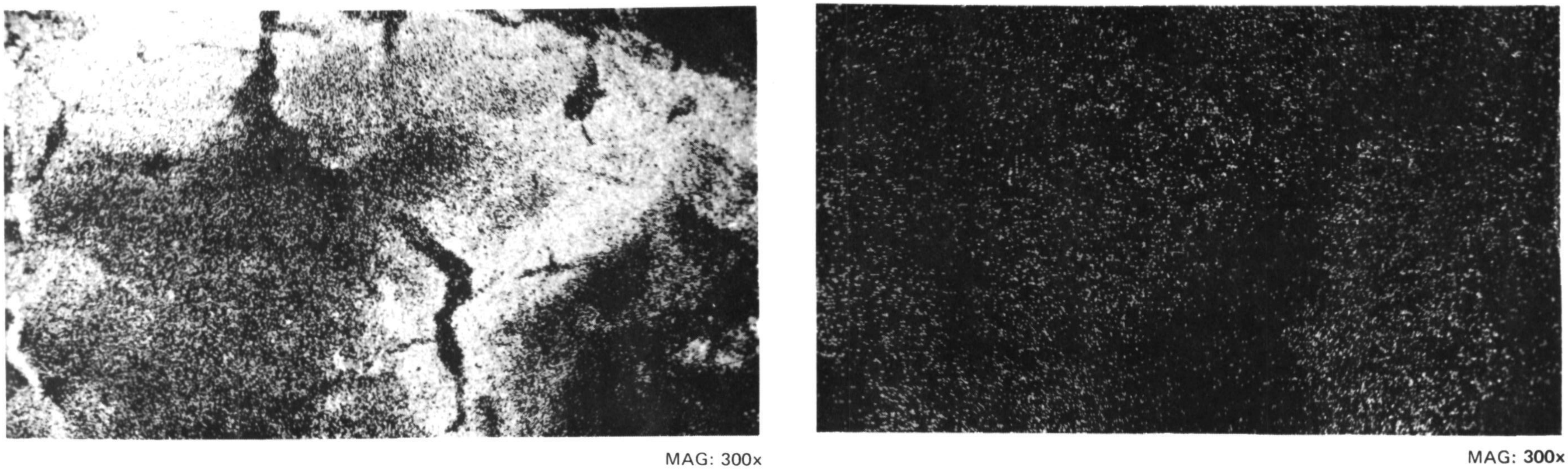

a) X–RAY SHOWING URANIUM (WHITE AREA)

b) X–RAY SHOWING FLUORINE

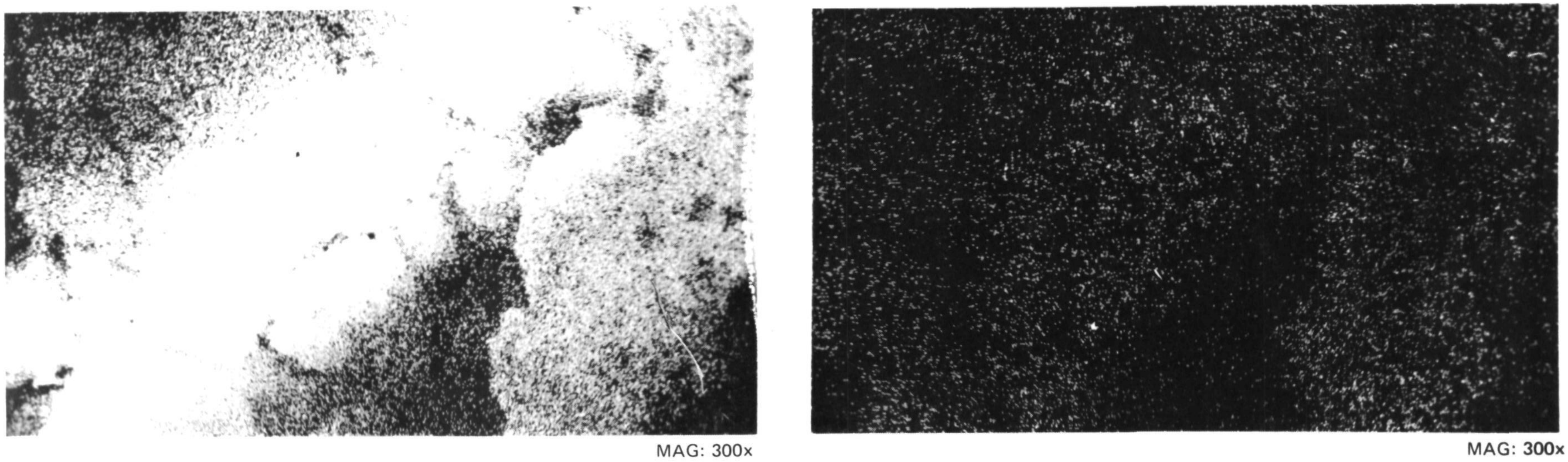

c) X–RAY SHOWING SILICON

d) X–RAY SHOWING OXYGEN

FIG. 45

SURFACE CHARACTERISTICS OF RESIDUE DEPOSITED ON I.D. OF FUSED SILICA TUBE AFTER HOT FLOW TEST WITH UF_6 INJECTION

TEST CASE 11
REFER TO TABLE III

a) PHOTOGRAPH OF CROSS–SECTION SHOWING TUBE AND COATING

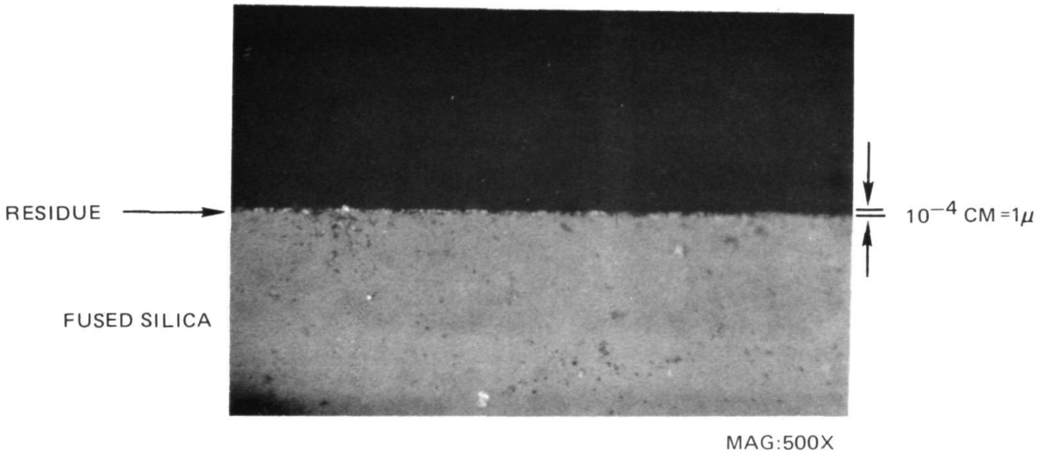

b) PROFILOMETER TRACE (TALYSURF 4) OF RESIDUE ON TUBE
SEE FIG. 46 FOR EXPANDED SCALE TRACE

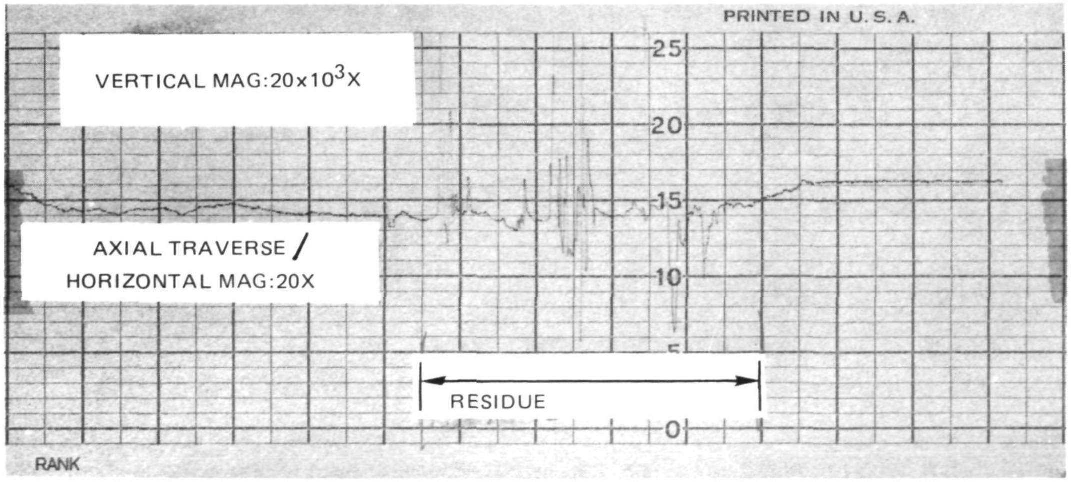

FIG. 46

PROFILOMETER TRACE (TALYSURF 4) OF RESIDUE DEPOSITED ON I.D. OF FUSED SILICA TUBE AFTER RF PLASMA TEST WITH UF_6 INJECTION

TEST CASE 11 REFER TO TABLE III

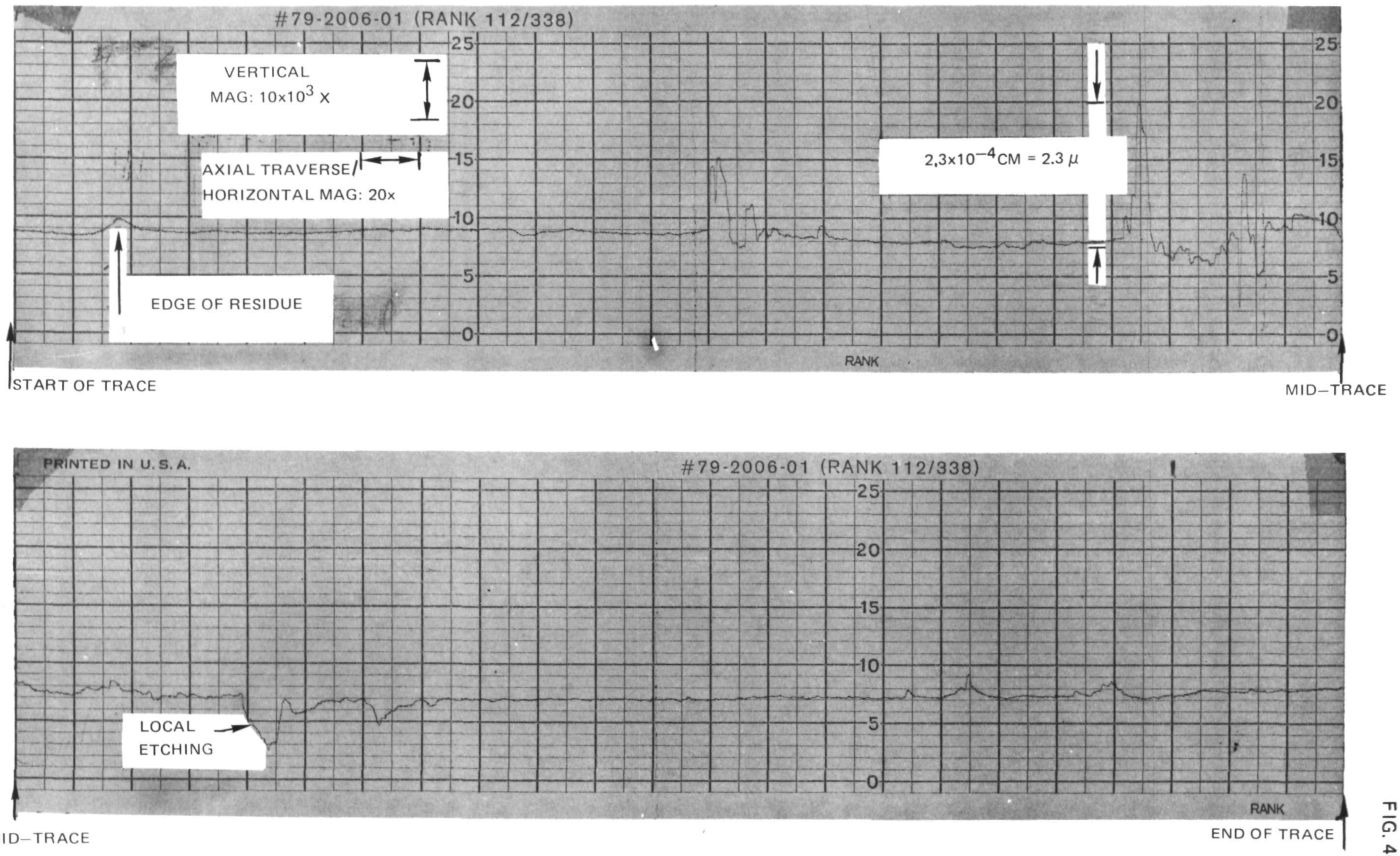

76–03–137–3

EXAMPLE OF SURFACE CHEMICAL ANALYSIS OF URANIUM COMPOUND RESIDUE USING SECONDARY ION MASS SPECTROMETER

238–U 254–UO 257–UF 270–UO_2 273–UOF 276–UF_2 286–UO_3

a) UO_2F_2 STANDARD REFERENCE

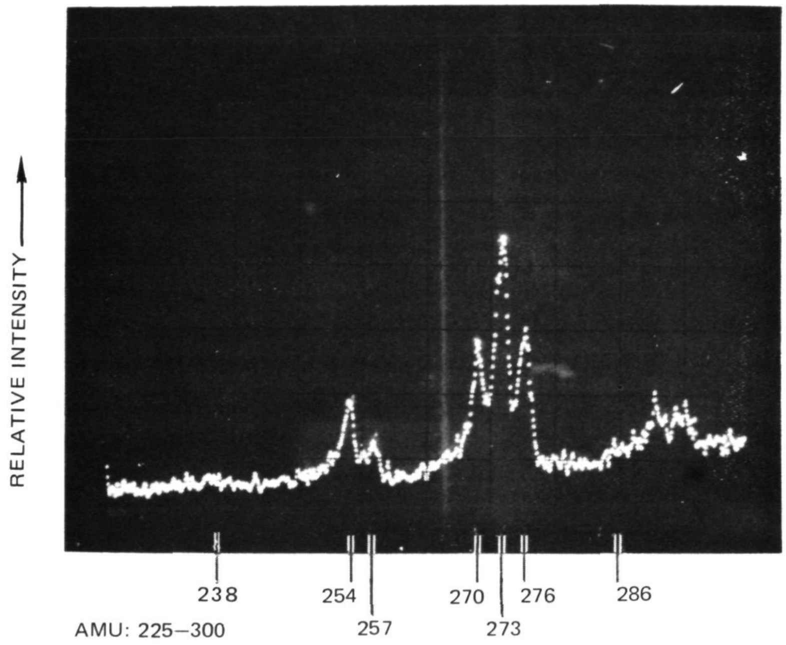

b) RESIDUE SAMPLE FROM FUSED SILICA TUBE AFTER RF TEST WITH PURE UF_6 INJECTION

WATER SOLUBLE RESIDUE TREATED WITH NITRIC ACID (HNO_3)
TO DRIVE OFF HF AND HEATED TO FORM OXIDE

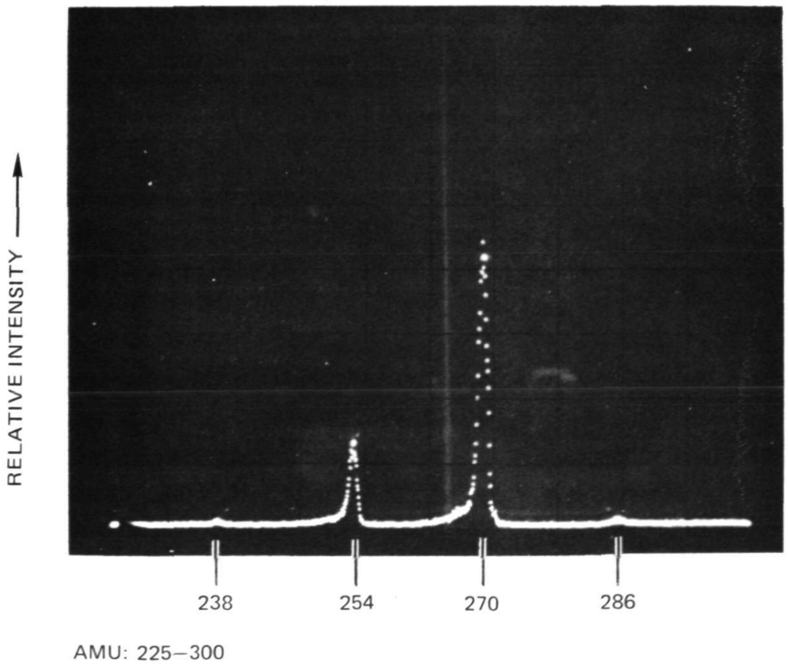

FIG. 48

EXAMPLES OF IR SPECTROPHOTOMETRIC ABSORPTION MEASUREMENTS

THIN WAFER KBr MATRIX USED WITH PERKIN ELMER MODEL 457

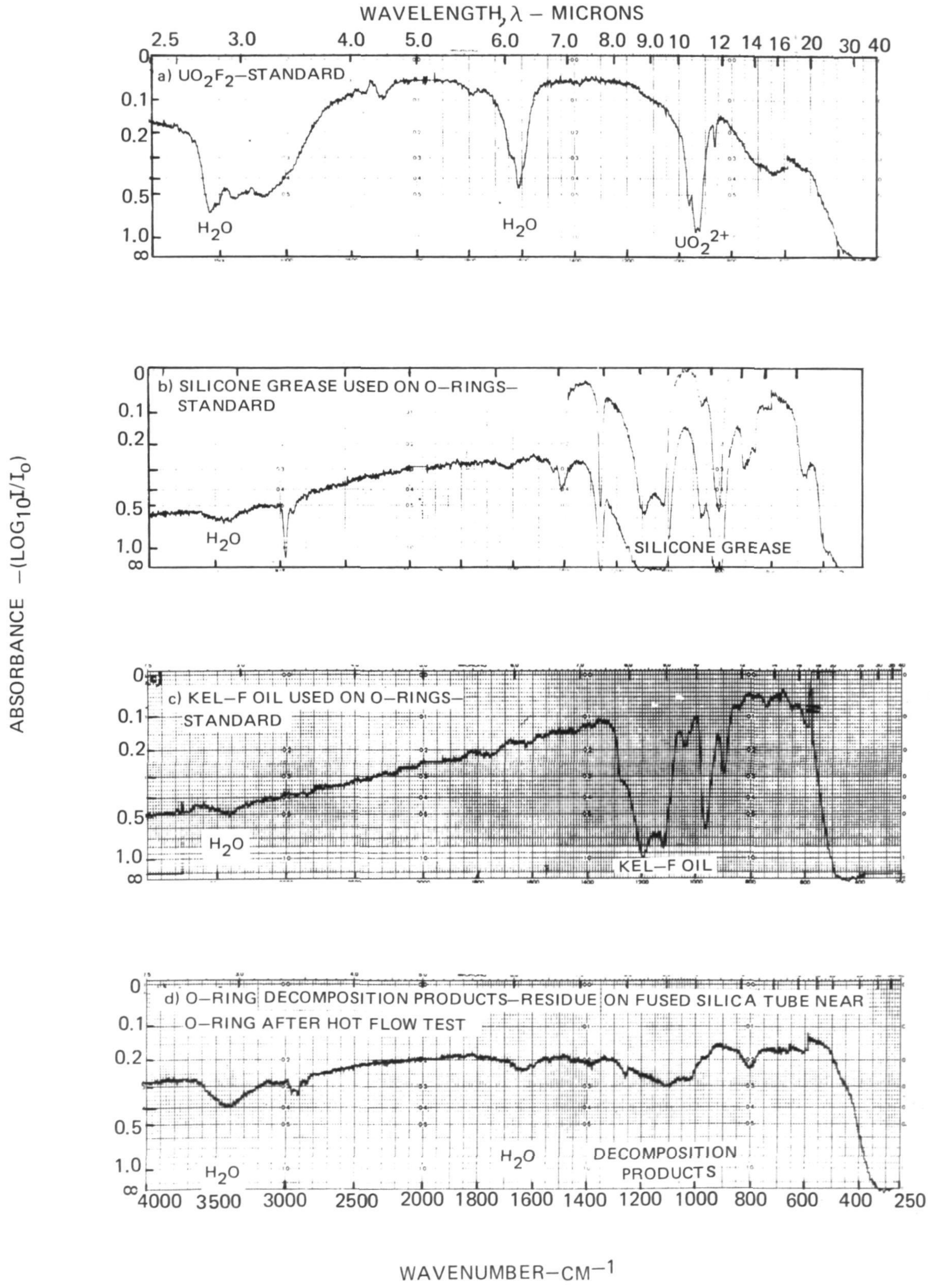

76–03–76–2

EXAMPLES OF IR SPECTROPHOTOMETRIC ABSORPTION MEASUREMENTS

THIN WAFER KBr MATRIX USED WITH PERKIN ELMER MODEL 457

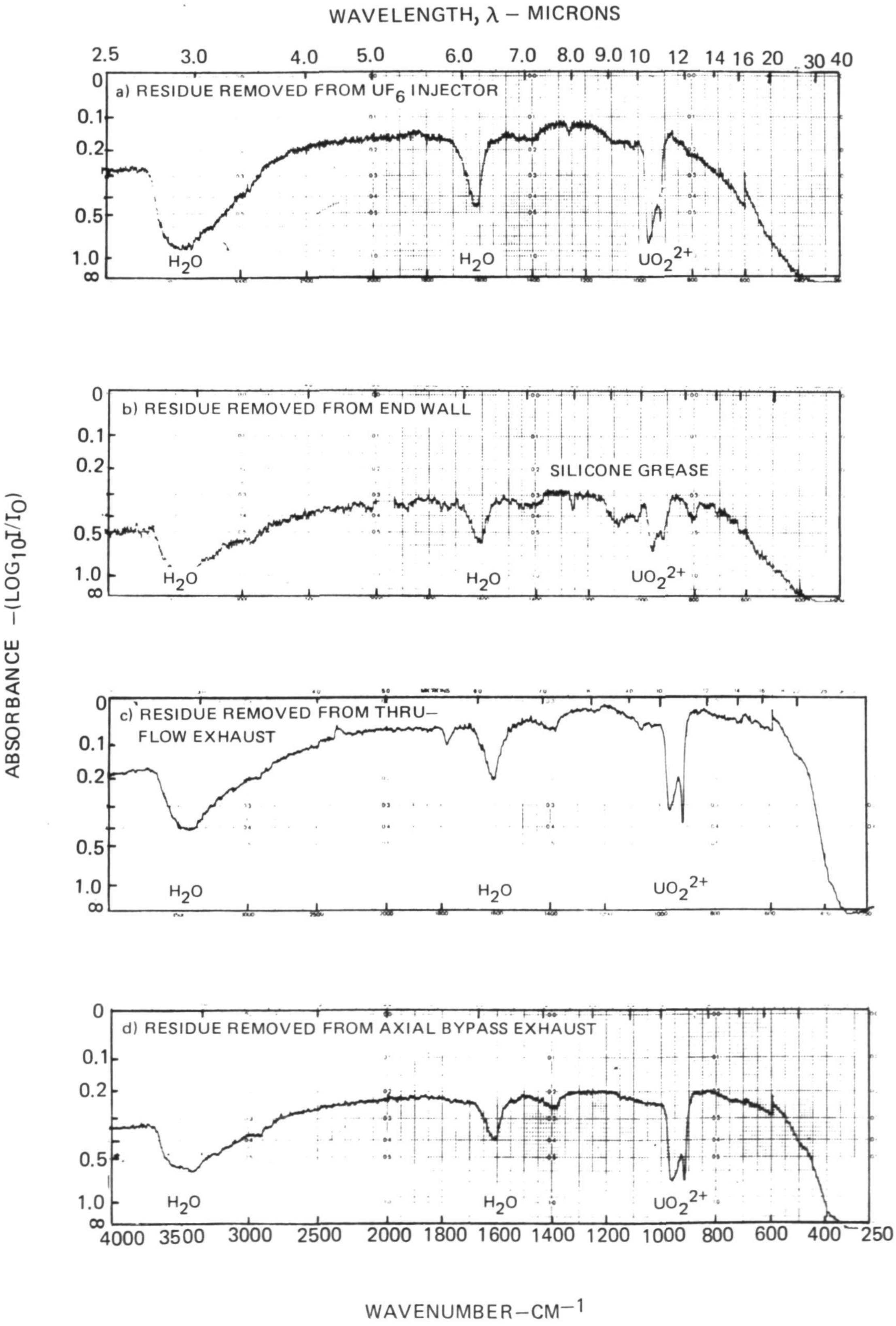

76–03–76–1

ELECTRON PHOTOMICROGRAPHS OF UO_2F_2 STANDARD REFERENCE MATERIAL

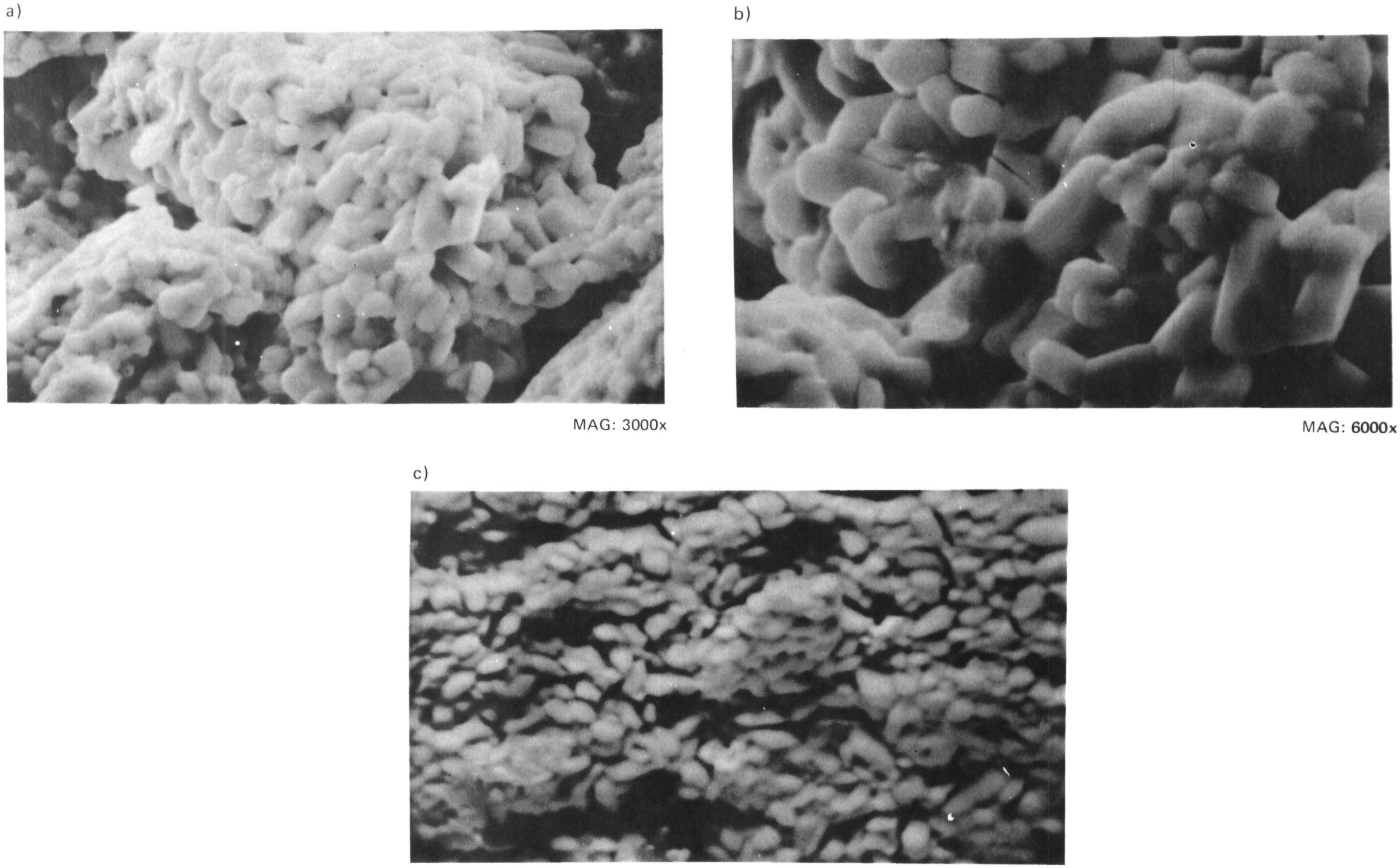

a) MAG: 3000x

b) MAG: 6000x

c) MAG: 2400x

FIG. 50

FIG. 51

PHOTOGRAPHS OF X–RAY MAPS OF UO_2F_2 STANDARD REFERENCE MATERIAL

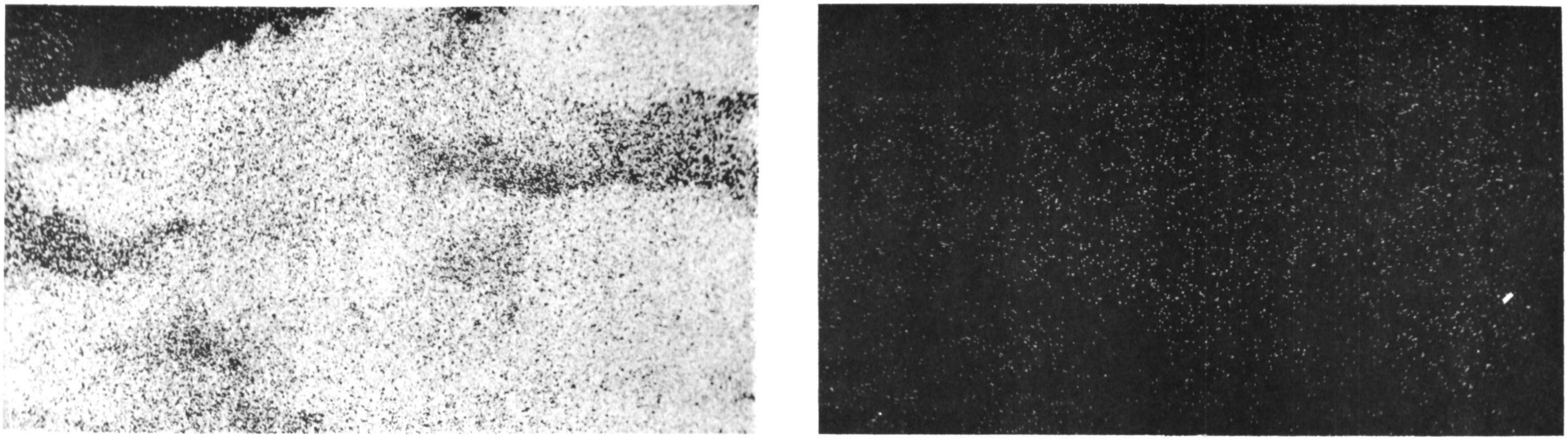

a) X–RAY SHOWING URANIUM (WHITE AREA)

MAG: 2400x

b) X–RAY SHOWING FLUORINE

MAG: 2400x

c) X–RAY SHOWING OXYGEN

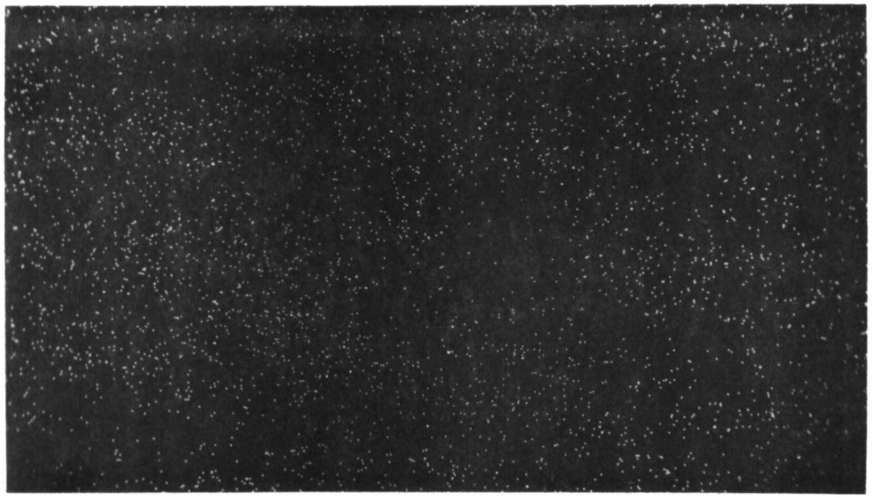

MAG: 2400x

FIG. 52

EXAMPLES OF URANIUM ABSORPTION SPECTRA IN WATER SOLUBLE RESIDUE

a) URANIUM SAMPLE FROM WATER SOLUBLE PORTION OF RESIDUE FROM AXIAL BYPASS EXHAUST DUCT

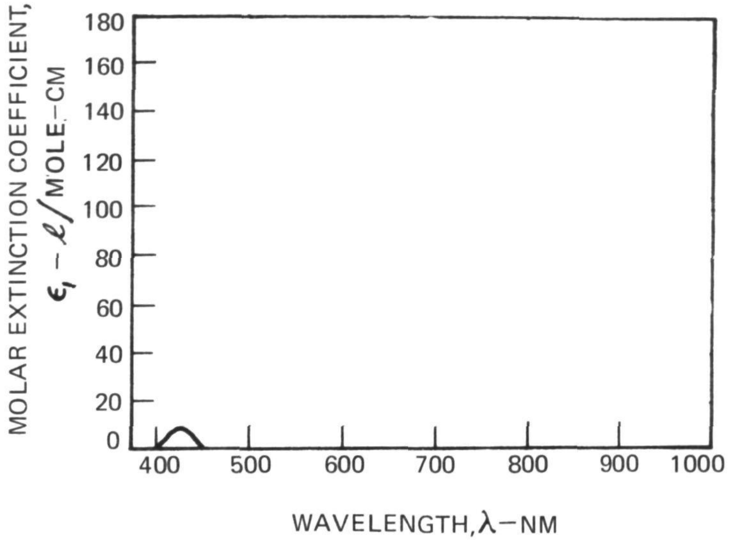

b) STANDARD ABSORPTION SPECTRUM OF URANIUM IN AQUEOUS SOLUTION

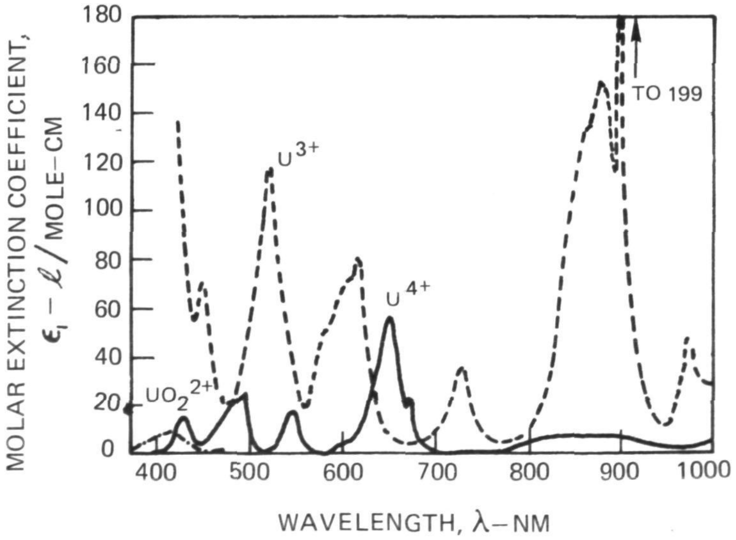

EXAMPLE OF X–RAY DIFFRACTION PATTERNS OBTAINED FROM POST TEST ANALYSIS OF RESIDUE FROM INSIDE SURFACE OF FUSED SILICA TUBE AND ENDWALL AFTER RF PLASMA TEST WITH PURE UF_6 INJECTION

NO PRIOR PREPARATION OF SAMPLES

ALL SAMPLES SUBJECTED TO CuK_α RADIATION IN A NORELCO DIFFRACTOMETER

a) HIGH $\dot{m}_{UF_6}$ CASE

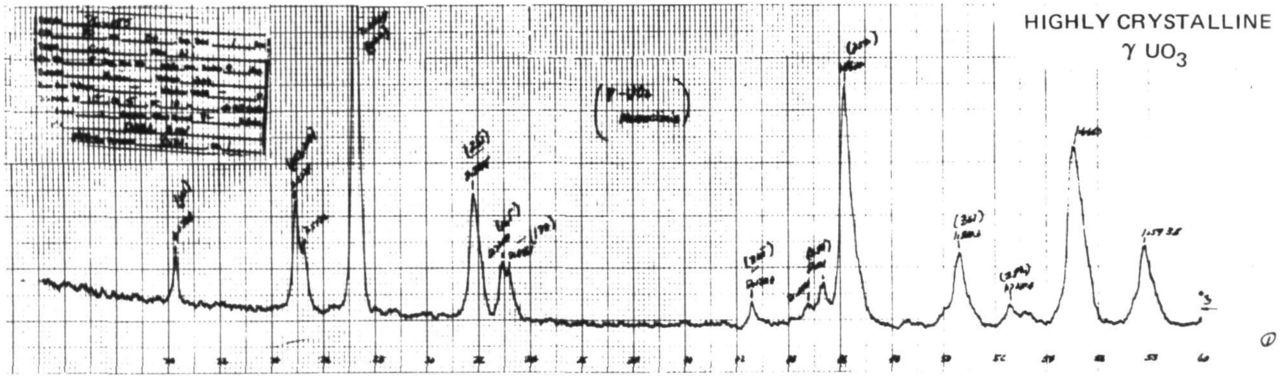

b) LOW $\dot{m}_{UF_6}$ CASE

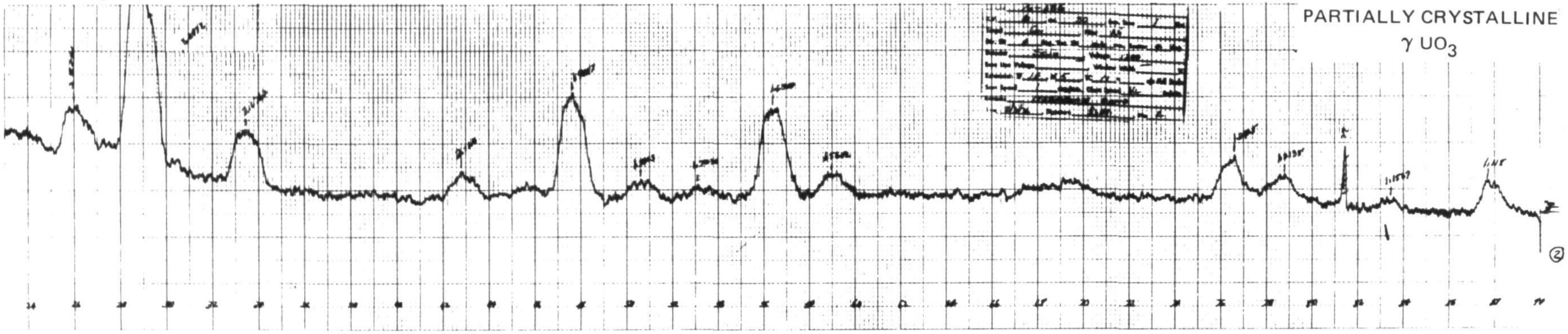

c) END WALL

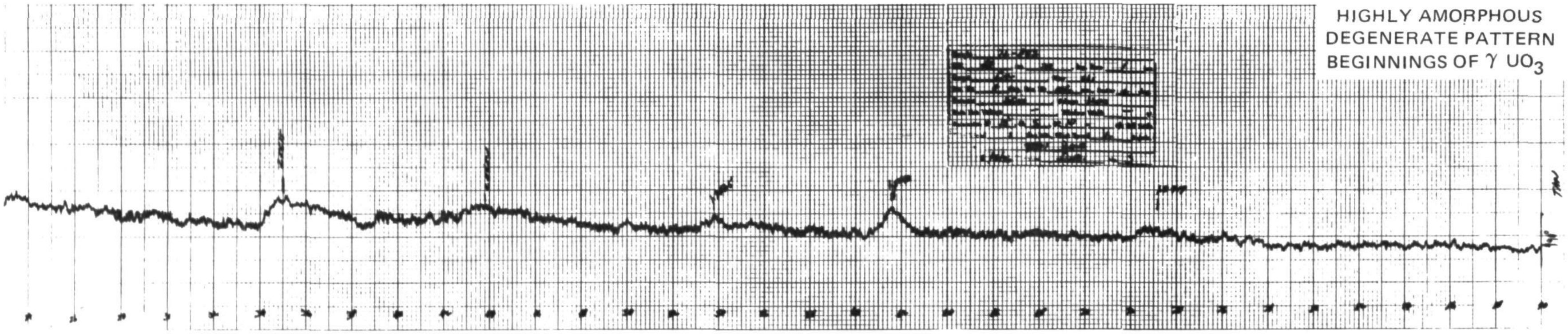

FIG. 53

FIG. 54

EXAMPLE OF ELECTRON DIFFRACTION ANALYSIS OF DISPERSED POWDER FROM UO_2F_2 STANDARD REFERENCE

a) PHOTOGRAPHS OF UO_2F_2 STANDARD REFERENCE

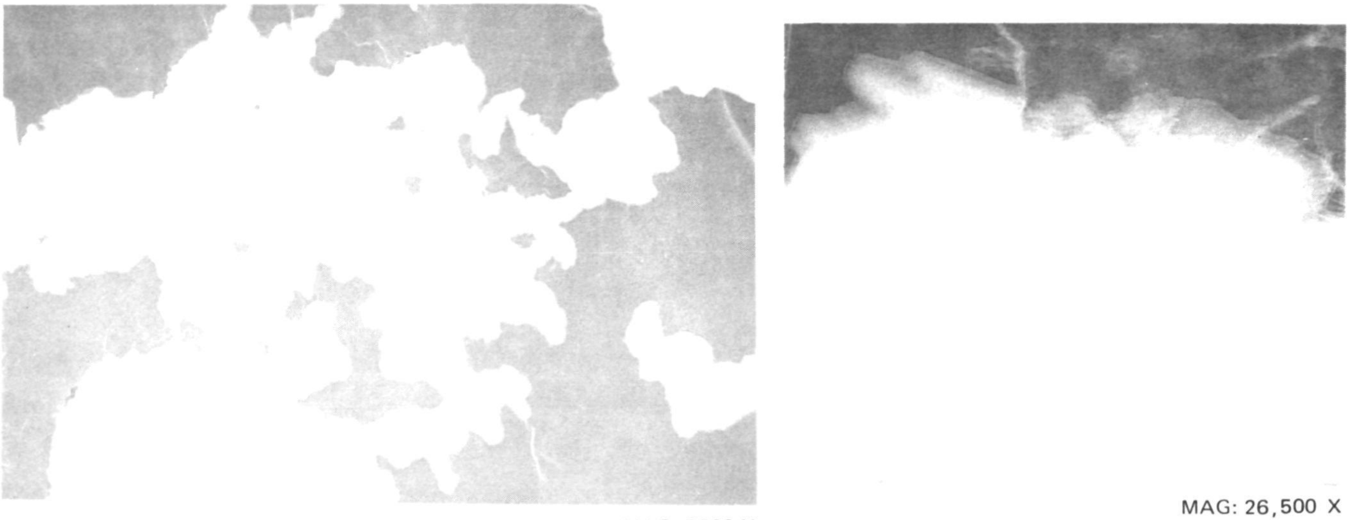

MAG: 3200 X

MAG: 26,500 X

b) PHOTOGRAPH OF ELECTRON DIFFRACTION PATTERN OBTAINED FROM ABOVE SAMPLE

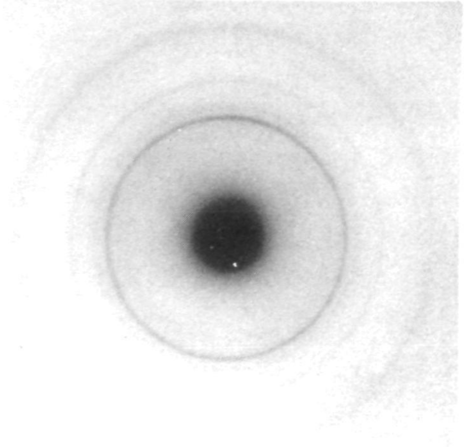

76–03–180–1

ELECTRON PHOTOMICROGRAPHS OF A SAMPLE RESIDUE FROM ENDWALL AFTER RF PLASMA TEST WITH PURE UF_6 INJECTION

SAMPLE NEAR CENTRAL PORTION

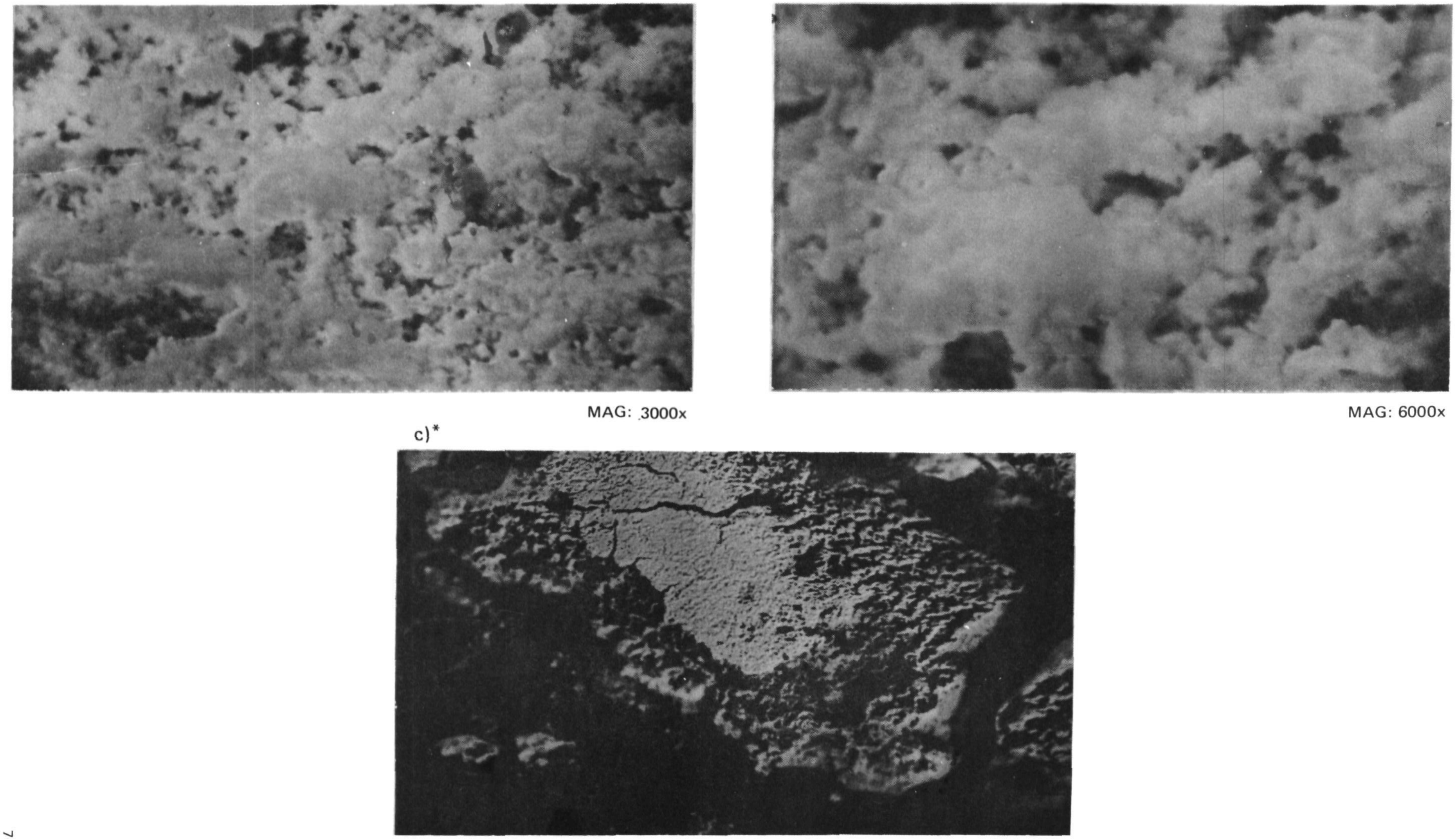
a) MAG: 3000x

b) MAG: 6000x

c)* MAG: 300x

*BACKSCATTERED ELECTRON MICROGRAPH SHOWING TYPICAL TOPOGRAPHICAL VARIATIONS

FIG. 55

PHOTOGRAPHS OF X–RAY MAPS OF A SAMPLE RESIDUE FROM END WALL AFTER RF PLASMA TEST WITH PURE UF_6 INJECTION

a) X–RAY SHOWING URANIUM (WHITE AREA)

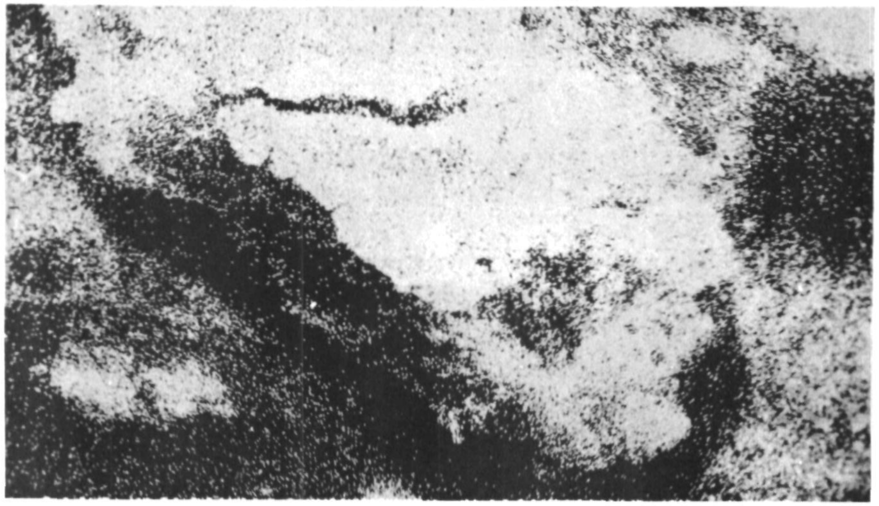

MAG: 300x

b) X–RAY SHOWING FLUORINE

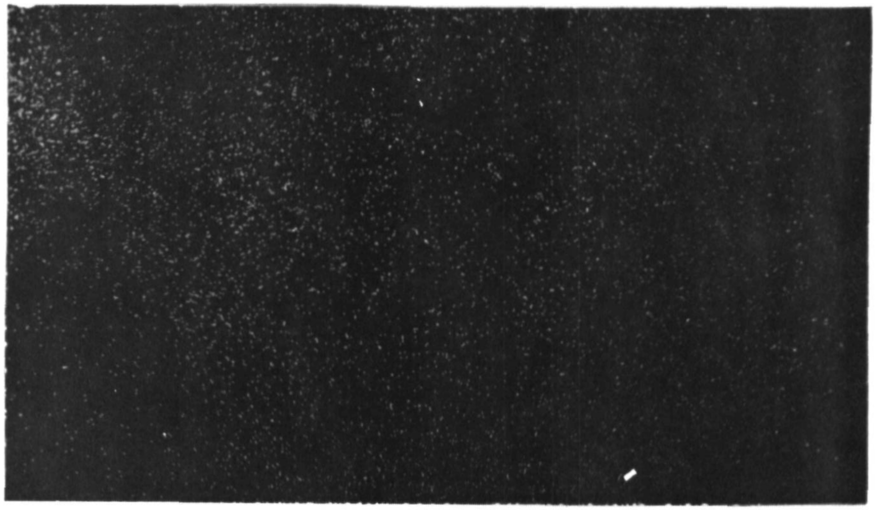

MAG: 300x

c) X–RAY SHOWING COPPER

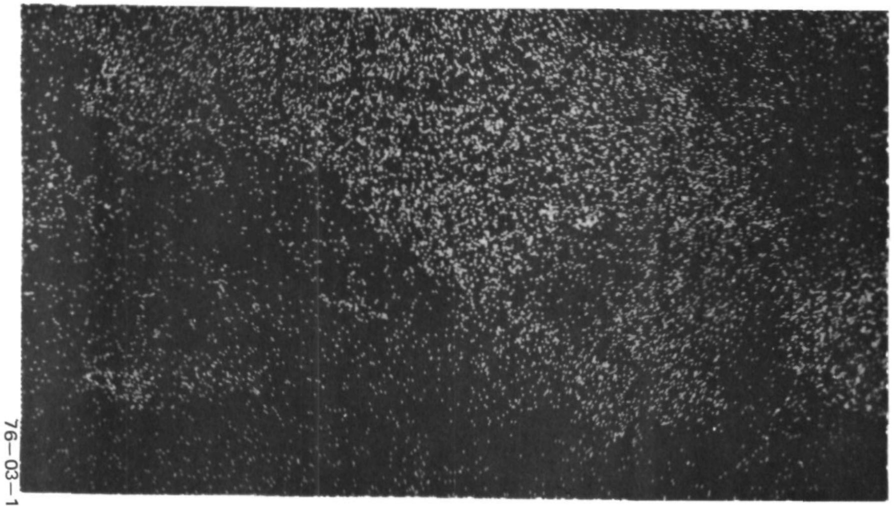

MAG: 300x

d) X–RAY SHOWING OXYGEN

MAG: 300x

FIG. 56

76–03–184–4

FIG. 57

EXAMPLE OF ELECTRON DIFFRACTION ANALYSIS OF DISPERSED RESIDUE REMOVED FROM END WALL AFTER RF PLASMA TEST WITH PURE UF_6 INJECTION

a) PHOTOGRAPHS OF RESIDUE

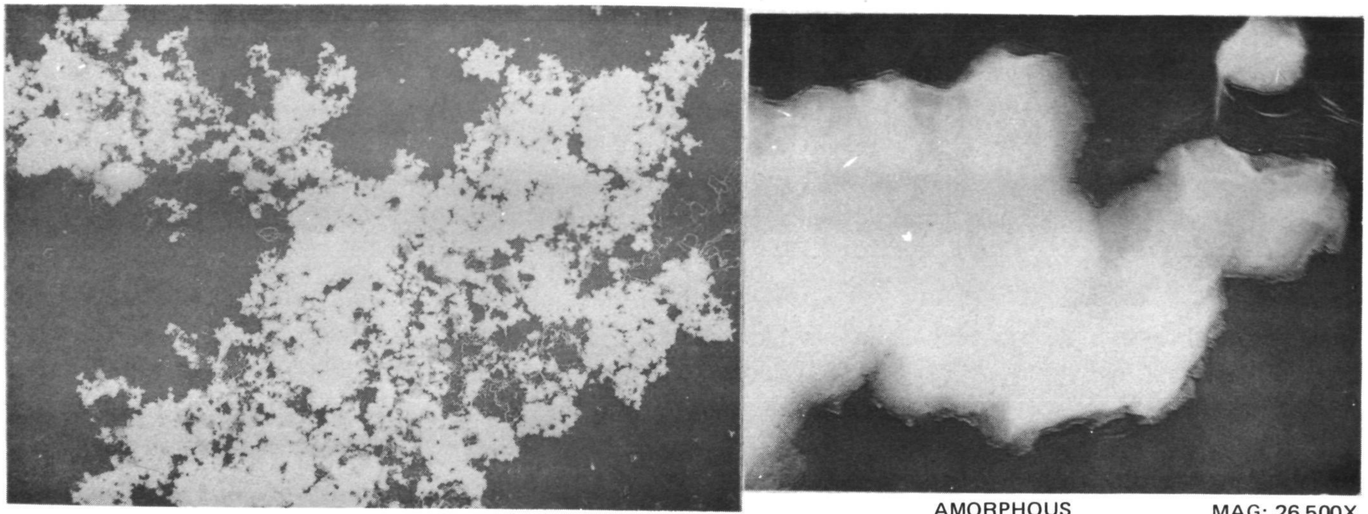

MAG: 3200X

AMORPHOUS

MAG: 26,500X

b) PHOTOGRAPHS OF ELECTRON DIFFRACTION PATTERNS OBTAINED FROM ABOVE SAMPLE

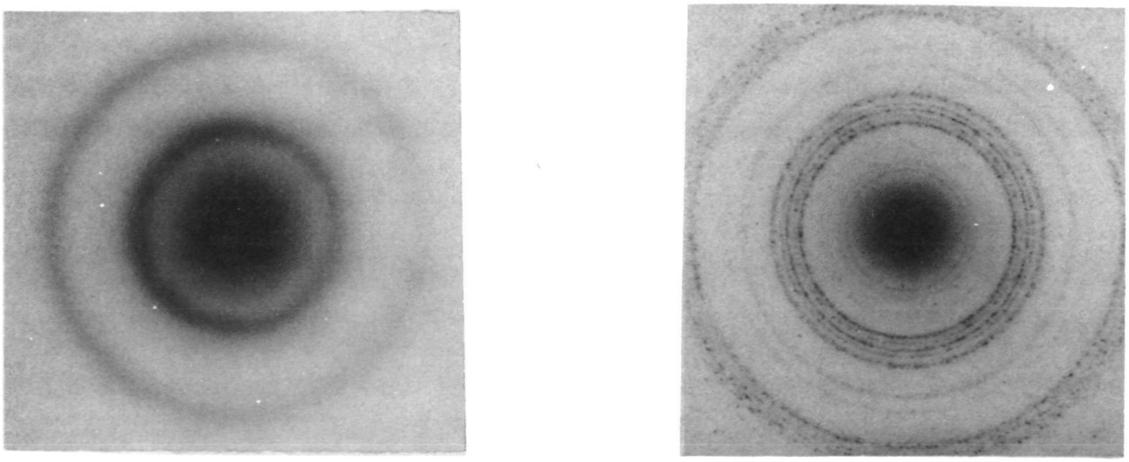

AMORPHOUS MATERIAL

$UF_4 + UO_2$*

*U_4O_9 ALSO POSSIBLE

FIG. 58

ELECTRON PHOTOMICROGRAPHS OF A SAMPLE RESIDUE FROM UF_6 INJECTOR AFTER RF PLASMA TEST WITH PURE UF_6 INJECTION

SAMPLE NEAR TIP OF UF_6 INJECTOR

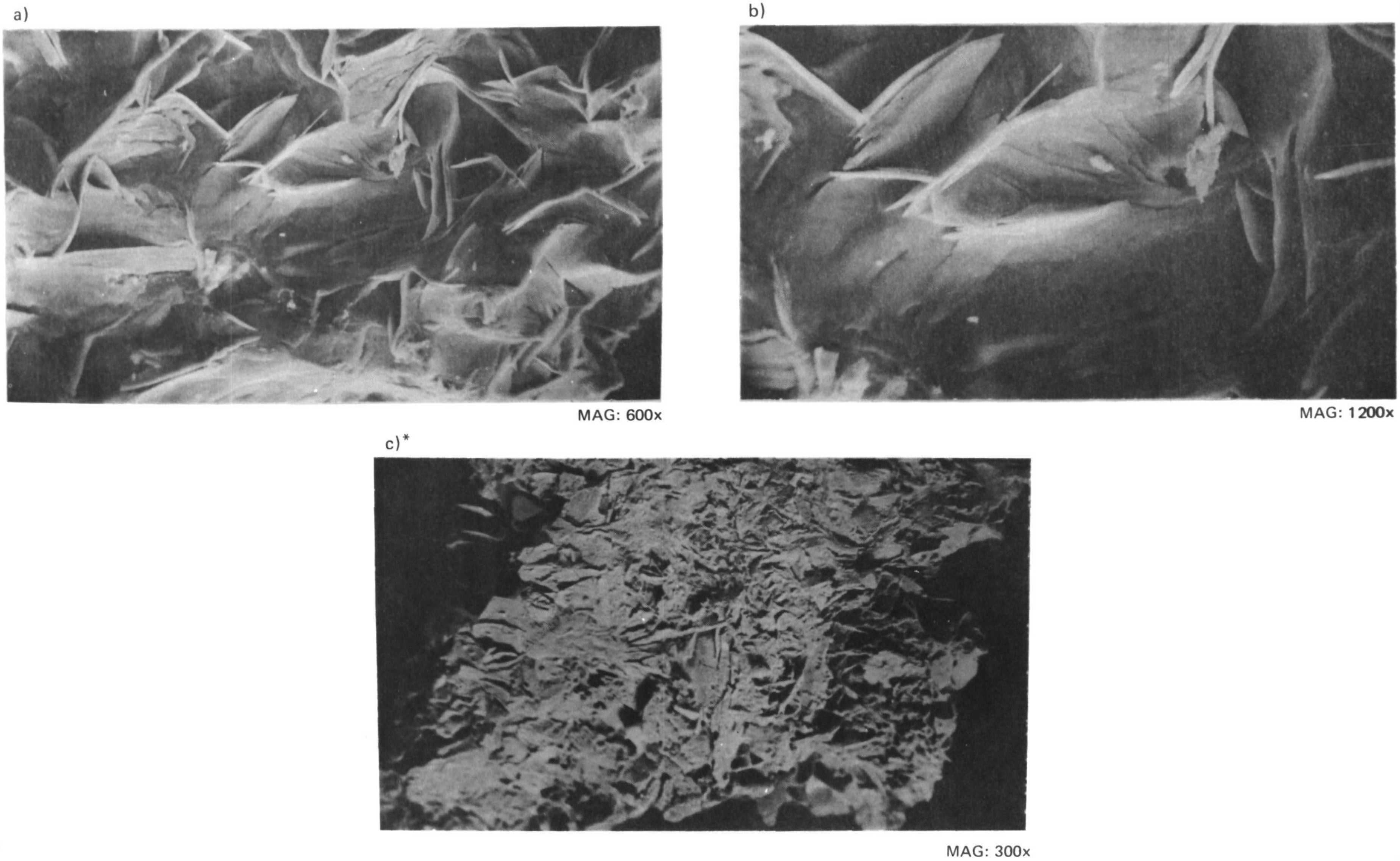

*BACKSCATTERED ELECTRON MICROGRAPH SHOWING TYPICAL TOPOGRAPHICAL VARIATIONS

FIG. 59

PHOTOGRAPHS OF X–RAY MAPS OF A SAMPLE RESIDUE FROM UF_6 INJECTOR AFTER RF PLASMA TEST WITH PURE UF_6 INJECTION

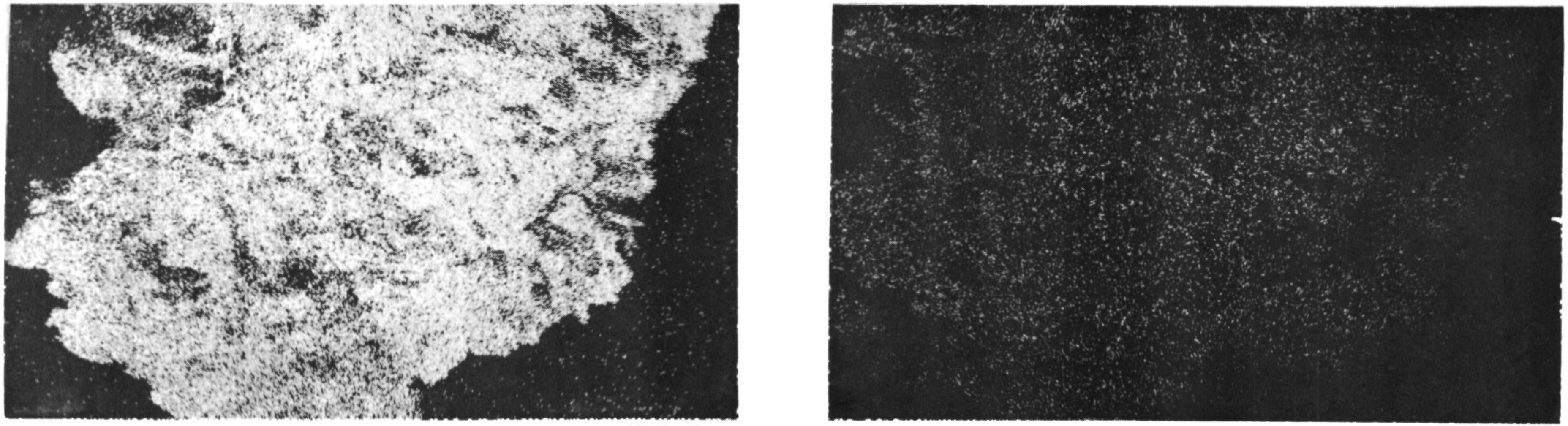

a) X–RAY SHOWING URANIUM (WHITE AREA)

MAG: 300x

b) X–RAY SHOWING FLUORINE

MAG: 300x

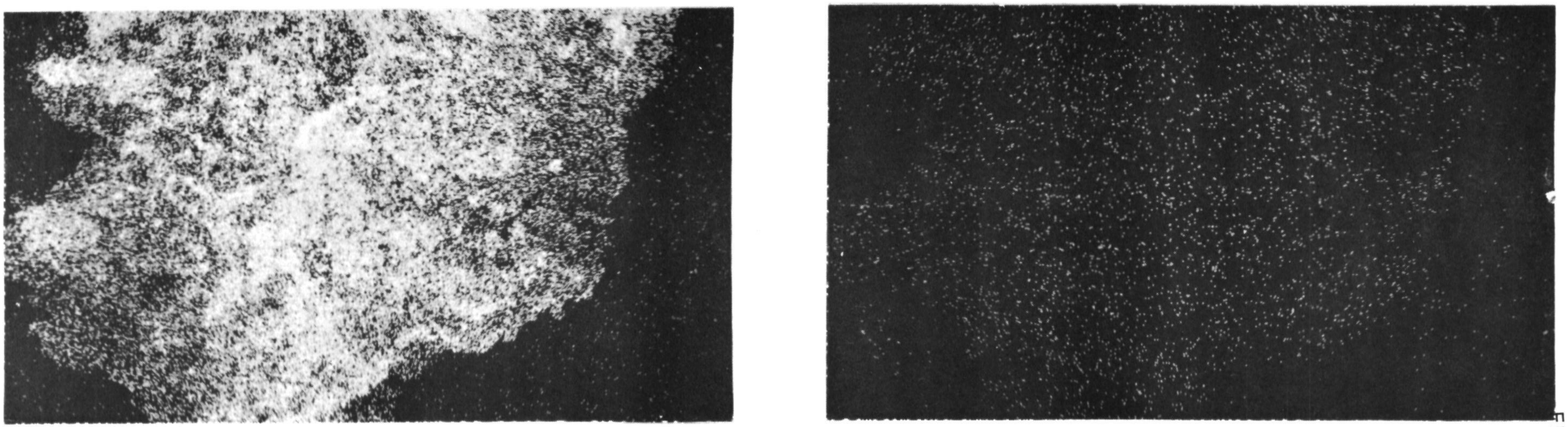

c) X–RAY SHOWING COPPER

MAG: 300x

d) X–RAY SHOWING OXYGEN

MAG: 300x

FIG. 60

EXAMPLE OF ELECTRON DIFFRACTION ANALYSIS OF DISPERSED RESIDUE REMOVED FROM UF_6 INJECTOR AFTER RF PLASMA TEST WITH PURE UF_6 INJECTION

a) PHOTOGRAPHS OF RESIDUE

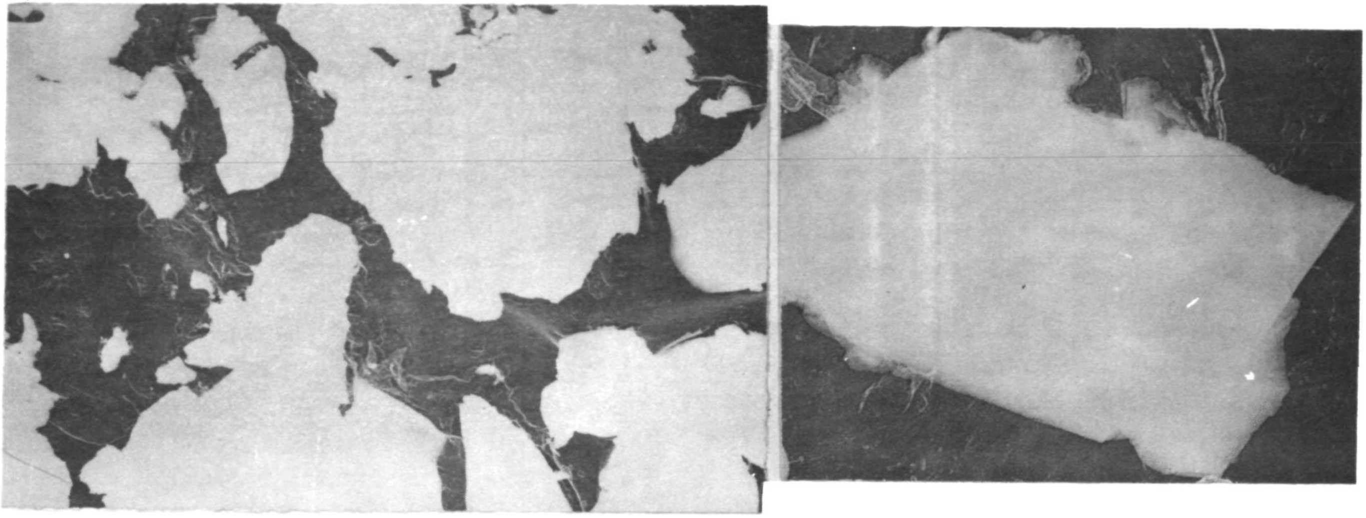

MAG: 3200X

b) PHOTOGRAPHS OF ELECTRON DIFFRACTION PATTERNS OBTAINED FROM ABOVE SAMPLES

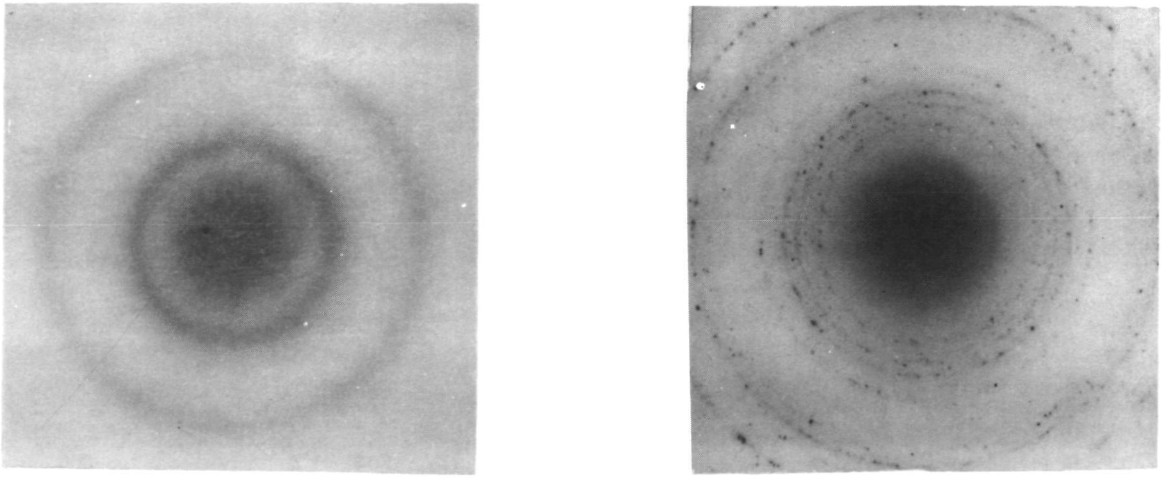

AMORPHOUS MATERIAL

$UF_4 + UO_2$*

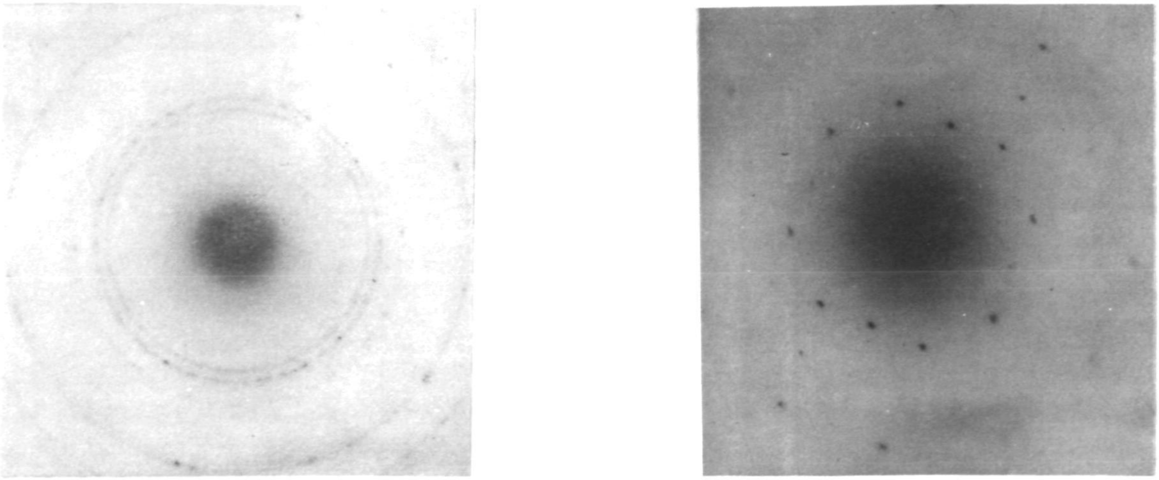

UO_2* + αUO_3**

UNKNOWN SINGLE CRYSTALS

*U_4O_9 ALSO POSSIBLE

**U_3O_8 ALSO POSSIBLE

76–03–180–2

FIG. 61

ELECTRON PHOTOMICROGRAPHS OF A SAMPLE RESIDUE FROM ON–AXIS THRU–FLOW EXHAUST DUCT AFTER RF PLASMA TEST WITH PURE UF_6 INJECTION

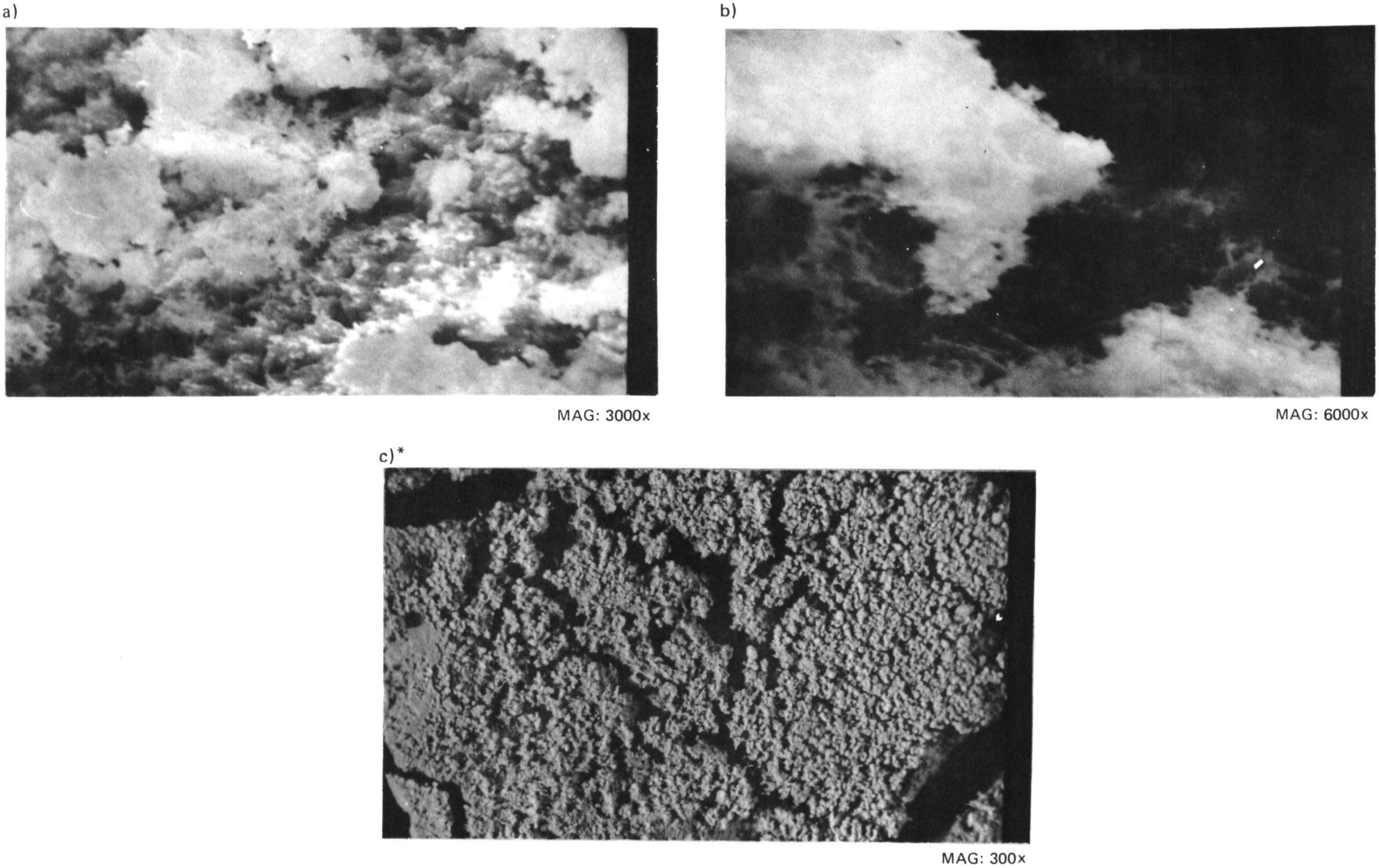

*BACKSCATTERED ELECTRON MICROGRAPH SHOWING TYPICAL TOPOGRAPHICAL VARIATIONS

PHOTOGRAPHS OF X–RAY MAPS OF A SAMPLE RESIDUE FROM ON–AXIS THRU–FLOW EXHAUST DUCT AFTER RF PLASMA TEST WITH PURE UF_6 INJECTION

a) X–RAY SHOWING URANIUM (WHITE AREA)

b) X–RAY SHOWING FLUORINE

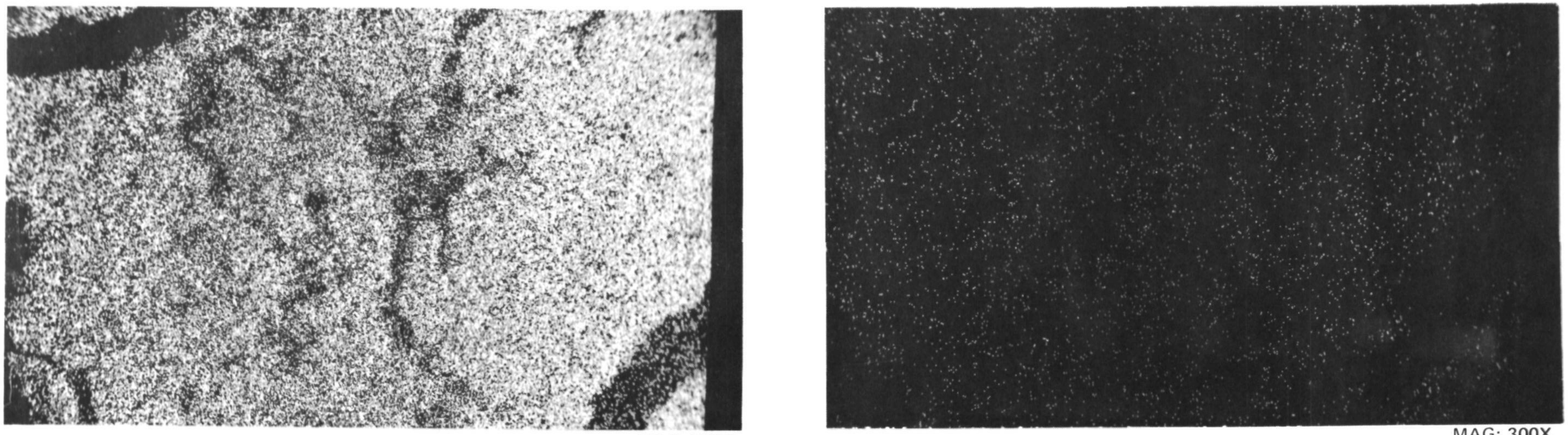

c) X–RAY SHOWING COPPER

d) X–RAY SHOWING OXYGEN

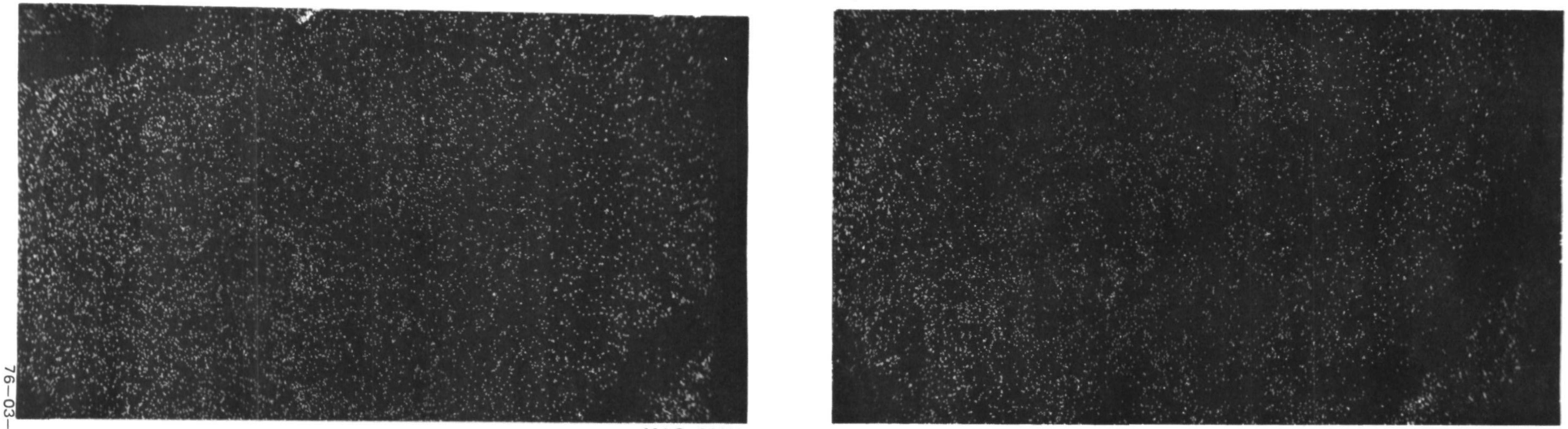

FIG. 62

FIG. 63

ELECTRON PHOTOMICROGRAPHS OF A SAMPLE RESIDUE FROM AXIAL BY–PASS EXHAUST DUCT AFTER RF PLASMA TEST WITH PURE UF_6 INJECTION

POSITION NEAR TO END WALL ASSEMBLY

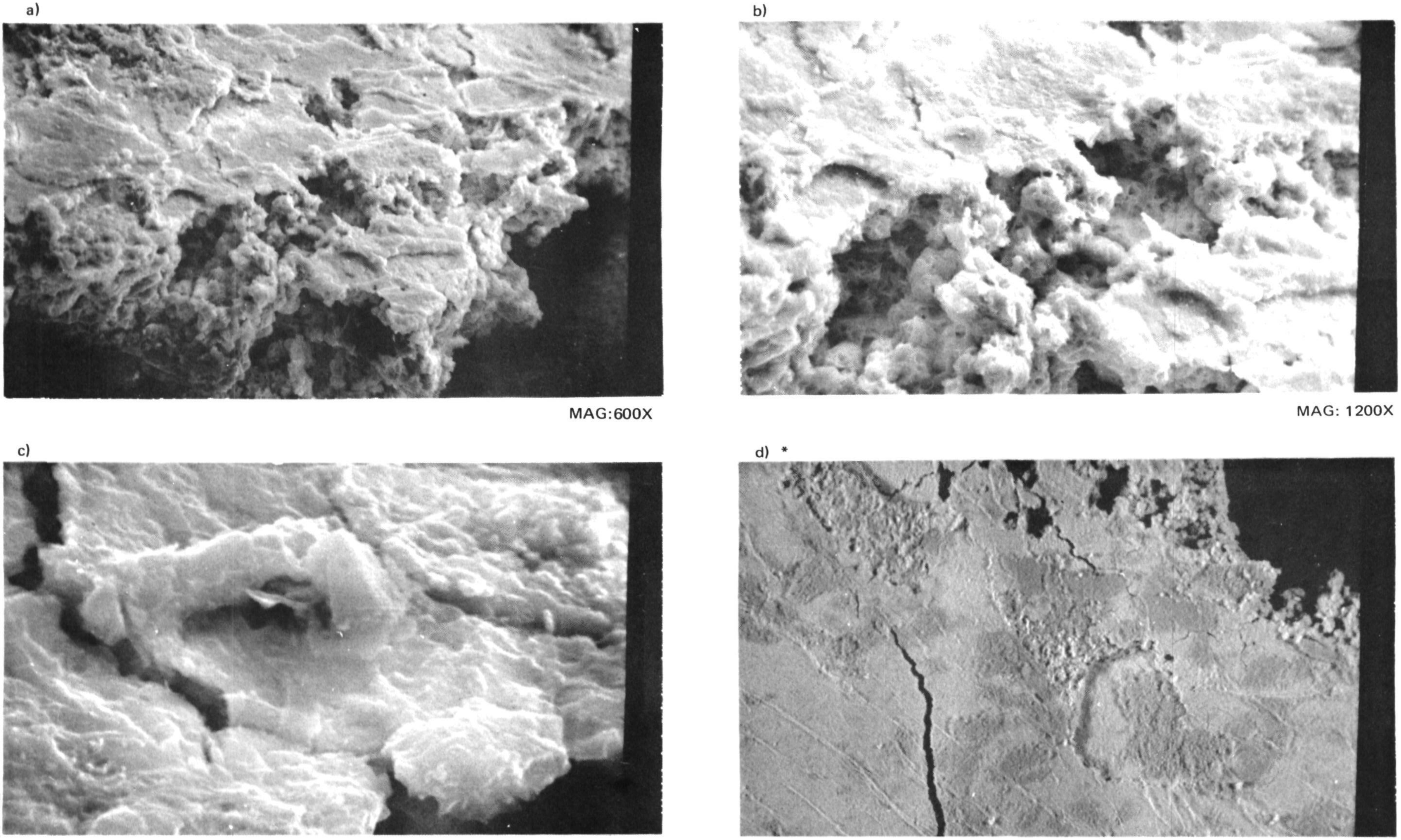

a) MAG:600X

b) MAG: 1200X

c) MAG: 6000X

d) * MAG: 300X

* BACKSPATTERED ELECTRON MICROGRAPH SHOWING TYPICAL TOPOGRAPHICAL VARIATIONS

FIG. 64

PHOTOGRAPHS OF X–RAY MAPS OF A SAMPLE RESIDUE FROM AXIAL BY–PASS EXHAUST DUCT AFTER RF PLASMA TEST WITH PURE UF_6 INJECTION

POSITION NEAR TO END WALL ASSEMBLY

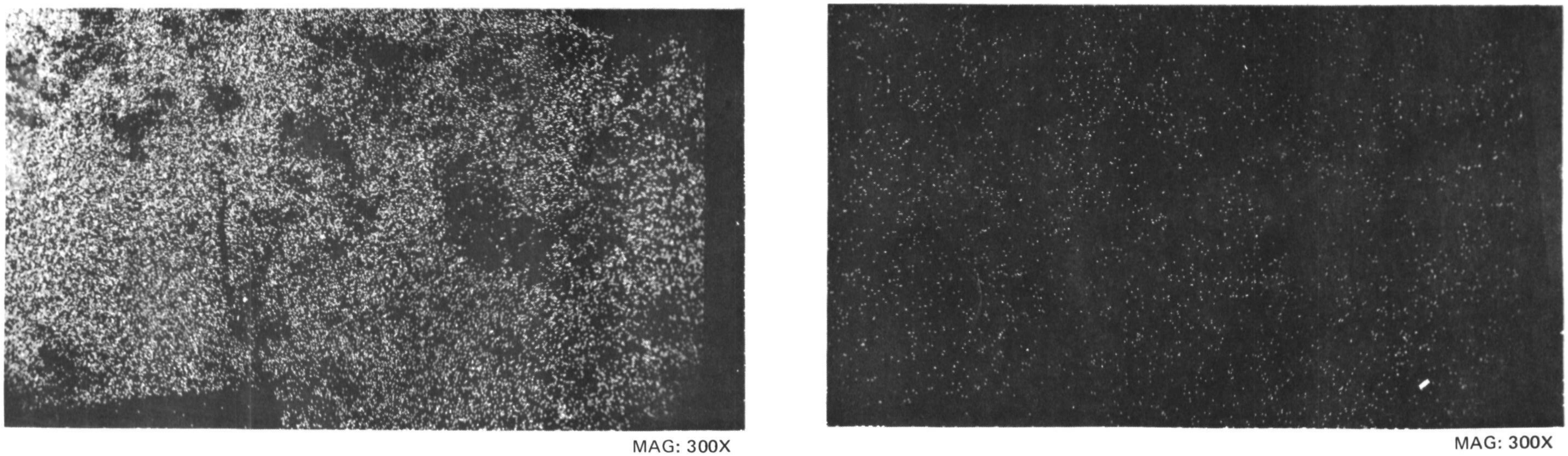
a) X–RAY SHOWING URANIUM (WHITE AREA)

b) X–RAY SHOWING FLUORINE

c) X–RAY SHOWING COPPER

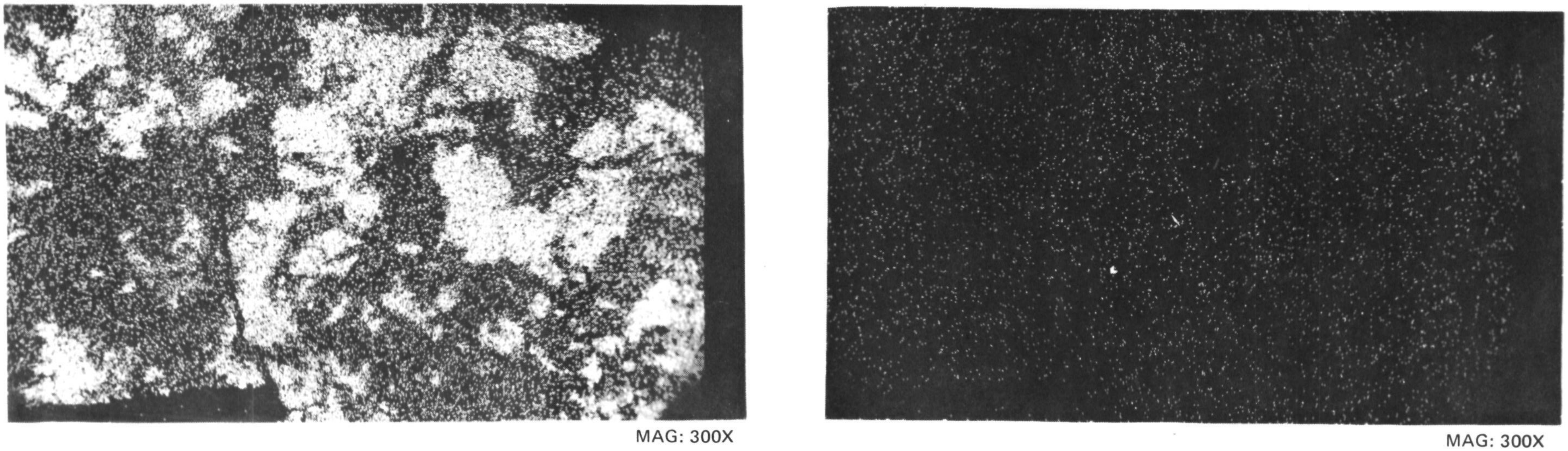
d) X–RAY SHOWING OXYGEN

FIG. 65

ELECTRON PHOTOMICROGRAPHS OF A SAMPLE RESIDUE FROM AXIAL BY–PASS EXHAUST DUCT AFTER RF PLASMA TEST WITH PURE UF_6 INJECTION

POSITION FAR FROM ENDWALL ASSEMBLY

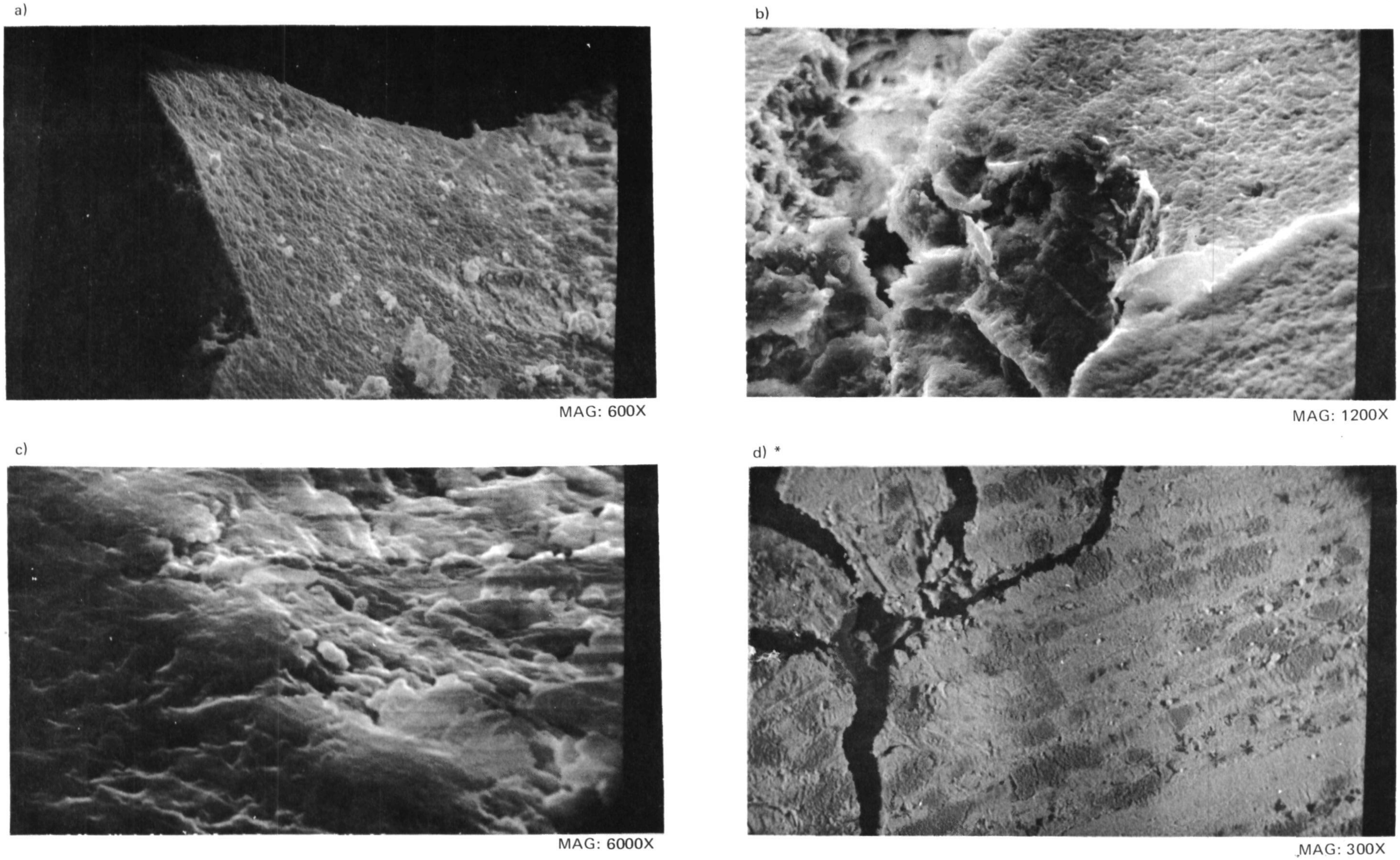

a) MAG: 600X

b) MAG: 1200X

c) MAG: 6000X

d) * MAG: 300X

* BACKSCATTERED ELECTRON MICROGRAPH SHOWING TYPICAL TOPOGRAPHICAL VARIATIONS

FIG. 66

PHOTOGRAPHS OF X–RAY MAPS OF A SAMPLE RESIDUE FROM AXIAL BY–PASS EXHAUST DUCT AFTER RF PLASMA TEST WITH PURE UF_6 INJECTION

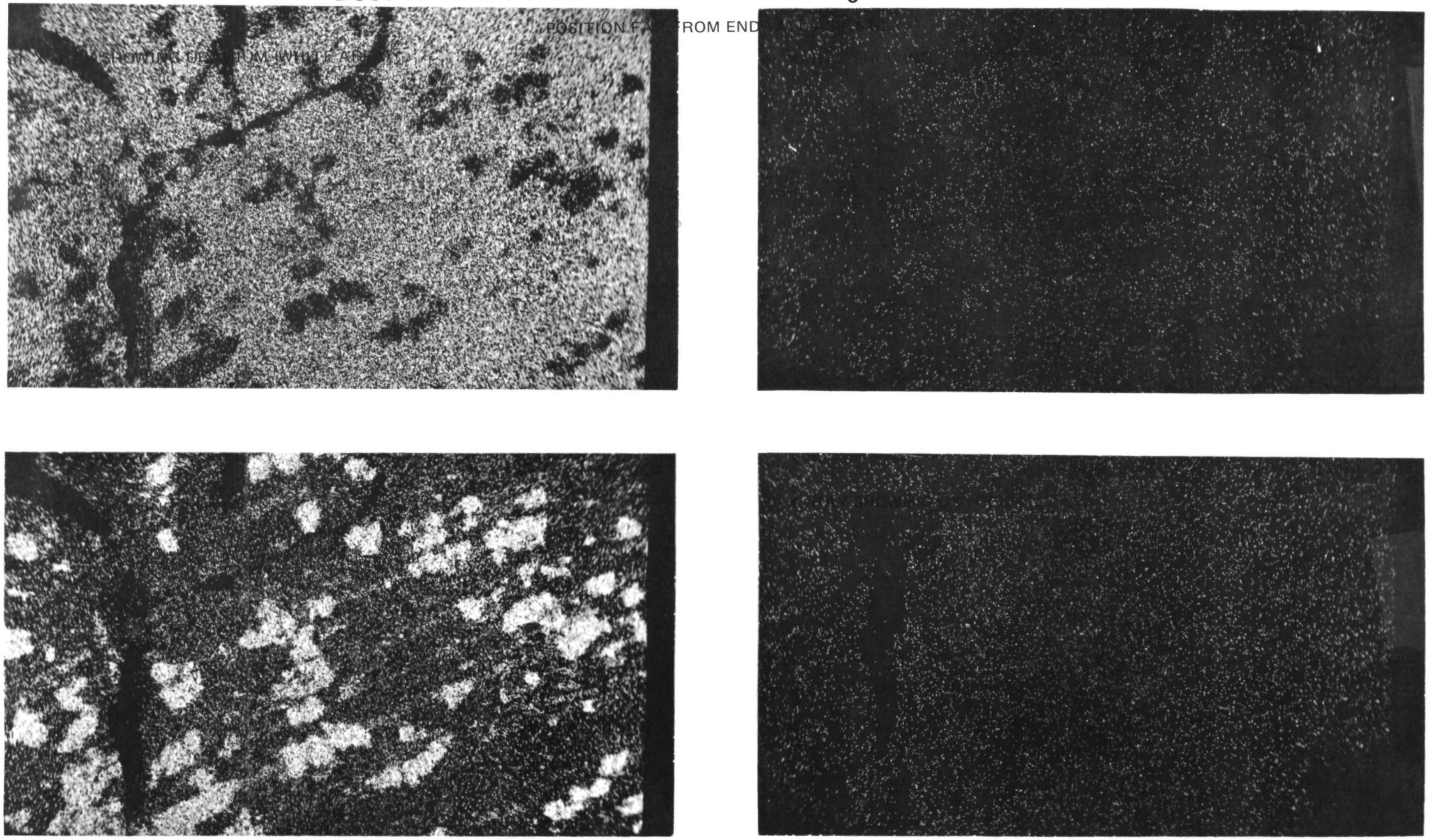

EXAMPLE OF X–RAY DIFFRACTION PATTERNS OBTAINED FROM POST TEST ANALYSIS OF RESIDUE FROM EXHAUST DUCTS AFTER RF PLASMA TEST WITH PURE UF_6 INJECTION AND OF STANDARD REFERENCE SAMPLE

NO PRIOR PREPARATION OF SAMPLES

ALL SAMPLES SUBJECTED TO CuK_{α} RADIATION IN A NORELCO DIFFRACTOMETER

a) ON –AXIS THRU– FLOW EXHAUST DUCT

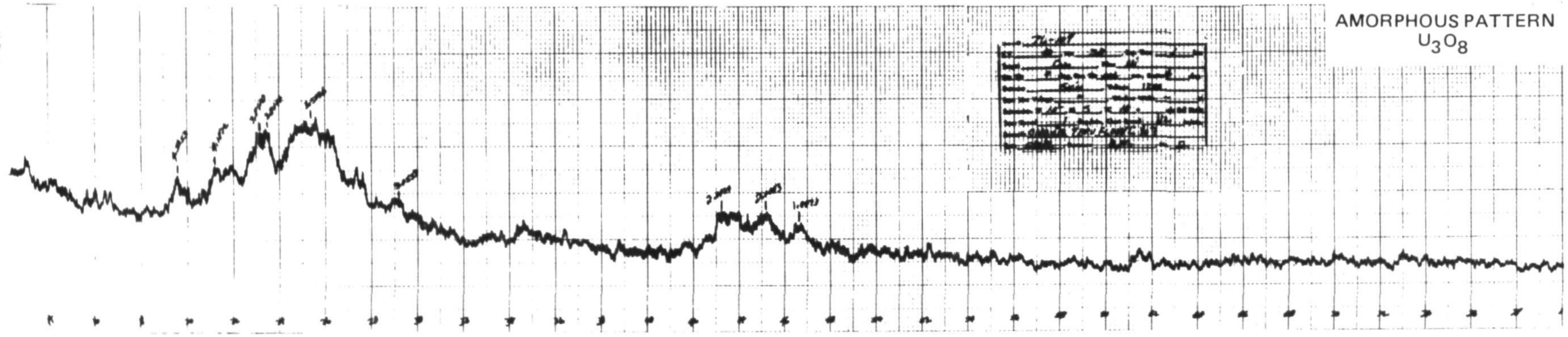

b) AXIAL BYPASS EXHAUST DUCT

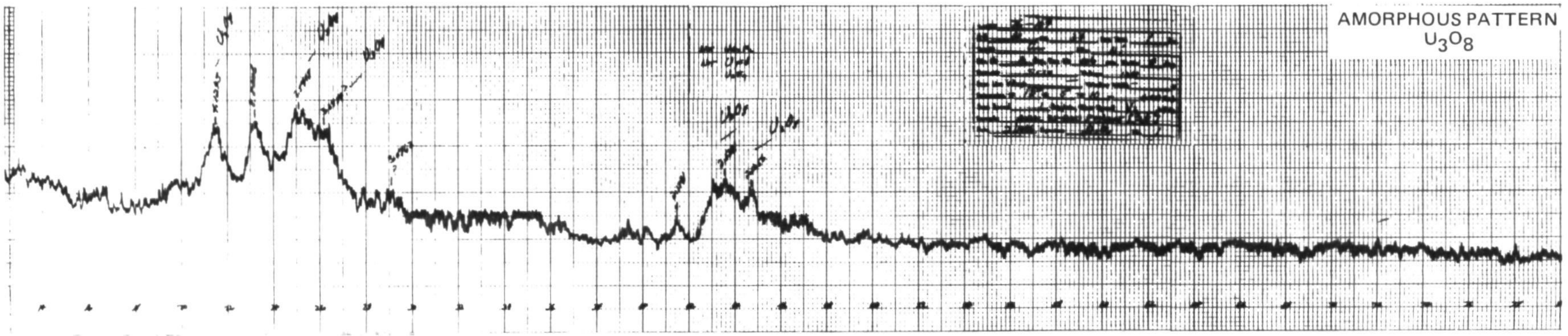

c) UO_2F_2 STANDARDREFERENCE SAMPLE

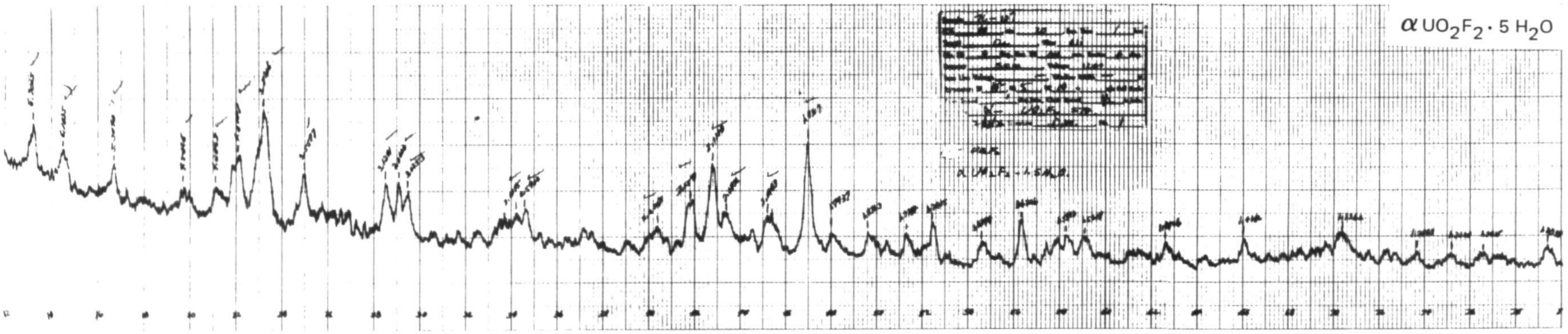

VARIATION OF X–RAY TRANSMISSION WITH URANIUM ATOM NUMBER DENSITY

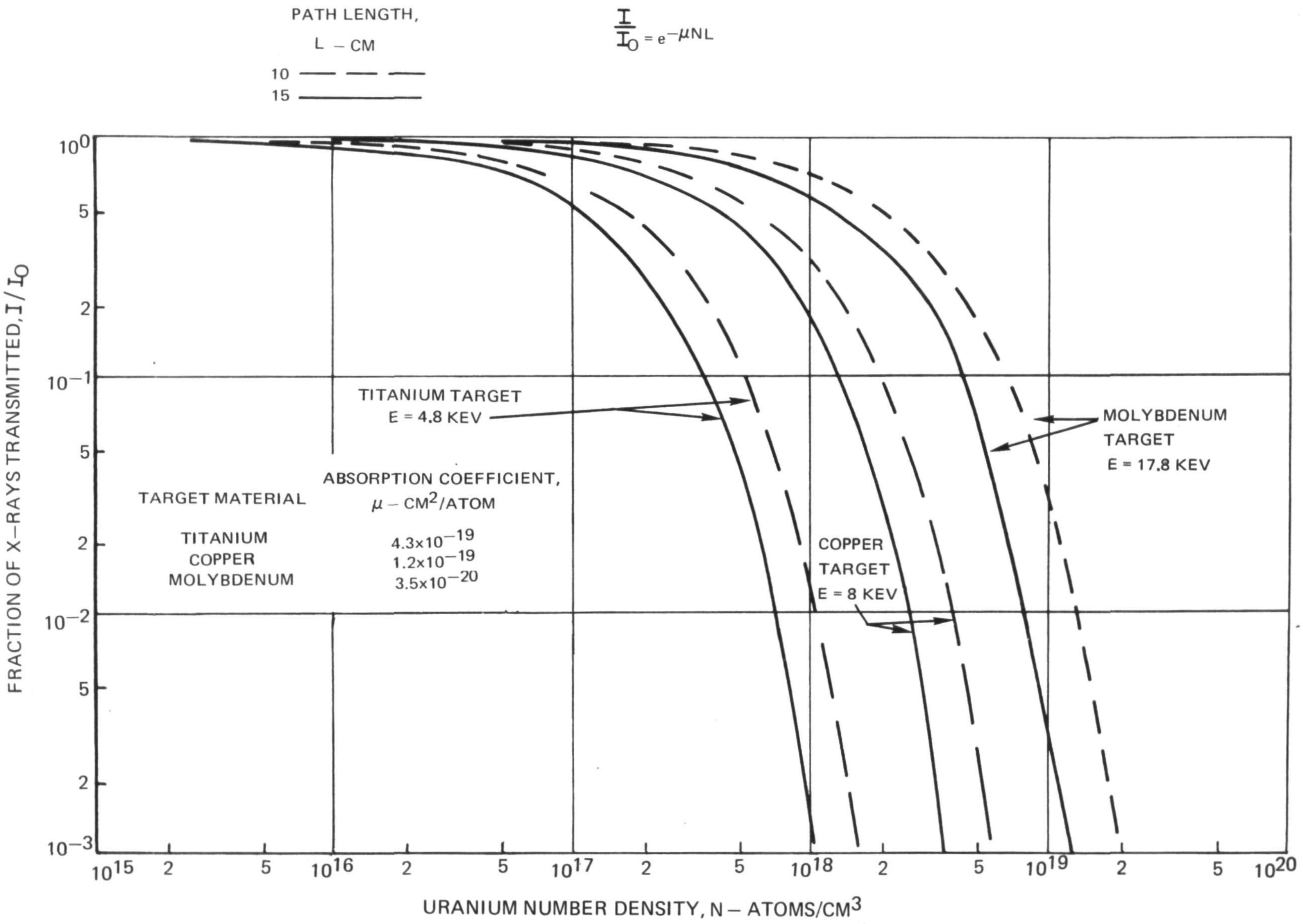

TARGET MATERIAL	ABSORPTION COEFFICIENT, μ – CM^2/ATOM
TITANIUM	4.3×10^{-19}
COPPER	1.2×10^{-19}
MOLYBDENUM	3.5×10^{-20}

SYSTEM FOR PRELIMINARY X–RAY ABSORPTION MEASUREMENT TESTS

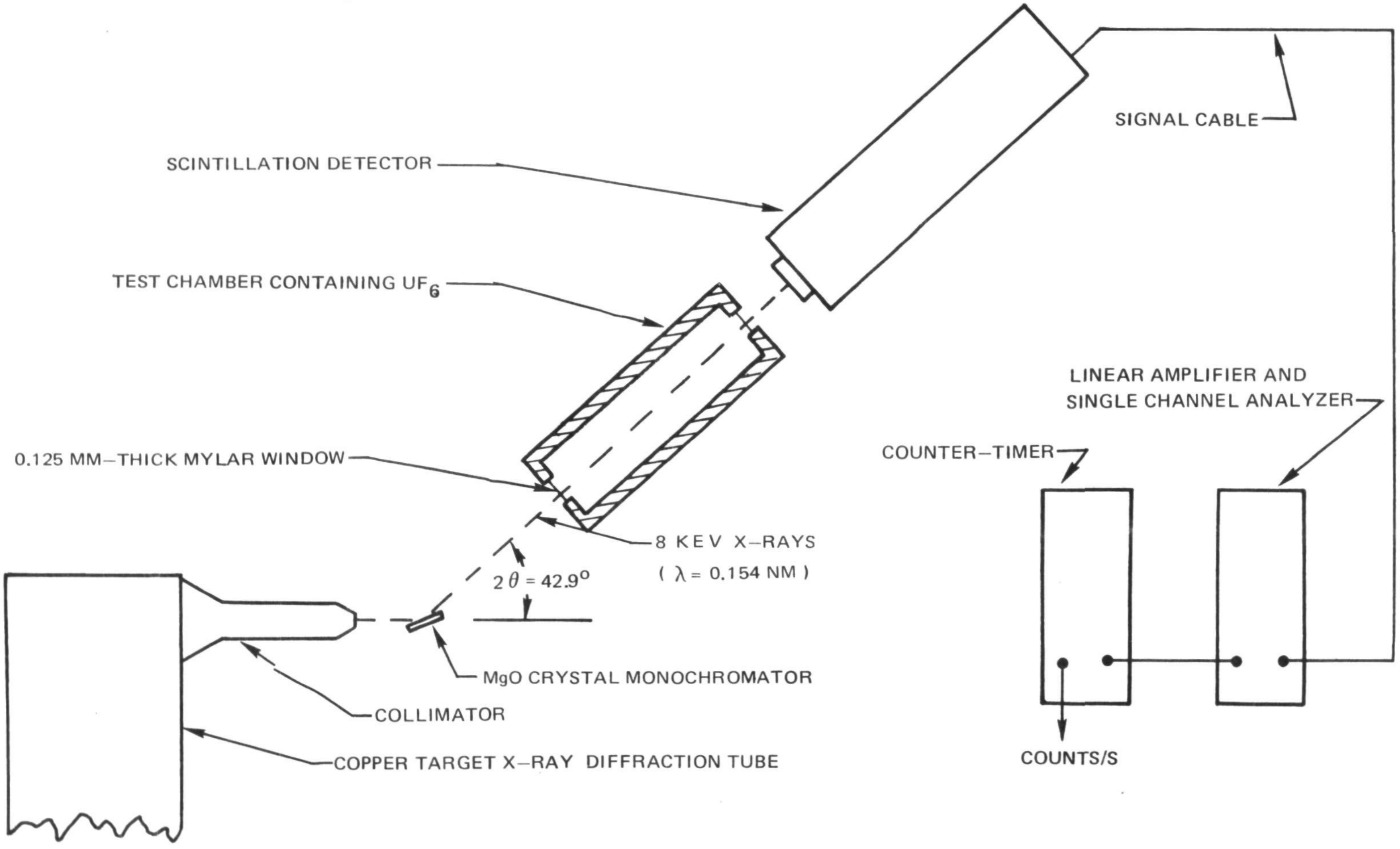

FIG. 70

MEASURED VARIATION OF TRANSMISSION OF 8 KEV X–RAYS WITH UF_6 PRESSURE

PATH LENGTH = 15 CM

TEMPERATURE = 300 K

SEE FIG. 69 FOR TEST CONFIGURATION DETAILS

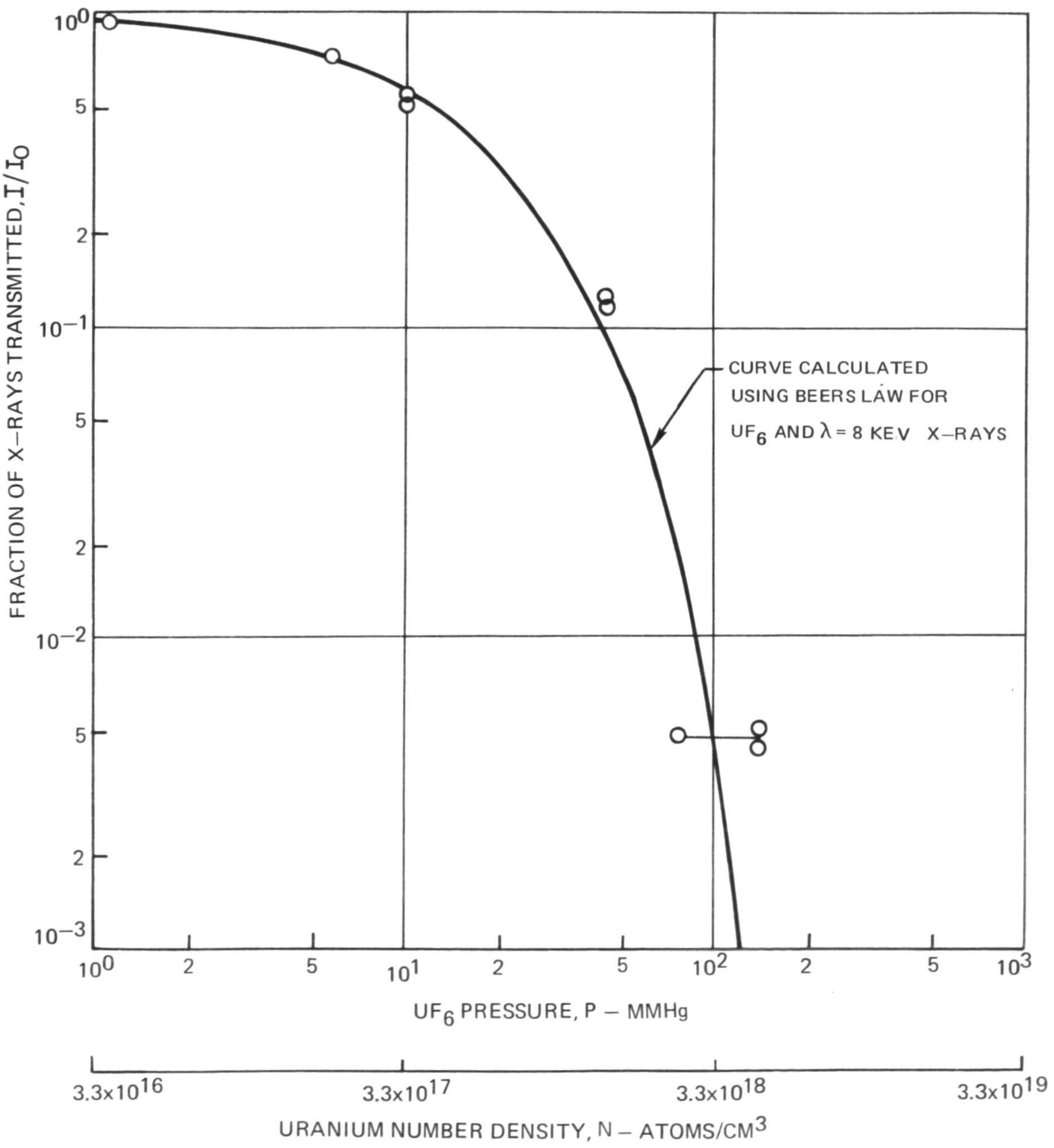

FIG. 71

SYSTEM FOR UF_6 AND ARGON X–RAY ABSORPTION MEASUREMENTS

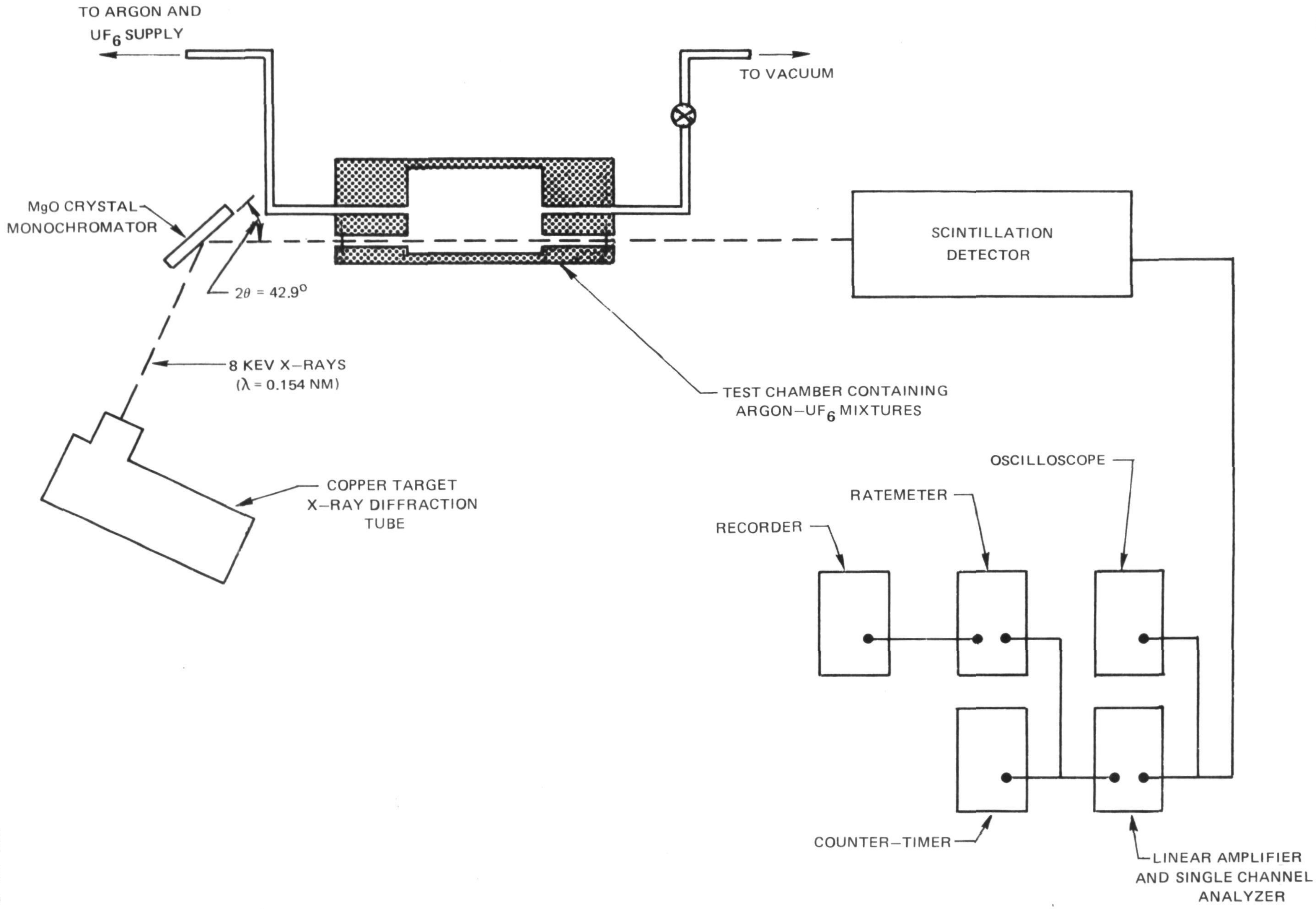

FIG. 72

TEST CHAMBERS FOR UF_6 AND ARGON X-RAY ABSORPTION MEASUREMENTS

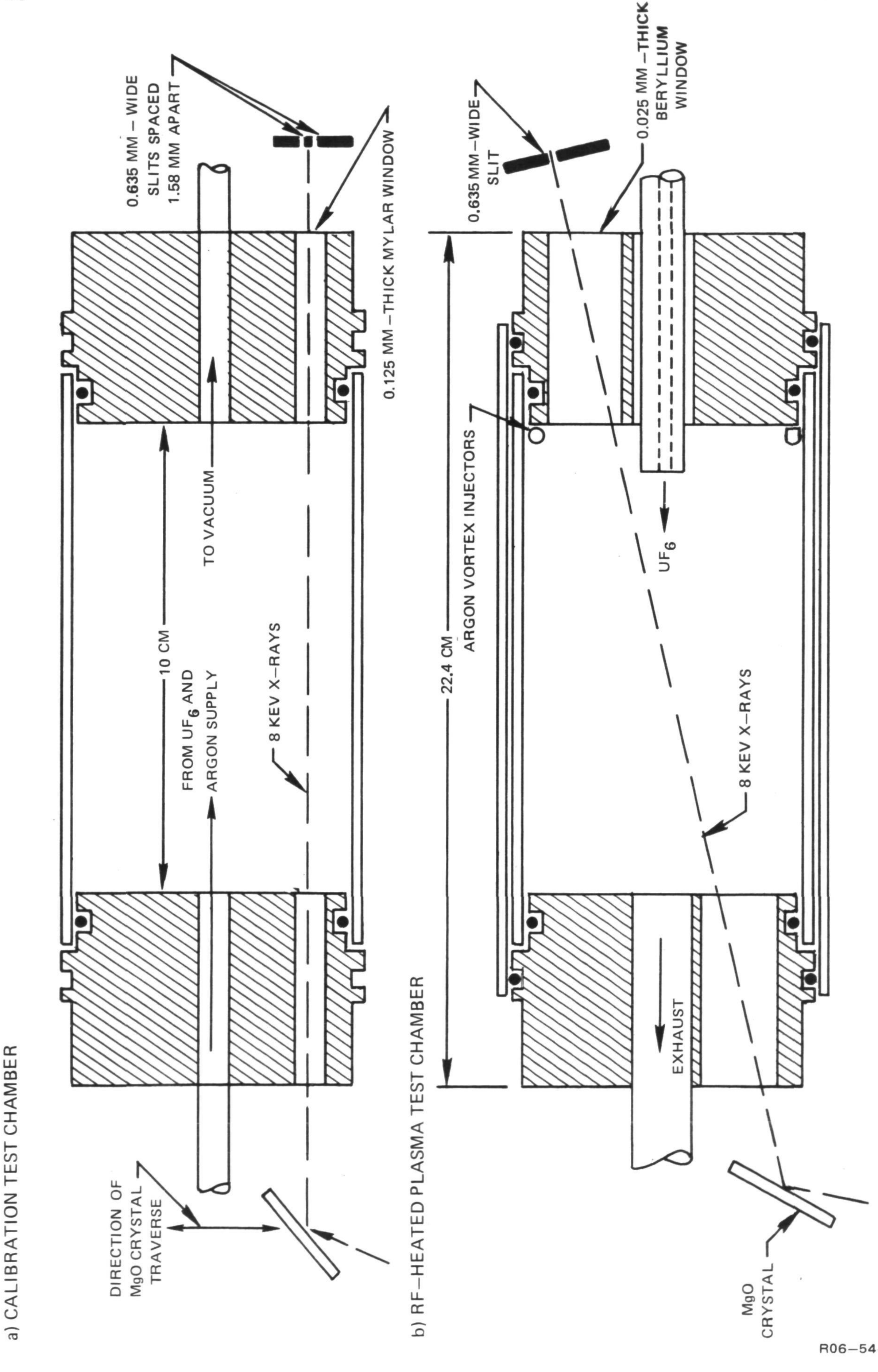

R06–54–4

FIG. 73

PHOTOGRAPH OF SYSTEM FOR UF_6 AND ARGON X–RAY ABSORPTION MEASUREMENTS IN CALIBRATION TESTS

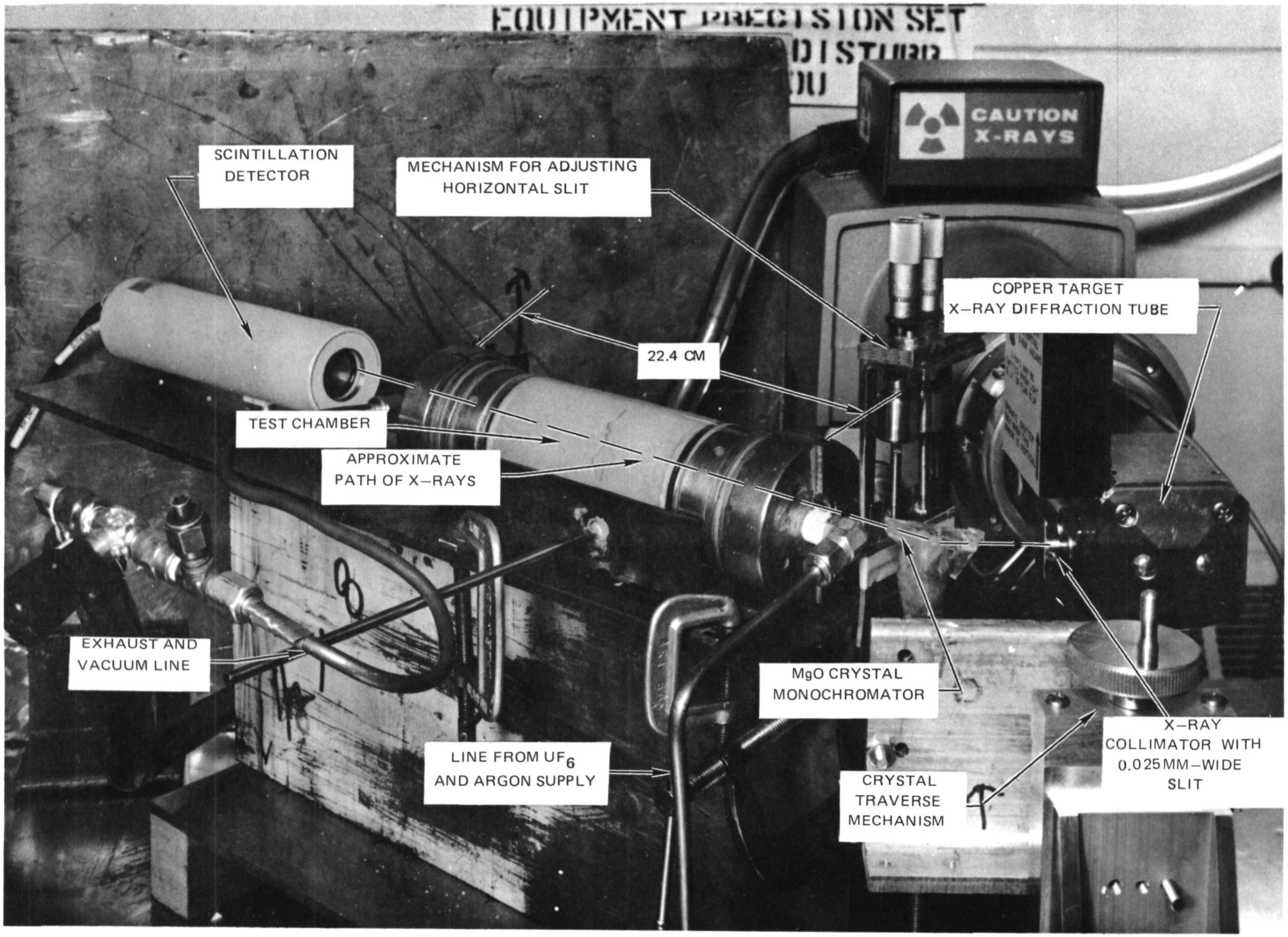

FIG. 74

PHOTOGRAPH OF SYSTEM FOR UF_6 X-RAY ABSORPTION MEASUREMENTS IN RF-HEATED PLASMA TESTS

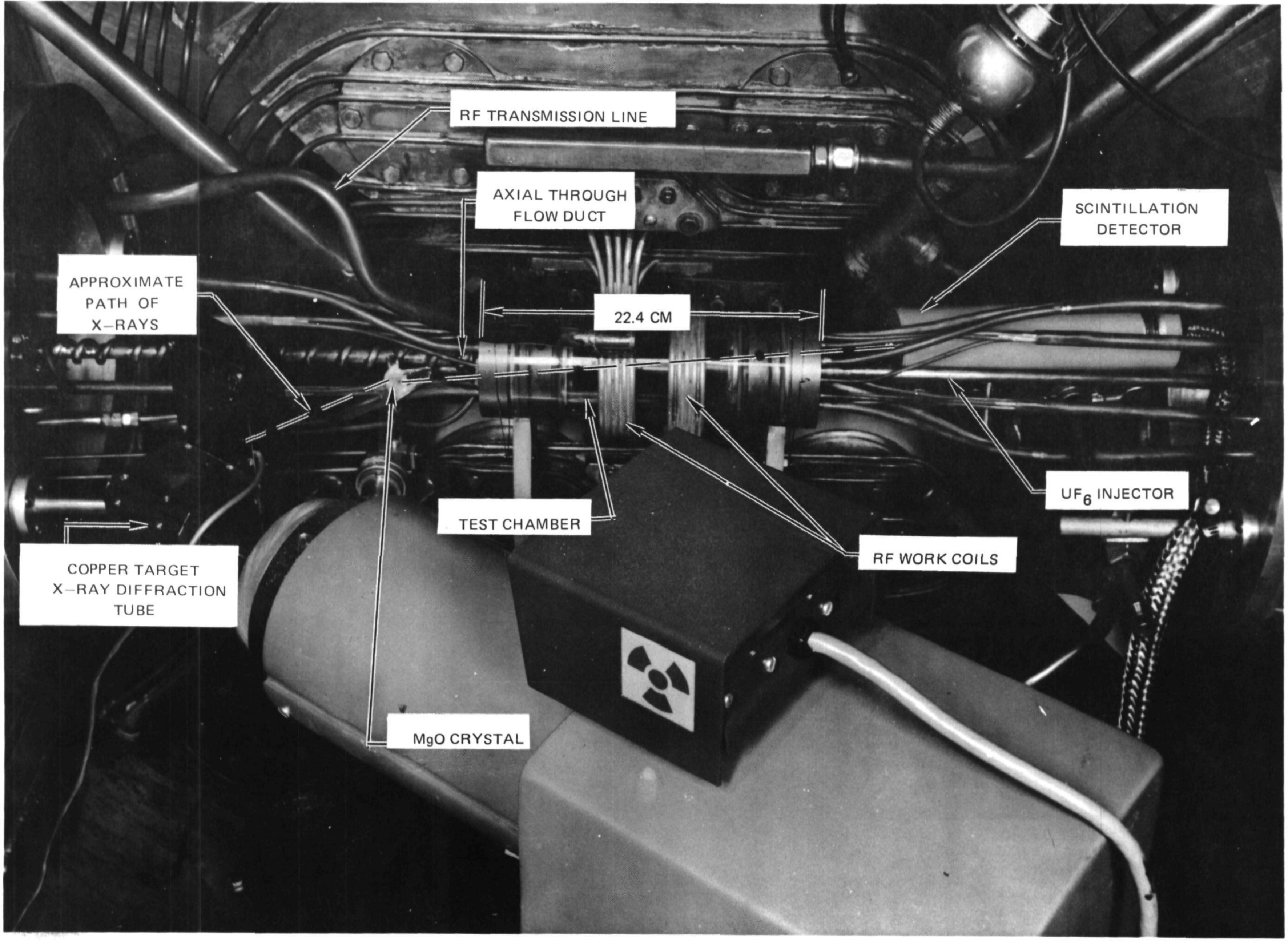

FIG. 75

MEASURED VARIATION OF TRANSMISSION OF 8 KEV X–RAYS WITH ARGON PRESSURE

TEMPERATURE = 300 K

SYMBOL	CONFIGURATION	CRYSTAL TRAVERSED?	PATH LENGTH, L – CM
○	CALIBRATION	YES	22.4
□	CALIBRATION	NO	22.4
△	RF TEST	NO	23.0

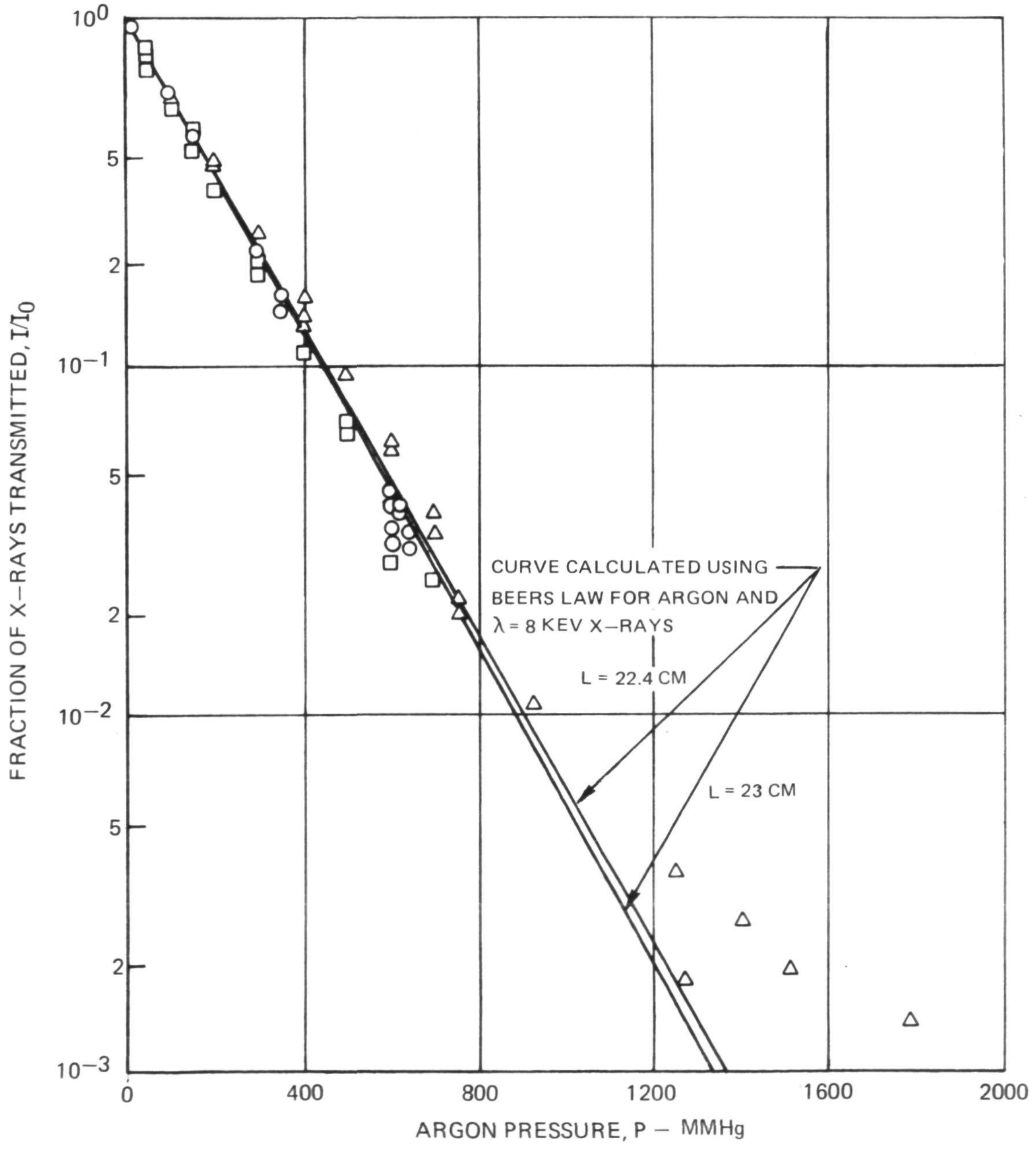

FIG. 76

MEASURED VARIATION OF TRANSMISSION OF 8 KEV X–RAYS WITH UF$_6$ PRESSURE

CALIBRATION TEST CONFIGURATION PATH LENGTH = 22.4 CM

TEMPERATURE = 300 K

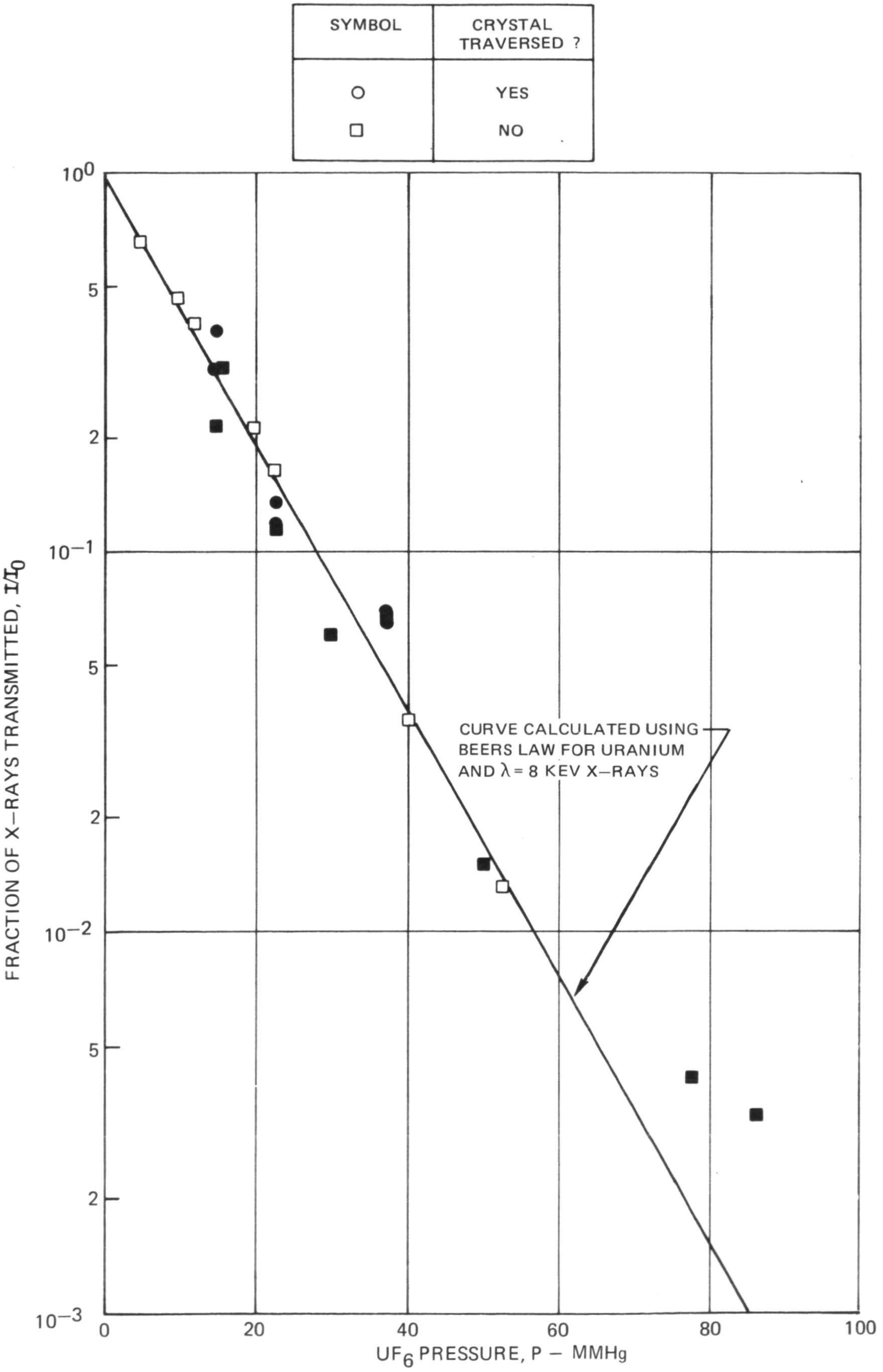

FIG. 77

MEASURED VARIATION OF TRANSMISSION OF 8 KEV X–RAYS WITH UF_6 PRESSURE FOR SEVERAL ARGON PRESSURES

CALIBRATION TEST CONFIGURATION

PATH LENGTH = 22.4 CM

TEMPERATURE = 300 K

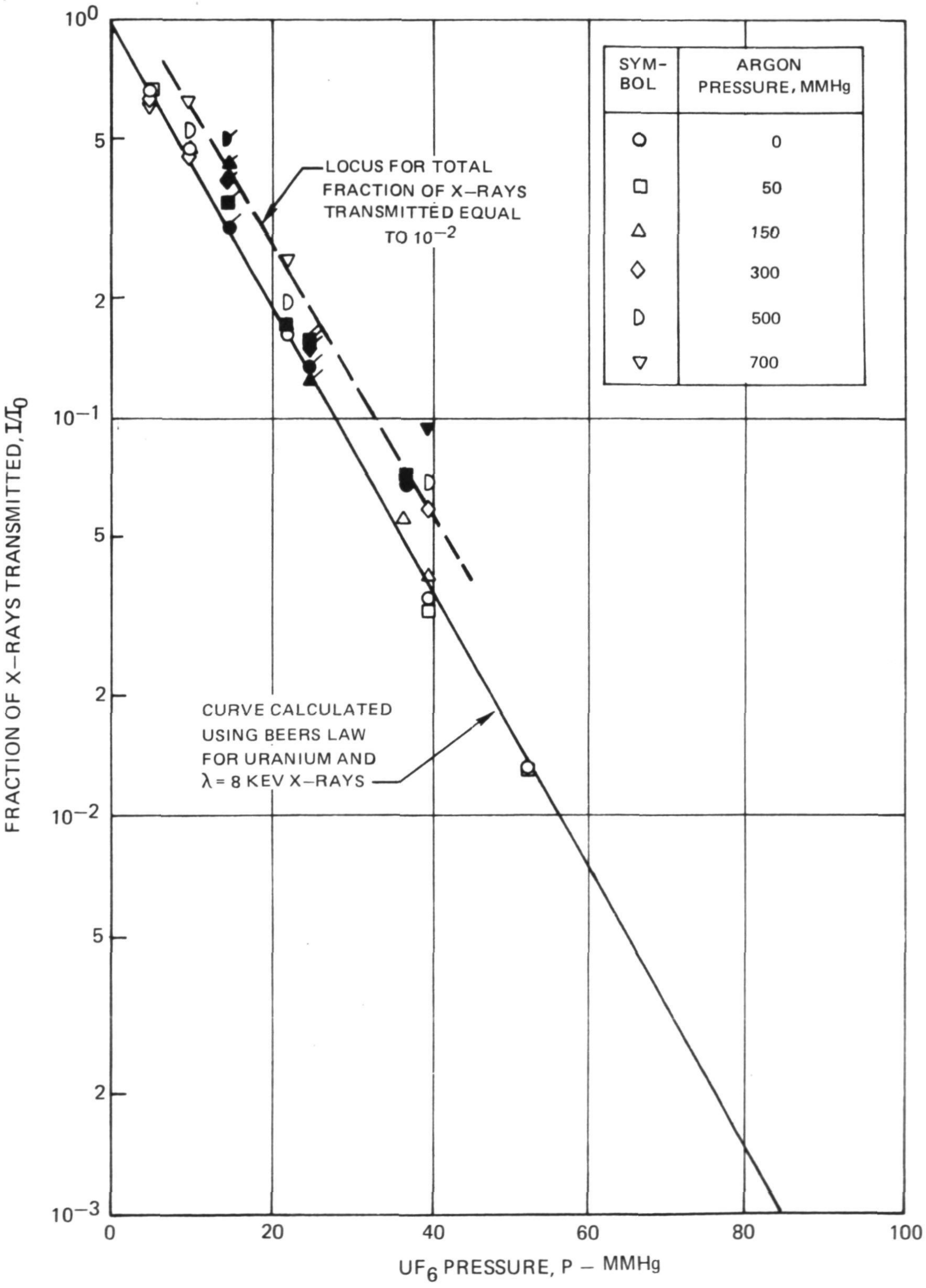

FIG. 78

MEASURED VARIATION OF TRANSMISSION OF 8 KEV X–RAYS WITH ARGON PRESSURE FROM RF–HEATED PLASMA TESTS

RF TEST CONFIGURATION

SYMBOL	PLASMA PRESENT?
●	NO
○	YES

NOTE: FLAGGED AND UNFLAGGED SYMBOLS DENOTE AXIAL BYPASS EXHAUST USED AND NOT USED, RESPECTIVELY

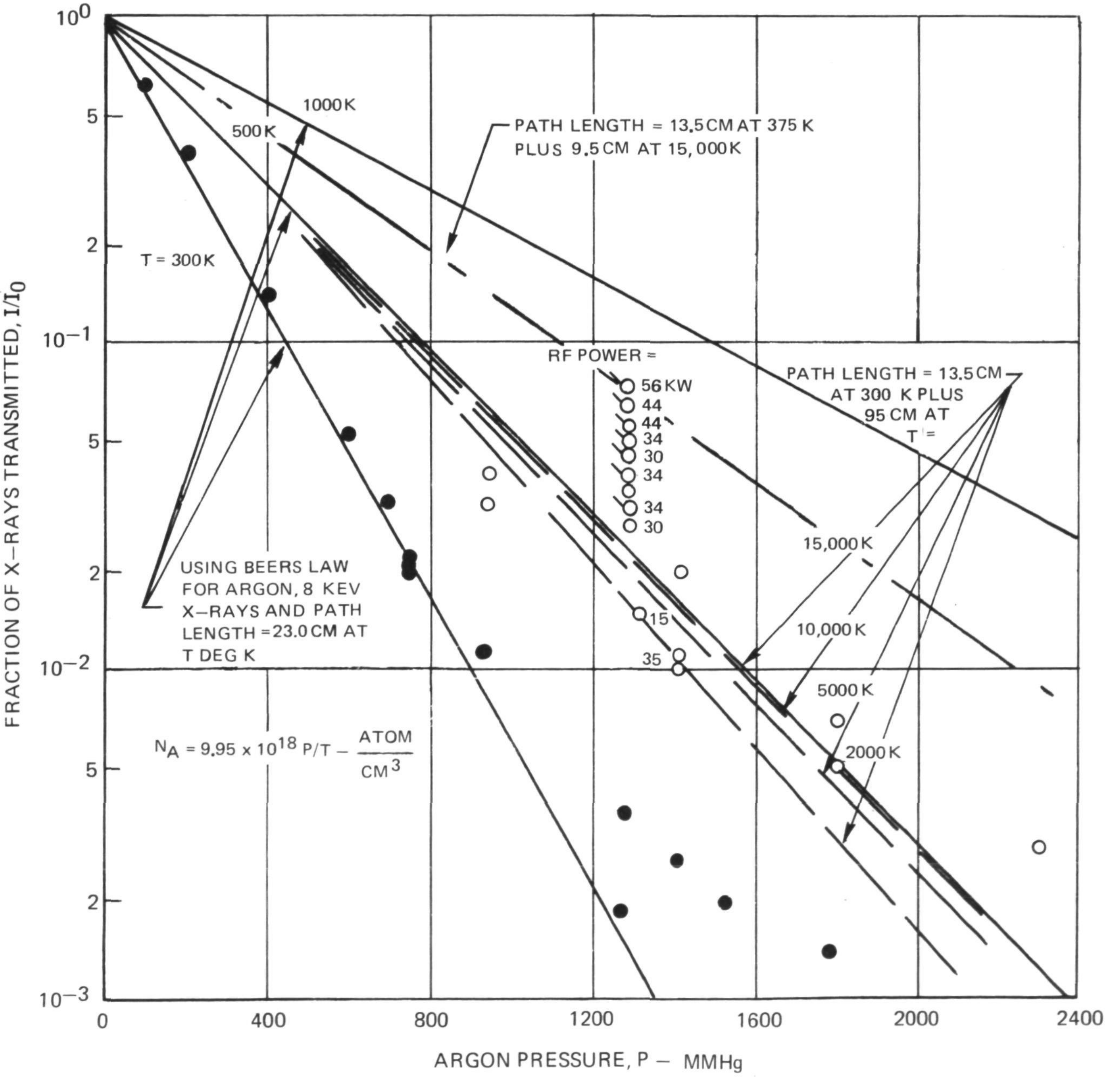

VARIATION OF FRACTION OF X–RAYS TRANSMITTED FOR ARGON AND UF_6–ARGON MIXTURES WITH RF POWER

SYMBOL	PLASMA GAS
○	ARGON
□	UF_6 + ARGON

SEE TEXT FOR EXPLANATION OF FLAGGED SYMBOLS

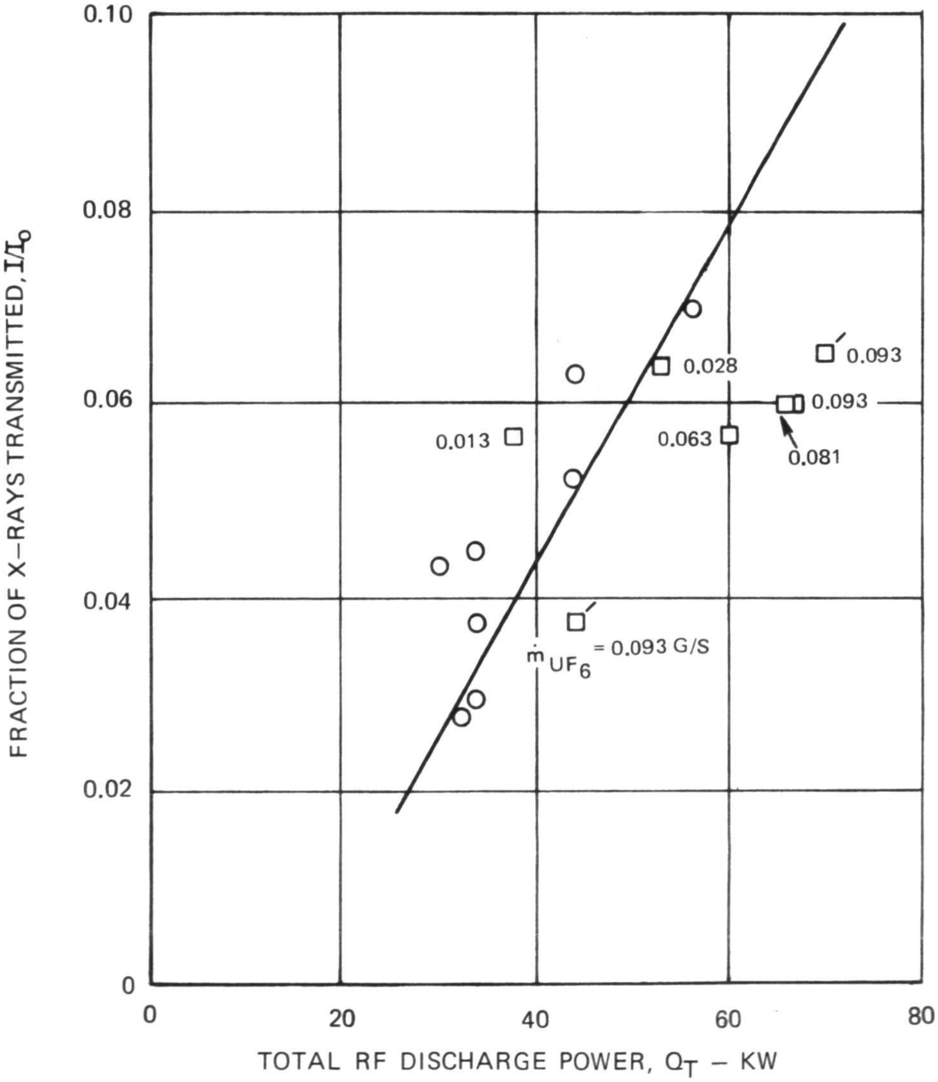

FIG. 80

VARIATION OF MEASURED URANIUM DENSITY WITH UF_6 FLOW RATE

SYMBOL	PATH LENGTH, CM
○	23.0
□	9.5

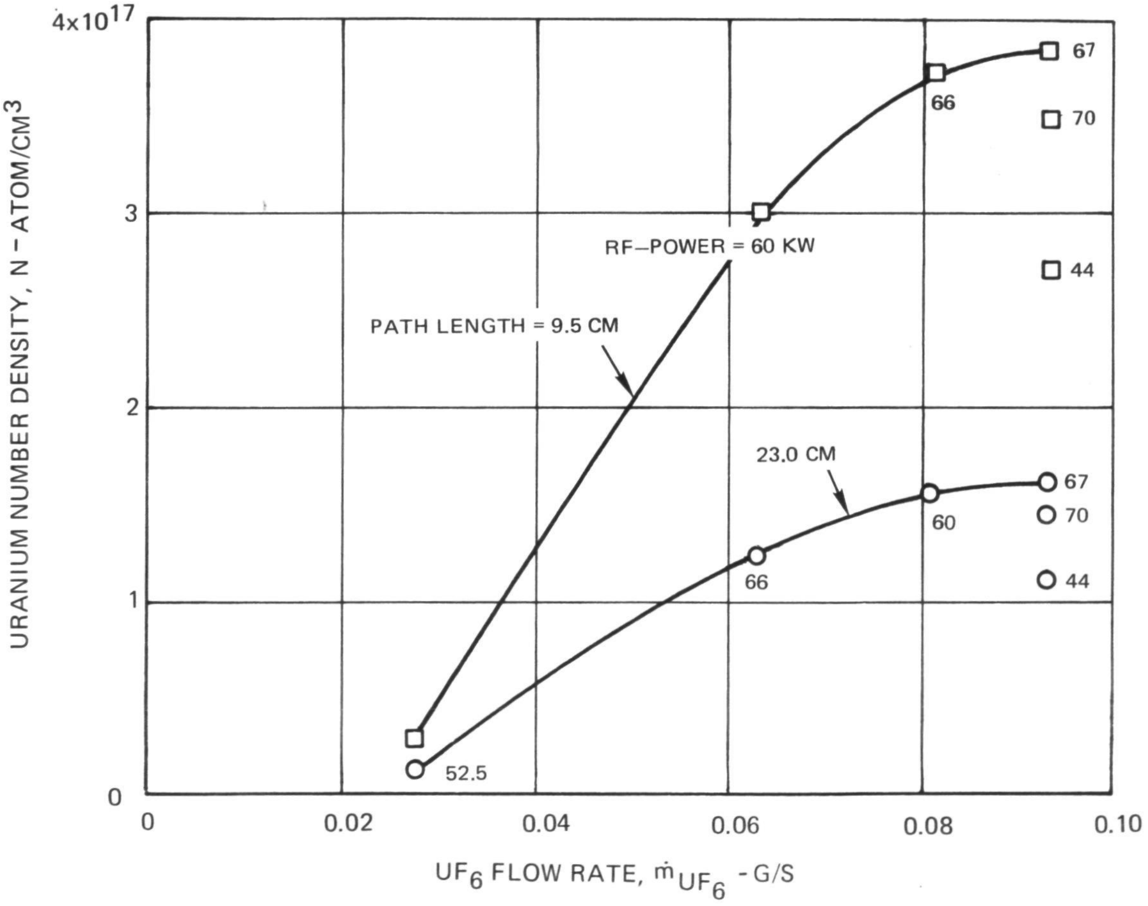

FIG. 81

PHOTOGRAPHS SHOWING THERMAL STRESS PRESENT IN FUSED SILICA TUBES AFTER SELECTED RF PLASMA TESTS WITH PURE UF_6 INJECTION

POLARIZED LIGHT USED

a) REFERENCE STANDARD

b) RELATIVELY HIGH THERMAL STRESS

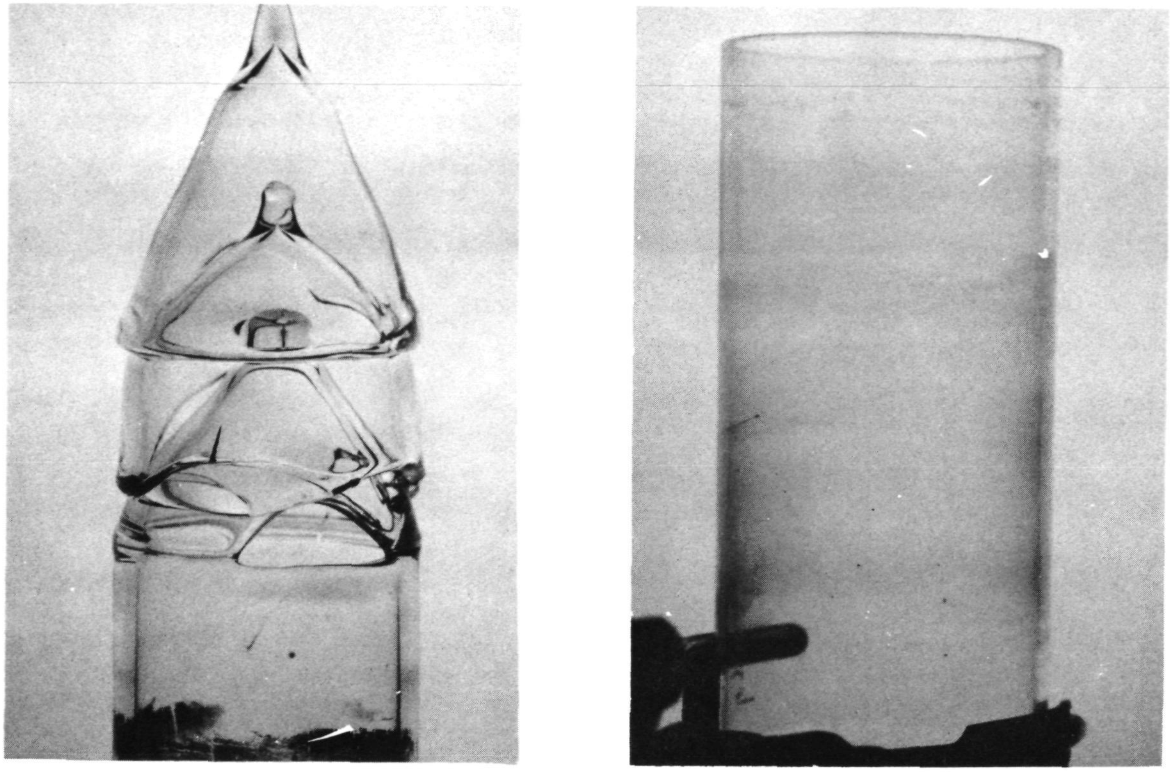

c) RELATIVELY LOW THERMAL STRESS

d) NEGLIGIBLE THERMAL STRESS

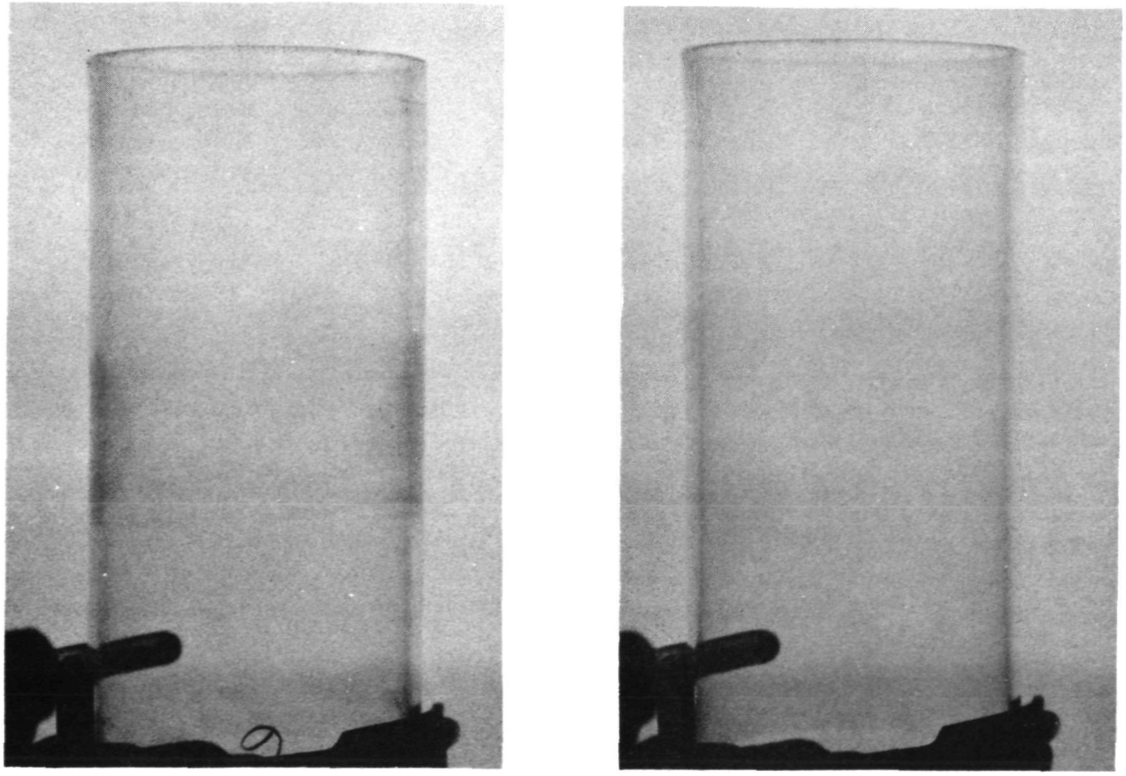

76– 03–251–1

FIG. 82

PHOTOGRAPHS OF SMALL–SCALE FUSED SILICA VESSELS (350 CC) USED WITH GRAM QUANTITIES OF UF_6 IN LABORATORY TESTS

SEE TABLE VI FOR CORRESPONDING TEST CONDITIONS

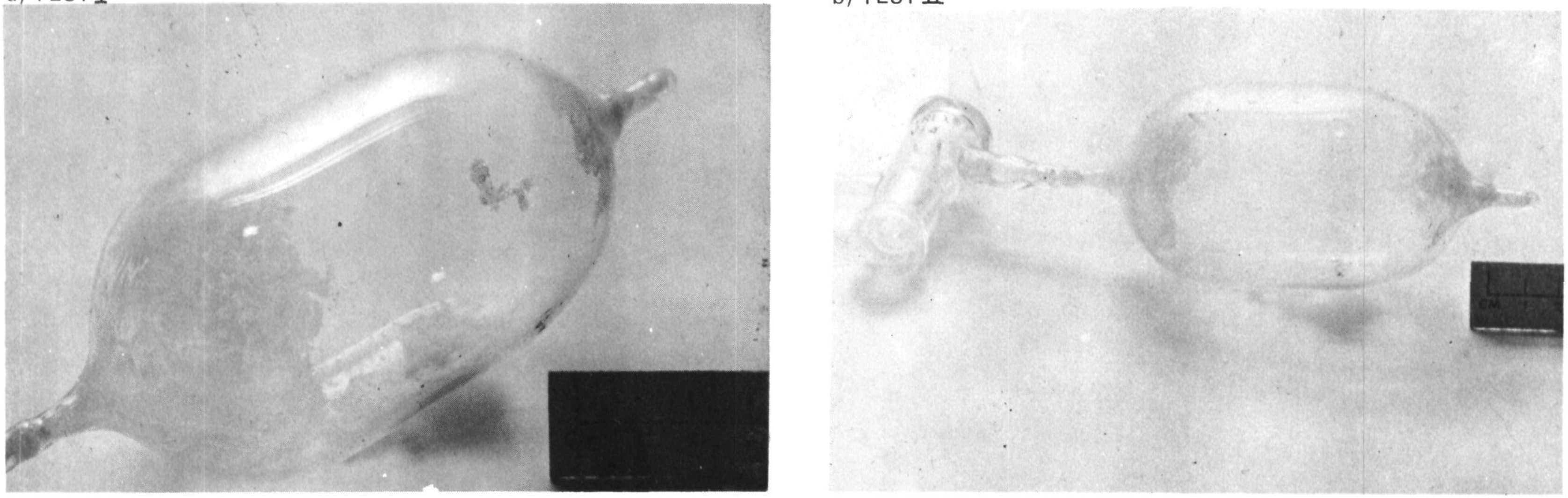

a) TEST I

b) TEST II

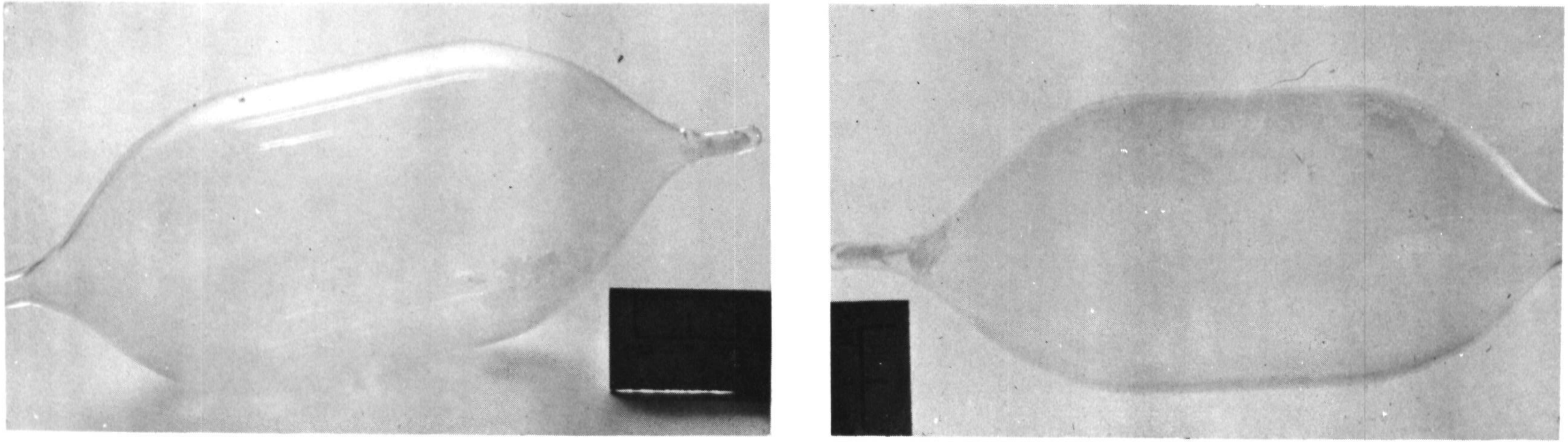

c) TEST III

d) TEST IV

FIG. 83

EXAMPLES OF IR SPECTROPHOTOMETRIC ABSORPTION MEASUREMENT STANDARDS

THIN WAFER KBr MATRIX USED WITH PERKIN ELMER MODEL 457

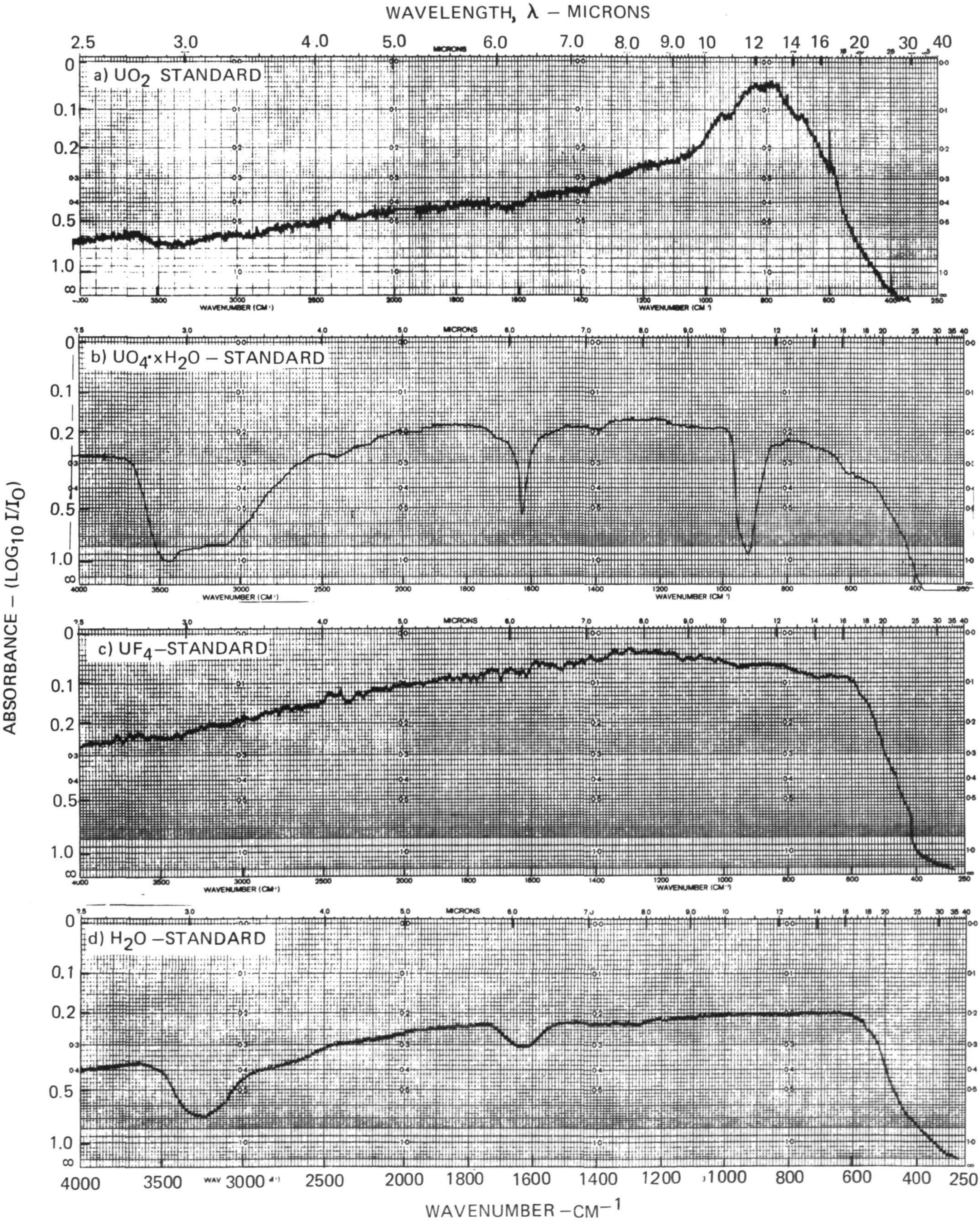

FIG. 84

EXAMPLES OF IR SPECTROPHOTOMETRIC ABSORPTION MEASUREMENTS

THIN WAFER KBr MATRIX USED WITH PERKIN ELMER MODEL 457

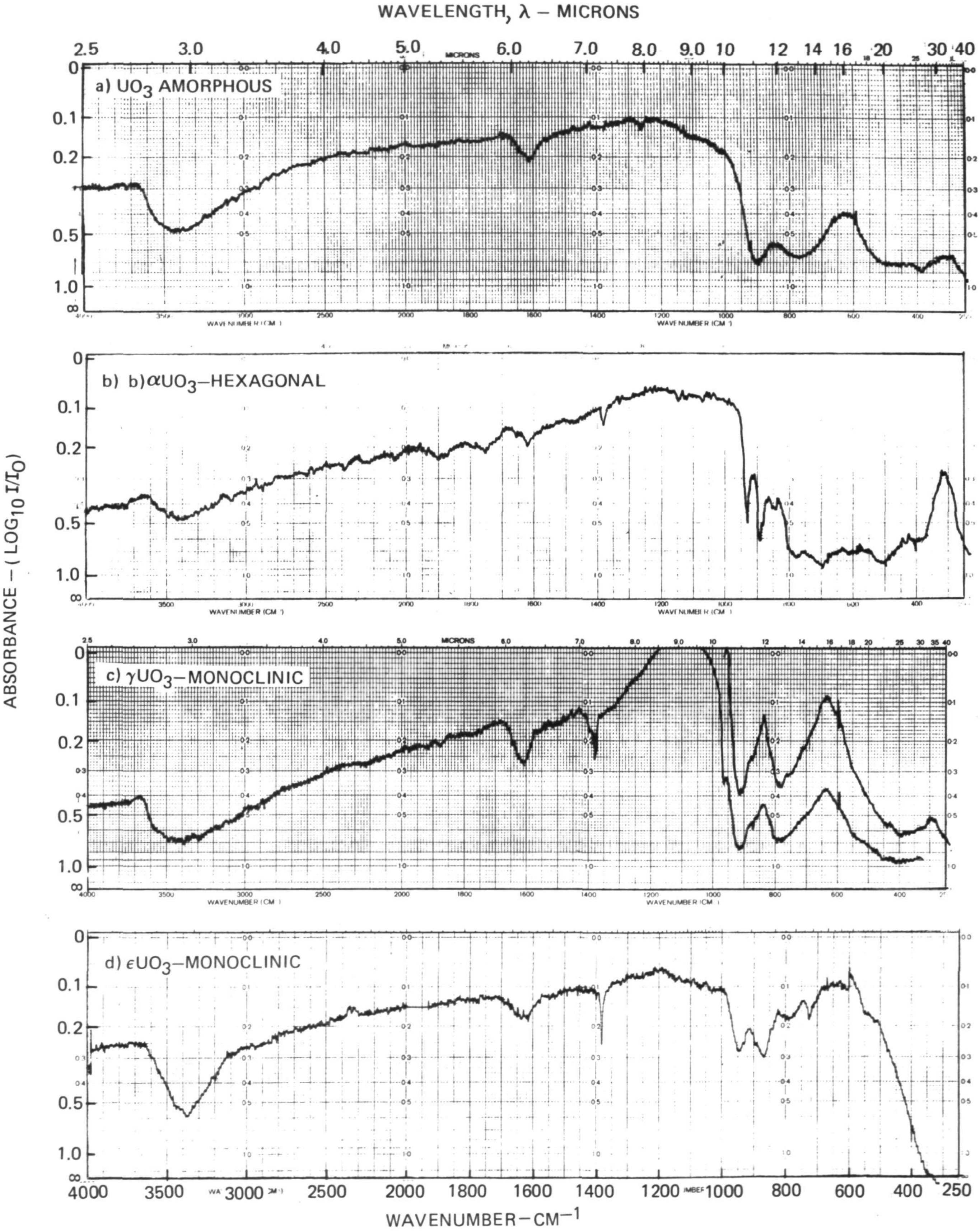

FIG. 85

EXAMPLES OF IR SPECTROPHOTOMETRIC ABSORPTION MEASUREMENTS

THIN WAFER KBr MATRIX USED WITH PERKIN ELMER MODEL 457

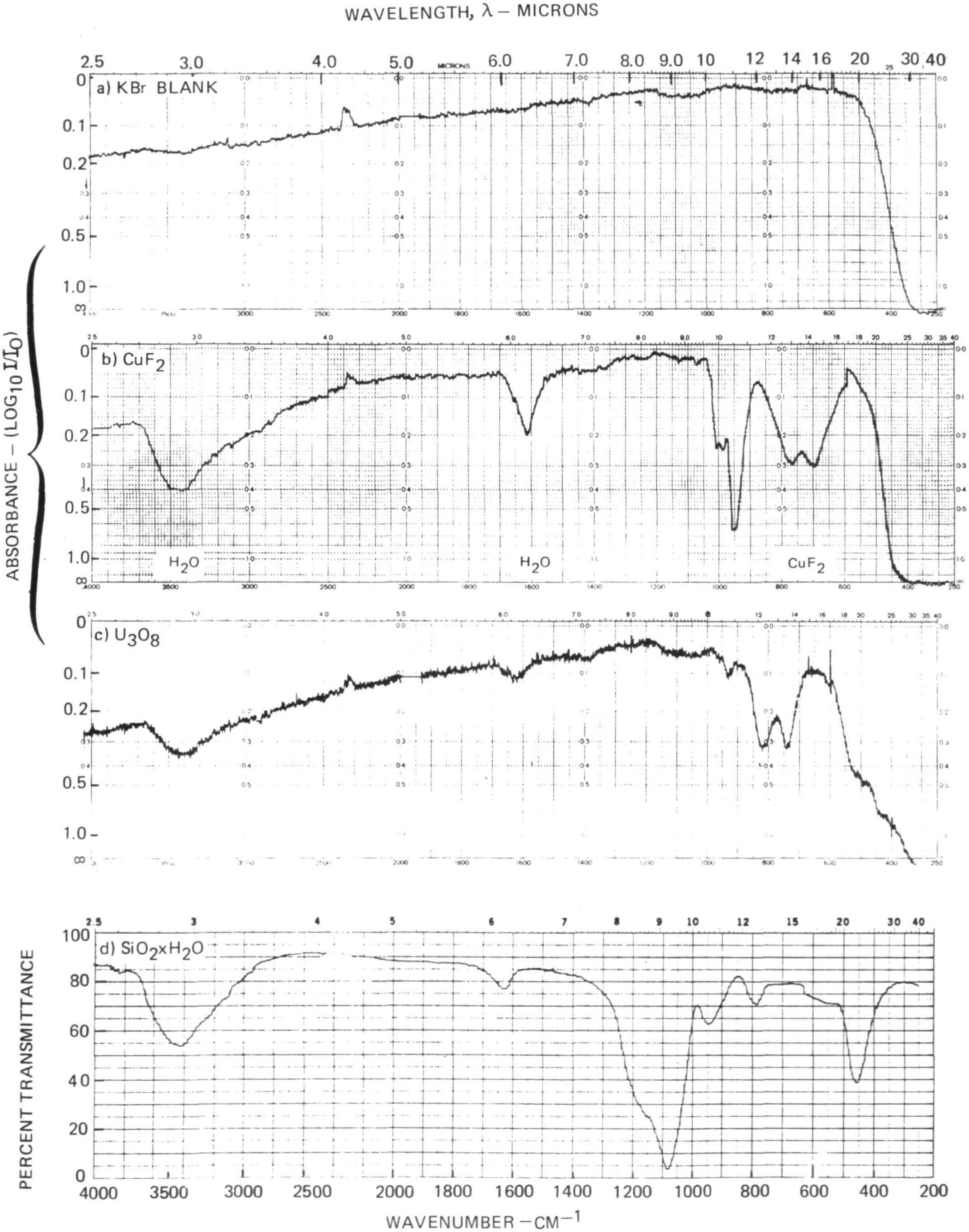

76–03–137–4

FIG. 86

EXAMPLES OF IR SPECTROPHOTOMETRIC ABSORPTION MEASUREMENT STANDARDS

THIN WAFER KBr MATRIX USED PERKIN AND ELMER MODEL 457

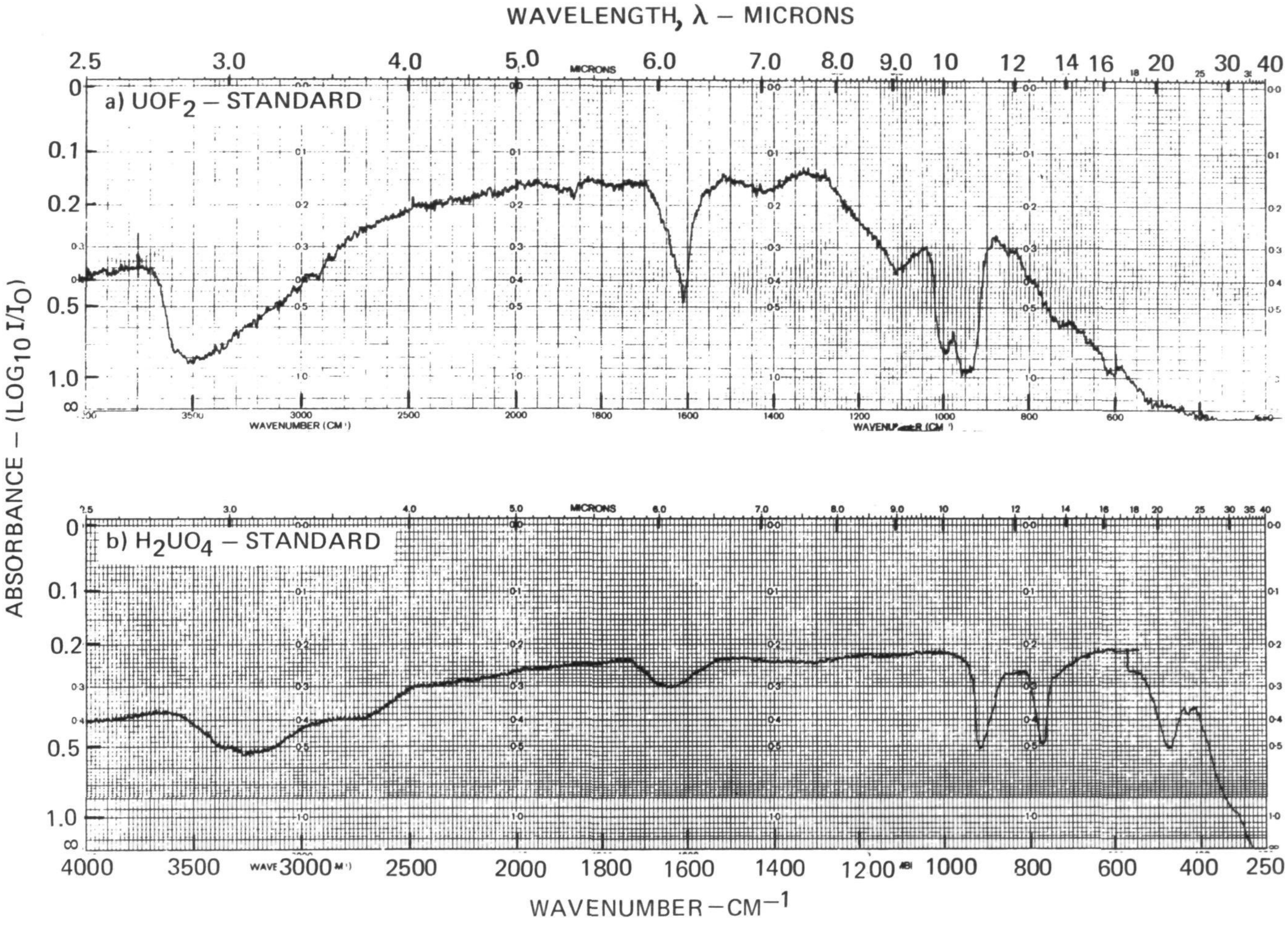

FIG. 87

RATE OF CORROSION FOR DIFFERENT MATERIALS BETWEEN 650K AND 1300K EXPOSED TO UF_6 AT 0.32 ATMOSPHERES

(REF. 20)

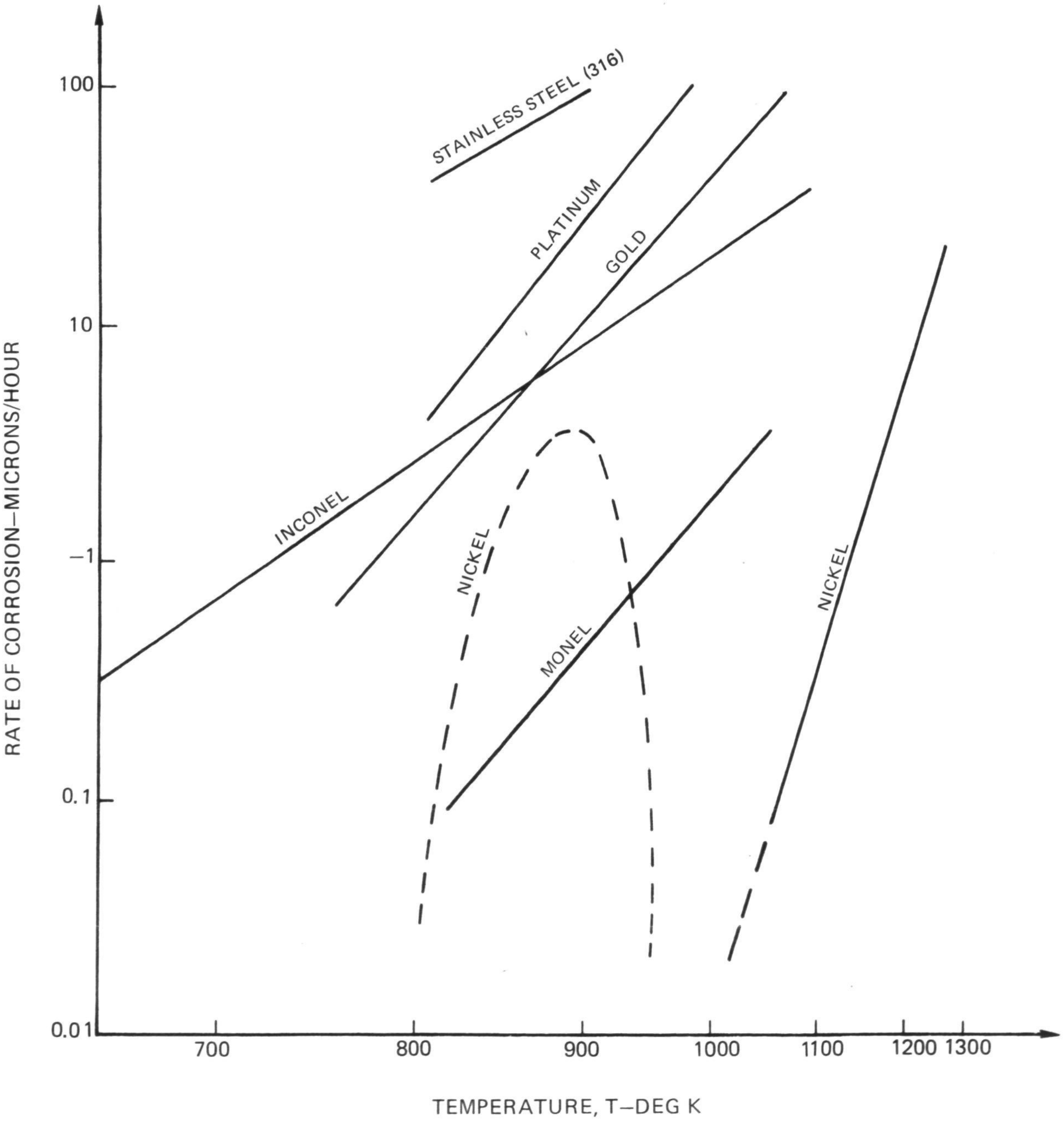

PHOTOGRAPHS SHOWING CORROSIVE EFFECTS OF HOT, PRESSURIZED UF_6 ON 316 STAINLESS STEEL BURST DISCS

THICKNESS: 0.005 CM
PRESSURE SIDE VIEWED IN ALL CASES

a) AS RECEIVED STANDARD

b) AS RECEIVED STANDARD

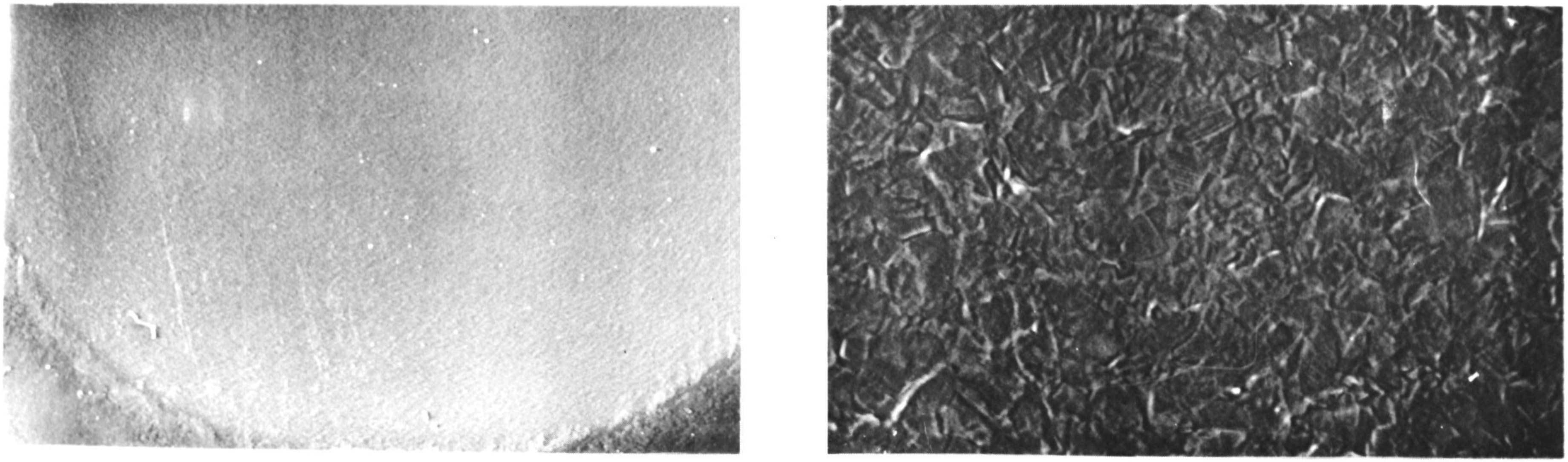

MAG: 10x

MAG: 1000x

c) FAILED PORTION OF BURST DISC

d) DETAILS OF INTERGRANULAR FRACTURE IN ADJACENT REGION

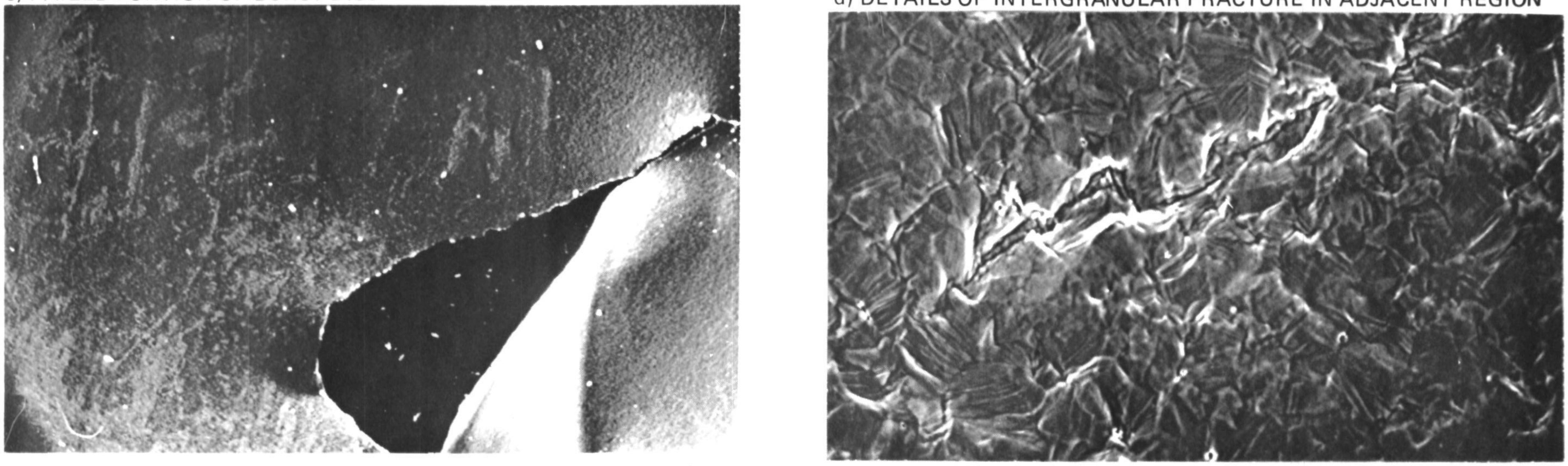

MAG: 10x

MAG: 1000x

FIG. 88

76–03–184–3

SCHEMATIC DIAGRAM OF 80 KW RF INDUCTION HEATER

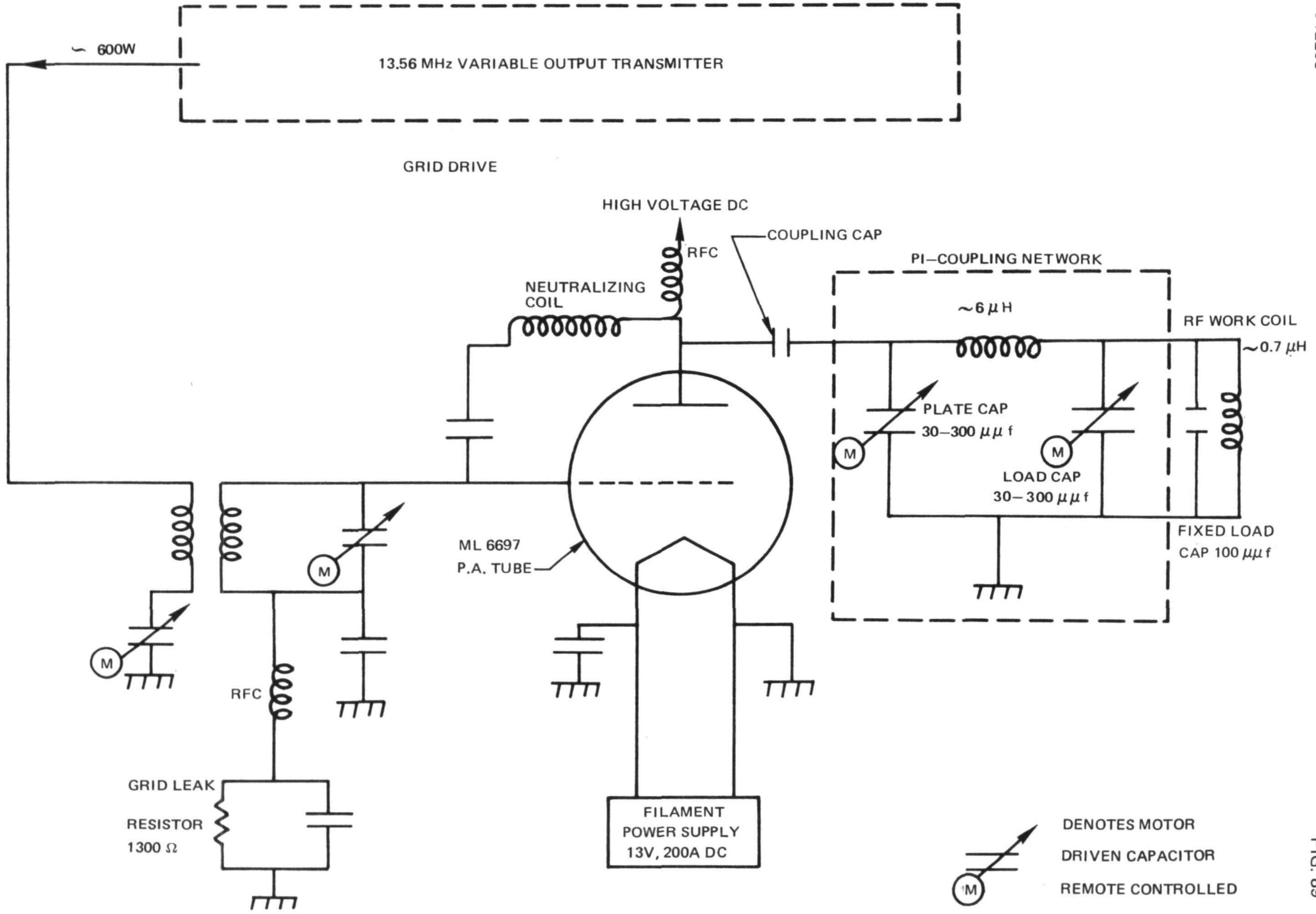

FIG. 89

FIG. 90

PHOTOGRAPH OF TEST CHAMBER EMPLOYED IN EXPLORATORY TESTS IN 80 KW RF INDUCTION HEATER

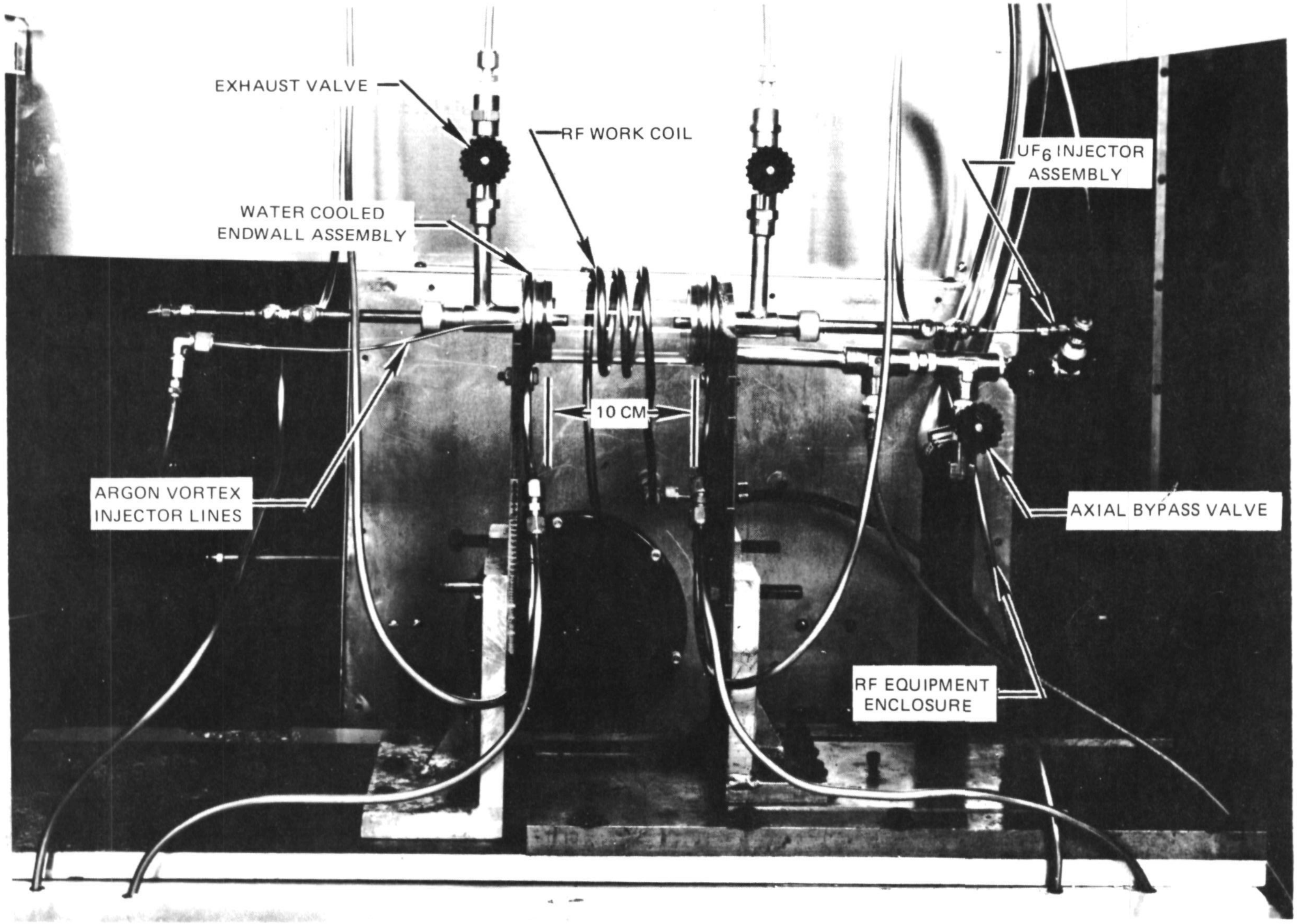

FIG. 91

SKETCH OF TEST CHAMBERS EMPLOYED IN 80 KW EXPLORATORY RF PLASMA TESTS WITH PURE UF_6 INJECTION

a) END WALL INJECTION WITH ON–AXIS THRU–FLOW EXHAUST AND PROVISION FOR AXIAL BYPASS

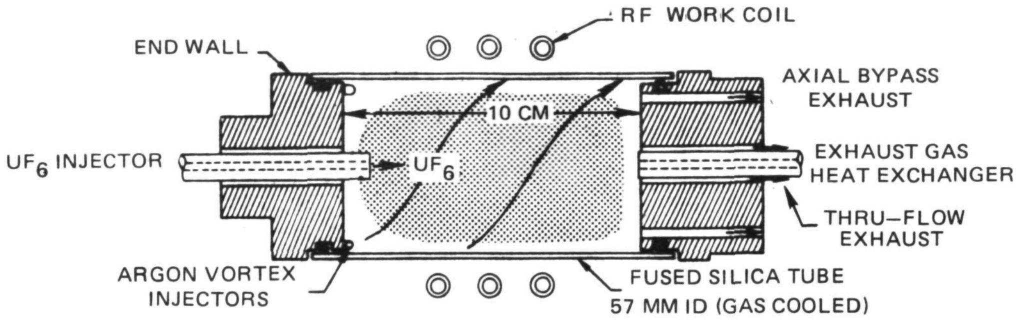

b) END WALL INJECTION WITH BLUFF BODY STABILIZATION AND ON–AXIS THRU–FLOW EXHAUST

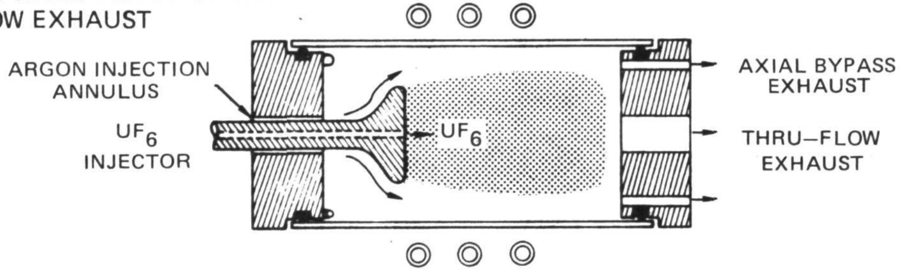

c) END WALL INJECTION WITH OFF–AXIAL ANNULAR EXHAUST

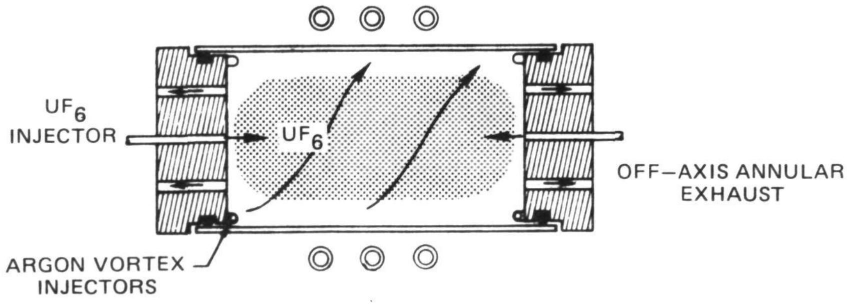

d) PERIPHERAL WALL INJECTION

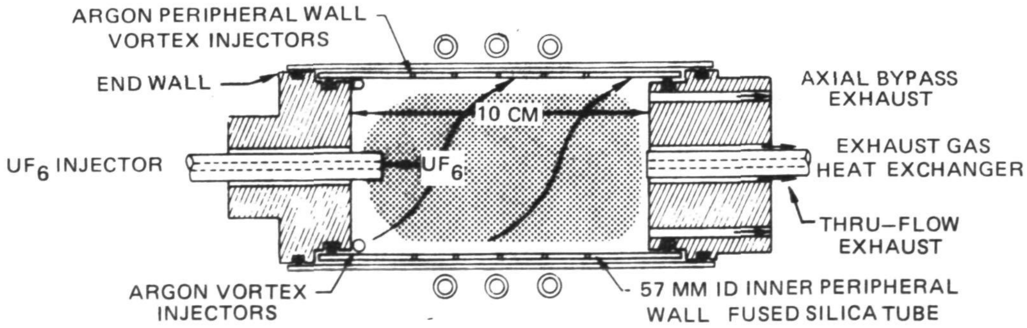

SKETCH OF CROSS–SECTION OF TEST CHAMBER EMPLOYED IN 80 KW AND (TRANSITIONAL) 1.2 MW RF INDUCTION HEATER EXPLORATORY TESTS

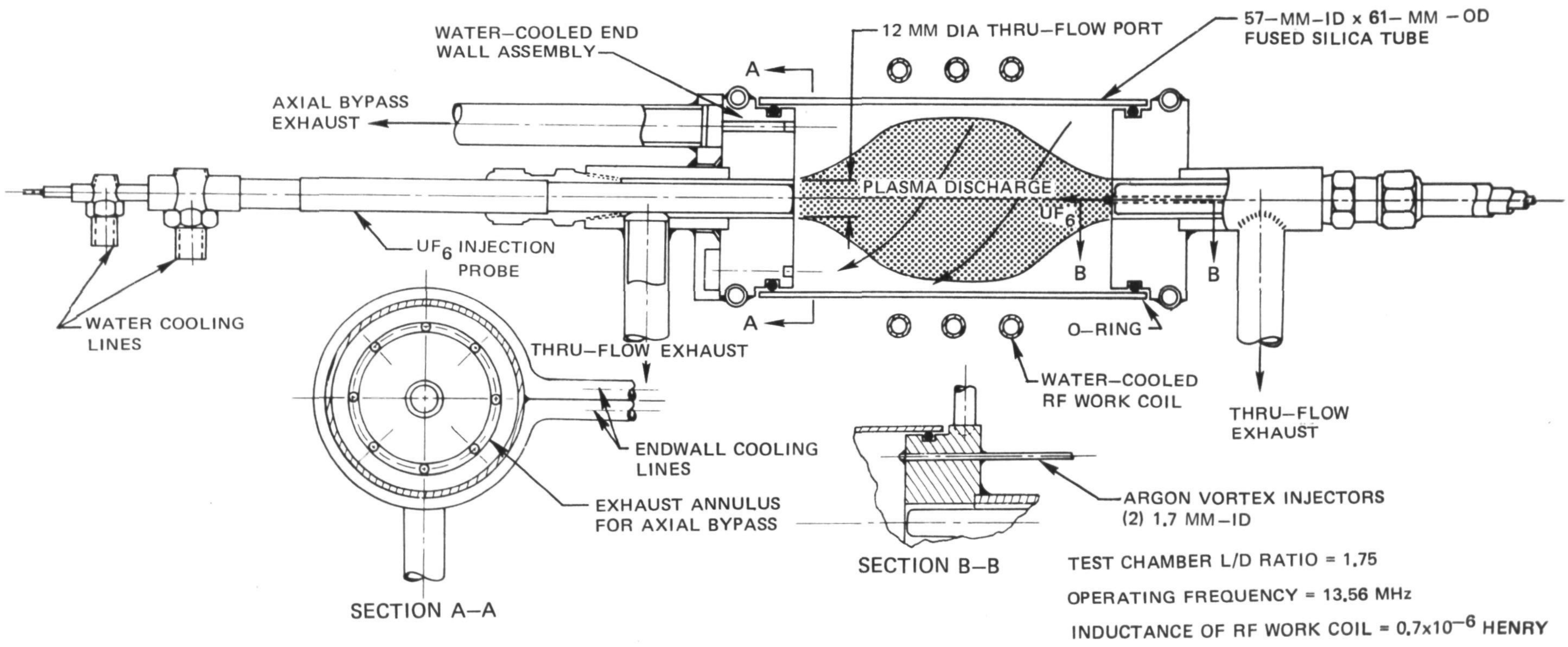

TEST CHAMBER L/D RATIO = 1.75

OPERATING FREQUENCY = 13.56 MHz

INDUCTANCE OF RF WORK COIL = 0.7×10^{-6} HENRY

FIG. 92

FIG. 93

SCHEMATIC OF DIAGNOSTIC SYSTEMS USED IN EXPLORATORY RF PLASMA TESTS

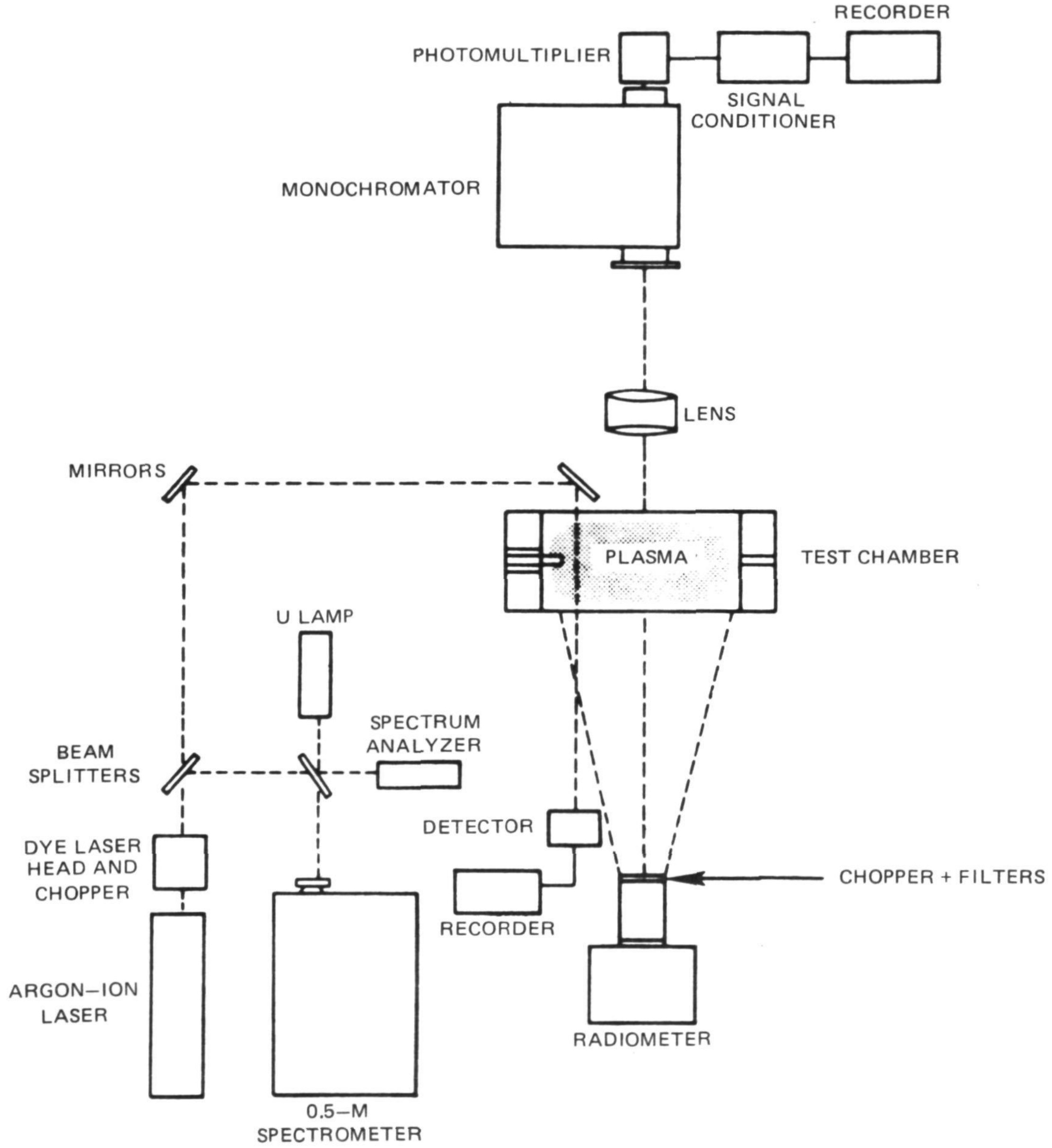

FIG. 94

TYPICAL OPERATING CONDITIONS AND RESULTS OF CORRESPONDING RADIATION MEASUREMENTS IN EXPLORATORY RF PLASMA TESTS WITH PURE UF_6 INJECTION

SEE FIG. 91(a) FOR SKETCH OF TEST CHAMBER FLOW CONFIGURATION

TESTS CONDUCTED IN 80 KW RF INDUCTION HEATER

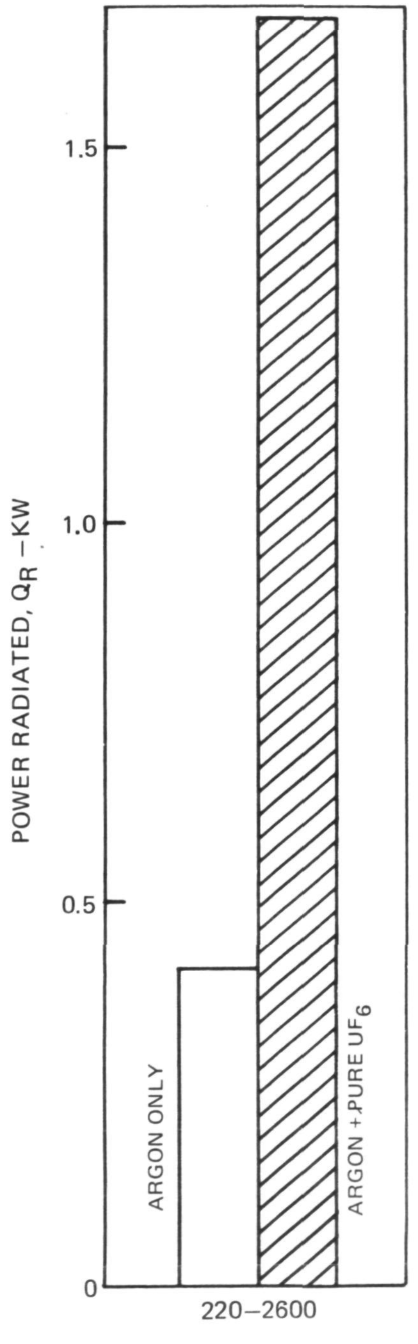

CONDITION	ARGON ONLY	ARGON + PURE UF_6 INJECTION
ARGON INJECTION FLOW RATE	0.16 G/S	0.16 G/S
ARGON INJECTION VELOCITY	57 M/S	57 M/S
UF_6 INJECTION FLOW RATE	–	0.04 G/S
UF_6 INJECTION VELOCITY	–	5 M/S
MASS RATIO, UF_6/Ar	–	0.25
POWER IN DISCHARGE	4.0 KW	7.5 KW
POWER RADIATED (220–2600 NM)	0.41 KW	1.7 KW
FRACTION OF TOTAL DISCHARGE POWER RADIATED	0.10	0.23
TEST TIME	5 MIN	4 MIN
PERCENT AXIAL BY–PASS FLOW	95%	95%
CHAMBER PRESSURE	1 ATM	1 ATM
OPERATING FREQUENCY	13.56 MHz	13.56 MHz

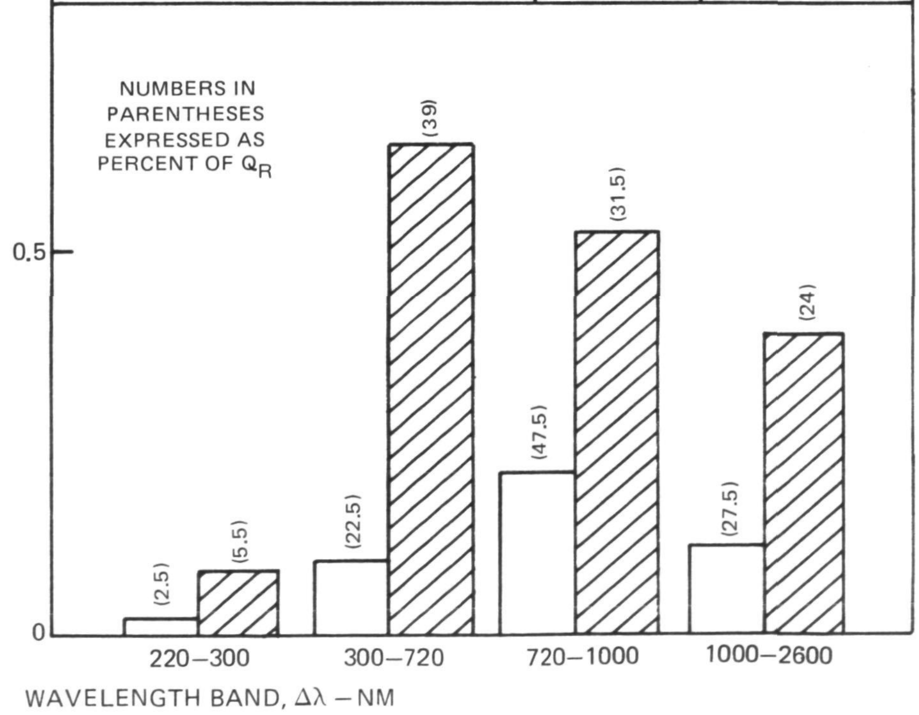

FIG. 95

PHOTOGRAPHS OF EXPLORATORY RF PLASMA TEST CONFIGURATION

a) ARGON ONLY

b) ARGON + UF_6

FIG. 96

RESULTS OF SPECTRAL EMISSION MEASUREMENTS FROM EXPLORATORY TESTS WITH PURE UF_6 INJECTION

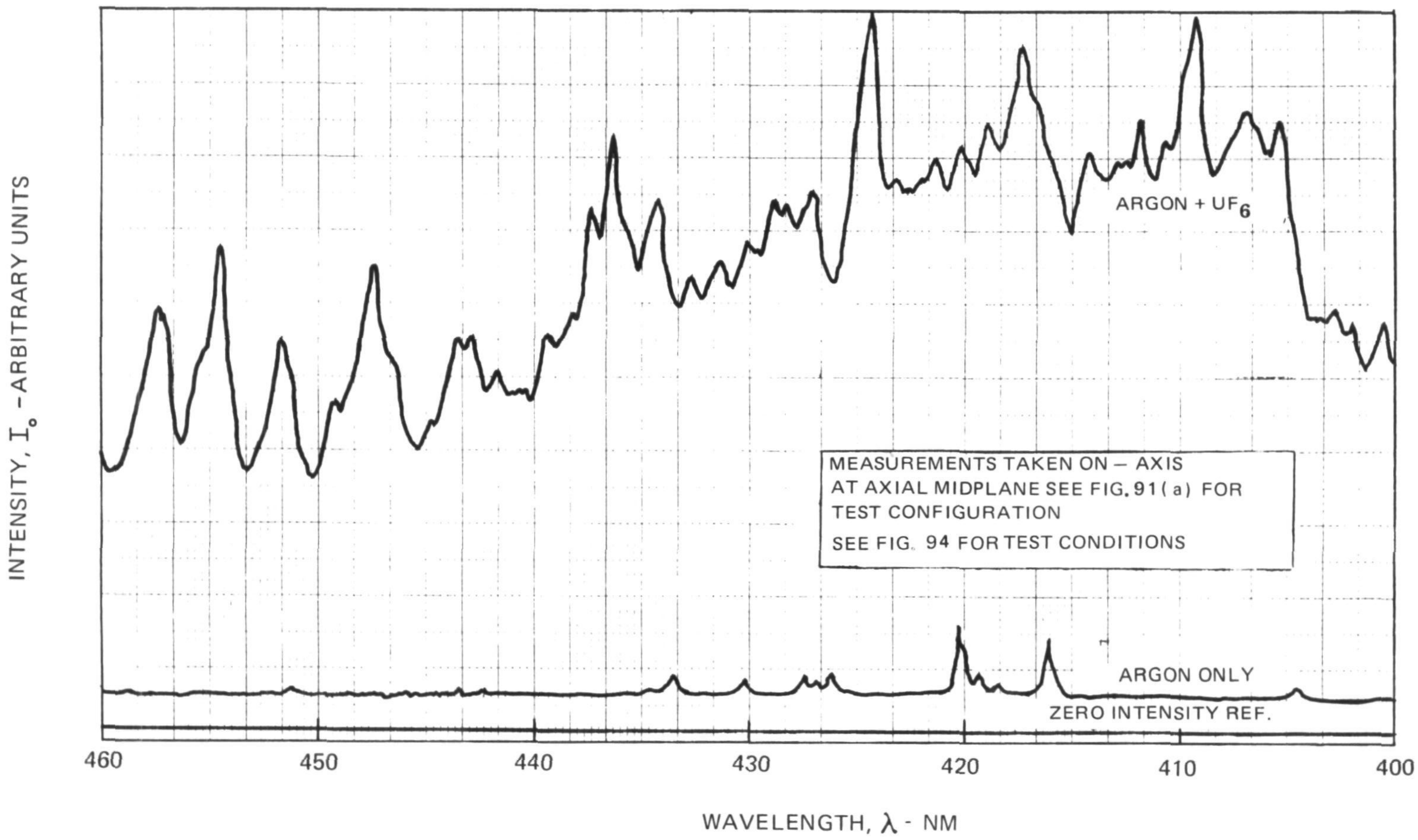

MEASUREMENTS TAKEN ON – AXIS AT AXIAL MIDPLANE SEE FIG. 91 (a) FOR TEST CONFIGURATION

SEE FIG. 94 FOR TEST CONDITIONS

FIG. 97

EXAMPLE OF ABSORPTION MEASUREMENTS OBTAINED IN EXPLORATORY RF PLASMA TESTS

SEE FIG. 93 FOR TEST CONFIGURATION AND DIAGNOSTIC EQUIPMENT

P_C = 1 ATM Q_T = 5 KW $T \approx 8000$ K L = 2 CM

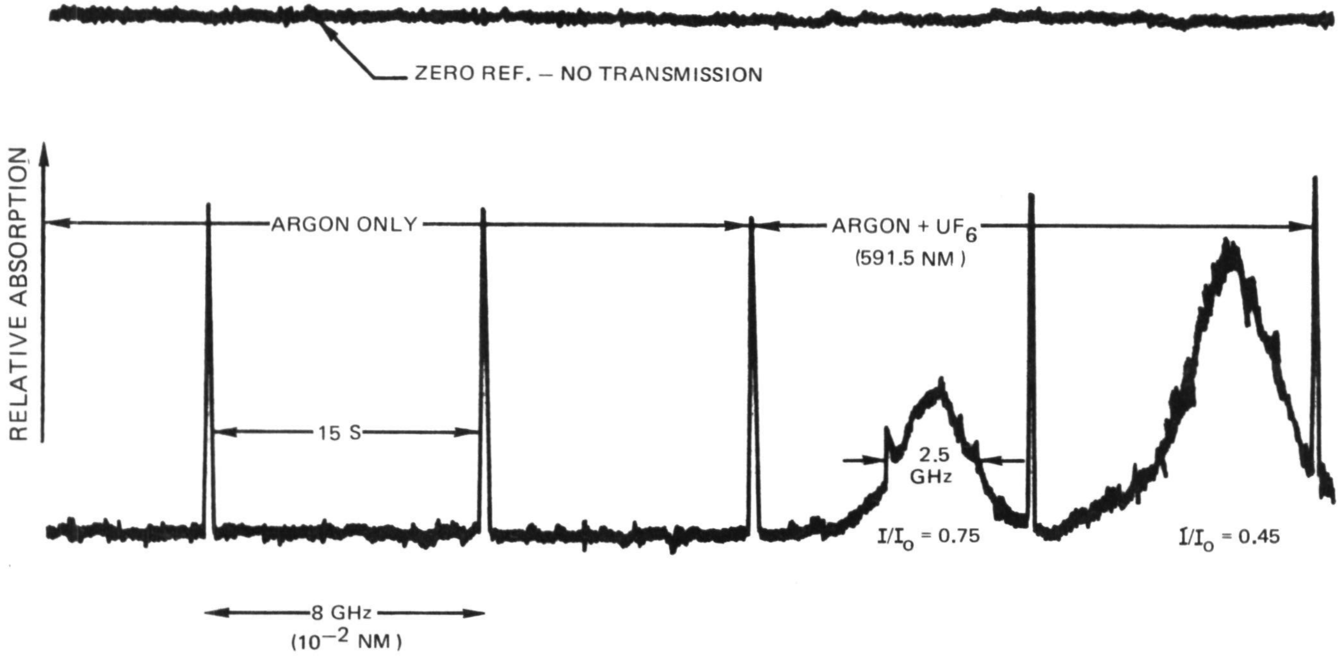

FIG. 98

PHOTOGRAPH OF FUSED SILICA TUBES USED IN 80 KW RF PLASMA EXPLORATORY TESTS WITH PURE UF_6 INJECTION

FOR CONFIGURATION SEE FIG. 91(a)

FOR CONFIGURATION SEE FIG. 91(c)

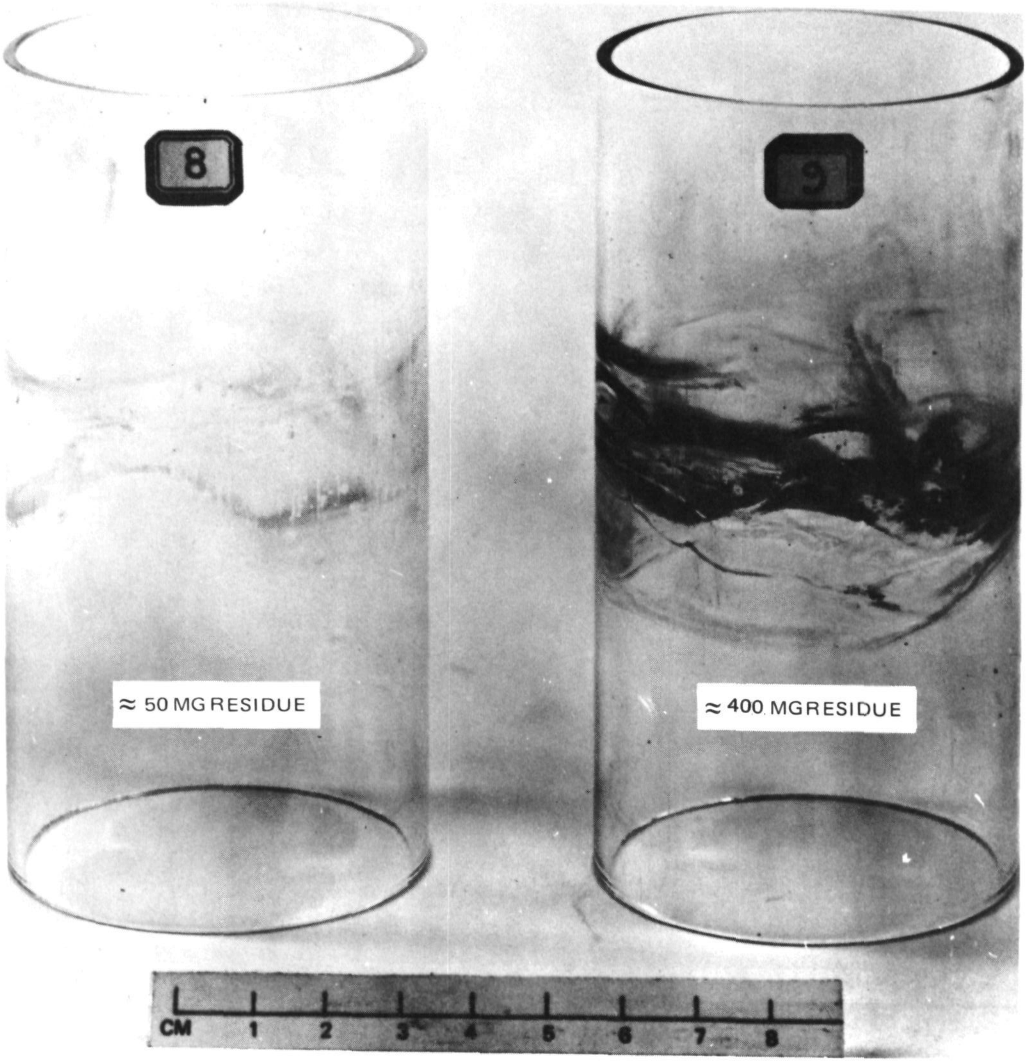

PHOTOGRAPH OF FUSED SILICA TUBES USED IN 1.2 MW RF PLASMA EXPLORATORY TESTS WITH PURE UF_6 INJECTION

SEE FIG. 8 FOR DETAILS OF TEST CONFIGURATION

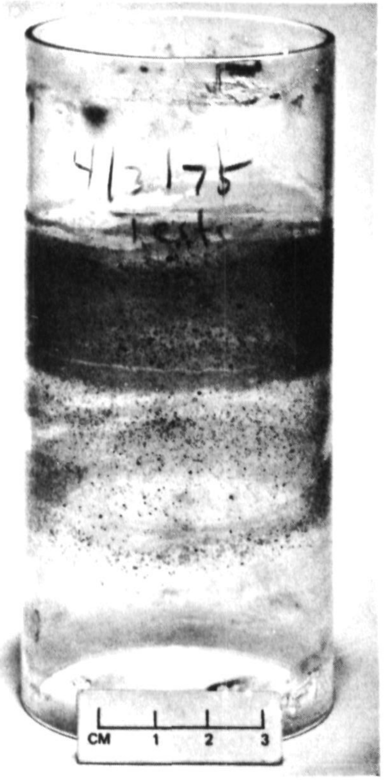

232.3 MG RESIDUE

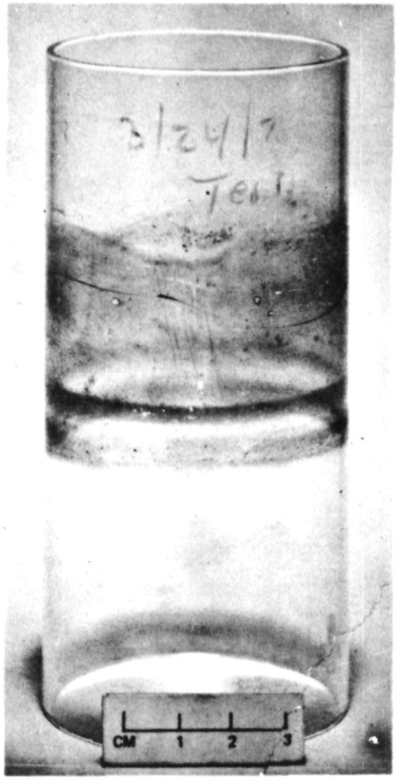

61.3 MG RESIDUE

52.1 MG RESIDUE

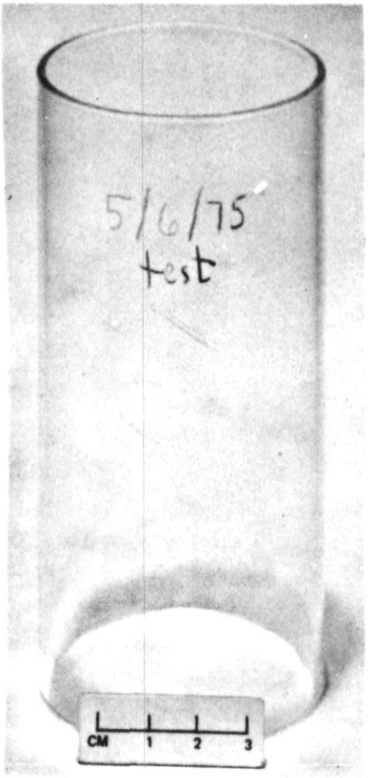

19.1 MG RESIDUE

FIG. 99

FIG. 100

EXAMPLE OF ELECTRON DIFFRACTION ANALYSIS

[UF$_4$, UO$_2$]

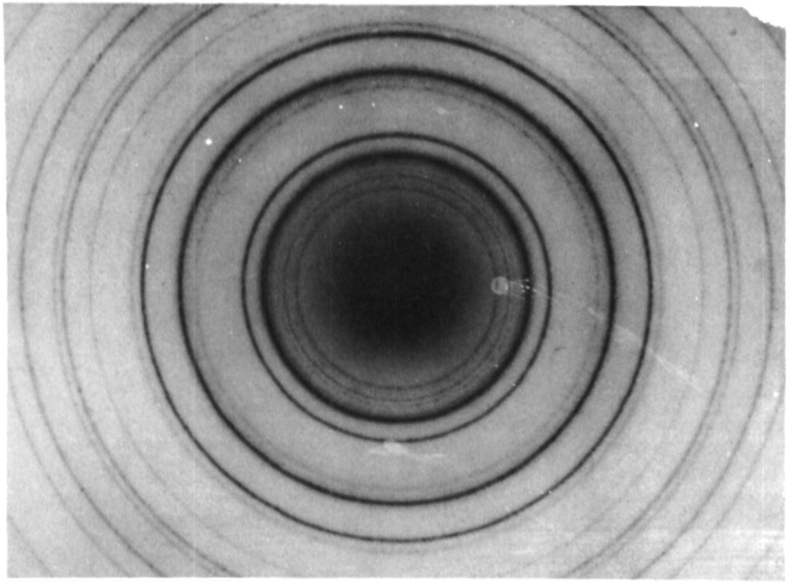

12-701

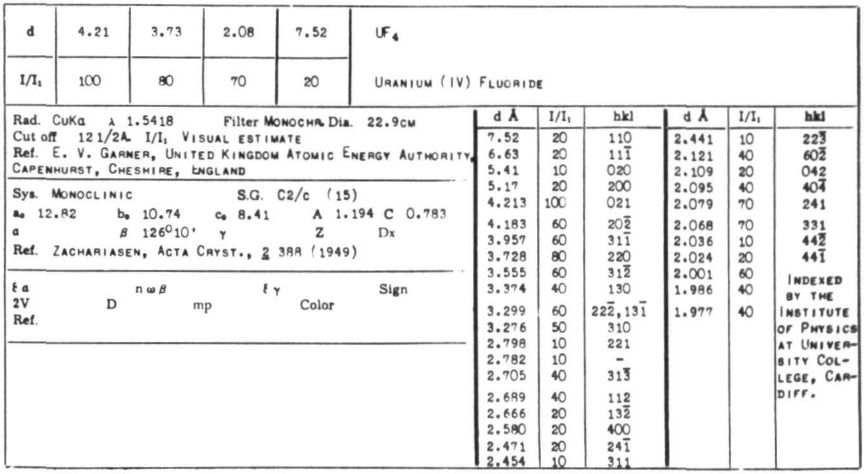

d	4.21	3.73	2.08	7.52	UF$_4$
I/I$_1$	100	80	70	20	Uranium (IV) Fluoride

Rad. CuKα λ 1.5418 Filter Monochr. Dia. 22.9cm
Cut off 12 1/2Å I/I$_1$ Visual estimate
Ref. E. V. Garner, United Kingdom Atomic Energy Authority, Capenhurst, Cheshire, England

Sys. Monoclinic S.G. C2/c (15)
a$_0$ 12.82 b$_0$ 10.74 c$_0$ 8.41 A 1.194 C 0.783
α β 126°10' γ Z Dx
Ref. Zachariasen, Acta Cryst., 2 388 (1949)

εα nωβ εγ Sign
2V D mp Color
Ref.

d Å	I/I$_1$	hkl	d Å	I/I$_1$	hkl
7.52	20	110	2.441	10	$22\bar{3}$
6.63	20	$11\bar{1}$	2.121	40	$60\bar{2}$
5.41	10	020	2.109	20	042
5.17	20	200	2.095	40	$40\bar{4}$
4.213	100	021	2.079	70	241
4.183	60	$20\bar{2}$	2.068	70	331
3.957	60	$31\bar{1}$	2.036	10	$44\bar{2}$
3.728	80	220	2.024	20	$44\bar{1}$
3.555	60	$31\bar{2}$	2.001	60	Indexed by the Institute of Physics at University College, Cardiff.
3.374	40	130	1.986	40	
3.299	60	$22\bar{2}, 13\bar{1}$	1.977	40	
3.276	50	310			
2.798	10	221			
2.782	10	-			
2.705	40	$31\bar{3}$			
2.689	40	112			
2.666	20	$13\bar{2}$			
2.580	20	400			
2.471	20	$24\bar{1}$			
2.454	10	311			

5-0550

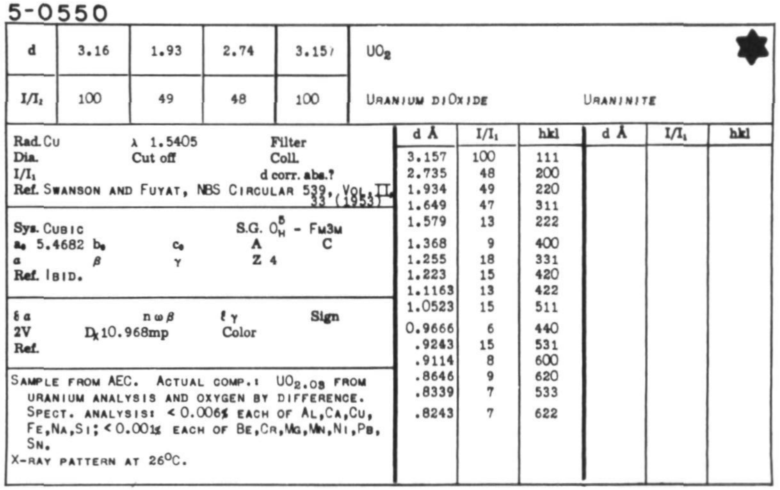

d	3.16	1.93	2.74	3.157	UO$_2$ ✸
I/I$_1$	100	49	48	100	Uranium Dioxide Uraninite

Rad. Cu λ 1.5405 Filter
Dia. Cut off Coll.
I/I$_1$ d corr. abs.?
Ref. Swanson and Fuyat, NBS Circular 539, Vol. II, 33 (1953)

Sys. Cubic S.G. O_H^5 - Fm3m
a$_0$ 5.4682 b$_0$ c$_0$ A C
α β γ Z 4
Ref. Ibid.

εα nωβ εγ Sign
2V D$_x$ 10.968 mp Color
Ref.

Sample from AEC. Actual comp.: UO$_{2.08}$ from uranium analysis and oxygen by difference.
Spect. analysis: < 0.006% each of Al, Ca, Cu, Fe, Na, Si; < 0.001% each of Be, Cr, Mg, Mn, Ni, Pb, Sn.
X-ray pattern at 26°C.

d Å	I/I$_1$	hkl	d Å	I/I$_1$	hkl
3.157	100	111			
2.735	48	200			
1.934	49	220			
1.649	47	311			
1.579	13	222			
1.368	9	400			
1.255	18	331			
1.223	15	420			
1.1163	13	422			
1.0523	15	511			
0.9666	6	440			
.9243	15	531			
.9114	8	600			
.8646	9	620			
.8339	7	533			
.8243	7	622			

FIG. 101

PHOTOMICROGRAPHS OF RESIDUE WALL COATING FROM 1.2 MW RF PLASMA TESTS WITH PURE UF_6 INJECTION

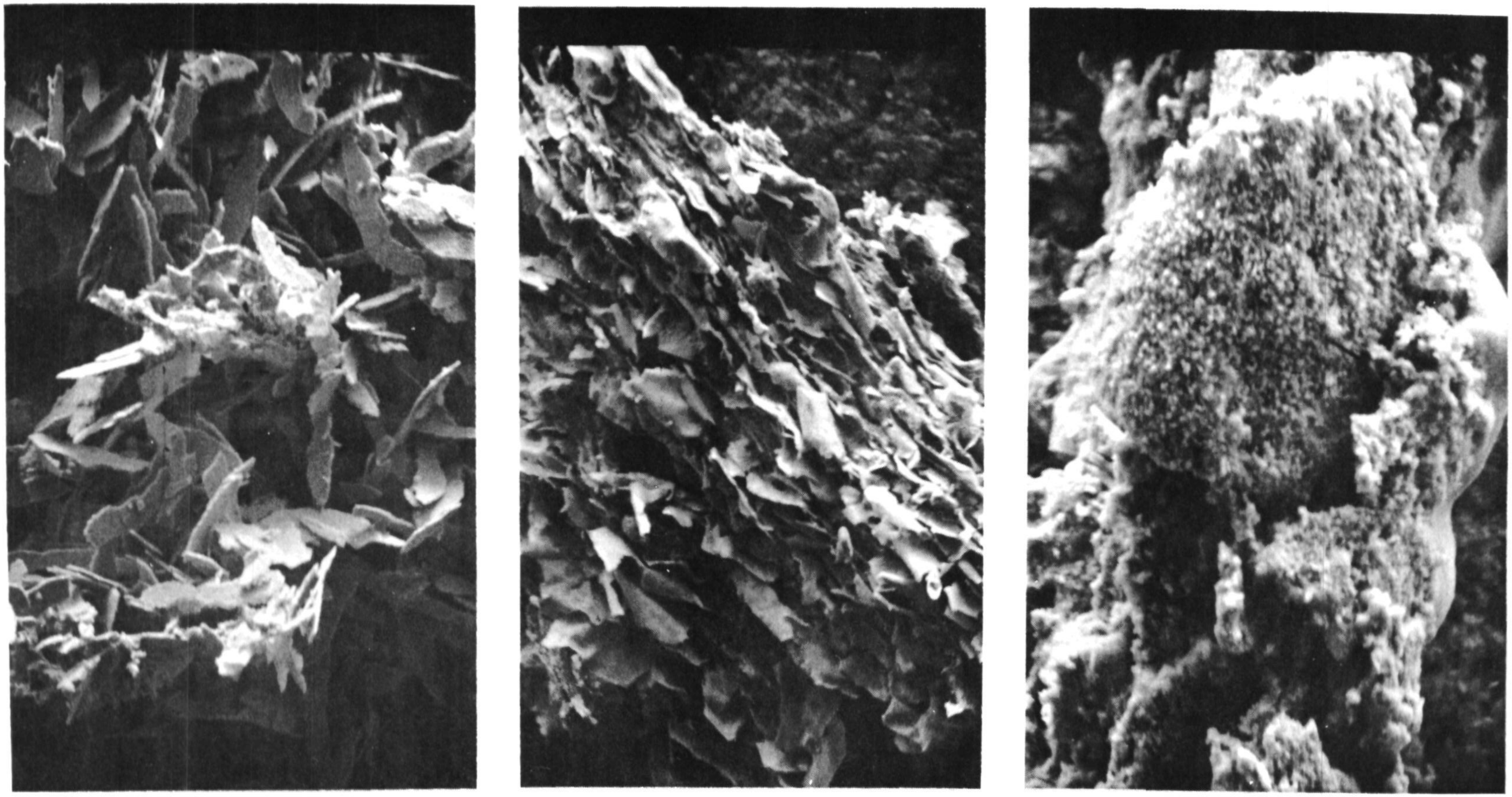

αUO_3, U_3O_8

U_4O_9, UO_2

UF_4

MAG: 800x

EXAMPLE OF X–RAY DIFFRACTION PATTERNS OBTAINED FROM POST TEST ANALYSIS OF RESIDUE WALL COATING

ALL SAMPLES SUBJECT TO COPPER kα RADIATION IN A DEBYE CAMERA

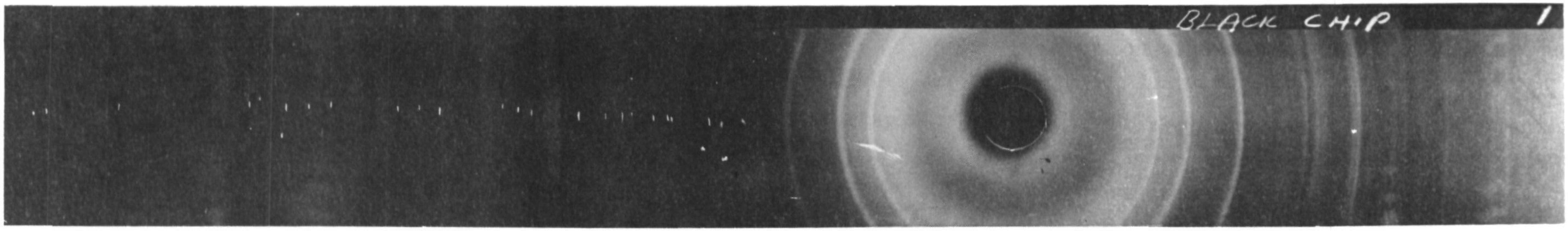

BLACK CHIP – α UO_3, U_3O_8

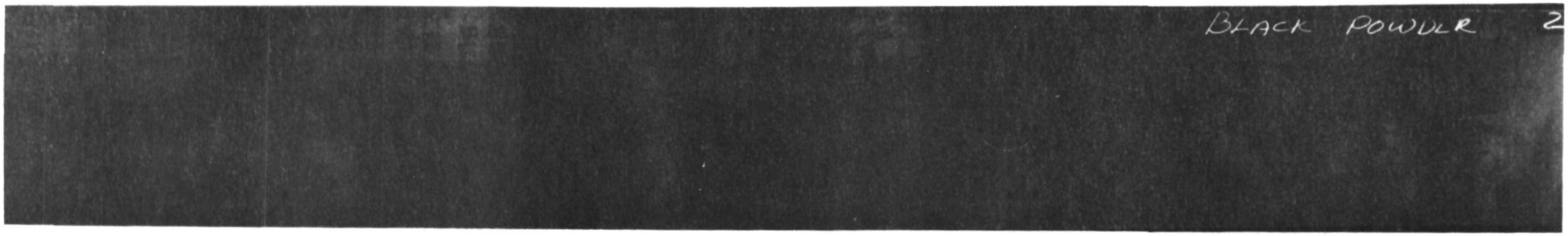

BLACK POWDER – α UO_3, U_3O_8

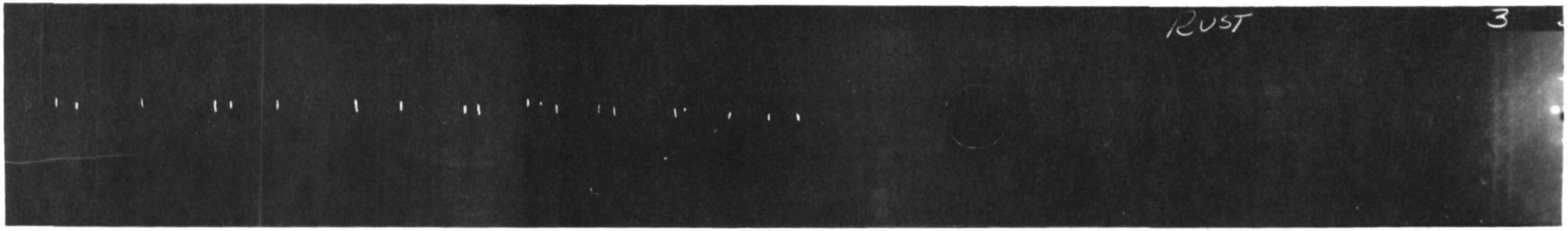

RUST POWDER – UO_2, U_4O_9

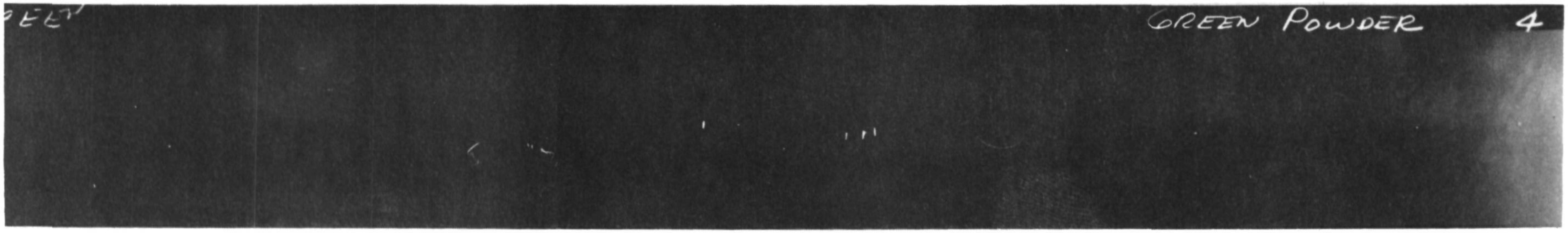

GREEN POWDER – UF_4

FIG. 102

FIG. 103

PHOTOGRAPH OF X–RAY DISTRIBUTION FOR U, F, AND O ON SAMPLE OF RESIDUE WALL COATING FROM POST TEST ANALYSIS

MAGNIFICATION: 350X

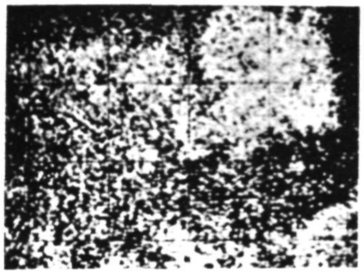

a) URANIUM

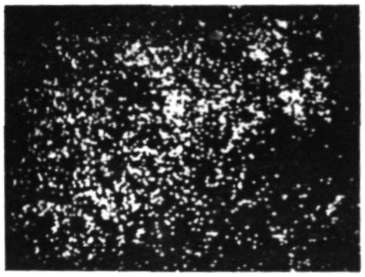

b) FLUORINE

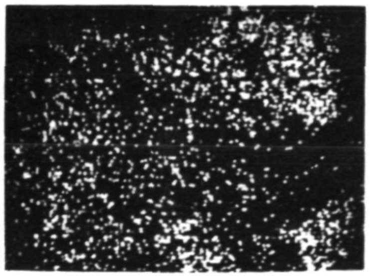

c) OXYGEN

EXAMPLE OF IR SPECTROPHOTOMETRY ABSORPTION MEASUREMENTS OBTAINED FROM POST TEST ANALYSIS OF RESIDUE WALL COATING

INSTRUMENT USED: PERKIN ELMER MODEL 457 USED IN CONJUNCTION WITH 3x–BEAM CONDENSER AND SPECULAR REFLECTANCE ACCESSORY

PREPARATION: THIN WAFER KBr MATRIX

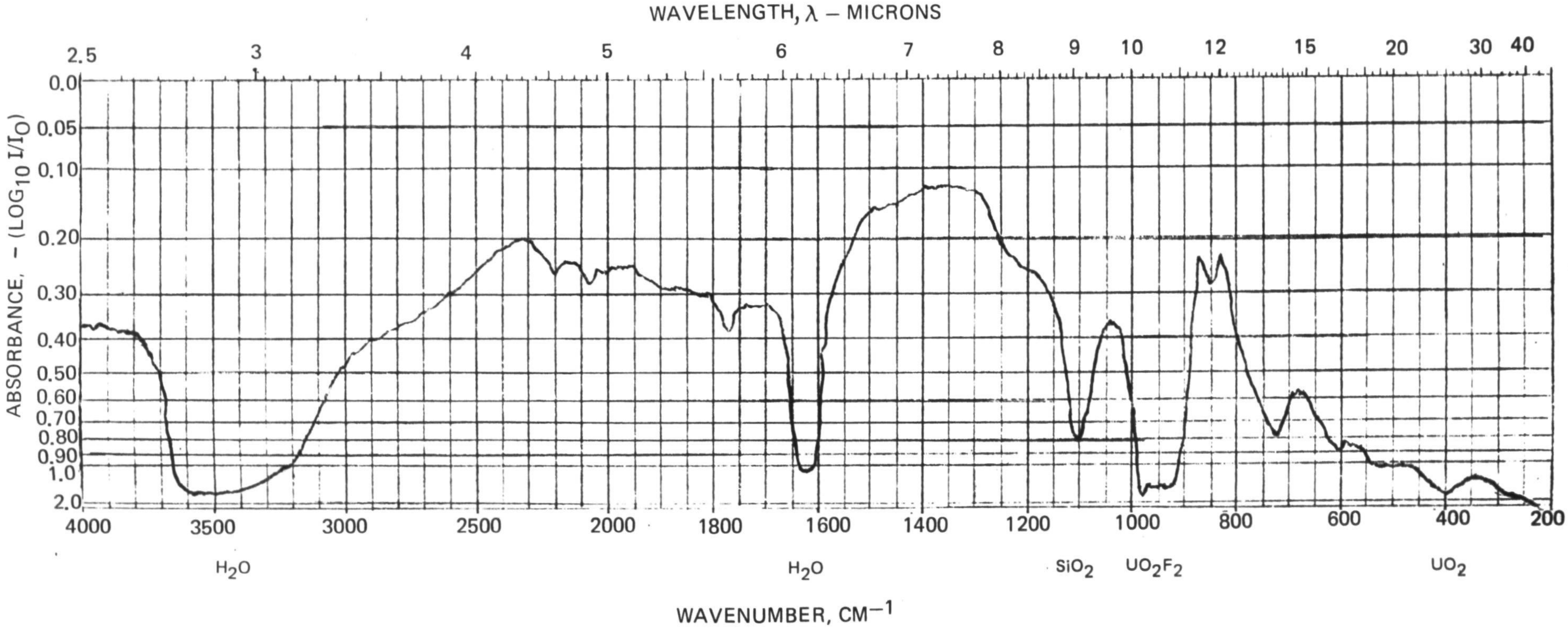

FIG. 104

FIG. 105

EXAMPLE OF ABSORPTION MEASUREMENTS OBTAINED IN 1.2 MW RF PLASMA TEST WITH PURE UF_6 INJECTION

SEE FIG. 8 FOR SKETCH OF TEST CONFIGURATION USED IN TESTS
(LASER BEAM TRAVERSED ON–AXIS AT AXIAL MID–PLANE)
SEE FIG. 93 FOR SCHEMATIC OF DIAGNOSTIC SYSTEM
(DYE LASER HEAD NOT USED IN THESE TESTS)

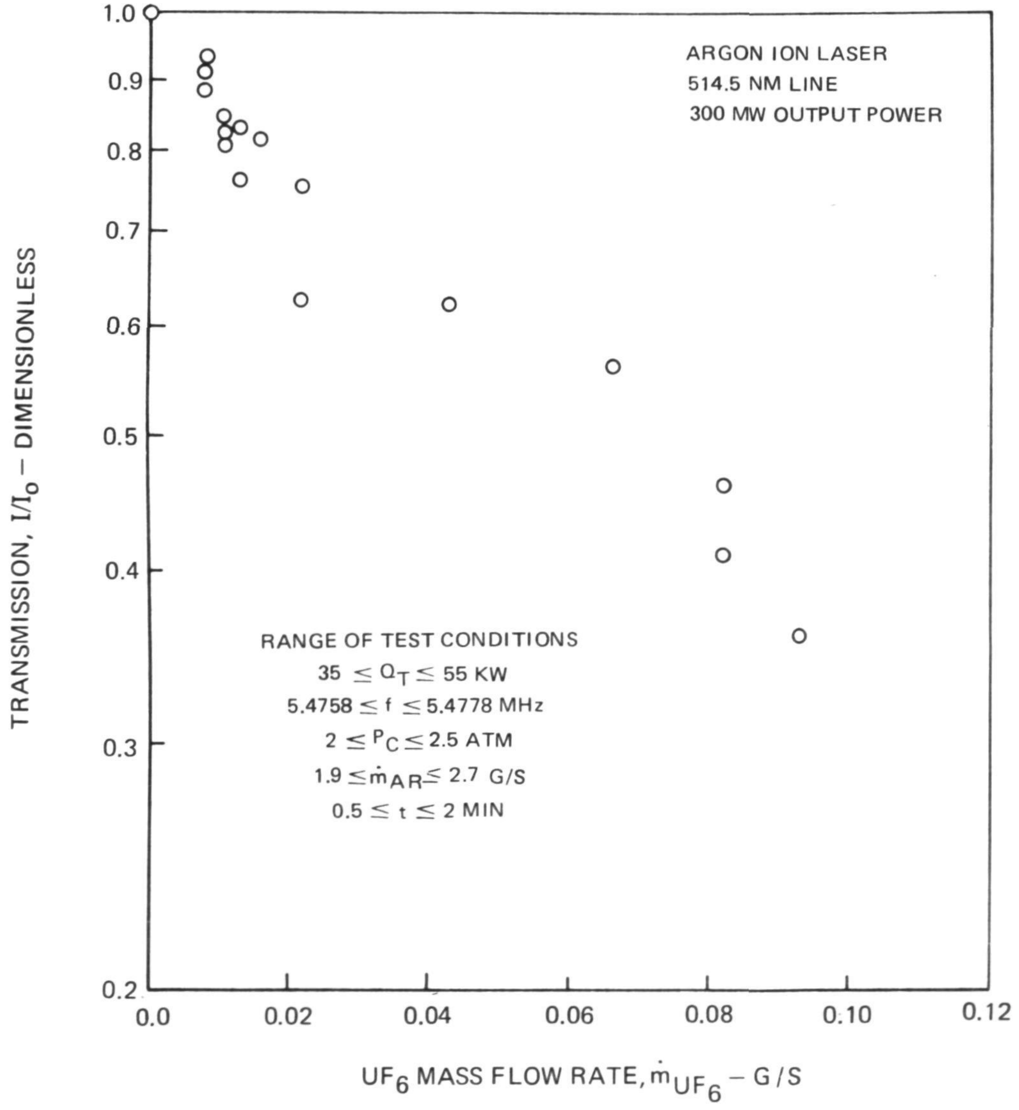

FIG. 106

PHOTOGRAPH OF RF ARGON PLASMA IN 1.2 MW RF INDUCTION HEATER TEST CHAMBER WITH PURE UF_6 INJECTION

$P_C = 2.4$ ATM $Q_T = 52$ KW f = 5.4778 MHz d = 2.9 CM

$\dot{m}_{AR} = 2.2$ G/S $\dot{m}_{UF_6} = 0.09$ G/S